UNIVERITÉ JOSEPH FOURIER - GRENOBLE I

École doctorale de Physique

THÈSE

présentée par

Martien Ilse den Hertog

pour l'obtention du titre de

Docteur de l'Université Joseph Fourier

Specialité: Nanophysique

CARACTÉRISATION DE NANOFILS DE SILICIUM PAR MICROSCOPIE ÉLECTRONIQUE EN TRANSMISSION

Soutenue le 06 mai 2009 devant la Commission d'Examen:

Professeur	Daniel LE-SI-DANG	Président
Docteur	Frank GLAS	Rapporteur
Docteur	Johan VERBEECK	Rapporteur
Docteur	Heike RIEL	Examinateur
Ingénieur	Pascal GENTILE	Examinateur
Docteur	Jean-Luc ROUVIÈRE	Directeur de thèse

Thèse préparée au sein du commissariat à l'Énergie Atomique (CEA) de Grenoble
Institut Nanosciences et Cryogénie (INAC)
Service de Physique des Matériaux et des Microstructures (SP2M)
Laboratoire d'Etude des Matériaux par Microscopie Avancée (LEMMA)

Contents

ACKNOWLEDGEMENTS

Writing this final part of my thesis fills me with dread! I have just confirmed my fears by reading that "... these last pages of a PhD thesis are the most widely read pages of the entire publication. It is here where you think that you will find out whether you have meant something in the life of the PhD candidate" (Spoon, 2003). My brain, quite fogged up after three years of thesis with exponentially increasing stress, and now utterly bewildered (but in a good way) after some vacation, will definitely forget to mention at least half of the people who have helped me, which could create a livelong wrath against me, or in the best of cases, make these people feel unappreciated. So you, whose name is not in the next few lines, I couldn't have done the work without your help and support, so please do not feel ignored, you were a great support! Also please note that the order of names is random.

Another idea that comes to mind is including some of the scientific stuff in here, so it will be actually read...

Many people have helped me during the three years of this thesis, either scientifically or by moral support. As I have written this thesis in English, learned to speak French with relatively few errors (merci Armand) during these three years and my native language is Dutch, I will address all persons in their own language.

D'abord, un grand merci à Jean-Luc, mon directeur de thèse, de m'avoir appris les bases de la microscopie électronique en transmission, ses nombreux idées et bonnes remarques, surtout dans la phase de rédaction, et son esprit dynamique. De plus j'ai énormément apprecié les discussions avec Pierre Desré sur la thermodynamique et ses explications claires, toujours données avec beaucoup de plaisir. L'étude des défauts a été énormément "boosté" par la collaboration avec Cyril. C'était un grand plaisir et avantage de travailler et de discuter sur le même sujet.

Je voudrais remercier l'équipe (INAC/SP2M/SINAPS) qui a fait croître de très jolis nanofils : Florian, Thiery, Pascal, Fabrice, Pierre Ferret, Thomas et Emmanuel. J'ai beaucoup apprécié les discussions, les idées et les échanges constructifs. Pour un microscopiste le plus important c'est d'avoir de bons échantillons, votre aide a été d'une très grande valeur. Je voudrais remercier en particulier Florian pour son aide en la thermodynamique et Fabrice pour son esprit dynamique et ses nombreuses idées.

I would like to thank all the people from IBM Zurich that were collaborating in the silicon nanowire project and where so kind to send me great nanowire samples: Heike Riel, Walter Riess, Mikael T. Björk and Siegfried Karg, and especially Heinz Schmid, who was always ready to give feedback, discuss the results and think about new samples. I appreciate this collaboration very much and hope we can continue the work in the future.

Pour les expériences : je remercie Eddy Romain-Latu (DOPT-LETI), Denis Rouchon (INPG, LEPMI - LETI), Eirini Sarigiannidou (INPG, LMGP, LTM - Minatec) et Jens Kreisel (INPG,

LMGP, UMR 5628 - Minatec) pour m'avoir aidé sur les manips raman. Violaine Salvador, Eric Gaultier et Hugo Dansas : merci beaucoup pour l'aide sur le FIB. Merci à PH pour avoir fait les images MEB de la Figure 5.17. Je remercie Carmello et Cecile pour m'avoir facilité les tâches administratives.

J'ai beaucoup apprécié l'ambiance au labo, qui existe grâce aux nombreuses personnes : Aurelien, toujours relax, Christophe (Gatel), qui m'a aidé à faire mes premiers pas en préparation des échantillons et à utiliser le 400 kV, Violaine, qui a réalisé au FIB l'échantillon clef du Chapitre 7, Hanako, qui a perfectionné mes techniques de préparation d'échantillons, Christophe (Arm), qui nous nourrit toujours avec de très bons gâteaux suisses faits par sa mère, ce qui favorise énormément la production scientifique, Guillaume, qui organise de bonnes sessions de grimpe, Pascale, la grande chef, grâce à elle, le labo tourne, Eric et PH, les hommes qui courent, Laure, toujours prête à t'aider, Dennis, merci pour m'avoir aidé à enrober les nanofils sous vide, Armand, qui a toujours corrigé mon francais ce qui est une denrée rare. C'est donc surtout grâce à lui que mon français est devenu à peu près abordable.

Furthermore I would like to thank some colleagues from LETI: David who has taught me holography and was always kind enough to help me out on the Titan when it was in a state, et ensuite Pierrette qui m'a beaucoup aidé avec les simulations du potentiel, et Michael et Peter, pour ajouter de l'ambiance en conf.

Je remercie Celine, bien que nous n'avons pas vraiment travaillé ensemble, j'ai bien apprecié les discussions de temps en temps, les déjeuners sympas et merci d'avoir corrigé le français dans ce thèse.

J'ai eu la chance de pouvoir faire ma thèse dans un projet Européen, ce que je considère comme une très bonne chose, d'une part car nous étions encadrés aussi en dehors du labo scientifique, d'autre part car ça m'a permis de voir de plus près ce qu'est un projet Européen, comment on monte ce genre de projets et quelles sont les difficultés rencontrées. C'est grâce à Isabelle Schuster, Nathalie Colombel et Robert Baptist que j'ai pu acquérir cette expérience.

Je remercie également tous mes collegues étudiants dans le projet CHEMTRONICS, et notamment Emanuela pour son support moral et Massimo, j'espère qu'on fera encore bientôt notre supermanip du siècle.

Je remercie également Jan Paul, Marion, Giovanni, Lotte, Onno, Florence, Philip, Stéphanie, Sarah, Betty, Thomas, André, Isa, Claire, Mathijs et Charles pour toutes les sorties de grimpe et de ski de rando qui font que la vie à Grenoble est tellement agréable.

Ik ben erg blij dat mijn nederlandse vrienden af en toe in of naast grenoble neerstrijken om te klimmen te skieen of te fietsen. Maaike, Hein, Heleen, Frederike, Paul, Ilona, Liesbeth, Maud, Annemiek, Tiemen, Charlotte, Nander, kom vooral nog maar vaak langs. En ook dat mijn oud huisgenootjes Karlijn, Saskia en Cyntia ook mijn nieuwe huizen komen bekijken. Ik vond het superleuk dat Anne, Rudi, Robin, Tamar, Irene, Pietje, Mimi, Nici, Robert, Femmie, Maaike, Ellen, Ilona, Paul, Nander, Karlijn, Har, Eric en Annelies helemaal vanuit het hoge noorden waren afgedaald om naar mijn promotie te komen. Heel erg bedankt! Mede dankzij jullie was het een super dag! Dank je wel Anne en Rudi voor altijd heel lief zijn en dank je wel Robin voor altijd met computer problemen helpen. Jakob: heel erg bedankt voor al je steun als ik het heel somber inzag en je hulp, je bent geweldig! Ik ben heel blij dat ik je hier heb ontmoet en dat we nu samen in een mooi huisje wonen!

The work and results reported in this publication were obtained with research funding from the European Community under the Sixth Framework Programme for the Marie Curie Host

Fellowships for Early Stage Research Training (EST) CHEMTRONICS Contract Number MEST-CT-2005-020513.

The views expressed are solely those of the authors, and the other Contractors and/or the European Community cannot be held liable for any use that may be made of the information contained herein.

Furthermore this work was supported by the ANR projects “CARTODOP” and “PREANS”.

Part I

INTRODUCTION TO NANOWIRES, ELECTRON MICROSCOPY AND SAMPLE PREPARATION

1

INTRODUCTION

Science is generally about extremes: stronger lasers, smaller particles, higher resolution or lower temperatures. We want to understand the physics of our system, control and manipulate the physical effects to our advantage so they might become useful eventually.

This thesis is about silicon nanowires that were grown using a catalyst particle, a typical example is shown in Figure 1.1. Nanowires are objects that are very small in two dimensions (50 nm = 0.00000005 m) and much longer in the third dimension (50 μm = 0.00005 m). Generally nanowires are either 'grown' or etched. Growth can be initiated using a nucleation center (for example a catalyst) and a precursor material, that supplies the atoms of the nanowire. Etching refers to a process were material is removed locally to create a nanowire. Nanowires are studied widely for their potential applications in microelectronics. In Chapter 2 the generation, history, goals and recent achievements in nanowire research are described.

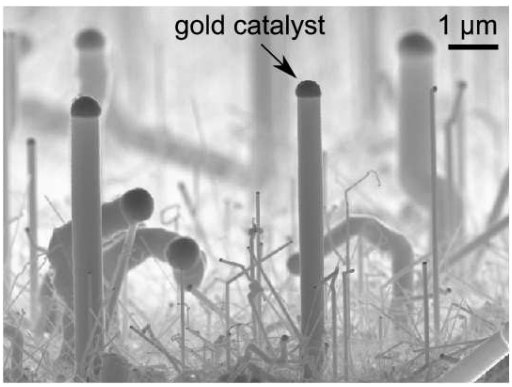

Figure 1.1: Scanning Electron Microscopy (SEM) image of a nanowire sample grown on a $\langle 111 \rangle$ oriented silicon substrate.

The goal of this thesis is to better understand and control nanowire growth by means of structural, chemical and electronic characterization, to allow integration of nanowires in devices on a longer time scale. Structural properties include the crystallographic growth direction, the presence of defects in the crystal and the facets on the nanowire sidewall. The nanowires in Figure 1.1 were grown with a gold catalyst. It seems that not all nanowires grow in the same crystallographic direction and small wires can change direction. We would like to control such phenomena. The chemistry of the nanowire is described by the chemical elements that are present besides the main component of the nanowire: silicon. Different elements that are present in the nanowire are either due to pollution from the growth chamber and the catalyst particle, or added on purpose to alter the electrical properties. In both cases we would like to know and control the location of these elements. Some elements, so called dopants, can be

present at very low concentrations (1 atom for every 10.000 atoms of silicon). Because the concentration is so low it is not possible to detect a chemical signal from these dopants. However the electronic properties of the silicon are modified because the dopant atom donates or accepts an electron from the silicon lattice. This change in electronic properties is something we can measure and indirectly we can learn the location and concentration of the dopant atoms.

The nanowires were characterized by Transmission Electron Microscopy (TEM) because of the spatial resolution of this technique with respect to the nanowire size. In TEM a very thin sample is illuminated by electrons and these electrons are detected on the other side of the sample. Several TEM based techniques were used that are described in Chapter 3. TEM is limited by two factors: the microscope and the sample. The state-of-the-art microscope, as well as other microscopes that were used, are described in Chapter 3. The advantage of nanowires for TEM is that they are already thin by themselves, therefore TEM sample preparation does not necessarily involve a thinning step that determines the sample quality. In Chapter 4 we show that the natural shape of nanowires can be used as an advantage for sample preparation.

An important feature of nanowires is that their size is very small in one dimension, resulting in a large surface area. This is exactly where and why problems arise, as phrased nicely by (Shpyrko et al., 2006): "By the time you reduce the size of an object or device down to one nanometer, practically everything is surfaces and interfaces. We need to understand what the new laws of physics and chemistry that govern the surface structures are." At surfaces and interfaces the crystal symmetry is broken and many dangling bonds remain which can create all types of defects that modify the surface properties.

Throughout this work the main unifying theme is the surface. Chemical characterization of the surface of nanowires in Chapter 5 shows that the catalyst material can diffuse over the nanowire sidewall, which modifies the sidewall faceting. Experiments show that the diffusion can be understood and controlled, which provides a tool to control the chemistry and facets of the nanowire sidewalls. In Chapter 7 active dopant atoms are detected in the nanowire volume because they locally change the electronic properties of the silicon, however the measurement is highly influenced by the surface properties, being the presence of charges at and near the surface.

Artefacts can be present in TEM images because the image is a 2D projection of the sample. Our eyes and brain routinely understand reflected light images but are ill-equipped to interpret TEM images. This was illustrated nicely by (Hayes, 1980) showing Figure 1.2:"When we see this image we laugh" (because we understand its true nature in 3D), "but when we see equivalent images in the TEM, we publish".

In Chapter 6 we show a similar artefact: different grains present in the nanowire can superpose in the image. These different grains are present due to crystallographic defects. The superposition of different crystal grains can be compared to the example in Figure 1.3. If two grids with the same spacing are overlaid with a slight angle, a new spatial frequency or spacing appears, that is not present in either one of the initial grids, a so called Moiré pattern. The same thing can happen for different crystal grains present in the nanowire and the resulting images have been attributed to a new silicon crystal structure on numerous occasions. We present clear evidence that no new crystal structure is present and the observed images and patterns are created by a superposition of different grains that are due to defects.

We will see throughout this thesis that some progress is made towards understanding and control of nanowire growth, and some findings could in principle be integrated in applications. Hopefully this PhD work can be useful to others to understand and optimize the properties of their nanowire system for the desired application.

Figure 1.2: Optical image of two Rhinoceros that are superposed. From experience we know that this is not one rhinoceros with two heads. Source (van der Walt, 2009).

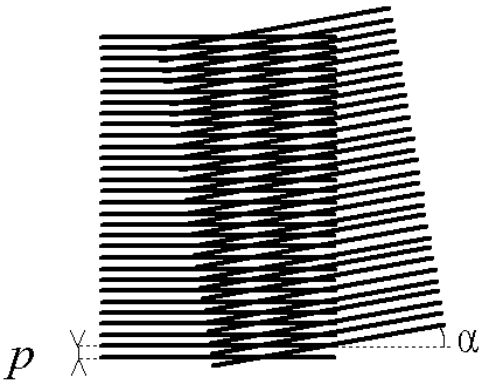

Figure 1.3: A Moiré pattern is created when two grids are overlaid with a slight angle, or if the mesh size of both grids is slightly different. Due to the rotation of one grid a new spatial frequency appears in this example (Wikipedia, 2009).

2

NANOWIRES: GROWTH, HISTORY AND APPLICATIONS

In this chapter the field of nanowire research is introduced. First it is described how a nanowire can be produced, then the history of nanowire research is recalled, ending with some recent examples. The main reasons why nanowires or nano-objects are studied is presented, as well as (potential) applications.

2.1 Nanowire synthesis

It was already stated that a nanowire is of nanometric dimensions in two directions, and larger in the third direction. Most nanowires have a diameter between 1 and 100 nm and a length of several microns. As nanowires are long in one dimension and very short in two other dimensions they are considered 1D materials. In literature many names can be found to describe similar 1D nanostructures, such as nanowhiskers, nanorods, nanobelts, nanocones and nanotubes, that refer to differences in dimensions and shape. The meaning of this nomenclature is summarized in Table 2.1 with an approximate indication of the dimensions and a reference of an example of such a structure.

Table 2.1: Nomenclature of Nanostructures

	diameter(nm)	length(μm)	cross section	Reference
Nanowires	1-100	1-100	cylinder	(Ross et al., 2005)
Nanowhiskers	$\geq$ 1000	10-1000	cylinder	(Wagner and Ellis, 1965)
Nanorods	1-100	1-2	cylinder	(Kim and Kim, 2003)
Nanobelts	1-100	1-100	rectangular	(Pan et al., 2001)
Nanocones	1-500	1-100	tapered cylinder	(Cao et al., 2005)
Nanotubes	1-100	1-100	hollow cylinder	(Iijima, 1991)

Nanowires can be synthesized either in a top down or a bottom up approach.

- Top down (Sun et al., 2005; Agarwal et al., 2008) means basically that we start with a bulk substrate and remove material locally (using lithography and etching techniques) to end up with a nanowire. This kind of nanowires can also be referred to as etched nanowires. The advantage of this approach is that very sophisticated optical and electron beam lithography methods, and (wet or dry) etching recipes, already exist for standard CMOS processing. For this reason shape, length, composition and location on the sub-

strate can be controlled very accurately and the dispersion in these parameters for an ensemble of nanowires can be very small. If electron-beam lithography is used to pattern the bulk substrate, the top down method is lengthy and expensive. The advantage of using electron beam lithography is that smaller features can be created than possible with optical lithography (Dornel et al., 2007; Dupré et al., 2008), which is faster and less expensive. The sidewalls of the nanowires can be relatively rough due to the etching process. For this reason another approach is explored which will be described in the following. However we should add that for applications in information technology the top down method seems more promising for the near future (at least for silicon nanowires), since a higher degree of control can be obtained than possible with grown nanowires, that will be described in the next section.

- Bottom up refers to a process were nanowires are grown starting from individual atoms, that are supplied by a precursor material. Usually the growth precursor is supplied as a gas, but also liquid (Tuan et al., 2008) and solid (Wong et al., 2005) precursors can be used. Generally a growth system is indicated by mentioning the phases that lead to the nanowire growth. Most often a catalyst particle (either solid or liquid during growth) is used to favor localized and directional growth of the nanostructure. A very successful method is the Vapour Liquid Solid (VLS) method where the precursor is supplied as a gas or as single atoms, that is incorporated into the liquid catalyst, from which it precipitates into a solid phase, that forms the nanowire (see Figure 2.1). If a molecular precursor (such as silane for silicon) is used that decomposes at the catalyst surface to supply the atoms to form the nanowire, the growth process is additionally described as Chemical Vapor Deposition (CVD) (used in this work). Another option is to directly supply the atoms to form the nanowire in a molecular beam, such a process is referred to as Molecular Beam Epitaxy (MBE). If the catalyst particle is in the solid phase during growth a similar growth system will be called Vapour Solid Solid (VSS) growth. In all catalyzed growth systems three steps can be distinguished: (i) the decomposition step at the surface of the catalyst particle, (ii) a diffusion step within the catalyst particle and (iii) an incorporation step from the catalyst into the nanowire.

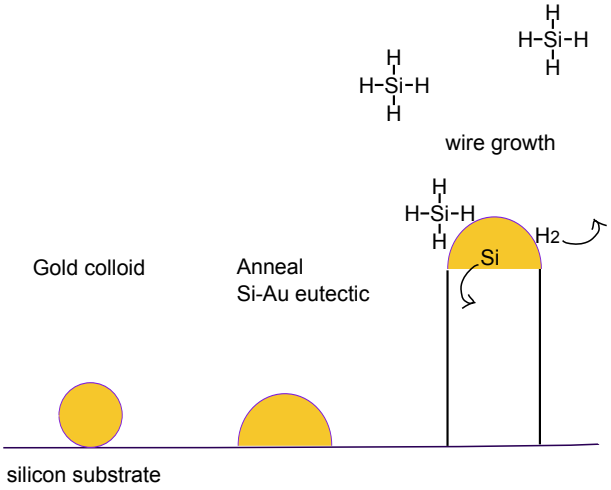

Figure 2.1: Principle of VLS growth. The gold catalyst is deposited in the form of colloids or as a thin film on the silicon substrate. The sample is annealed either to cause de-wetting of the thin film and form catalyst droplets or to remove the organic capping of the colloids. Then the precursor gas, silane, is flowed over the substrate. At the catalyst particle silane decomposes and silicon is incorporated into the catalyst particle. When supersaturation of the catalyst particle is reached, silicon precipitates at the catalyst-substrate interface, which leads to the growth of a nanowire.

in this PhD work most studied nanowires were synthesized by a bottom up approach using a catalyst particle. Therefore the bottom up approach is described in some more detail. In the bottom up approach the unidirectional growth of the crystal can be favourised by a catalyst particle, but also catalyst free growth systems are known (Park et al., 2002). A very widely used catalyst material is gold. Other metals are also reported such as Al (Wang et al., 2008), Cu (this work) (Arbiol et al., 2007), Fe (Li et al., 2005), In (Jeon and Kamisako, 2008) and Zn (this work) with varying success. Generally gold is a very successful catalyst. For the silicon-gold couple this is because Si/Au has a very deep eutectic (the silicon gold mixture becomes liquid already at 360 ^{0}C). The eutectic diagram of the gold-silicon alloy is shown in Figure 2.2. For this reason VLS growth is possible at relatively low temperatures (below 600 ^{0}C) which virtually eliminates non-catalyzed decomposition at the wire sidewalls, which is not desired as this leads to the growth of conical nanowires. The drawback of using gold as a catalyst is the possibility that gold traces remain in the nanowire volume or on the surface, which is not desired in electrical applications since gold is known to create deep traps (Tavendale and Pearton, 1983).

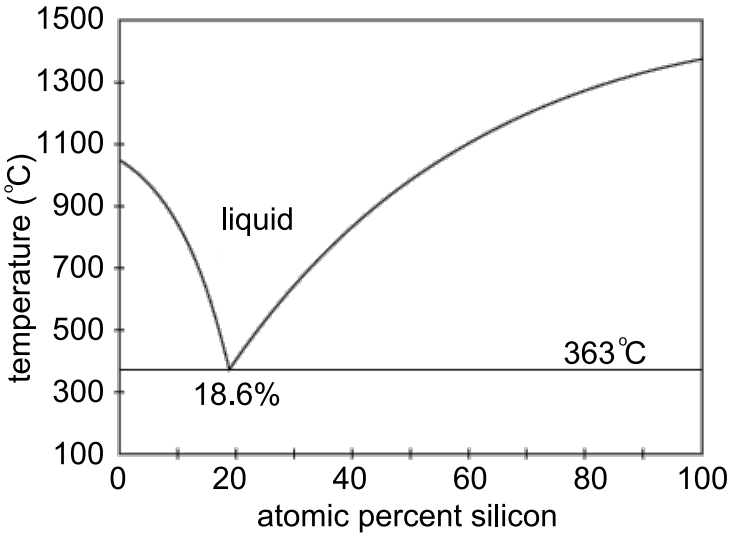

Figure 2.2: Eutectic diagram of the gold-silicon system.

In catalyst free nanowire growth systems the nucleation center for crystal growth is not very well understood and several mechanisms can be present.

The difference in growth rate of different crystallographic facets can be responsible for the nanowire growth. The normal of the facet with the highest growth rate determines the growth direction of the nanowire (Ikejiri et al., 2007). This mechanism is also found for seeded growth of for instance tellurium nanowires in solution (Mayers and Xia, 2002). The type of facets that develop can depend on the substrate orientation. Different crystallographic facets are formed with respect to the crystalline orientation of the substrate for the uncatalyzed growth of GaAs structures/nanowires (Ikejiri et al., 2007). Directional growth on only one type of crystal plane can also be induced by chemical deactivation of growth on the sidewall facets using a selective capping agent (Xia et al., 2003) or by physical prevention of growth in lateral directions, for example growth in nanopores (Buttard et al., 2008). Directional 1D growth can also be induced by a lattice mismatch between substrate and nanowire material (Park et al., 2005). Furthermore it has been shown that the polarity of the substrate surface can determine if nanowire growth occurs (Lee et al., 2008). A more extensive bibliography of nanowire growth systems can be found elsewhere (Mouchet, 2008).

2.2 History

The first work on silicon nanowires was done by Wagner and Ellis (Wagner and Ellis, 1965; Wagner, 1966; Wagner and Doherty, 1968). They managed to grow silicon wires using the Vapour Liquid Solid (VLS) mechanism using gold as the catalyst. Although the size of the wires wasn't really nanometric (the wires had diameters ranging from mm to $200\,\mu\mathrm{m}$) a lot of topics that are still relevant for the nanowire community are described in their work. They describe that nanowires are growing in three preferential crystallographic directions: $\langle 111\rangle$, $\langle 110\rangle$ and $\langle 112\rangle$. They observed defects in the nanowires, the breakup of the catalyst particle that creates branch growth, and kinking (a change of growth direction) of the nanowires. An effect of temperature gradient on kinking probability was found (Wagner and Doherty, 1968). This paper is still one of the few papers to indicate the cause of kinking (although a temperature gradients is certainly not the only cause for kinking).

An important question, that has puzzled the nanowire community since the beginning, is whether the diameter of the nanowire has an effect on the growth velocity. In early literature (Givargizov, 1975) it is observed that small diameter nanowires are shorter after the same growth time. This is interpreted using thermodynamical analysis to be due to Ostwald ripening (or the Gibbs-Thomson effect) that causes larger diameter nanowires to grow faster than small diameter nanowires. It was found that the rate limiting step is the decomposition at the catalyst particle. In literature it is generally agreed that the diffusion step is fast and no concentration gradients are present in the catalyst particle. In recent literature it is shown that depending on the growth conditions either the decomposition step or the incorporation step can be the rate limiting step (Schmidt et al., 2007a). Also it is shown that the thermodynamic analysis can lead to false conclusions as equilibrium/reversibility is not guaranteed especially in the decomposition step (Oehler et al., 2009b).

Very interesting results were obtained more recently by in-situ Transmission Electron Microscopy (TEM). It was shown that the growth velocity is independent of wire diameter (Kodambaka et al., 2006b)[1] and that gold is diffusing from the smaller catalyst particles over the nanowire surface to the larger catalyst particles, which leads to tapering of the nanowire (Hannon et al., 2006). High resolution in-situ TEM showed that in a nanowire growth system with a solid catalyst the growth proceeds via ledge flow (Hofmann et al., 2008). Three groups can be identified to be world leaders in nanowire research: Charles Lieber's group at Harvard (U.S.), Lars Samuelson's group in Lund (Sweden) and Ulrich Gösele's group in Halle (Germany).

2.3 Goals and applications of nanostructure research

Several research goals can be distinguished in the very broad field of nanostructure research. First there is obviously the discovery of new physics. Since nanowires are very small in one direction, they are regarded as 1D materials. The confinement in one or more directions can give rise to physical properties very different from the bulk material.

The other reason to study nanostructures, such as nanowires or nanotubes, is the numerous potential applications, for example their application as composite materials (Ajayan et al., 2000; Allaoui et al., 2002) or meta-materials (Yao et al., 2008), as sensors (Agarwal et al., 2008; Verd et al., 2005; Penzaa et al., 2008) and as building blocks in nanodevices (Björk et al., 2008) (Lee et al., 2007). Furthermore carbon nanotubes are studied for their electrical transport properties

[1] The growth velocity is independent of wire diameter due to the (UHV) growth conditions (Schmidt et al., 2007a).

(Kilbride and et al, 2002) (Benoit et al., 2002) and high thermal conductivity (Choi et al., 2001). Nanowires are extremely promising as electrical devices (Björk et al., 2008), electro-optical devices (Lee et al., 2007), solar cells (Tsakalakos, 2008; Kempa et al., 2008) and as anodes in lithium batteries (Chan et al., 2008). Nanowires seem also very promising for thermoelectric applications (Hochbaum et al., 2008) since the surface roughness suppresses the thermal conductivity by increasing the phonon scattering (Moore et al., 2008). Surface roughness in silicon nanowires is a topic closely related to the faceting of the nanowire sidewall in the growth direction. It was shown by (Ross et al., 2005) that the sidewall of silicon nanowires exhibits a periodic faceting in the growth direction of the nanowire. In Chapter 5 it is shown that this type of faceting is due to the presence of gold on the nanowire sidewall. This provides a tool to actively design a nanostructure for its purpose.

Also nanowires have very interesting optical properties. A recent and very exciting example is that bulk metamaterials made of nanowires show a negative refraction index for all incident angles in the visible region (Yao et al., 2008).

Other applications of nanowires and tubes make use of the large change in their resistivity (and/or the corresponding change in resonance frequency) if molecules absorb to the sidewall. These effects can be used to produce sensors and actuators (Nano- Electro- Mechanical-Systems (NEMS)) with very high sensitivity, that operate at high frequency (100 MHz) (He et al., 2008; Agarwal et al., 2008; Penzaa et al., 2008; Verd et al., 2005).

Especially silicon nanowires are very interesting for electrical applications in information technology since they are compatible with CMOS technology and might favourize the use of the third dimension on a chip. However successful introduction of nanowires into a device requires good control over surface properties and doping. Doped nanowires have been reported using both top down methods (Kempa et al., 2008) and bottom up methods (Björk et al., 2008; Yang et al., 2005).

However the dopant distribution (Diarra et al., 2007) and activity (M. Fernández-Serra and Blase, 2006) can be influenced by the size of the nanostructure, therefore it seems very important to characterize the electrical properties of the nanowires indirectly by transport measurements (Björk et al., 2009) and directly by measurement of doping concentration and distribution. In the following an overview of possible techniques to detect dopants is presented, including their capabilities and limitations.

2.4 Need for characterization of nanostructures

Since nano-objects are becoming smaller and characterization techniques are steadily improving, it is now possible to probe the atomic structure of a nanowire in 3D. The detection of single gold atoms inside a silicon nanowire by Scanning Transmission Electron Microscopy (Allen et al., 2008) is an excellent example.

For the architecture of nanodevices it is of great importance to be able to control the electrical (and optical) properties down to the atomic level. This is a problem for nanostructures, since no characterization technique exists that can probe active dopant atoms in the volume of the structure with nm-scale spatial resolution.

Techniques do exist to obtain information on dopant distribution on surfaces, such as Scanning Spreading Resistance Microscopy (SSRM) (Eyben et al., 2005), Scanning Capacitance Microscopy (SCP) (Biberger et al., 2008), Kelvin Force Microscopy (KFM) (Ligowski et al., 2008) or

Scanning Tunneling Microscopy (STM) (Berthe et al., 2008), however these techniques involve putting a small scanning tip onto the specimen which would prove problematic in the case of a nanowire. Techniques to directly measure dopant atoms in the volume such as Scanning Transmission Electron Microscopy (STEM) (in combination with Electron Energy Loss Spectroscopy (EELS)) (Voyles et al., 2002; Molina et al., 2007), Secondary Ion Mass Spectroscopy (SIMS) (Zelsacher et al., 2007) or Atom Probe Tomography (ATP) (Hoummada et al., 2007; Blavette et al., 1999) can map successfully the (3D) dopant distribution in the volume of the sample. However these methods are sensitive only to the chemistry of the structure[2], not the electronic properties, therefore no information on the activity of the dopant atoms is obtained, which becomes very important in nano-scaled devices (Diarra et al., 2007; M. Fernández-Serra and Blase, 2006).

Electron Holography has been successfully used to map active dopant distributions in bulk semiconductor devices (Rau et al., 1999; Cooper et al., 2007a; Twitchett et al., 2004), but to date no record exists that uses this technique on thin nanostructures such as nanowires[3]. It has been supposed that electron holography is not suited to analyze nanostructures since the signal obtained using this technique depends on both the thickness of the specimen and the specimen surfaces that can cause depletion through the volume of the wire (Cooper et al., 2008). A certain specimen thickness is required to provide enough material to cause a detectable phase shift, this depends both on doping concentration and the specific material. Relatively thick (100 - 500 nm) bulk specimens are routinely studied by electron holography (Cooper et al., 2007a; Twitchett et al., 2004). A problem observed in conventional specimens prepared from silicon wafers is that part of the thickness of the sample doesn't contribute to the phase signal: the so called inactive layer (Rau et al., 1999). The inactive layer is strongly dependent on the dopant concentration and can be more than 100 nm thick (Cooper et al., 2008), which leads to a lower value of the built in potential. This surface layer is mostly due to damage caused by the Focussed Ion Beam (FIB) milling during sample preparation (Rau et al., 1999), but surface depletion will also contribute (Twitchett-Harrison et al., 2007; Sze, 1985). In spite of this issues we will show in Chapter 7 that active dopant detection is possible in nanowires.

Electron microscopy is an important tool to improve knowledge about nanostructures due to its high spatial resolution. In this work Transmission Electron Microscopy was used as the main tool to study silicon nanowires. Details about this technique are presented in Chapter 3. In Chapter 5 the surface properties of the nanowires are discussed, which are influenced by the gold diffusion. Also the gold diffusion itself, and parameters to control this diffusion, are studied. In Chapter 6 the crystal structure of nanowires is described in more detail and it is shown that more or less complicated defects can be present in the nanowire volume, depending on catalyst material. In Chapter 7 we will show that state of the art off-axis electron holography is capable of detecting active dopants in nanowires as thin as 60 nm.

[2] EELS is also sensitive to the electronic structure

[3] To our knowledge one record exists where holography on nanowires is reported (Chung and Rabenberg, 2006). In this publication relatively thick (200-300 nm) core-shell nanowires were studied.

3

ELECTRON MICROSCOPY

In this chapter the electron microscopy techniques used in this work are described. The main aim of this chapter is to briefly recall the relevant theory that is necessary to analyze the experimental part of this PhD work. The most important source is "Transmission Electron Microscopy " (Williams and Carter, 1996), a very complete, readable and enjoyable microscopy book. First we describe which microscopy techniques were used and why these techniques were used. Then the relevant theory of each microscopy technique will be recalled briefly. Some more attention will be paid to electron holography, since this technique is relatively new to the toolkit of the electron microscopist, especially at CEA-Grenoble. At the end of the chapter characterizing properties of the microscopes used in this work are given.

3.1 Questions and Techniques

The aim of this PhD work is to characterize the structural, chemical and electrical properties of silicon nanowires. As no specific technique exists that probes all these properties simultaneously, different microscopy techniques were used. The following properties were most interesting to us, and studied with an appropriate technique:

1. The crystallographic growth direction and size of the nanowires were studied using High Resolution TEM (HRTEM) and electron diffraction (Chapter 6).

2. The epitaxial relationship between nanowires and growth substrate was studied using HRTEM and diffraction (Chapter 6).

3. The presence or absence of defects was studied using HRTEM and electron diffraction (Chapter 6).

4. The nanowire sidewall properties were studied using Scanning Transmission Electron Microscopy (STEM), HRTEM and diffraction (Chapter 5). The sidewall can be smooth or faceted, in which case different crystallographic facets can be present.

5. The behavior of the gold catalyst particle was investigated. Traces of the catalyst particle can remain on the nanowire sidewall depending on growth conditions. Scanning Transmission Electron Microscopy (STEM) was used routinely in high and low resolution, mainly on nanowires grown with a gold catalyst. This technique was used to study the amount of gold present on the nanowire sidewalls and its distribution, using a High Angle Annular Dark-field (HAADF) detector. Energy Dispersive X-ray Spectroscopy (EDX)

was used to verify if the bright clusters observed on gold catalyzed nanowires were indeed gold (Chapter 5).

6. The modification of the crystal potential due to doping was measured using off axis electron holography. Holography was used to measure the crystal potential of undoped nanowires, and to measure the change in crystal potential between doped and undoped regions of the same nanowire with the aim of determining the doping concentration (Chapter 7).

First, the TEM and STEM technique, used for point 1-4, will be recalled in the next two section. TEM and STEM are the two approaches that can be used to illuminate the sample with electrons. In TEM the sample is illuminated with a parallel electron beam and an image is obtained. In STEM a small probe is scanned over the sample and the intensity on the detector at each point is recorded to form the image. At the end of Section 3.3 it will be shown that the relation between both methods can be described by the theory of reciprocity. The theory of reciprocity predicts that if certain conditions are fulfilled, the same image can be obtained using both methods. Second, the techniques used for point 5 and 6 are described, that are variations on either STEM or TEM techniques.

3.2 Transmission Electron Microscopy

In the following the process of image formation in a TEM is recalled briefly and the concept of the transfer function is introduced. This will illustrate the resolution limit of TEM based techniques and how the resolution is influenced by imperfections of the electron source and the optical system .

For readers unfamiliar with TEM, more basic details and advantages of TEM can be found in Appendix A.1 and Appendix A.2.

In TEM a material is studied using electrons that are both particle and wave. The electron wave, after it has passed through the specimen, is called the object wave, which has an amplitude $a(\overrightarrow{r})$ and a phase $\phi(\overrightarrow{r})$ and its wave function can be written as

$$\psi(\overrightarrow{r}) = a(\overrightarrow{r})e^{i\psi(\overrightarrow{r})} \tag{3.1}$$

The object wave passes trough the objective lens and is magnified by the projector system. The objective lens introduces abberations that can be described by the contrast transfer function (CTF) of the microscope $T(\overrightarrow{q})$, given by (Williams and Carter, 1996)

$$T(\overrightarrow{q}) = A(\overrightarrow{q})E(\overrightarrow{q})\exp(i\chi(\overrightarrow{q})) \tag{3.2}$$

where $A(\overrightarrow{q})$ is the aperture function and $E(\overrightarrow{q})$ is the envelope function. Both the aperture and the envelope function have the effect of damping the CTF at higher spatial frequencies. The envelope function is influenced both by the spatial and temporal coherence of the electron source. The envelope function can be written as (Völkl et al., 1999)

$$E(\overrightarrow{q}) = K_S(\overrightarrow{q})K_T(\overrightarrow{q}) \tag{3.3}$$

where $K_S(\overrightarrow{q})$ is the spatial envelope function (also called the source envelope) and $K_T(\overrightarrow{q})$ is the temporal envelope function that is influenced by the defocus spread caused by chromatic abberations, instabilities in the high tension and objective lens current and mechanical vibrations (Fejes, 1977), and given by

$$K_T(\overrightarrow{q}) = \exp\left(-\left(\frac{(\pi\Delta\lambda\overrightarrow{q}^2)^2}{2}\right)\right) \tag{3.4}$$

where Δ is defined as the defocus spread that depends on instabilities of the high tension, the energy spread of the emitter and the objective lens current ripple. $K_S(\overrightarrow{q})$ describes the influence of the finite size of the source on the spatial coherence and is generally written as (Frank, 1973)

$$K_S(\overrightarrow{q}) = \exp\left\{\frac{\left[\pi\delta(\Delta f\overrightarrow{q} + C_s\lambda^2\overrightarrow{q}^3)\right]^2}{\ln 2}\right\} \tag{3.5}$$

where C_s is the spherical aberration of the objective lens, Δf is its defocus and δ is the illumination angle (see Appendix A.3).

The most important component of the transfer function, the phase distortion function $\chi(\overrightarrow{q})$, is given by

$$\chi(\overrightarrow{q}) = \frac{2\pi}{\lambda}\left(C_s\frac{\lambda^4\overrightarrow{q}^4}{4} + \Delta f\frac{\lambda^2\overrightarrow{q}^2}{2} + \text{Higher Order Contributions}\right) \tag{3.6}$$

More details about the transfer function can be found in Appendix A.2.1.

The resolution of the microscope at Scherzer defocus (see Appendix A.2.1) is given by [1]

$$r_{sch} = \frac{1}{1.51}C_s^{\frac{1}{4}}\lambda^{\frac{3}{4}} \tag{3.7}$$

Therefore a reduction of the spherical aberration results in a higher resolution. The magnified wave that arrives at the detector is called the image wave given by

$$\Psi(\overrightarrow{r}) = A(\overrightarrow{r})e^{i\Phi(\overrightarrow{r})} \tag{3.8}$$

with $A(\overrightarrow{r})$ the amplitude and $\Phi(\overrightarrow{r})$ the phase. However the detector can only detect electron current density or intensity, which is given by

$$|\ \Psi(\overrightarrow{r})\ |^2 = A(\overrightarrow{r})^2 \tag{3.9}$$

So the phase of the electron wave cannot be measured directly. In Section 3.8 it will be shown that the phase can be measured using electron holography .

[1] This is the lowest frequency at which the CTF becomes zero, or the first cross over.

3.3 Scanning Transmission Electron Microscopy

In STEM mode a small probe is scanned over the sample and the intensity on a detector is collected at each point to form the STEM image. Three STEM detectors can be present: a Bright Field (BF), an Annular Dark Field (ADF) and a High Annular Dark Field (HAADF) detector. The transmitted beam can be detected on the BF detector. Electrons that are deviated over small angles with respect to the transmitted beam can be detected on the annular ADF detector (angles between 10 and 40 mrad). Electrons impinging on the ADF detector can be diffracted electrons, therefore the image is sensitive to diffraction contrast. Electrons deviated over very large angles can be detected on the HAADF detector (angles > 40 mrad). The electrons collected by the HAADF detector are incoherently scattered (Pennycook, 2002). The contrast in HAADF STEM depends on the atomic number Z, meaning that heavy elements (i.e. gold) can be easily distinguished from lighter ones (i.e. silicon). The intensity on the detector is related to the atomic number Z

$$I = mtZ^{\eta} \tag{3.10}$$

where m is a scaling constant, t is the sample thickness and η is a constant between $\sqrt{2/3}$ and 2. For quantitative analysis η has to be determined very precisely, which is complicated since η depends on many parameters: for example the beam convergence angle, the detector convergence angle, the sample, the orientation of the sample and the beam characteristics (such as abberations).

The analysis presented by (Pennycook and Nellist, 1999) is recalled in the following, to show that the atomic cross section for scattering over high angles reduces to the atomic scattering factor f, that depends on the atomic number Z.

In the Einstein model of thermal vibrations the atomic scattering cross sections can be defined for coherent and incoherent scattering. The coherent scattering cross section is reduced by the Debye-Waller factor M according to

$$\sigma_c = f^2 e^{-2Ms^2} \tag{3.11}$$

where $s = {}^{\sin\theta_B}/_{\lambda}$ describes the scattering angle and is half of the change in wave vector due to diffraction, and θ_B is the Bragg angle. The electrons that are not coherently scattered are incoherently scattered, therefore the incoherent scattering cross section is given by

$$\sigma_{ic} = f^2(1 - e^{-2Ms^2}) \tag{3.12}$$

Several influences can be incorporated in M, which is given by $M = 8\pi^2\overline{u^2}$, being the thermal vibrations of the atoms ($\overline{u_t}$), the so-called Thermal Diffuse Scattering (TDS) as well as the static atomic displacements ($\overline{u_s}$) (caused by strain). For a sufficient high scattering angle σ_c tends to zero while σ_{ic} tends to the full atomic scattering factor f^2 (Pennycook and Nellist, 1999). f is given by (Williams and Carter, 1996)

$$f = \frac{1+\frac{E}{m_o c^2}}{8\pi^2 a_0}\left(\frac{\lambda}{\sin\theta}\right)^2 (Z - f_x) \qquad a_o = \frac{h^2\epsilon_o}{\pi m_o e^2} \tag{3.13}$$

where E is the energy of the incoming electron beam, m_o is the rest mass of the electron, c is the speed of light in vacuum, a_o is the bohr radius, h is Planck's constant ($6.6262x10^{-34}$ Js), ϵ_o is the permittivity of the vacuum, e is the charge of an electron, λ is the wavelength of the electron, θ is the half scattering angle and f_x is the scattering factor for x-rays, which is well known (Doyle and Turner, 1968). The advantage of the HAADF STEM technique with respect to the other STEM or TEM techniques is that the image can be directly interpreted in terms of the atomic scattering factor. Because only incoherently scattered electrons are regarded there is no phase contrast and the image contains no artefacts or contrast reversals that can be present in coherent imaging techniques.

As mentioned before the TEM and STEM modes are related by the principle of reciprocity. "Reciprocity is a wave optical argument first raised by Helmholz in 1860 for optical instruments stating that ray trajectories can be inverted because of the nature of the stationary wave equation" (Rose and Kisielowski, 2005) which means in principle that as long as the electron ray paths contain equivalent angles (of convergence and collection) at some point in the electron optical system, the image contrast will be identical (Williams and Carter, 1996). The detector plane of the STEM can be inverted with the source plane of the TEM. This is illustrated in Figure 3.1. The result is that if the beam convergence angle in TEM (α_T) on the sample is similar to the detector collection angle in BF STEM (β_S) and the convergence angle in STEM (α_s) is similar to the collection angle in TEM (β_T) the images are the same. In the same way ADF and HAADF images can be obtained in the TEM using hollow cone illumination (precession of the electron source to generate a large convergence angle) and an annular objective aperture (in the back focal plane), that acts as a beamstop for the direct beam so only electrons scattered over large angles can contribute to the image (Bals et al., 2004; Bals et al., 2005).

The resolution in STEM is, like the resolution in TEM, limited by the transfer function (Equation (3.6)). The resolution in STEM is mostly influenced by aberrations due to the condensor system, since the condensor system is most important for the formation of the probe. However in STEM no image forming lens is present after the sample, in contrast to TEM. Due to electron energy loss caused by collisions of electrons with the sample, the energy spread in the electrons that have passed the sample is increased. Since electron lenses suffer from chromatic aberrations the increase in energy spread of the electron beam that has passed the specimen degrades the resolution in a TEM image, whereas the STEM image is not influenced. It is therefore clear that reciprocity only holds for elastic scattering.

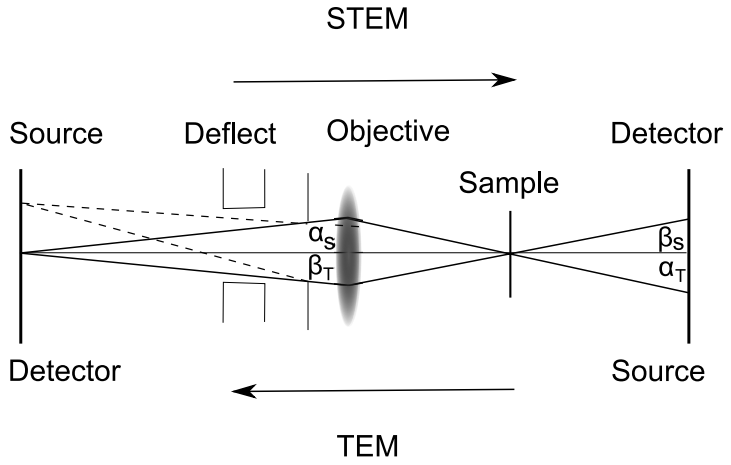

Figure 3.1: Ray diagram illustrating the reciprocity relationship of STEM (electrons going from left to right) and conventional TEM (electrons going from right to left). The same image is obtained in both modes of operation if α_S = β_T and α_T = β_s adapted from (Cowley and Spence, 2000; Williams and Carter, 1996).

3.4 Electron Energy Dispersive X-ray Spectroscopy

Electron Energy Dispersive X-ray Spectroscopy is known either as EDX or EDS. An x-ray detector can be added to detect x-rays that are emitted by the sample under the influence of the electron irradiation (see Figure A.1). All elements emit a characteristic x-ray spectrum, therefore this signal can be used to obtain chemical information on the sample. An elemental map of the sample can be made using EDX. The microscope is used in STEM mode when doing EDX analysis and the x-ray signal is collected at each point.

3.5 Electron Energy Loss Spectroscopy (EELS)

EELS studies electrons that have passed the sample and lost a certain amount of their energy on the way due to inelastic interactions with the sample atoms. Each element has a specific energy loss "signature" therefore the energy loss spectrum can be used to map the chemical composition of the sample. The fine structure of the energy loss spectrum is sensitive to the electron distribution in the sample, and therefore to the type of atomic bonds present in the sample (Krivanek, 1991). To be able to perform this technique the microscope has to be equipped with an energy filter, to separate the electrons with different energy. Such a filter consists of a magnetic prism (electrons with different energy are deviated over different angles) and a series of lenses to form an image or a spectrum. This technique was used in this work only to verify that the silicon loss peaks of silicon NW's showing an anomalous diffraction pattern were identical to the normal diamond cubic silicon loss peaks (Chapter 6), to exclude the possibility that a different crystal structure caused the anomalous diffraction patterns.

As a technique, EELS is more complicated than EDX, and is therefore a technique of specialists. The introduction of commercial energy filters (the Gatan GIF or Zeiss omega filter) has made the technique more widespread. Dedicated research groups exist (i.e. the group of Christian Colliex in Orsay) as well as dedicated conferences (i.e. JEELS (JEELS, 2008)).

3.6 Electron Tomography

The aim of electron tomography is to image the sample in 3D. Two requisites are key to be able to perform this technique: you need a microscope with a (relatively) large gap between the polepieces of the objective lens, and a sample holder that is relatively slim so you can tilt your sample to high angles without touching the polepieces (see the first necessity). A tomogram is actually a series of images: the sample is tilted through the available tilt range and every 1 or 2^0 degrees an image is acquired. The series can be reconstructed using a more or less sophisticated algorithm, and if reconstruction is successful a 3D image of the sample is obtained. Several programs (that can be often downloaded freely on the internet) exist to this purpose such as IMOD, ImageJ and X-plore3D (FEI software).

A tomography series was obtained on silicon nanowires grown with a gold catalyst and some images extracted from the tomogram are shown in Figure 5.6. However the reconstruction of the tomogram proved difficult since the nanowire moved during the series. Due to a lack of time no further attempts at tomography were made.

3.7 Lorentz Lens Microscopy

This section describes briefly the field of Lorentz microscopy, since most holograms were obtained using a Lorentz lens.

Historically Lorentz microscopy is a general term for microscopy techniques that make use of the Lorentz force to image magnetic domains (Chapman, 1984). The electron is deflected due to an in- plane magnetization by the Lorentz force. In a normal TEM the specimen is situated in the magnetic field of the objective lens (Appendix A.2). In this configuration magnetic structure in the sample will surely be modified. A solution for this problem can be to lift the specimen up, out of the magnetic field, but in this case spherical aberrations will become more important which degrades the resolution. Another alternative is to use a different lens, the Lorentz lens, that is generally integrated in the lower polepiece of the objective lens, to image the specimen.

For this reason Lorentz microscopy can also indicate that a Lorentz lens is used to form the image, as is the case in this PhD work. For magnetic specimens the advantage of using the Lorentz lens is obvious: the specimen is no longer in an external magnetic field (also the objective lens can be used in this case to magnetize the sample in-situ (Masseboeuf, 2008)). For non-magnetic specimens the advantage of using the Lorentz lens is the increase in field of view. However the resolution is decreased, since the Lorentz lens suffers from large aberrations. At 200 kV the resolution in Lorentz mode is around 2.5 nm (see also Section 3.9).

3.8 Electron Holography

In 1947 Dennis Gabor, a Hungarian-British physicist, proposed the method of interference imaging and gave it the name holography, from a Latin word meaning "whole writing". His idea was that using interference imaging the phase and amplitude of the electrons could be recorded separately, and abberations due to the electron lenses could be removed from the phase image, allowing a higher resolution (Gabor, 1948).

The principle of any holographic technique is to interfere a wave that contains (phase and amplitude) information of the sample with a reference wave. If electrons are used as the wave 20 forms of holography can be distinguished (Cowley, 1992). Electron holography is a powerful tool since electrical and magnetical properties of the sample can be measured simultaneously (Midgley, 2001).

In this work only off-axis Holography is used, therefore only this technique is described. In this section the theory of electron holography will be explained. An emphasize is put on the meaning of what is actually measured: the Mean Inner Potential (MIP) V_0, which is the average Coulomb potential within the crystal (Kruse et al., 2006).

3.8.1 The principle of off-axis holography

A part of the sample is illuminated with a broad parallel beam. The electrons that passed through the sample (with wavevector k_{obj}) interfere with the electrons that passed the vacuum (with wavevector k_{ref}) due to a wire charged by an applied voltage U_b: the biprism. Generally the biprism is placed in the plane of the selected area aperture and the intermediate lens is tuned such that the SA plane is no more an image plane (in the Titan this mode is called Mh). In Figure 3.2 a schematic of the setup is shown. S1 and S2 are the virtual sources of both

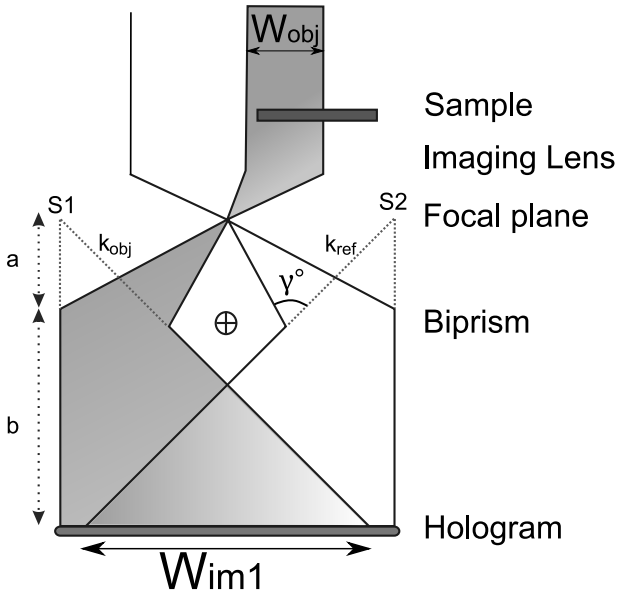

Figure 3.2: Schematic diagram that illustrates the principle of Off-axis Electron Holography. A charged wire called the biprism is used to interfere a reference wave (with wavevector k_{ref}) with the object wave (with wavevector k_{obj}). $S1$ and $S2$ are the two virtual sources that interfere, forming an interference pattern or hologram of width W_{im1}. The width of the object wave is W_{obj}. γ is the deflection angle of the wave due to the action of the biprism, adapted from (Cooper, 2006).

rays. The parallel electron beam is made highly astigmatic using the condenser stigmaters to achieve parallel illumination and increase spatial coherence in the direction perpendicular to the biprism (see also Appendix A.3). In the direction parallel to the biprism the beam is more focused on the sample to increase the number of electron counts (see Figure 3.3).

The field of view W_{im1} refers to the width of the interference pattern in the first image plane and is determined by the width of the reference and object wave that are superposed. W_{im1} can be obtained using the analysis with Young's experiment and is given by (Missiroli et al., 1981)

$$W_{im1} = 2\left(\gamma b - R\frac{a+b}{a}\right) \tag{3.14}$$

where γ is the deflection angle of the ray due to the action of the biprism (see Figure 3.2) and R is the radius of the biprism and a and b are distances indicated in Figure 3.2 that are taken positive.

The Lorentz lens magnifies the object by a factor M, therefore the width of the hologram in the first image plane W_{im1} is given by

$$W_{im1} = W_{obj}M = W_{im1}\frac{a+b}{F} \tag{3.15}$$

where M is the magnification and F is the focal length of the Lorentz lens. The projector lenses magnify the first intermediate image with a magnification M_p and the hologram has a width $W_{CCD} = M_p W_{im1}$ on the CCD detector.

γ is related to the biprism voltage U_b, where $\gamma = \gamma_0 U_b$ (Völkl et al., 1999) and γ_0 depends on the acceleration voltage and biprism radius.

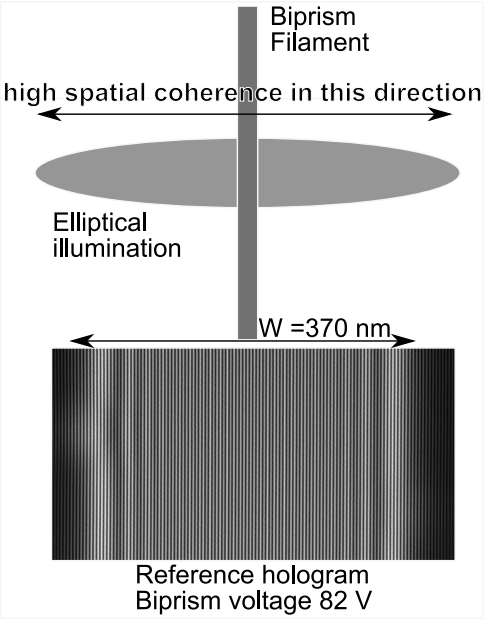

Figure 3.3: Schematic diagram that illustrates the elliptical illumination of the biprism to achieve high spatial coherence in the indicated direction. A reference hologram (without specimen) is shown below to clarify the direction of the fringes. Adapted from (Lehmann, 2004).

γ can be modified by changing U_b to obtain the desired (spatial) sampling frequency in the hologram. The fringe spacing S_{im1} in first intermediate image is given by (Midgley, 2001)

$$S_{im1} = \lambda \left(\frac{a+b}{2a\gamma} \right) \tag{3.16}$$

The contrast C, or fringe visibility, is defined

$$C = \frac{N_{max} - N_{min}}{N_{max} + N_{min}} \tag{3.17}$$

where N_{max} and N_{min} are the maximum and minimum number of electron counts respectively.

The fringe visibility C is determined by the spatial coherence, but other factors contribute

$$C = C_{sc} C_{inel} C_{ins} MTF \tag{3.18}$$

where C_{sc} describes the contrast reduction due to the partial spatial coherence of the electrons, C_{inel} is the contrast reduction due to inelastic interaction with the specimen, C_{ins} is the contrast reduction due to instabilities (the temporal coherence) and MTF is the contrast reduction due to the modulation transfer function of the detector (Lehmann, 2004). The influence of C_{inel} can be minimized by studying thin specimens.

The wave function that passed through vacuum is called the reference wave ψ_{ref} and the wave function that passed through the sample the object wave ψ_{obj}. At the level of the detector the intensity of the two interfering image waves $\Psi_{ref}(\overrightarrow{r}) = A_{ref} \exp(i2\pi k_{ref} \overrightarrow{r} + i\phi_{ref})$ and $\Psi_{obj}(\overrightarrow{r}) = A_{obj}(\overrightarrow{r}) \exp(i2\pi k_{obj} \overrightarrow{r} + i\phi_{obj}(\overrightarrow{r}))$ is measured, given by (Lichte, 2008b; Midgley, 2001; Völkl et al., 1999):

$$\begin{aligned} I_{holo}(\overrightarrow{r}) &= \mid \Psi_{ref} + \Psi_{obj} \mid^2 \\ &= \mid A_{ref}\ \exp(i2\pi k_{ref}\overrightarrow{r} + i\phi_{ref}) + A_{obj}\ \exp(i2\pi k_{obj}\overrightarrow{r} + i\phi_{obj}) \mid^2 \\ &= A_{ref}^2 + A_{obj}^2(\overrightarrow{r}) + 2A_{ref}A_{obj}(\overrightarrow{r})C\cos[2\pi(k_{obj} - k_{ref})\overrightarrow{r} + \Delta\phi(\overrightarrow{r})] \end{aligned} \tag{3.19}$$

where $\Delta\phi(\overrightarrow{r}) = \phi_{obj}(\overrightarrow{r}) - \phi_{ref}$. Note that the vector $\overrightarrow{r}$ is a vector in the (x, y) plane only. From this formula it follows that the amplitude information is contained in the contrast C, and the phase information $\Delta\phi(\overrightarrow{r})$ is contained in modifications of the carrier frequency q_c, given by $k_{obj} - k_{ref}$ or otherwise stated, the location of the fringes (Lichte, 2008b). Off-axis Electron Holography therefore allows direct measurement of the amplitude and phase of the image wave, something that is impossible using normal TEM (Section 3.2). Now the next question arises: what information is contained in the phase? The phase change $\Delta\phi$ between an electron that passed the sample and an electron that passed through vacuum is given by (Mankos et al., 1996)

$$\Delta\phi(\overrightarrow{r}) = C_E \int V(x, y, z)dz - \frac{e}{\hbar}\int\int \underline{B}(x, y)d\underline{S} \tag{3.20}$$

Where C_E is an interaction constant depending on acceleration voltage. The exact value of C_E (taking into account relativistic effects) is given by (here v is the relativistic electron velocity) (Völkl et al., 1999)

$$C_E = \frac{2\pi}{\lambda E}\frac{E_0 + eE}{2E_0 + eE} = \frac{2\pi e}{hv} \tag{3.21}$$

where E_0 is the rest energy of an electron in vacuum. For 200 keV electrons the value of C_E is 7.29x10^6 rad V^{-1} m^{-1}. $\hbar$ is Planck's constant divided by 2π, $\underline{B}$ is the magnetic flux (or induction) and $\underline{S}$ is normal to the area mapped out by the trajectories of the electrons going from source to detector through the vacuum and the sample (Midgley, 2001). In the absence of magnetic information in the sample this formula can be simplified to

$$\Delta\phi = C_E \int V(x, y, z)dz \tag{3.22}$$

In Appendix A.2.3 a simple analysis that justifies this formula is recalled (Williams and Carter, 1996).

Since generally it is assumed that $V(x, y, z)$ is constant in the z direction of the specimen, this formula can be found in its most simple form as $\Delta\phi = C_e V t$ (with t the thickness of the specimen) in literature (Völkl et al., 1999).

In summary: the phase change $\Delta\phi$ (between electrons that traversed the vacuum and electrons that traversed a specimen of thickness dz) can be directly related to the crystal potential $V(x, y, z)$ (in the absence of magnetic fields).

3.8.2 Spatial and phase resolution

The precision of the potential measurement using electron holography depends both on the phase resolution and the thickness of the specimen (Equation (3.22)). The phase resolution is determined by the number of electrons per resolved pixel N_{el} and the fringe contrast C (Equation (3.17)), and given by (Lenz, 1988)

$$\Delta\phi_{min} = \frac{\sqrt{d}}{C\sqrt{N_{el}}} \tag{3.23}$$

The phase resolution also depends on the definition of signal to noise, the so-called SNR ratio (Lichte, 2008b). For simplicity we consider a signal significant if its value is greater than the average noise value, in contrast to other authors where a significant signal is defined as twice the average noise value (Lichte, 2008b). The constant d is either 2 (Lenz, 1988; Harscher and Lichte, 1996), when it is supposed that spacing and direction of the hologram fringes can be exactly determined. Or d is 14, if it is assumed that no a-priori knowledge about the x and y components of the spatial frequency vector is present (de Ruijter and Weiss, 1993). $d = 14$ results in a poorer phase resolution, as more parameters have to be fitted.

Additionally we estimate the phase resolution by recording two empty (reference) holograms one after the other. The phase image obtained by reconstruction of the empty holograms will give a relatively good idea of the noise present in the optical system during the acquisition time (Cooper et al., 2007a). In Section 3.8.5 a comparison between these three approaches is presented.

The spatial resolution is approximately three times the fringe spacing (and 1-2 fringe spacings for weak phase objects (Lichte, 2008b; Ishizuka, 1993)), which will be explained in more detail in the next section.

An interference pattern will form only if the sample is illuminated by (partially) coherent electrons [2], for this reason a Field Emission Gun (FEG) is generally used when performing holography. In Section 3.2 the influence of spatial and temporal coherence on the transfer function was already introduced. The coherence of the electron source determines the fringe visibility and therefore the quality of the holograms that can be obtained (see Equation (3.23)). Increasing the biprism voltage U_b has the effect of increasing the distance between the virtual sources and increasing the width W of the hologram (Equation (3.14)). This will decrease the fringe spacing resulting in an increase in spatial resolution and in field of view, but also decrease the fringe contrast due to the loss of coherence of the virtual sources (Midgley, 2001), this is explained in more detail in Appendix A.3. A decreased fringe contrast results in a lower phase resolution (Equation (3.23)). The optimal parameters are therefore always a trade-off between spatial resolution and phase resolution. The experimentally used parameters are introduced in Section 3.8.5.

3.8.3 Hologram reconstruction procedure

Previously we showed that the intensity in the hologram is described by a cosine function (Equation (3.19)), and that the phase information is contained in modifications of the the interference fringes. In this section it is shown how the phase information can be extracted from the

[2] Since each electron is perfectly coherent with itself, theoretically holograms could be obtained even from incoherent sources if single electron detection would be possible.

hologram.

Historically hologram reconstruction was performed using a light optical reconstruction method on an optical bench. Since fast computers and digital recording using CCD camers are available roughly two types of reconstruction techniques can be distinguished, that either fit a function to the hologram intensity in direct space (Lehmann et al., 1994; Fujita et al., 2006) or use a filtering in reciprocal space (Völkl et al., 1999).

The first method has the advantage of being faster, and could result in a higher resolution (or larger field of view at the same resolution) since it is no longer required to sample the finest detail with two to three fringes. The problem of reconstruction techniques using real space is that the intensity in the hologram is not only described by the cosine function of the carrier frequency, but contains modulations of lower spatial frequency due to Fresnel fringes caused by diffraction on the biprim, and these modulations limit the accuracy of the fit if they are not included in the model.

The second reconstruction technique makes use of a Fourier transform, filtering in reciprocal space by multiplication with a mask and an inverse Fourier transform. In this PhD work only this second method was used and is therefore described in more detail in the following.

We recall that the reference amplitude A_{ref} does not depend on position $\overrightarrow{r}$ in the image and can therefore be set to one for convenience. The object amplitude $A_{obj}(\overrightarrow{r})$ and the phase difference $\Delta\phi(\overrightarrow{r})$ do depend on position. To reconstruct the hologram the Fourier Transform of the intensity (Equation (3.19)) is expressed

$$FT(I_{holo}(\overrightarrow{r})) = FT(1) + FT(A^2_{obj}(\overrightarrow{r})) + C\,FT(2A_{obj}(\overrightarrow{r})\cos(2\pi\,\overrightarrow{q}_c\,\overrightarrow{r} + \Delta\phi(\overrightarrow{r}))) \quad (3.24)$$

Generally this is rewritten as (Völkl et al., 1999)

$$\begin{aligned} FT(I_{holo}(\overrightarrow{r})) = {} & \delta(\overrightarrow{q}) + \delta(\overrightarrow{q}) \otimes FT(A^2_{obj}(\overrightarrow{r}))+ && \text{Centre band} \\ & \delta(\overrightarrow{q} - \overrightarrow{q}_c) \otimes C\,FT(A_{obj}(\overrightarrow{r})\exp(i\Delta\phi(\overrightarrow{r}))+ && \text{Side band } -\overrightarrow{q}_c \\ & \delta(\overrightarrow{q} + \overrightarrow{q}_c) \otimes C\,FT(A_{obj}(\overrightarrow{r})\exp(-i\Delta\phi(\overrightarrow{r}))) && \text{Side band } +\overrightarrow{q}_c \end{aligned} \quad (3.25)$$

The equation contains four terms. A Dirac peak at the origin ($\overrightarrow{q} = 0$) describes the uniform intensity of the reference wave. A second peak at the origin describes the intensity distribution in a normal TEM image. A peak centered at the frequency $\overrightarrow{q} = -\overrightarrow{q}_c$ represents the Fourier transform of the image wave function and a peak at $\overrightarrow{q} = \overrightarrow{q}_c$ corresponds to the complex conjugate of the image wave function. The last two peaks represent the sidebands in the reciprocal space and are also indicated in Figure 3.5, where the reconstruction procedure is illustrated schematically.

The dirac Delta function δ is used to express at which frequency $\overrightarrow{q}$ each signal exists. This is convenient since the two sidebands now appear clearly in the expression. The convolution of the delta function and the FT is the multiplication of $\exp(\overrightarrow{q}_c)$ and $\exp(i\Delta\phi(\overrightarrow{r}))$[3].

A mask is positioned around one of the sidebands to remove all other frequencies and select only the frequencies present in the sideband. The size of the mask determines the spatial

[3] The convolution theorem states that the convolution of two functions $f(x)$ and $g(x)$ is equal to the product of their respective Fourier Transforms: $f(x) \otimes g(x) = FT(f(x))FT(g(x))$ (Kreyszig, 1999)

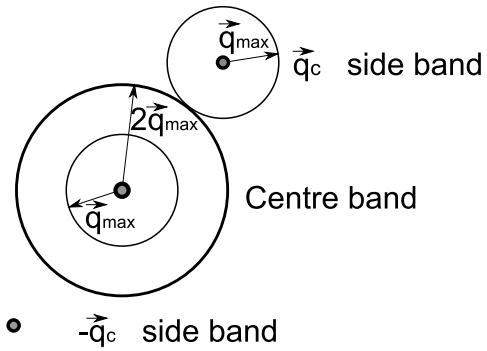

Figure 3.4: A schematic diagram showing the optimum masks in Fourier space for a normal object. The vector modulus $\overrightarrow{q}_{max}$ is the largest frequency included in the mask and therefore defines the maximum spatial resolution in the reconstructed object. Adapted from (Midgley, 2001).

frequency sampling of reciprocal space and inversely, the region of direct space where the information is averaged. A large mask favourizes a high spatial resolution and a small mask a good signal to noise ratio.

For a normal object the amplitude A_{obj} is nonzero and therefore, if the maximum spatial frequency present in the object is $\overrightarrow{q}_{max}$, the maximum spatial frequency present in the FT is $2\overrightarrow{q}_{max}$ because of the A^2_{obj} term in Equation (3.25). Therefore the method is very efficient if $\overrightarrow{q}_{max} < \overrightarrow{q}_c/3$ and the ideal mask size is $1/3\ \overrightarrow{q}_c$ in order to seperate properly the object amplitude from the phase (see Figure 3.4) (Ishizuka, 1993). If the object is a weak phase object at the Gabor frequency (Lichte, 1991) A_{obj} is zero and the mask size can be taken equal to the carrier frequency, although in practice the mask is generally chosen smaller than $\overrightarrow{q}_c$ to remove high frequency noise (Midgley, 2001). Several types of masks are generally used, for example an 8th order Butterworth filter[4] (Völkl et al., 1999) or a Lorentzien mask (Houdellier, 2006). In this work a Gaussian mask was used given by

$$f(\overrightarrow{q})_{gauss} = \exp\left(\frac{-(\overrightarrow{q} - \overrightarrow{q}_c)^2}{2\sigma^2}\right) \tag{3.26}$$

with $R_{mask} = 3\sigma$. The mask is applied using a soft cut at R_{mask}. The Gaussian mask is very smooth and therefore little phase oscillations are introduced with respect to the butterworth filter. If two empty holograms are reconstructed with a Gaussian mask or 8^{th} order Butterworth filter respectively the (standard deviation of the) phase oscillations in the obtained phase images is 6 and 14 mrad respectively[5]. Because the edges of the Butterworth filter are relatively steep, relatively large oscillations are created in the image (see Figure 3.6). The type of mask that should be used also depends on the particular hologram. For example the phase image in Figure 7.5 could only be reconstructed using a Butterworth filter, probably because the Butterworth filter is wide around $\overrightarrow{q}_c$ and falls off rapidly at R_{mask}. In this case the phase information is therefore more accurately transmitted.

Once the mask is applied the sideband is moved to the origin of reciprocal space and an inverse Fourier transformation is performed to obtain the phase and amplitude images.

This mathematical procedure is basically the same as the Geometrical Phase Analysis (Hÿtch et al., 1998), where local frequency variations can be related to the geometrical phase.

To illustrate the effect of the mask size in the reconstruction process, a hologram of an object

[4] The Butterworth filter is given by $B_B(\overrightarrow{q}) = \left(1 + c \cdot (\overrightarrow{q}/\overrightarrow{q}_{max})^{2\tau}\right)^{-1}$, where c is a constant (usually $c = 1$), τ describes the order of the filter and $\overrightarrow{q}_{max}$ denotes the cut-off frequency of the filter (Völkl et al., 1999).

[5] The holograms were obtained at $U_b = 101$ V, 20 s exposure time and a magnification of 58k.

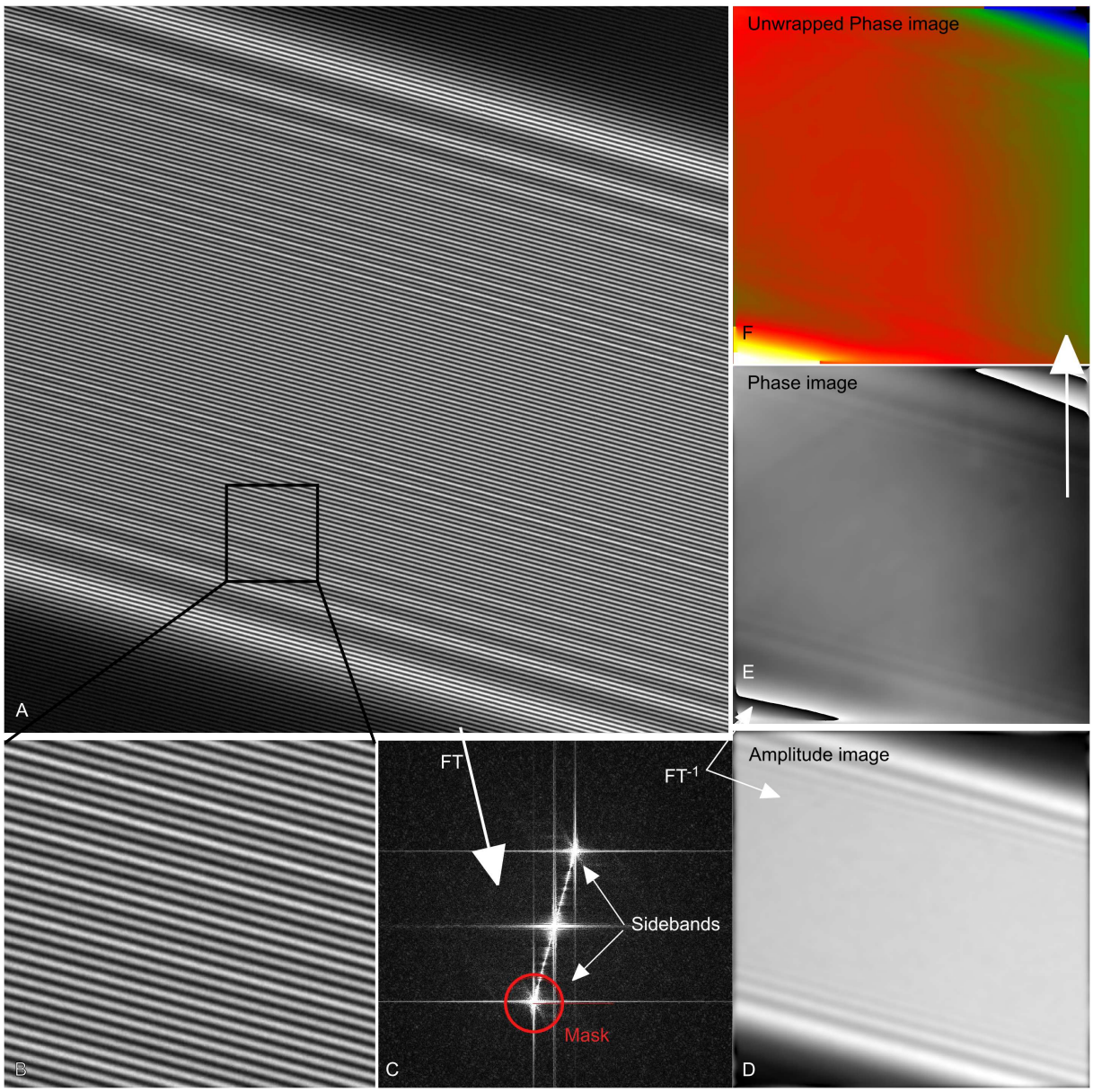

Figure 3.5: The reconstruction procedure of an hologram. (A) Empty hologram (B) Zoom of the indicated region showing the carrier frequency. (C) The Fourier transform showing the centerband (the first two terms in Equation (3.25)) and the two sidebands (the last two terms in Equation (3.25)). A mask is applied to one of the two sidebands. (D) Inverse Fourier transformation results in the complex image that is composed of (E) the amplitude and (F) the phase component. (F) The unwrapped phase image.

with two abrupt interfaces was simulated (inset Figure 3.6). The pixel size in the simulated hologram is 1 nm and one fringe is sampled by 4 px and no aberrations or distortions are included in the hologram. The phase in the object is 0.5 rad. This hologram was reconstructed using different mask sizes and types, Gaussian and 8th order Butterworth (Völkl et al., 1999), to investigate the effect of the mask on the width of the object in the reconstructed phase image (the profiles in Figure 3.6). The width of the object was 28 nm.

If the mask size is $\sim 1/3$ of the carrier frequency a spatial resolution of 12 nm is expected for normal objects. This value is indicated in Figure 3.6 for the Gaussian mask of this size. The width of the interface is spread out over a slightly larger region and 12 nm corresponds to the interface width if the phase signal is between 10 and 90% of its maximum value.

If the 8th order Butterworth filter with radius $\sim 1/3\ \overrightarrow{q}_c$ is used the interface is much sharper, however oscillations appear around the object edges, which will increase noise in the phase image.

We can see that for the Gaussian masks all line profiles are described by the same Full Width Half Maximum (FWHM) value, that is equal to the width of the simulated object. Therefore it seems that the width of the object can be measured accurately irrespective of mask size, if the object is larger than the spatial resolution.

In the experimental holograms the spatial resolution was estimated by three times the fringe spacing and a Gaussian mask with the radius $\sim 1/3$ of the carrier frequency (Table 3.1 of Section 3.8.5) was used.

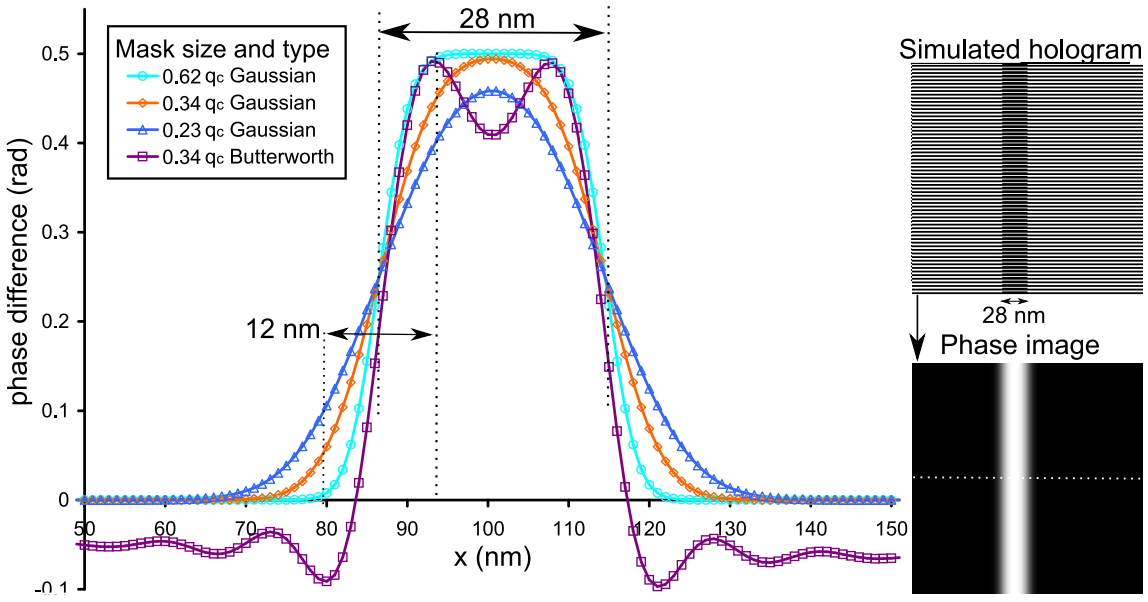

Figure 3.6: A hologram of an object with two abrupt interfaces was simulated (upper inset) and reconstructed using different mask sizes. The apparent width of the interface in the reconstructed phase image is plotted, as obtained by a line profile in the phase image (lower inset) as indicated by a dotted line. Several mask sizes were used and the width of the interface region if the mask size is $\sim 1/3$ of the carrier frequency is indicated. The FWHM of all line profiles obtained with a Gaussian mask can be related to the width of the object, independent of mask size.

Because the phase is evaluated numerically there can be phase jumps of 2π if the phase difference exceeds 2π. These phase jumps have to be removed as they do not contain any physical information about the sample. This procedures is known as phase unwrapping. Unwrapping

algorithms of the Goldstein, Flynn or Hybrid type have been used (Völkl et al., 1999). The unwrapped phase image is shown in Figure 3.5F. Phase fluctuations are visible in the phase image (Figure 3.5E) that was obtained from an empty hologram. This illustrates that aberrations in the projector system and in lenses in the Gatan Imaging Filter (GIF) and imperfections of the CCD camera (due to shear-distortion in their transfer fiber optics (Völkl et al., 1999)) can contribute to the measured phase difference. For this reason it is common practice to acquire a reference hologram, which is an empty hologram without the sample, acquired directly after the acquisition of the hologram with object information and using exactly the same illumination parameters. The phase image can be corrected for the camera distortions and lens aberrations by substraction of the phase in the reference hologram (Völkl et al., 1999). Another advantage of using a reference hologram is that the mask can be centered on the pixel with the highest intensity in the sideband of the reference hologram. As in the reference hologram the carrier frequency is not modulated the center of the sideband in reciprocal space is relatively easy to detect by automatic reconstruction procedures (Völkl et al., 1999).

The importance of the reference hologram is shown in Figure 3.7. In Figure 3.7A the phase image obtained by reconstruction of two empty holograms made directly after one another is shown. Clearly the phase is much flatter than in Figure 3.5F, because a reference hologram has been used for reconstruction. Also in Figure 3.7B the phase image obtained from reconstruction of two empty holograms are shown, however in this case the reference hologram was obtained some time after the acquisition of the first hologram. Clearly the phase is no more flat and the width of the hologram has decreased due to fluctuations in the imaging system (projector lenses and GIF) and variations in the biprism (drift and charge fluctuations). A similar analysis for holograms acquired on the CCD camera above the GIF did not show less drift. Therefore it is important that the reference hologram is acquired directly after acquisition of the hologram containing sample information.

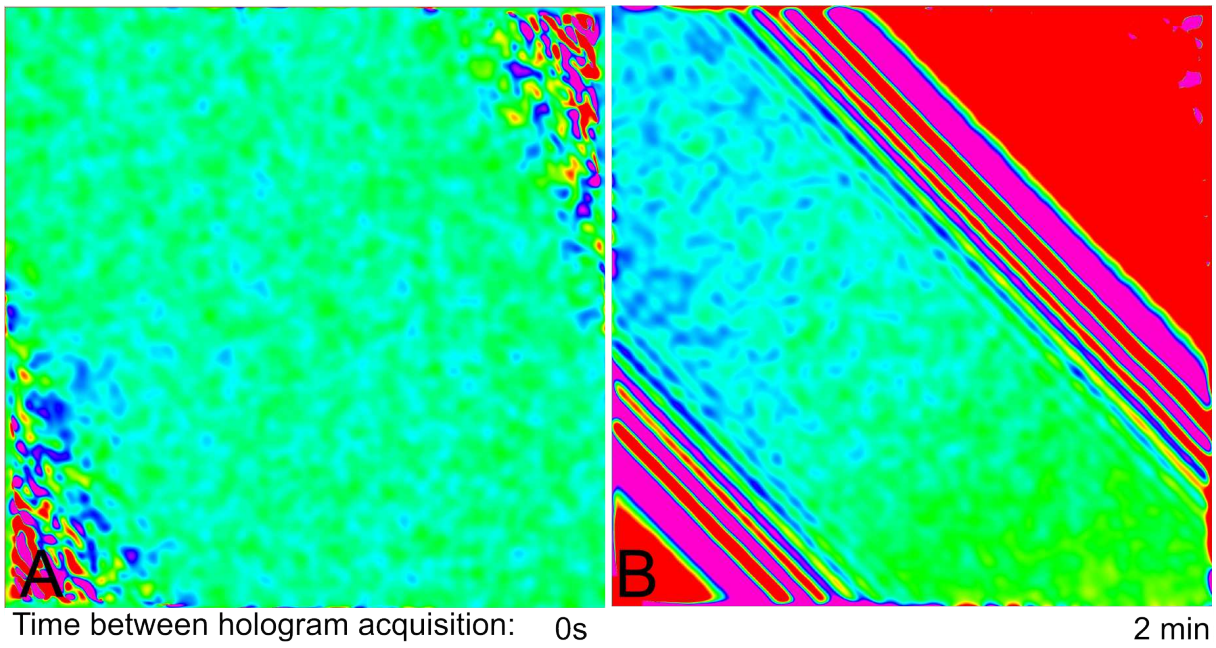

Figure 3.7: Influence of drift on the reconstructed phase image. (A) The first hologram was reconstructed with a reference taken either directly after the hologram or (B) 2 minlater. The colorscale range is the same. The holograms were obtained at 100 V biprims voltage through the GIF, at a magnification of 58k.

In practice gradients can be present in the phase image, that do not necessarily reflect physical information about the specimen. If the center of the sideband does not fall onto a pixel

in Fourier space, but somewhere in between, this mismatch can cause a linear gradient in a specimen-free region (Völkl et al., 1999) or an increased signal to noise ratio, especially in the reconstructed amplitude images. It is common practice to remove such gradients by defining a suitable reference region in an unperturbed region of the hologram. A least squares fit to the gradient in the reference region and substraction of the fitted gradient from the phase image, will remove this artefact. However we have studied only nanowires which are well defined, free standing, cylindrical objects [6]. We suppose that due to the cylindrical symmetry of the nanowire a phase image that is symmetrical witch respect to the nanowire axis is expected. In Figure 3.8A a phase image is shown of a nanowire, where a phase gradient is present. If a reference region is chosen at either side of the nanowire, the phase will be flattened on this side, but the gradient will be increased on the other side of the nanowire. For this reason we use two reference regions symmetrically with respect to the nanowire, to obtain a phase image that is symmetrical with respect to the nanowire axis (Figure 3.8B), which seems physically correct. This is particularly important if the residual field in the vacuum has to analyzed.

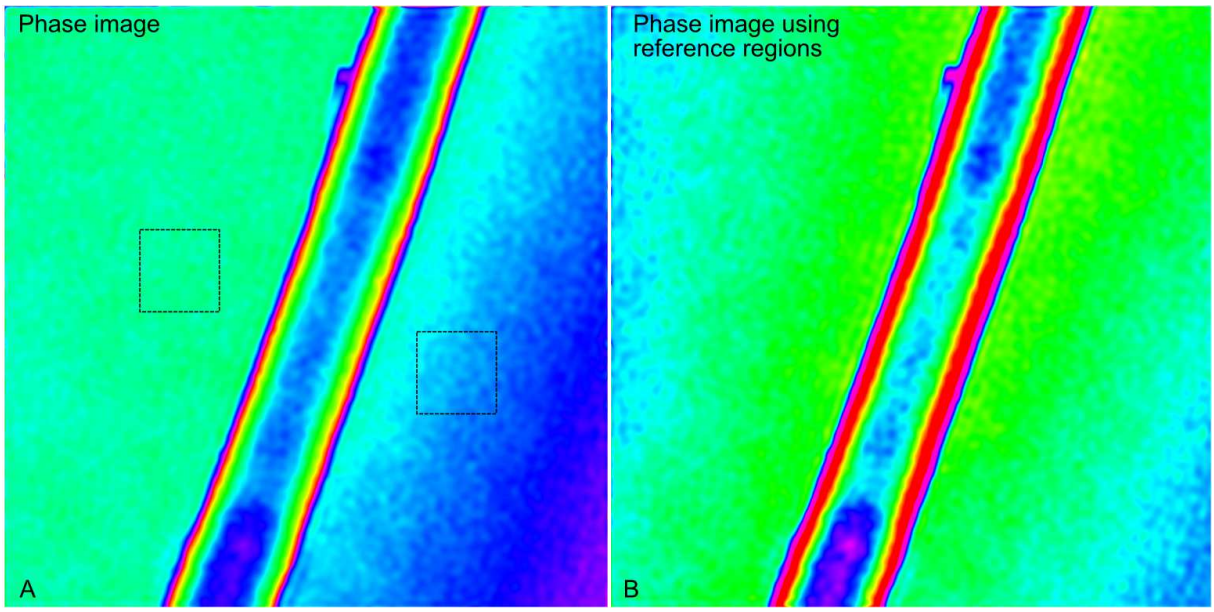

Figure 3.8: Influence of the reference region on the phase image. (A) the phase image (B) The phase image if two reference regions symmetrical to the nanowire as indicated in (a) are used.

3.8.4 The Mean Inner Potential

Now it seems useful to explore in some more detail what the crystal potential, or also called Coulomb potential (Kruse et al., 2006), exactly is, and how it can be measured.

The electrostatic potential in the crystal $V(r)$ is a positive number and reaches a maximum at a nucleus (Williams and Carter, 1996). The potential energy of an electron outside the crystal in the vacuum at infinite distance from the crystal is chosen zero by definition. Such a definition reflects the experimental situation in a microscope, where an electron starts from a nearly infinite distance from the specimen and traverses the specimen (Kruse et al., 2006). The potential energy of the electron $\mho(r)$ in the crystal decreases since $\mho(r) = eV(r)$ where e is the charge of an electron that is negative.

An electron in a crystal can be described by a sum of bloch waves, that are all solutions to the

[6] Actually the nanowire section is a hexagon (Section 6.3.3), but can be considered a cylinder in a first approximation.

Schrödinger equation. The time-independent Schrödinger equation is given by (Williams and Carter, 1996)

$$\left(-\frac{h^2}{8\pi^2 m}\nabla^2 + \mho(r)\right)\Psi(r) = E\Psi(r) \tag{3.27}$$

where the first term describes the kinetic energy and the second term the potential energy and E represents the total energy. Because the crystal is periodic (at least in the x and y direction), so is $V(r)$. Therefore the crystal potential can be expressed as a Fourier series that sums over all the lattice points in reciprocal space (Williams and Carter, 1996)

$$V(r) = \sum_g V_g e^{2\pi i g\cdot r} \tag{3.28}$$

Diffracted electrons interact strongly with the crystal: a diffracted electron is directly in the bragg condition to be re-diffracted back into the original beam and so on. Due to these dynamical diffraction effects the phase change of a dynamically scattered electron that passes through a specimen with thickness t cannot be understood using a simple formula but has to be calculated by solving the Schrödinger equation.

However in low resolution electron holography the specimen is tilted carefully off zone axis by approximately 4^o to minimize diffraction contrast and the kinematical approximation is used (Equation (3.22)). The limit of the kinematical approximation (and also the weak phase object approximation) is the length of the extinction distance. In silicon the extinction distance for diffraction on a $\{111\}$ plane is 79.3 nm and longer for other crystal plane at 200 kV (Stadelmann, 2008). The thickness of most samples studied by electron holography was between 50 and 60 nm. Therefore the kinematical approximation should hold reasonably well. For comparison, this approximation was shown to hold for a 64 nm thick specimen of FePd-$FePd_2$ by multislice simulations (Masseboeuf, 2008). It should be noted that in literature on electron holography the same approximation is used for thick silicon specimens (100-500 nm) (Cooper et al., 2007a; Twitchett et al., 2004).

So if Equation (3.22) is used, clearly the potential across the sample thickness reduces to integration of the V_0 term. It follows from Equation (3.28) that the sample thickness is supposed to be formed of an integer number of silicon crystal cells. Using off axis electron holography V_0, the zeroth order Fourier coefficient of this series (Equation (3.28)) is measured among all the V_g coefficients. In the kinematical approximation we suppose that the V_0 coefficient is not influenced by the other V_g coefficients.

The Poisson equation relates the potential $V(r)$ to the field E and charge density in a material ρ by the relation

$$\nabla^2 V(r) = -\frac{dE}{dx} = -\frac{\rho}{\epsilon} \tag{3.29}$$

where ϵ is the permittivity of the material. The average crystal potential is formed by the density of electrons and nuclei. The result is that the Poisson equation can be written for a crystal potential taking this into account (Zuo, 2004)

$$\nabla^2 V(r) = -e\frac{Z(r) - \rho_e(r)}{\epsilon_o} \tag{3.30}$$

where $Z(r)$ is the nuclear charge density, $\rho_e(r)$ is the electron density and ϵ_0 is the permittivity of free space ($8.85419 \cdot 10^{-12}$ F m^{-1}).

In electron diffraction and x-ray diffraction studies with the aim to carefully measure the electron charge distribution inside a material, also diffraction over large angles is used (Zuo, 2004) to refine the obtained charge density values. Using these techniques very accurate values of the atomic scattering factor can be obtained. The atomic scattering factor is a measure of the amplitude of an electron wave scattered from an isolated atom ($f(\theta)$) or from a unit cell of a crystal structure (the structure factor $F(\theta)$). The atomic scattering factor for forward scattering is related to V_0 according to the model of neutral free atoms, and given by (Ibers, 1958; Völkl et al., 1999)

$$V_0 = \frac{h^2}{2\pi m_0 e\Omega}\sum_j f_j(0) = \frac{h^2}{2\pi m_0 e\Omega}F = \frac{h^2}{2\pi m e\Omega}F\frac{m}{m_0} \tag{3.31}$$

where Ω is the volume of the crystal unit cell and $f_j(0)$ are the atomic scattering amplitudes for the forward scattering of electrons (zero scattering angle) ($f_j(0)$ is 0.5828 nm for Si (Völkl et al., 1999; Doyle and Turner, 1968)). Using this formula the mean inner potential for silicon can be calculated to be 13.9 V. This value is an upper limit for V_0. The accepted value that can be found in literature is 11.5 or 12 V (Williams and Carter, 1996; Völkl et al., 1999). A problem of the non-binding approximation is that it overestimates V_0 because redistribution of valence electrons due to bonding is not taken into account (Völkl et al., 1999).

It was argued by (Völkl et al., 1999) that the calculations performed by Doyle and Turner (Doyle and Turner, 1968) are based on the relativistic Hartree-Fock atomic wave functions, which would suggest that the mean inner potential depends on the energy of the incident electron, since for high energy electrons relativistic effects have to be taken into account. Since the MIP is defined as a property of the material itself it should not depend on the electrons that are used to probe the material (Völkl et al., 1999). The correction of the scattering factor for relativistic effects is accomplished by multiplying with $m/m_0 = [1 - (v/c)^2]^{-1/2}$, where v is the speed of the electron in vacuum and c is the speed of light in vacuum. In the last equality of Equation (3.31) relativistic effects are taken into account by replacing m_0 by the relativistic mass of the electron m, and multiplication of F by m/m_0, which does not modify the equation. For this reason the use of relativistic scattering factors is not be a problem.

Another model can be used to calculate a lower limit of V_0 from the structure factor by assuming that the crystal is made of ions at the lattice points with the remaining valence electrons distributed uniformly (Radi, 1970; Völkl et al., 1999). Although the structure factor can be measured very accurately, no simple formula exists at present to convert $F(\theta)$ to V_0, only boundary values can be calculated. The difficulty lies in describing accurately the redistribution of valence electrons due to binding. Including the effect of binding in the calculation of V_0 can be accomplished using Density Functional theory (DFT) (Kruse et al., 2006). The values obtained by DFT agree reasonably well with experimental measurements of the MIP (Kruse et al., 2006), that all have their precision. Interestingly the differences between the MIP of the same material found in literature can vary even by one or a few volts (Völkl et al., 1999). Therefore it seems clear that measuring this material property accurately remains a challenge. The mean inner potential can be measured using interferometry of films, holography, Reflection high-energy electron diffraction (RHEED) and electron diffraction (Völkl et al., 1999).

Spence and Zuo (Spence and Zuo, 1992) remarked that V_0 has two important interpretations: first as a measure of diamagnetic susceptibility (the reaction of a material to an applied field) and second as a measure of "size" of the atom. For this reason V_0 is most sensitive to the state

of ionicity of atoms in a crystal and depends strongly on the redistribution of valence electrons. Using this argument a more intuitive meaning of the MIP can be obtained: It is known that generally an electron is scattered over larger angles for increasing interaction with inner shell electrons or the nucleus. Inversely electrons that are not scattered (the direct beam) interact mostly with valence electrons and the average potential in the crystal. Obviously V_0 is sensitive to doping concentrations for this reason. Also there seems to be an effect of sample size on the MIP (Popescu et al., 2007), also observed in this work (Section 7.9). If the argument presented above is followed this size effect is either due to a redistribution of valence electrons, a change in lattice parameters (redistribution of nuclei) which would mean that the lattice is deformed and strain is present, or a combination of both effects for decreasing object size. The size effect was interpreted by Popescu et al (Popescu et al., 2007) as a compressive strain of surface atoms in the gold clusters. Calculations of the MIP by DFT show the opposite effect (Kruse et al., 2006): the MIP decreases for decreasing crystal thickness below two monolayers (this is not commented in the text and a thickness of two monolayers is thinner than the onset of the effect observed in (Popescu et al., 2007)).

In semiconductors the measurement of the crystal potential can be used to gain access to active doping concentrations in the specimen. Since doping of the specimen modifies the charge density and therefore also the crystal potential (Equation (3.29)). If a crystal is doped by a $p-$type dopant atom (a hole is donated to the crystal lattice, or an electron is accepted hence the name acceptor) or $n-$type dopant atom (an electron is donated to the crystal lattice, hence also called donor), the location of the valence and conduction bands are modified with respect to the Fermi energy of the material. For this reason a potential difference is observed when going from the p to the $n-$type material. This potential change is called the built-in potential V_{bi} (Sze, 1985):

$$V_{bi} = \frac{\kappa T}{e} ln \left(\frac{N_A N_D}{n_i^2} \right) \tag{3.32}$$

where κ is the Boltzmann's constant (1.380658x10^{-23} J/K), n_i is the intrinsic carrier concentration in silicon (9.65x10^9 cm^{-3} (Sze, 1985)) and N_A and N_D are the acceptor and donor concentrations respectively. The derivation of this formula is shown in Appendix A.4. This formula can be used only in the absence of other charges, since their presence will also modify the location of valence and conduction bands with respect to the Fermi level in both $p-$ and $n-$type material and therefore the potential change over the junction will be different. This relation is valid only for non-degenerate semiconductors.

The step in phase that is measured over a p-n junction can therefore be related to the change in MIP between the p- and n-doped regions (Equation (3.22)). The change in MIP is equal to the built-in potential and can be used to estimate doping concentrations (Equation (3.32)).

3.8.5 Holography on the TITAN

An FEI TITAN was used for holography. Some characterizing properties of this microscope for the use of electron holography are presented in the following. The results are compared to the performance of a JEOL 2100F (Schofield et al., 2008). The phase resolution as a function of biprism voltage is calculated (Equation (3.23)) and compared to the noise value.

The fringe-spacing, that is determining for the resolution, the contrast that can be obtained in the hologram (Equation (3.17)), and the field of view were analyzed as a function of biprism voltage for two different exposure times of 2 and 20 s respectively, as shown in Figure 3.9. For

these measurements holograms were recorded at a nominal 2k9 magnification in Lorentz mode and only the biprism voltage was varied. Since holograms were recorded through a Gatan energy filter, that introduces an additional magnification of ∼20, the effective magnification is approximately 58k. This corresponds to a pixel size of 0.28 nm on a 2 k CCD camera.

The hologram width or field of view was measured between the two large Fresnel fringes at the sides of the hologram. The calibration was performed using HRTEM images of nanowires, since the magnification in Lorentz mode depends sensitively on defocus (Formanek, 2004). The field of view and fringe spacing were measured with respect to the size of the sample. S_{im1} and W_{im1} (Equation (3.14) and Equation (3.16)) introduced in Section 3.8.1 are determined in the first image plane and are related to the object plane by

$$W_{im1} = W_{obj}M \qquad S_{im1} = S_{obj}M \qquad \text{where} \qquad M = \frac{a+b}{F} \tag{3.33}$$

The experimentally measured values for the field of view and fringe spacing refer only to W_{obj} and S_{obj}. For these experiments an exposure time of 2 and 20 s was used (during working hours).

The results presented in Figure 3.9 are classical curves and in agreement with Equation (3.14) and Equation (3.16). A fit to the data using Equation (3.14) and Equation (3.16) as shown in Figure 3.9A,C, allows calculation of the biprism radius R and the interaction constant γ_0 if a, b and F (the focal length of the Lorentz lens) are known. At present these values are not precisely known for the Titan and they should either be measured or obtained from the manufacturer for further characterization of the microscope.

The same field of view (e.g. 552 nm) can be obtained on the Titan and on the JEOL. On the Titan with a contrast of 40 % and a fringe spacing of 3.1 nm (Figure 3.9) and on the JEOL with the same contrast but a fringe spacing of 2.4 nm (Schofield et al., 2008) and therefore a better spatial resolution. However the exposure time was 2 s in the experiments presented in (Schofield et al., 2008). A short acquisition time limits the number of electron counts, and therefore the phase resolution (Equation (3.23)) (the phase resolution obtained in (Schofield et al., 2008) is not mentioned there).

In Figure 3.10 and Table 3.1 the phase resolution estimated using Equation (3.23) with d either 2 (Lenz, 1988) (Harscher and Lichte, 1996) or 14 (de Ruijter and Weiss, 1993) is given and compared to the noise (the standard deviation of the variations) in a phase image obtained by reconstruction of two empty holograms made directly after one another (Cooper et al., 2007a). The phase resolution was calculated at two different acquisition times being 2 and 20 s respectively, and compared to the noise. The spatial resolution was estimated to be three times the fringe spacing. The mask size during reconstruction was $\sim 1/3$ of the carrier frequency. The same data describing the phase resolution and noise can also be found in Table 3.1, where also the contrast and spatial resolution can be compared.

The spatial resolution Δr_{min} is used to determine the number of electron counts per resolved pixel (N_{el}) in the phase image using

$$N_{el} = \frac{\Delta r_{min}^2}{S_{px}^2} N_{av} \qquad N_{av} = \frac{N_{max}+N_{min}}{2}, \tag{3.34}$$

where S_{px} is the px size (0.28 nm) and N_{av} is the average number of electron counts in the hologram.

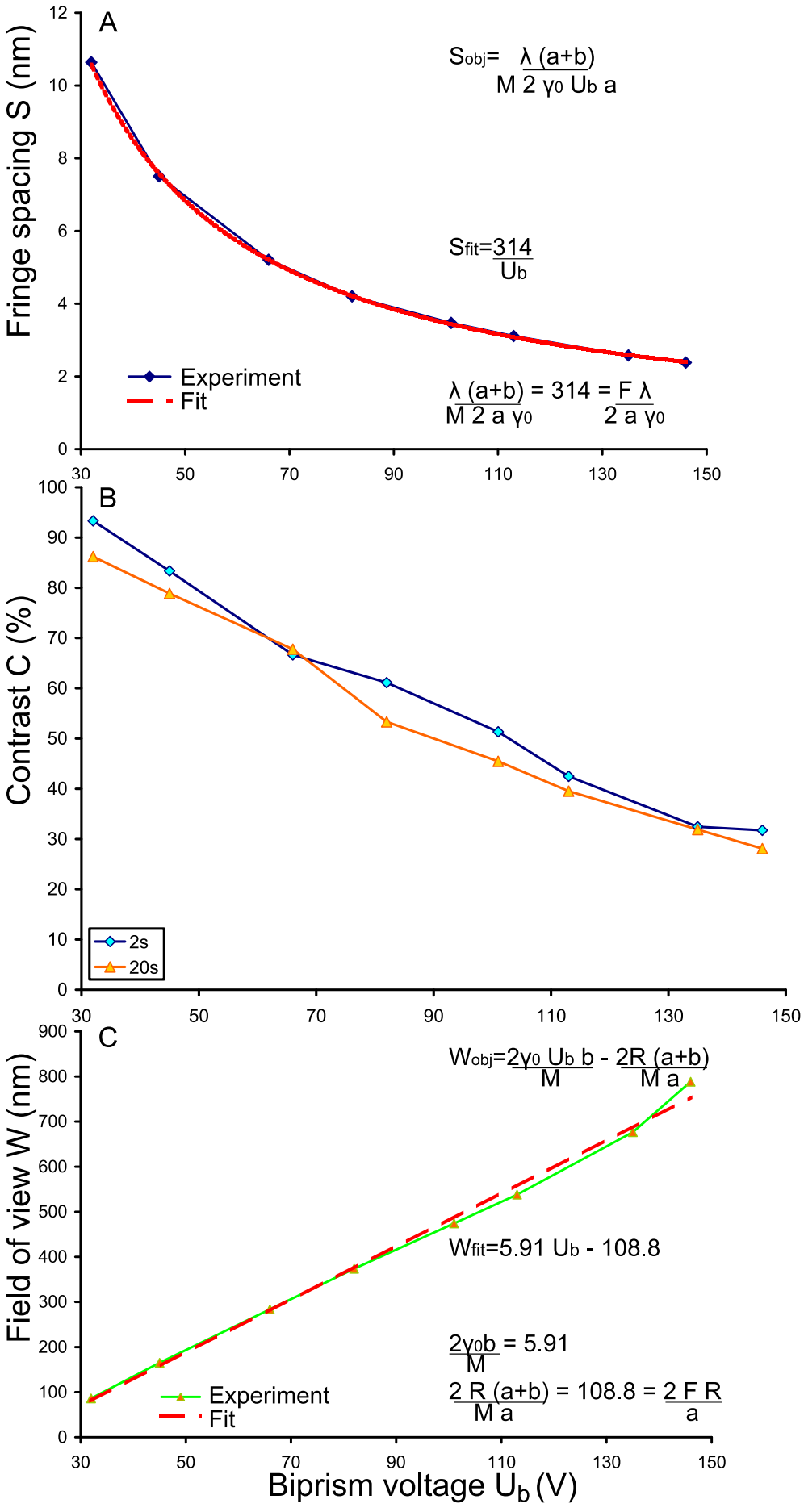

Figure 3.9: (A) Fringe spacing (nm) (B) Contrast (%) and (C) Field of view (nm) as a function of biprism voltage U_b (V).

It should be noted that literature is not extremely clear on how N_{el} should be calculated. N_{el} is either defined as the total electron dose in the measured area (de Ruijter and Weiss, 1993; Völkl et al., 1999) or as the number of electrons per resolved pixel (Lichte, 2008b; Völkl et al., 1999)[7]. The noise in the hologram that limits the phase resolution is due to Poisson distributed shot noise with a standard deviation $\sigma = N_{el}^2$ (Völkl et al., 1999). It seems reasonable that we are interested in the effect of the shot noise for the smallest resolvable details, therefore we chose to interpret N_{el} as the number of electrons per resolvable detail, as determined by the spatial resolution. The definition of N_{el} does influence the calculated phase resolutions slightly. If (N_{el}) is defined as the total electron dose in the measured area the phase resolution is limited by the noise contribution (present in a phase image that is obtained by reconstruction of two empty holograms).

Figure 3.10 and Table 3.1 shows that indeed the phase resolution and noise are lower for an acquisition time of 20 s (open symbols) than for a short acquisition time of 2 s (filled symbols), as expected. The noise contribution is approximately equal to the phase resolution using $d = 14$ for an exposure time of 2 s. For a long exposure time of 20 s the noise contribution is similar to the calculated phase resolution with $d = 14$ at low biprism voltage, and below this value ($d = 14$) at high biprism voltage. A relatively long exposure time (around 20 s) and biprism voltage U_b of 100 V was generally used to obtain the holographic data presented in Chapter 7. Therefore a phase resolution ≤ 0.01 rad can be expected in this work. In Chapter 7 it will be shown that the phase fluctuations introduced by inhomogeneities in the sample are the limiting factor for quantitative interpretation of the data, and not the intrinsic phase resolution of the technique.

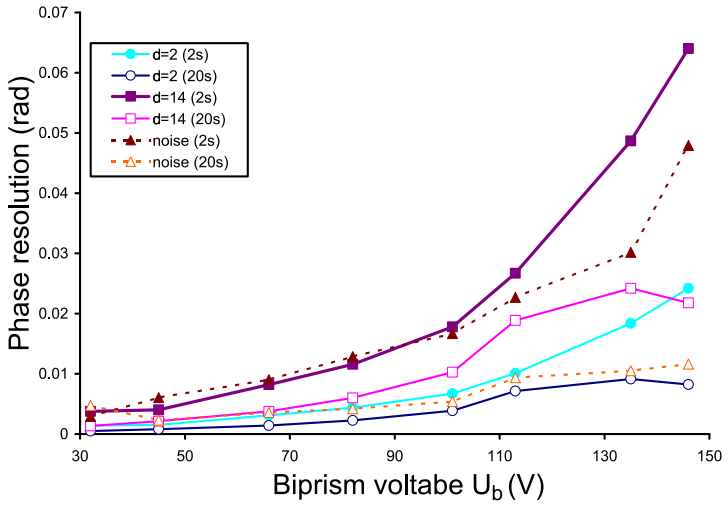

Figure 3.10: Phase resolution as a function of biprism voltage U_b (V). Open symbols denote an exposure time of 20 s and filled symbols of 2 s. The phase resolution is calculated using Equation (3.23) with d is either 2 (◯) or 14 (□). The noise contribution is estimated from the standard deviation in a phase image obtained by reconstruction of two empty holograms obtained directly after one another (△, dashed lines).

A sampling of about 8 pixels/fringe for the finest spacing was used, which means that the CCD is over-sampled, as 2 pixels/fringe are sufficient to sample the signal at the Nyquist rate (Geocities.com, 2009). This oversampling is illustrated schematically Figure 3.11. In Figure 3.11A the fringes are sampled at the Nyquist rate. In Figure 3.11B the sampling frequency is four times as high and the spatial resolution is four times worse, because the spatial resolution depends on the fringe spacing S. The magnification is the same in both schematics and the biprism voltage is used to change the sampling frequency. However the over-sampling of the CCD has the

[7] Both definitions of N_{el} can be found in (Völkl et al., 1999)

Table 3.1: The contrast C%, spatial resolution, phase resolution with different values for d and noise in the phase image for different values of the biprism voltage at two exposure times.

Biprism U_b (V)	Contrast C%	Spatial res. (nm)	Phase res. $d = 2$ 20s (rad)	Phase res. $d = 14$ 20s (rad)	Noise (rad) 20s	Phase res. $d = 2$ 2s (rad)	Phase res. $d = 14$ 2s (rad)	Noise (rad) 2s
32	86	32	0.0005	0.0013	0.0048	0.0014	0.0038	0.0029
45	79	23	0.0008	0.0021	0.0023	0.0015	0.0040	0.0060
66	68	16	0.0014	0.0037	0.0036	0.0031	0.0082	0.0090
82	53	13	0.0023	0.0060	0.0042	0.0044	0.0116	0.0129
101	45	10	0.0038	0.0103	0.0054	0.0067	0.0178	0.0167
113	40	9	0.0071	0.0189	0.0093	0.0101	0.0267	0.0227
135	32	8	0.0091	0.0242	0.0105	0.0184	0.0487	0.0302
146	28	7	0.0082	0.0218	0.0116	0.0242	0.0640	0.0479

advantage that the hologram is less sensitive to noise, which allows long acquisition times and a high phase resolution (Equation (3.23)). For this reason the choice was made to gain in phase resolution at the expense of spatial resolution.

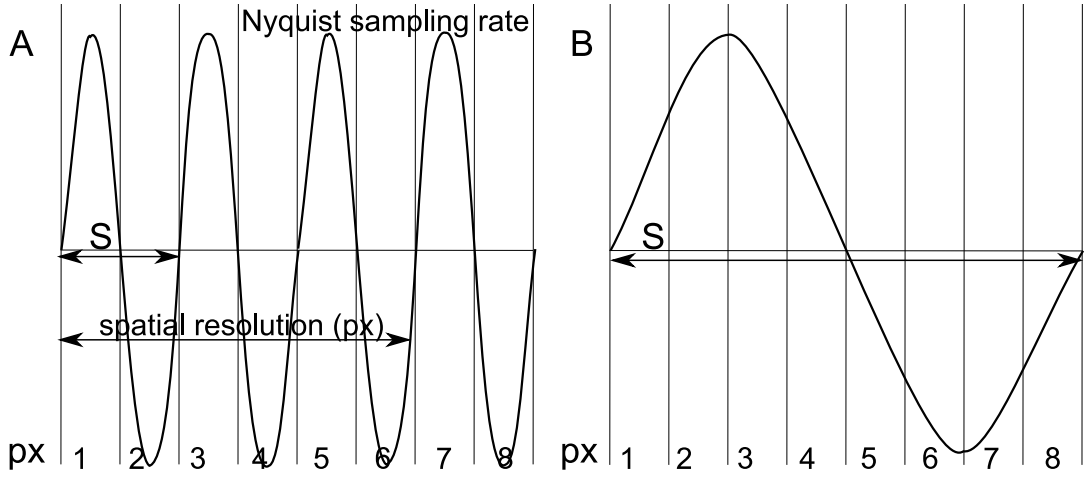

Figure 3.11: Schematic illustrating the sampling frequency. The magnification is the same in both images, only the biprism voltage is changed. (A) Sampling of the hologram fringes at the Nyquist rate (2 $^{\text{pixels}}/_{\text{fringe}}$). (B) Sampling of the hologram fringes at a spatial frequency four times as large. The spatial resolution is better in (a) where S is smaller, because three hologram fringes are necessary to sample the finest detail (Section 3.8.2). However in (b) the hologram intensity is less sensitive to noise and therefore long acquisition times are possible and a better phase resolution can be obtained at the expense of a worse spatial resolution.

3.9 The TEM hardware

In this work primarily two microscopes were used: a JEOL 4000 EX equipped with a LaB_6 gun for HRTEM and a probe corrected FEI Titan for STEM in combination with EDX and Holography. STEM images were acquired with the Titan, however the superior resolution of STEM with respect to TEM was not of crucial importance for this work. Incidentally a JEOL 2010 FX was used to acquire diffraction patterns. A ZEISS ultrascan scanning electron microscope (SEM) equipped with an in-line detector was used for quick and efficient analysis of a great number of samples without special specific specimen preparations, but the image quality is

not as good as that obtained in STEM. The SEM was used to see if gold was present on the nanowire sidewall (Chapter 5).

In Table 3.2 the resolution for different techniques and the spherical aberration coefficients are indicated. The Titan is equipped with a probe corrector that allows very high resolution in STEM mode. Typical residual aberration coefficients after correction of the probe for a spatial resolution of 1 Å (using FEI TIA software that makes use of a Zemlin tableau) are shown in Table 3.3. In Figure 3.12 two STEM images before and after the installation of the probe corrector are shown of a silicon nanowire with gold clusters on the surface. Clearly the image quality in terms of signal to noise ratio is much better. The resolution is improved since in the second image silicon dumbbells can be observed (lattice spacing of 1.36 Å). The drawback of the probe corrector is the lengthy alignment procedure ($\sim 1\,\mathrm{h}$ if their are no additional problems) which requires a specific sample.

The Titan is equipped with BF, ADF and HAADF detectors for STEM, an EDX detector (EDAX, Saphire), a Gatan Tridium GIF (energy filter) and a rotatable biprism for Holography.

The phase resolution of this microscope is 0.01-0.002 rad (for exposure times of 4-128 sec. respectively (Cooper et al., 2007a)), as already shown in the previous section. Several different sample holders are present that allow standard tilting over two axes, tomography, in situ heating and biasing of the sample.

Table 3.2: Spatial resolution (nm) in TEM and STEM mode and and abberation coefficients (mm) of the objective lens (TEM) and condensor system (STEM) of the microscopes that were used in this work.

Microscope & Mode	Resolution at Scherzer defocus (nm)	C_s
JEOL 4000 EX TEM	0.17	1 mm
JEOL 2010 FX TEM	0.34	4.5 mm
FEI Titan 200 kV TEM	0.23	1 mm
FEI Titan 200 kV Lorentz lens	2.5	12 m
FEI Titan 300 kV TEM	0.19	1 mm
FEI Titan 300 kV STEM	0.08	8.3 μm
Zeiss SEM 2-30 kv	1 nm	

Table 3.3: Typical aberration coefficients of the condensor system for a spatial resolution of 1 Å (FEI, 2007) in STEM. The last 4 aberration coefficients are aligned at the factory.

Coefficient	Residual aberration
C1 Defocus	1.6 nm
Scherzer defocus	-17.7 nm
A1 2ford astigmatism	1.6 nm
A2 3fold astigmatism	122 nm
B2 Axial coma	41 nm
C3 Spherical aberration C_s	8.3 μm
A3 4fold astigmatism	8.3 μm
S3 Star aberration	2.1 μm
A4 5fold astigmatism	528 μm
D4 Three lobe aberration	106 μm
B4 Axial coma	106 μm
C5 Spherical aberration	32 μm
A5 6fold astigmatism	836 μm

The Titan can also be used in TEM mode. TEM mode was used only to acquire calibrated bright field or high resolution images of samples that were studied in electron holography.

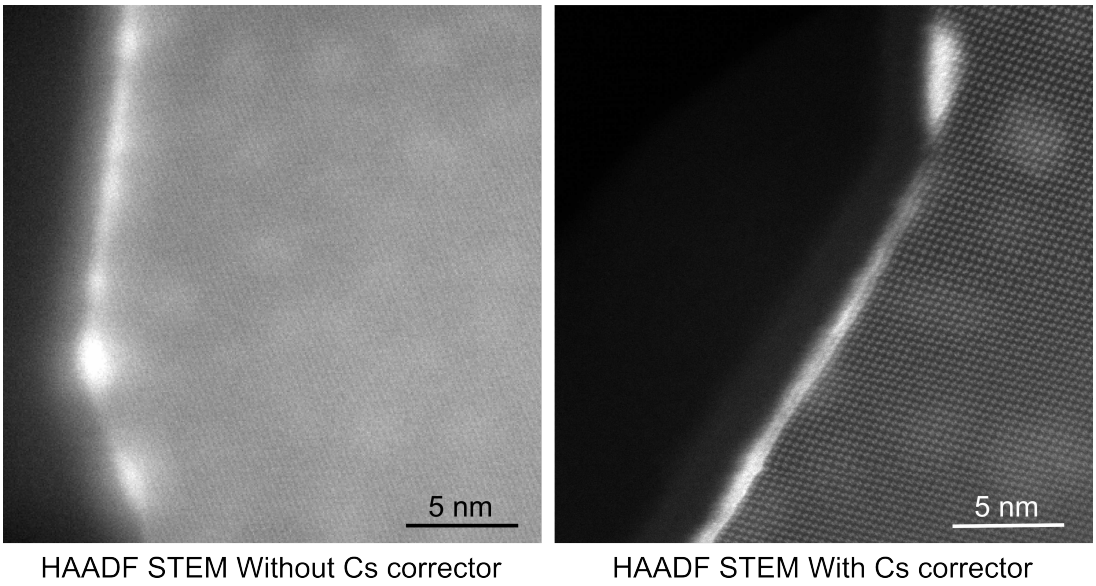

Figure 3.12: HRSTEM images of a nanowire with gold clusters on the surface. On the left before installation of the C_s corrector, on the right with C_s corrector. Clearly the image quality (signal to noise) and resolution (with the C_s corrector silicon dumbbells can be distinguished) have improved considerably.

Although the resolution of the Titan in TEM mode is lower than the JEOL 4000 EX, this is not directly obvious to the user due to the increased spatial coherence of the Field Emission Gun (FEG) of the Titan. In Figure 3.13 the intensity transfer function of the JEOL 4000 EX is shown, compared with the transfer function of this microscope if the electron gun was a more coherent electron source, the transfer functions were simulated using JEMS (Stadelmann, 2008). Due to the increased coherence of the gun, the damping function of the CTF is decreased and passbands are present for distances $< r_{sch}$. Reflections of higher order crystal planes can be observed in the FT (due to these passbands), corresponding to distances $< r_{sch}$.

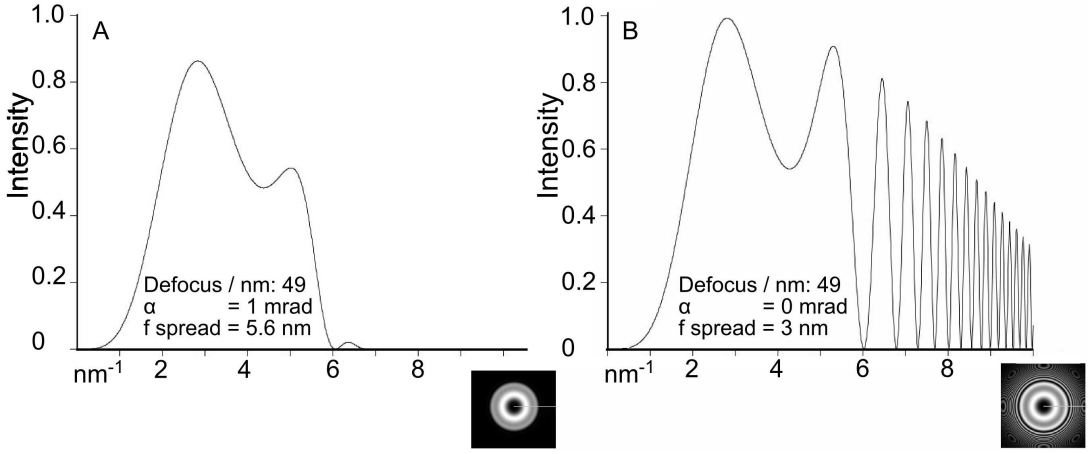

Figure 3.13: (A)The intensity transfer function of the JEOL 4000 EX at Scherzer defocus (-49 nm) including spatial and temporal envelopes and with a beam convergence angle α of 1 mrad and defocus spread of 5.6 nm. (B) The intensity transfer function of the same microscope at Scherzer defocus with a beam convergence angle α of 0 mrad and defocus spread of 3 nm to illustrate the effect of an increased coherence of the source on the transfer function. Both transfer functions were simulated with JEMS (Stadelmann, 2008).

3.10 Summary

Many different TEM based techniques were used in this work and a state of the art microscope was used. The more original part of this work was obtained using holography and, to a lesser extent using STEM.

Now that the different methods that were used to study nanowires have been described, the necessary preparation steps and different possibilities to create a specimen suitable for TEM observations are shown in the next chapter.

4

SAMPLE PREPARATION

"TEM is only as good as your sample" (Colin Humphreys). This chapter describes the sample preparation techniques used in this work. Some are standard techniques, others are existing techniques that are new to be used with nanowires.

4.1 Dispersion Sample

The most straightforward way to prepare a nanowire sample is to disperse the nanowires on a holey carbon grid (or alternatively a plane carbon film). The nanowires can be dispersed in two ways. The first possibility is to disperse the nanowires in solution. To accomplish this the nanowire substrate (the growth substrate containing the nanowires) is placed in a small quantity of pure ethanol (Carlo Erba RSE) and sonicated in an ultrasonic bath for several minutes. A drop of the nanowire suspension is then put onto the TEM grid (Ted Pella Prod. No 01890 and 018162). To avoid damage of the carbon grid it is best to place the grid on a flat substrate where a cavity is made directly underneath the carbon grid. In this way the film cannot attach to the substrate and cannot be teared apart when removing the grid from the substrate.

Another way of creating a dispersion sample is to place the grid (copper side down seems to work slightly better) directly on the nanowire substrate and move it around gently. Sometimes just touching the grid to the substrate is sufficient to achieve a satisfactory density of nanowires on the TEM grid, sometimes the grid should be rubbed to the nanowire sample. In general the sample preparation works very good if the nanowire density on the nanowire substrate is high and the nanowires are long ($\geq 10\,\mu$m).

The advantage of this second option is that the sample is generally cleaner since a lot of dirt is picked up in solution. A general problem of dispersion samples is that the wire density is low. To increase the nanowire density the nanowires should be dispersed in the smallest quantity of liquid possible, or the nanowire substrate (preferable with a high density of nanowires) should be rubbed several times to the TEM grid.

4.2 Cross section Sample

The preparation of a cross section sample is a very classical TEM sample preparation technique. Two parts of the sample are glued together, a small slice is cut from the obtained sandwich structure, which is thinned down further using mechanical polishing and a hole is created with

thin regions on the side by ion milling (Ayache et al., 2007). The most successful cross section sample was prepared by putting Gatan G1 glue on the nanowires and placing a dummy piece of silicon on top without applying pressure. The ensemble was put under vacuum for half an hour[1] and the two halves were clamped together. This sample was put in the oven for 4 hours. Small slices were cut from the glued sample perpendicular to the interface using a diamond saw (by Escil). These slices were thinned down further by mechanical polishing on a Buehler polisher using diamond coated disks. The sample was thinned down to approximately 20 μm. The final hole in the sample was made using Ar ion milling using a Gatan PIPS at an energy of 3 keV and angles of 7°. An example of such a sample is shown in Figure C.1 and Figure 6.3.

We didn't find this technique very successful for nanowires. Several problems were experienced using this technique and we only succeeded in making two useful samples. The problems were:

- The nanowire density was not very high on the growth substrate and therefore no wire was found on the thin parts of the TEM sample
- Immersion of the nanowires in a polymer (Epofix Resin, Struers) under vaccuum was tried. The immersion worked very well (using an optical microscope the nanowires could be visualized and were still present on the substrate, without being deformed by the polymer). However the polymer detached from the substrate when polished very thin, therefore no wires could be observed on the TEM sample.

For this reason a sample preparation method was explored that allows to study the nanowire on the substrate, without having to polish the sample or immerse the nanowire to protect it. This method is described in the next section.

4.3 Cleaving

The cleaving method (Williams and Carter, 1996) and small angle wedge cleaving method (Walck and McCaffrey, 1997) are already known for bulk TEM sample preparation. We have extended this technique in its most simple form to observe nanowires as-grown on the growth substrate in the TEM. A small wedge is cleaved or broken off the substrate on which nanowires are grown and this wedge is tilted so that the substrate surface is parallel to the electron beam.

In Figure 4.1 the cleaving process is described in detail:

- Figure 4.1A shows the setup: a light microscope (Escil Motic) with a long working distance is placed inside a fume cupboard. Since inhalation of objects with this aspect ratio is not recommended (Poland et al., 2008), it is best to work in the fume cupboard and wear a P3 mask to protect for small dust particles (this is quite important because in this setup one has to enter with the head inside the fume cupboard to be able to use the optical microscope).
- In Figure 4.1B the nanowire sample is shown glued on a post-it. The post-it ensured that no cleaved parts of the sample will fly away. For bulk samples it can be preferred to perform cleaving in liquid for this reason, but in the case of nanowires this will make the nanowires bend due to capillary forces, and the sample will be less clean.

[1] In a previous attempt to prepare this particular nanowire substrate the glue failed to keep the two parts of the sample together. Because in this case the nanowire density was very high we supposed that the limited strenght of the glue was caused by limited embedding of the nanowires in the glue due to air bubbles, which could be removed by a vacuum treatment.

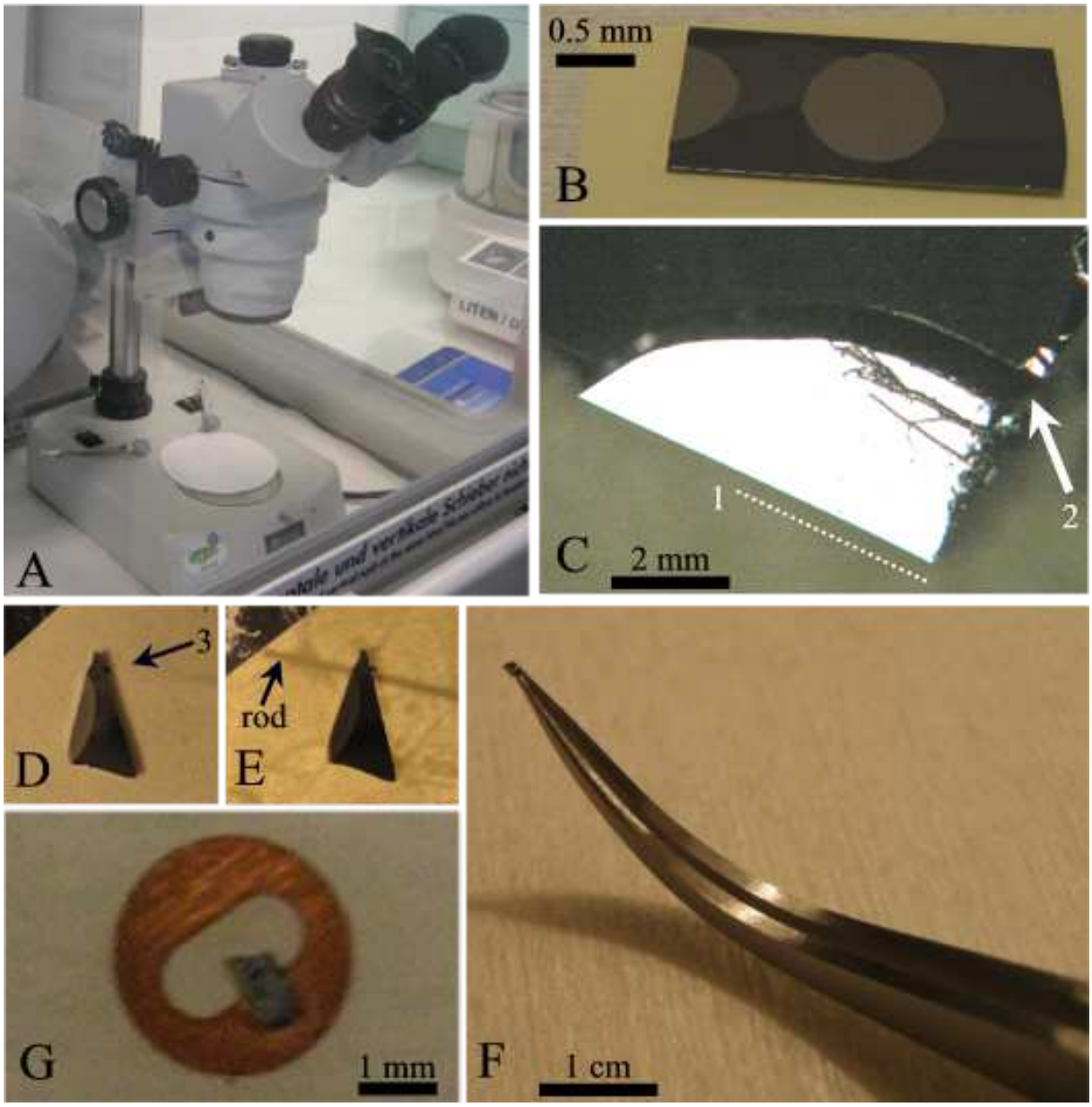

Figure 4.1: Different steps to prepare a cleaved sample (A) Preparation of the setup: an optical microscope inside a fume cupboard (B) The nanowire substrate (substrate on which nanowires have been grown) is shown glued on a post-it, the nanowires are facing up. The dimensions of the sample are 1 by 2 cm. The visible circles on the silicon wafer are the regions where nanowires were grown, since the catalyst material was deposited as a droplet containing gold colloids. (C) First a scratch and successive cleaving on the dotted line marked by 1 was already performed. Then successful cleaving of a wedge was performed. The arrow marked by 2 indicates were several scratch marks were made using a diamond pen. (D) If the sample is too long it has to be shortened. A scratch mark is made on the wedge, indicated by an arrow marked by 3. (E) The sample is cleaved using a fine rod as indicated in the image (diameter ~ 0.3 mm) and inverted tweezers. (F) The sample is picked up using inverted tweezers, ready to be glued. (G) The final sample.

- In Figure 4.1C a successfully cleaved sample is shown. The dotted line marked by one indicates the first cleaving line to obtain a nanowire sample containing nanowires from the middle of the growth substrate, since nanowires growing at the edge of the sample can be damaged during handling. The arrow marked by two indicates where several scratches were made using the diamond scribe to perform the second cleaving step. In this case the scratches are made parallel to the substrate edge. The crack in the sample will start to propagate in the same direction but since a surface is very near it has a tendency to deviate to the surface, which results in the desired wedge angle. The cleaving step to obtain the small wedge angle (the angle is generally between $30°$ and $45°$) is relatively difficult, since the crystal doesn't contain a low energy plane in this direction. Most of the nanowire samples were grown on a $\langle 111 \rangle$ oriented silicon wafer, for this reason one could argue if we are actually cleaving or rather breaking the sample in small pieces. Generally several attempts have to be made to obtain a satisfying angle. The most robust way to obtain a wedge angle is as described previously, but sometimes the sample will break apart in several smaller pieces (due to unsuccessful cleaving) that may result in a wedge angle as well.

- In Figure 4.1D a small wedge of the sample is shown that is too long to fit in the TEM. Therefore the sample has to be shortened by an additional cleaving step. A scratch is made by the diamond scribe indicated by an arrow marked by three.

- In Figure 4.1E the ultimate cleaving step is performed. A thin rod is placed under the cleaving mark. Curved tweezers (turned upside down like in Figure 4.1 F) are used to exert a force on both sides of the scratch mark and the rod underneath. Since the substrate is generally thick, some force can be needed.

- When the cleaving is successful and a sample small enough to fit inside the TEM sample holder is obtained without damaging the nanowires, the sample is picked up with inverted tweezers (Figure 4.1F). In this way the sample can be stored safely until it is glued to a TEM grid. Samples were generally glued using superglue.

- A finished sample is shown in Figure 4.1G. Samples were electrically connected to the copper TEM grid using a droplet of silver glue. Care was taken to dry the glue using mild heating of the sample under a lamp and putting the sample under vacuum for at least 24 hours. Alternatively samples were glued using a conducting epoxy.

A quick observation of the samples can be done using a high quality optical microscope (Olympus B061). Wire diameters as small as 50 nm can be distinguished due to light diffusion (Figure 4.2).

The advantages of this method are that

1. Nanowires are observed as-grown on the substrate and therefore the coherence of the sample is maintained.

2. The fact that the nanowires are growing epitaxially on the substrate can be used or studied. If the nanowires are in epitaxy it is possible to align all nanowires simultaneously on the same zone axis .

3. No chemical or solution is used during the sample preparation which means that the nanowire surfaces are clean[2].

[2] Cleaved samples can sustain long cleaning treatments using a plasma cleaner to remove organic components, which is important to limit contamination during HAADF STEM observations. This is in contrast to wires deposited on a carbon grid, because the carbon grid is gradually removed during cleaning as well.

4. The nanowires are electrically connected to the substrate, which is generally highly doped silicon, therefore charging of the sample under the influence of the electron beam is reduced.

The disadvantages of this sample preparation is that longer and/or thinner nanowires will vibrate slightly under the electron beam far away from the substrate, this seems to be caused by electrostatical interaction between the (charged) sample and the electron beam. Conventional imaging (at low resolution) and holography are still possible under these circumstances, but HRTEM is not. Cleaving is performed by hand, and therefore the wedge angle is generally not below 30°. Therefore high resolution can be performed only on the first hundred nanometer of the cleaved edge, which means that it is not possible to study the wire catalyst interface since at this region the sample will be already too thick. We should note that although the technique allows to study large quantities of undamaged nanowires, there are generally no wires directly on the cleaved edge.

A particularly successful example of this kind of sample preparation is the nanotrees shown in Figure 6.5. All images shown in Chapter 7 were obtained on cleaved samples, unless otherwise indicated. In Figure 4.2 optical microscope images and a TEM image are shown of the same cleaved sample, to show how well the nanowires are preserved on the substrate.

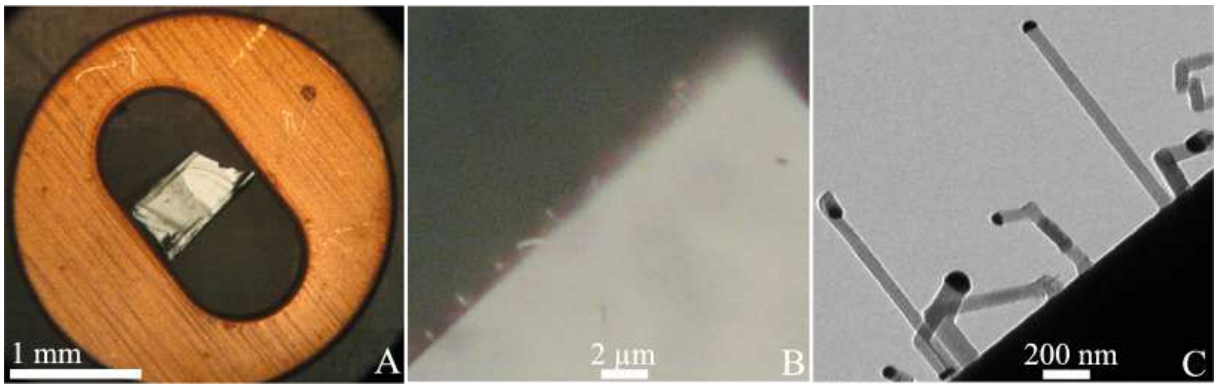

Figure 4.2: An example of a cleaved specimen (A) Optical microscope image of the nanowire stubstrate attached to the TEM grid (B) Optical microscope image showing the nanowires near the cleaved edge (C) TEM BF image (lorentz lens) showing the nanowires on the substrate

4.4 Wire Section

In the previous sections nanowires were prepared to be observed in a direction perpendicular to the growth direction. Interesting information can also be obtained by observing a nanowire section along the growth direction, what we call hereafter a nanowire section or wire section. A wire section sample allows to see more clearly if vertical defects are present in the nanowire volume and which crystal facets are present on the nanowire sidewall. Three techniques to obtain wire section samples have been used and two techniques were successful.

First a focused ion beam (FIB) can be used. A dual beam FEI Strata FIB was used working at 30 keV[3]. In Figure 4.3 a series of SEM images is shown leading to the sample. The technique has several disadvantages: only one nanowire cross section can be obtained in 2-3 hours of work, the surface of the wire is damaged by the Ga ions, therefore no clear facets can be distinguished, there is an amorphous surface layer present on the wire slice also due to Ga ion damage and

[3] Skillful FIB sample preparation was performed by Violaine Salvador.

additional stress can be introduced by the metal coating (Alexandre, 2008). Since the outer shell is damaged only relatively thick nanowires are suitable to prepare by FIB. An example of an FIB prepared wire section sample is shown in Figure 6.13.

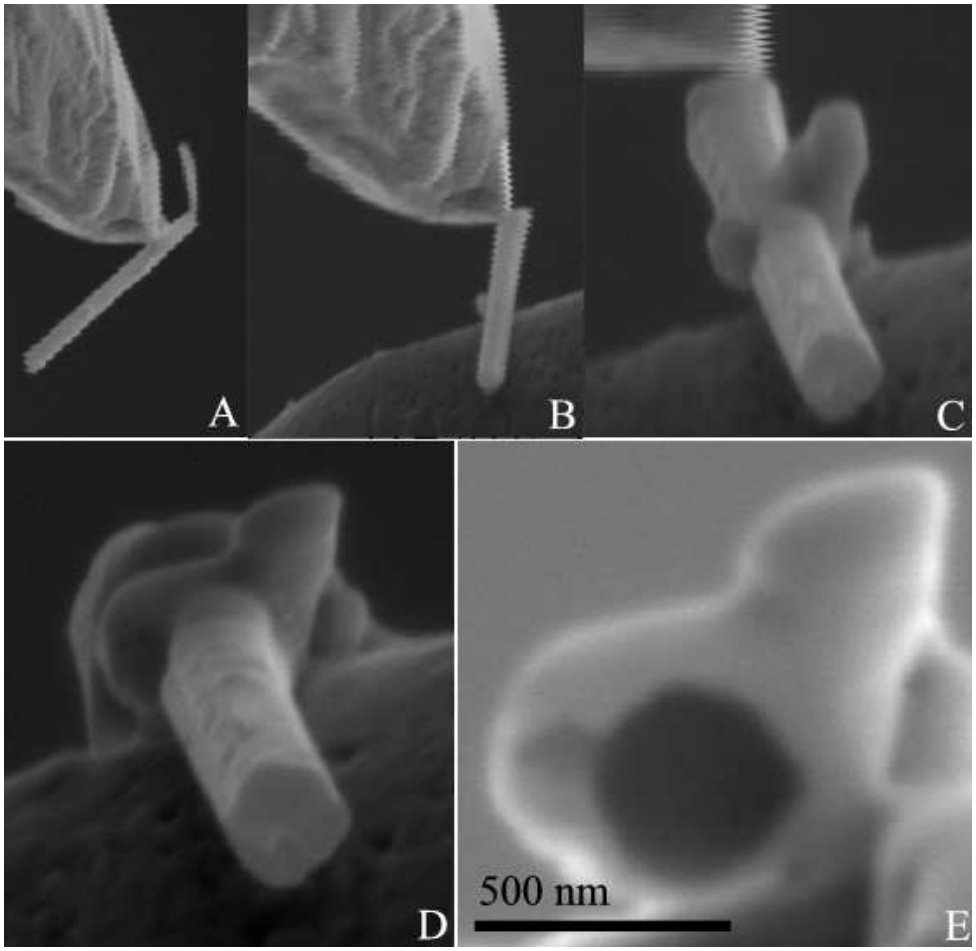

Figure 4.3: Different steps to prepare a wire cross section sample using the FIB. The images are made using the electron beam (A) The nanowire is connected to the omniprobe using ion beam induced tungsten (W) deposition. The wire was broken at the base by moving the omniprobe up (B) The nanowire is approached to the TEM grid (C) The nanowire is attached to the TEM grid again using W deposition (D) The nanowire is thinned down and cut free from the omniprobe using Ga ions (E) The sample is thinned down slice by slice using 30 kV ions. Final thinning was performed at 16 kV until a sample with a thickness of approximately 200 nm is obtained. The sample was scanned at grazing incidence using the same ion energy to gently remove some of the amorphous material due to damage.

Another possibility is to deposit the nanowires in a controlled way on a clean substrate. The key step is to deposit the nanowires mutually parallel on the substrate. Parallel alignment can in principle be achieved by manually sliding a nanowire substrate over a clean substrate. For more control and convenience a tool was used for the wire deposition, shown in Figure 4.4 (modified by Georgios Katsaros [4]). Aligned deposition of the nanowires was accomplished by sliding the nanowire sample over the target substrate with a constant velocity. Mechanical screws were used to position the nanowire sample with respect to the target substrate.

In Figure 4.5 an optical microscope image shows the deposited wires. The wires are generally well aligned. Two substrates that are prepared in such a way can be glued together, and the sample can be thinned down mechanically, as described in Section 4.2.

[4] DSM/INAC/SPSMS/LATEQS Service de Physique Statistique, Magnetisme et Supraconductivite

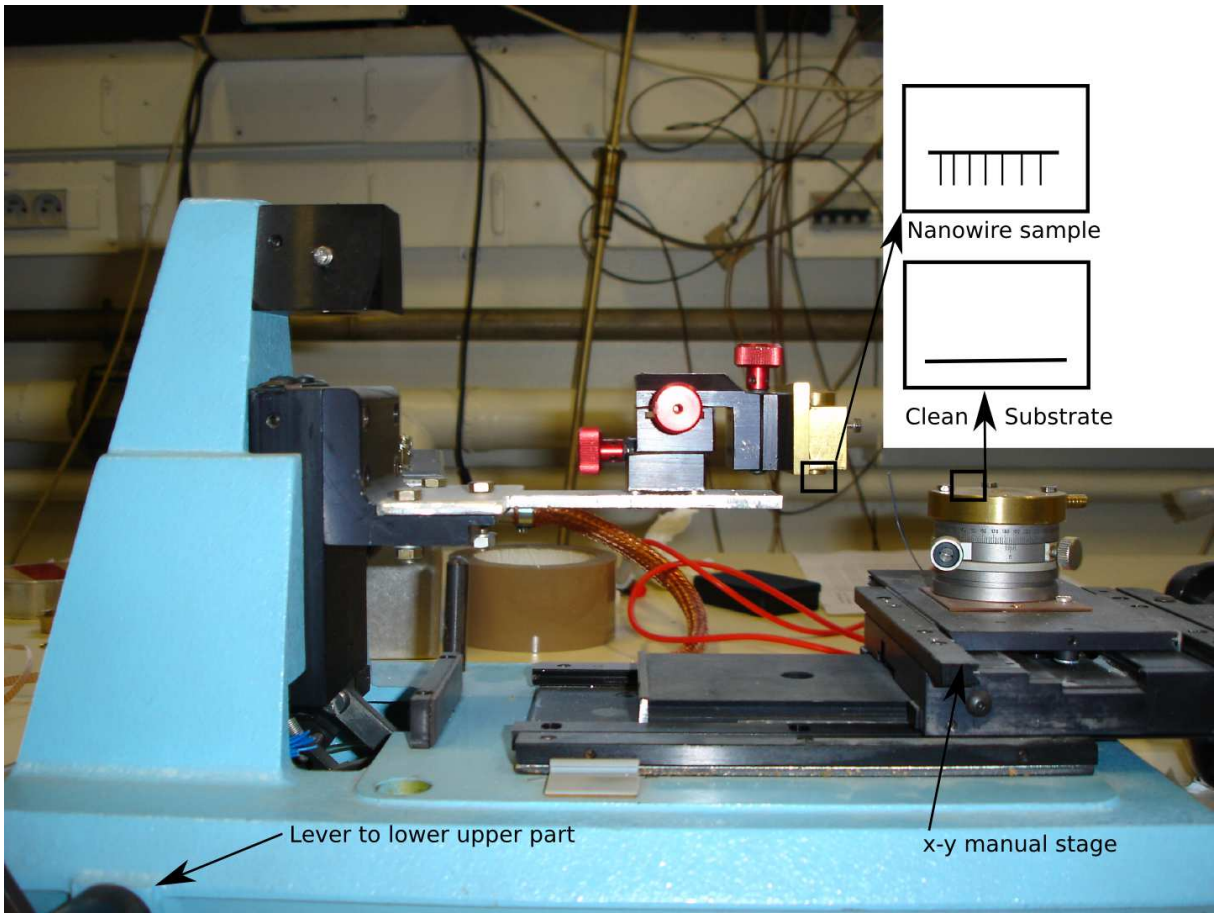

Figure 4.4: Tool to deposit aligned nanowires on a clean substrate.

A clean silicon substrate was used for the deposition of the nanowires. Presumably this has the advantage that the native oxide on the nanowire can bond in a few hours with the native oxide on the substrate. For this reason the nanowires are well attached to the substrate, without the real need for a glue. Evidence for this hypothesis is the fact that it turned out to be impossible to move or pick up silicon nanowires deposited on silicon using the omniprobe in the FIB, since they appeared to be very well attached to the substrate. This problem was absent if nanowires were deposited on a metal. An example of a wire section sample is shown in Figure 6.7. The nanowire deposition method works well for long nanowires. Also the nanowire density on the growth substrate should be sufficiently high.

Basically a wire section sample can also be obtained by preparing what is classically called a plan view (Ayache et al., 2007). For the preparation of a plane view the sample substrate is thinned down from the back. Attempts were made to prepare a plane view sample by immersing the nanowires in an epoxy or (sputtered at $600°$) silicon dioxide, while being still attached to the substrate. The sample preparation was not successful since the epoxy wasn't mechanically stable enough when polished sufficiently thin. In the case of silicon dioxide the sample was highly unstable under the electron beam, probably due to charging and the stress present in the sample due to the fact that silicon and silicon dioxide have different dilatation coefficients.

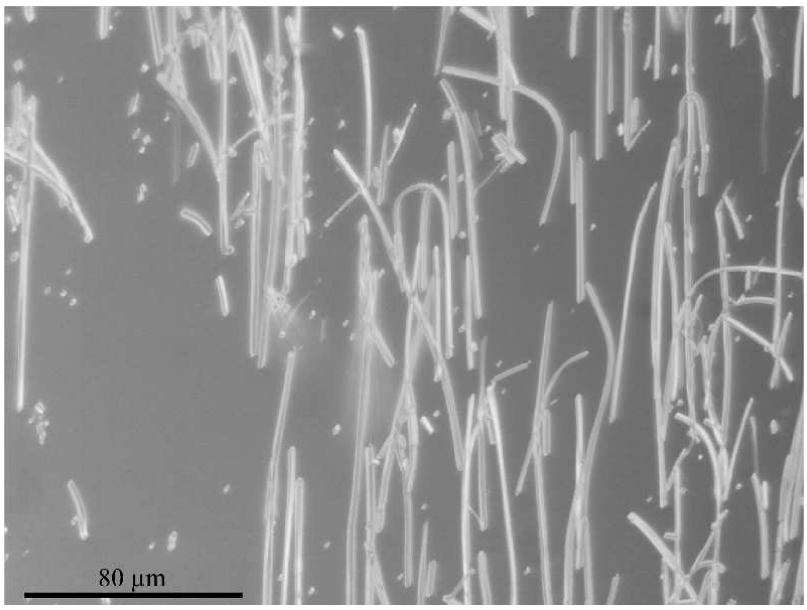

Figure 4.5: Silicon NW's grown with a copper catalyst deposited using a slide tool at a silicon $\langle 110 \rangle$ substrate. Clearly the wires are aligned along the slide direction. The diameter of the nanowires was $\sim 100\,\text{nm}$.

4.5 Summary

In this chapter conventional TEM sample preparation methods were recalled, and new methods for nanowire samples were introduced, that were developed from existing methods. TEM sample preparation is actually determining for the results that can be obtained, since the limiting factor is either the sample or the microscope.

Part II

NANOWIRE SURFACE PROPERTIES AND HOW TO CONTROL THEM

5

CONTROL OF GOLD SURFACE DIFFUSION ON SILICON NANOWIRES

In this chapter silicon nanowires synthesized by VLS with gold as the catalyst are described. The focus lies on the surface characterization of the nanowires and the control of the nanowire surface properties.

It was found that if gold is used as the catalyst particle, the gold can diffuse over the nanowire sidewall and after growth gold clusters are observed on the nanowire sidewall. We show that the gold diffusion can be controlled using the growth parameters silane partial pressure and temperature and also an influence of the nanowire size is observed (Section 5.4). A qualitative model to explain this phenomenon is derived. The presence of gold has an influence on the faceting of the nanowire in the growth direction, the so called sawtooth faceting (Ross et al., 2005) (see Figure 5.13), and different crystallographic facets can be present.

The shape and distribution of the gold clusters observed after growth is described in Section 5.3. A simple model is presented describing the dewetting of the gold liquid layer that is present on the nanowire surface during growth Section 5.6. Although this simple model is valid only for macroscopic systems, it describes the experimental results surprisingly accurately. [1] [2] [3]

5.1 Introduction

Here a brief overview of the literature concerning gold diffusion on silicon nanowires and its importance for applications is given, to situate this chapter.

An important point for the application of nanowires grown by the VLS method using gold as the catalyst in devices is whether gold is incorporated at the nanowire either on the nanowire surface or in the nanowire volume. Indeed in many applications, for instance electric applications, it is important to have no gold incorporation, as gold is known to create deep electron traps (Tavendale and Pearton, 1983). Gold has been detected in the nanowire volume (Allen et al., 2008; Putnam et al., 2007) and on the nanowire surface (Werner et al., 2006). It was

[1] Parts of these results were published in (den Hertog et al., 2007) (den Hertog et al., 2008) (Dhalluin et al., 2007).

[2] The studied nanowires were grown by Florian Dhalluin (CNRS UMR 5129), Fabrice Oehler (CEA/DSM/INAC/SP2M/SINAPS) and Pascal Gentile (CEA/DSM/INAC/SP2M/SINAPS), Grenoble. The nanowires containing phosphorus doped segments were grown by Heinz Schmid (IBM Zurich).

[3] The dewetting model and thermodynamic analysis were developed in collaboration with Prof. P. Desré (Retired, former professor at E.N.S.E.E.G. and scientist at L.E.T.I., Grenoble).

shown by (Hannon et al., 2006) that the gold catalyst particle can constantly lose an amount of gold and that this gold would form 1-1.5 gold monolayers on the wire surface. The result of a constant loss of catalyst material is that the nanowire grows tapered, which is incompatible with long narrow cylindrical nanowires if no extra gold is provided by the substrate. A few publications have reported conditions modifying the presence of gold at the nanowire surface (T.Kawashima et al., 2008; Kodambaka et al., 2006a; Pan et al., 2005). Kodambaka et al (Kodambaka et al., 2006a) have shown that addition of oxygen during nanowire growth can alter the gold surface diffusion since the nanowire surface is modified by the oxygen. However the quality of the wires appears to be reduced. Pan et al. (Pan et al., 2005) reported the presence of gold-rich precipitates on the boron-doped regions of the nanowires whereas there was no gold on the undoped regions.

We will show that the presence of gold at the surface of nanowires can be controlled either with temperature or silane partial pressure or with the initial size of the gold catalyst[4]. We were not able to detect the possible presence of gold within the nanowire volume. This topic has been addressed by atom probe tomography (Perea et al., 2006), secondary ion mass spectrometry (Putnam et al., 2007) and STEM (Allen et al., 2008).

5.2 Experimental details

The nanowires were grown using the VLS mechanism as described in Section 2.1.

Silicon nanowires were grown by chemical vapor deposition via the vapor-liquid-solid process on Si $\langle 111 \rangle$ substrates in a low pressure chemical vapor deposition (LPCVD) reactor at a base pressure held constant at 20 mbar. Gold was used as the catalyst and silane (SiH_4) as the Si source. Hydrogen (H_2) was used as the carrier gas. Pretreatment of the silicon wafer used as the growth substrate is performed in several steps:

1. 20 min in an ultrasonic bath in acetone.
2. 20 min in an ultrasonic bath in isopropanol.
3. Cleaning in deionized water
4. 2 min in 10% HF solution.
5. Cleaning in deionized water

After pretreatment of the silicon wafer, either 2 nm of gold was deposited in a vacuum of 10^{-6} Pa, or gold colloids of 10-100 nm (Ted Pella) were dispersed on the silicon substrate. The substrate was then loaded in the reactor and annealed between 500 and 900 °C under a H_2 flow for several minutes, in order to form nanocatalysts by dewetting of the Au layer. After cooling down the substrate to the growth temperature, SiH_4 was introduced by keeping the total pressure (SiH_4 and H_2) constant. The H_2 flow was 3.7 l min^{-1}. Wires were grown at different silane partial pressures ranging from 0.054 to 1.023 mbar and at temperatures ranging from 430 to 650 °C. In Table 5.1 these growth conditions are compared with literature values, showing that our growth parameters are mainly in the low partial silane pressure range. The growth process is schematically shown in Figure 2.1.

Also experiments were performed where the temperature was modified during growth, to gain insight into the gold surface diffusion rate. For instance, experiments were performed where

[4] Published in (den Hertog et al., 2008).

Table 5.1

Reference	Temperature (°C)	Partial SiH_4 pressure (mbar)
This work	430 - 650	0.054 - 1.023
(Latu-Romain et al., 2008)	500 - 850	0.03 - 1.6
(Schmidt et al., 2005)	400	0.1
(Cui et al., 2001)	440	6
(Wu et al., 2004)	435	6
(Schmid et al., 2007)	440	0.133 - 0.634

the sample was held at the growth temperature for a certain time (anneal time) after growth had finished.

The presence or absence of gold nanoclusters at the surface of silicon nanowires was observed either with a ZEISS SEM or with a FEI Titan in STEM mode at 300 kV (see Section 3.1 and Section 3.9). High-angle annular dark field (HAADF) STEM images and energy dispersive X-ray analysis (EDX) measurements were realized on the Titan microscope to determine the chemical content of the nanoclusters (Section 5.3). For STEM observations samples were prepared as described in Section 4.1 and Section 4.3. All observations were performed ex situ, after growth had finished.

5.3 Gold clusters: detection & dispersion

First the nanowire samples where gold clusters are present on the nanowire surface are described. A complete explanation of how these gold clusters are formed will be presented in Section 5.4 and Section 5.6. At this stage only the experimental observations are presented.

Typically these nanowires were grown at high temperature (>500 °C) and low partial silane pressure (<1 mbar), and the nanowire diameter is relatively large (>100 nm).

Let us start with the gold cluster shape. We find that when gold clusters are present, they always have the same average size. Figure 5.1 shows a characteristic HAADF STEM image of a nanowire covered with gold nanoclusters. The nanowire was grown at 575 °C with 0.077 mbar silane partial pressure. The presence of gold in the brighter regions was confirmed using EDX analysis (see Figure 5.1). The nanoclusters have a diameter around 3 nm and a height between two and four gold layers (on average 3 gold layers), i.e. 0.6-1.3 nm, as measured at the side of the nanowire (see Figure 5.2). The clusters are present under a native SiO_2 layer which forms after growth when the wires are put in the atmosphere. An example is shown in Figure 5.2: a HAADF STEM image at the side of a nanowire grown at 575 °C with 0.13 mbar silane partial pressure. Clearly two monolayers of gold can be observed on the wire sidewall. The native oxide layer is just visible (a dotted line is drawn to guide the eye), but is clearly observed if the image contrast is modified. It has a thickness of $\simeq 2$ nm.

The quantity of gold on the wire sidewall was calculated using the "particles" option, included in the Digital Micrograph^{TM} software (Gatan) to obtain the area on the nanowire surface covered by gold[5]. Approximately 35% of the wire surface is covered by gold clusters (measured on nine images of different nanowires, grown at slightly different growth conditions, see Fig-

[5] The gold quantity was also determined by counting of the particles and assuming an average size, which leads to approximately the same results.

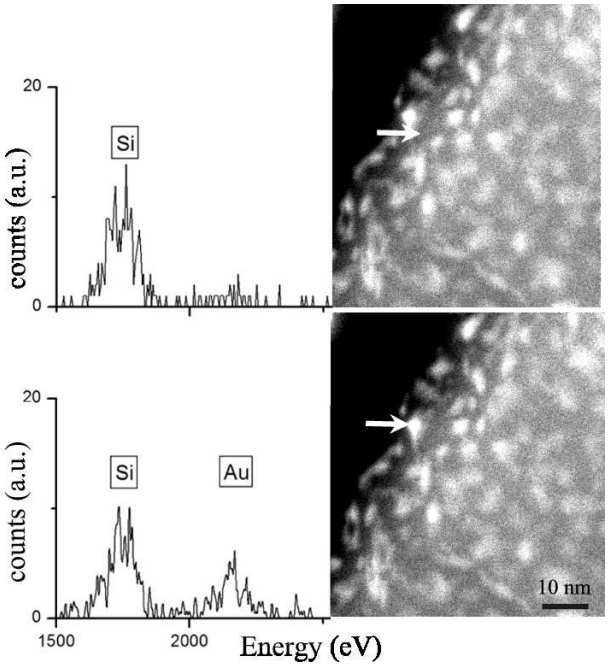

Figure 5.1: EDX spectra and STEM images of a Sinanowire grown at 575 °C with 0.077 mbar silane partial pressure. An arrow indicates where the EDX spectrum has been taken. The brighter particles are unambiguously gold rich clusters, as three typical gold lines appear in the EDX spectrum around 2200 eV. Sample 4342

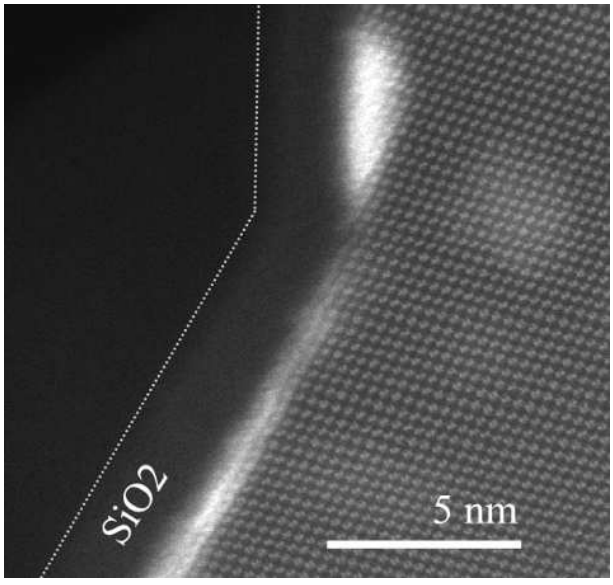

Figure 5.2: HAADF STEM image on the side of a nanowire grown at 575 °C with 0.13 mbar silane partial pressure. Clearly two monolayers of gold can be observed on the silicon (111) plane. The silicon oxide layer is not very well visible; therefore a dotted line is drawn to guide the eye. Sample 5062

ure 5.3), implying that the quantity of gold decorating the wire sidewall is equivalent to approximately one monolayer. This number is in good agreement with the value found by Hannon et al (Hannon et al., 2006). The gold coverage (in ML's) is plotted as a function of growth temperature for two different values of the partial silane pressure in Figure 5.3. No correlation between the growth conditions and the amount of gold present on the nanowire sidewall is observed and the amount of gold present is approximately equal to one monolayer. The fluctuations are attributed to the limited precision of the measurement.

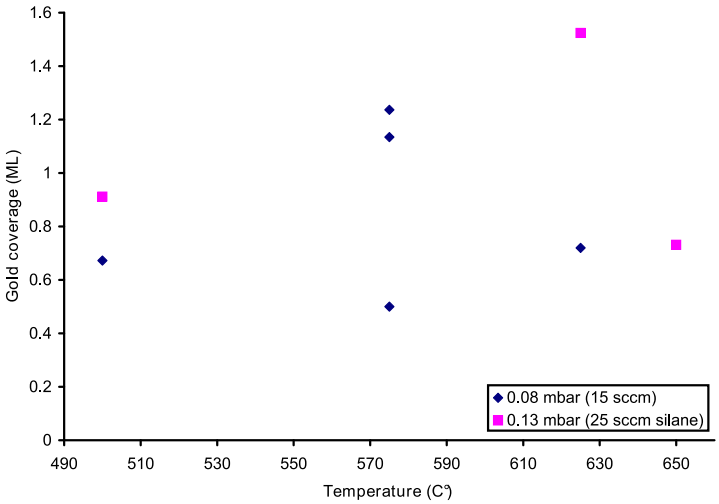

Figure 5.3: The gold coverage in monolayers (ML) as a function of growth temperature for two different silane partial pressures. Samples 4388 4387 4366 4343 4300 4389 4294 4290

Generally the gold coverage seems uniform, but in some images gold appears to be present only on certain facets.

In STEM differences in gold coverage were observed at growth conditions using a relatively high partial silane pressure (see Figure 5.4), which is close to the silane partial pressure that can completely block the gold diffusion, this is explained in more detail in the next section.

Some SEM images show that less gold is present on certain facets, coherent with (Wiethoff et al., 2008). This is illustrated in Figure 5.5. In STEM differences in gold coverage depending on faceting are more difficult to observe, possibly because in STEM two surfaces are superposed, both containing an amount of gold clusters, where in SEM only one surface can be studied.This effect is illustrated in Figure 5.6. Two images extracted from a tomography dataset are shown that were made 30 ° apart. Clearly two facets are free of gold clusters (Figure 5.6B), however this is only observed if these two facets line up. At other tilt settings the gold cluster distribution seems homogeneous (Figure 5.6A).

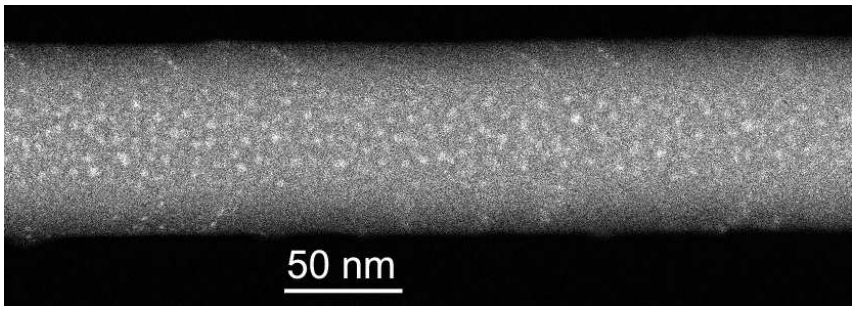

Figure 5.4: STEM image of a nanowire grown at 500 °C with 0.52 mbar silane partial pressure showing a modified and decreased gold cluster density on the nanowire side oriented perpendicular to the direction of observation. Sample 4643

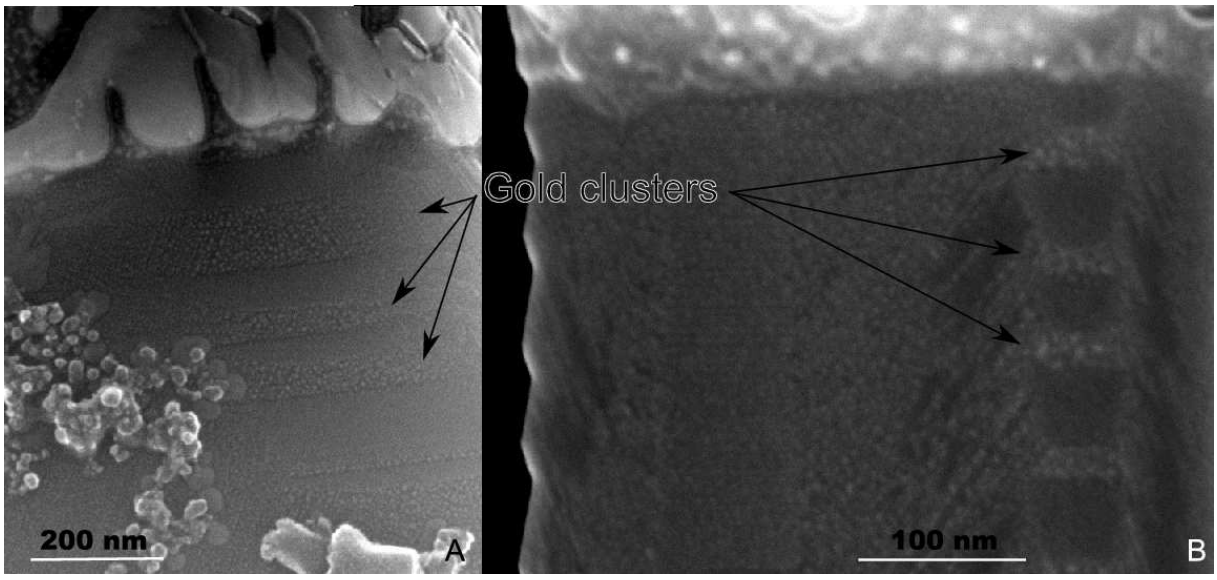

Figure 5.5: SEM images showing gold clusters and faceting on nanowires. Clearly more gold clusters are present on the facets that are pointing down, as indicated by arrows ({111} facets, Section 5.5). Samples 4411 4567

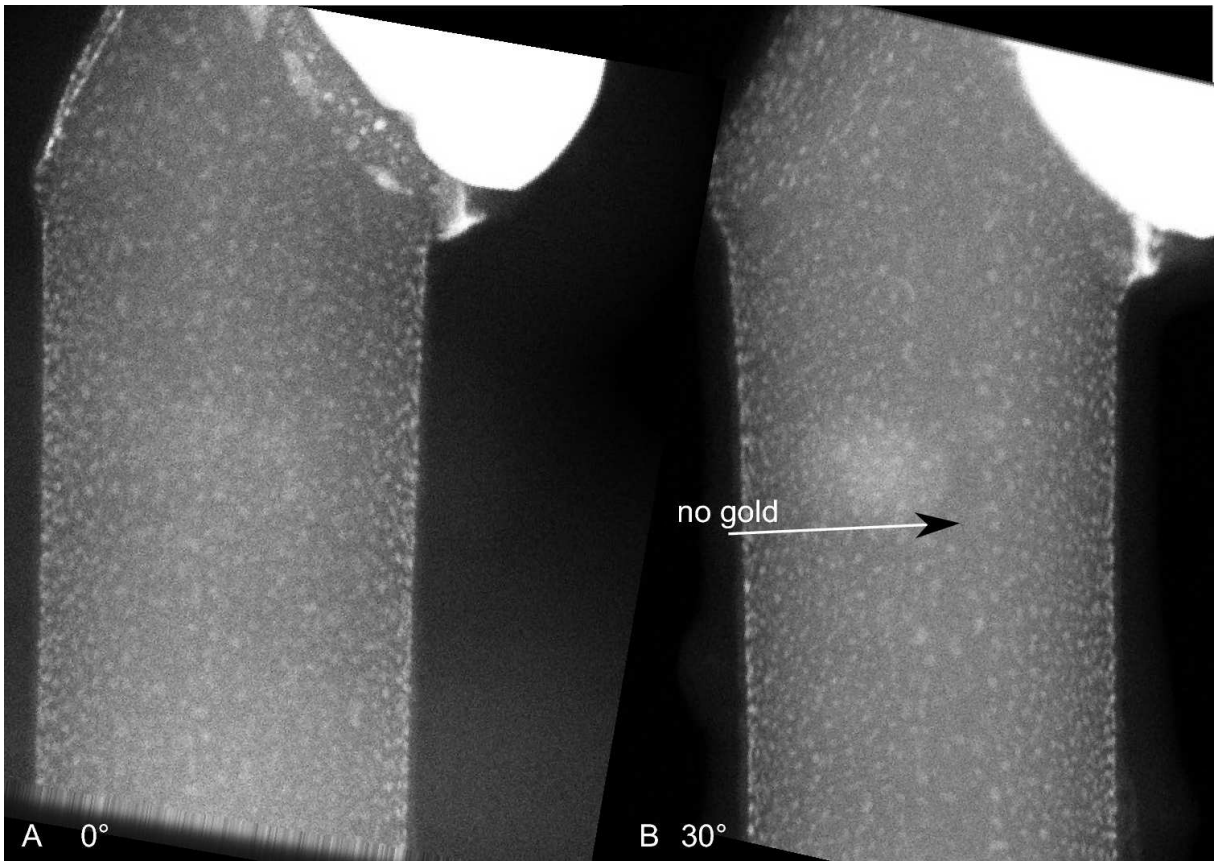

Figure 5.6: STEM images at different tilt settings (extracted from a tomography dataset) of a nanowire grown at 500 °C with 1.023 mbar silane partial pressure. Clearly two facets are free of gold clusters, however this is observed only if these two facets superpose. Image (B) is tilted over 30 ° with respect to (A). Sample 5122

5.4 Control of gold surface diffusion

By changing the experimental growth conditions as mentioned (Section 5.2), we were able to determine the main parameters that influence the presence or absence of gold nanoclusters on the side of the nanowire. These are silane partial pressure, growth temperature and wire diameter, see Table 5.2. In the following we illustrate the effect of these three parameters through a selection of nanowire images that summarizes what has been observed in many images. Finally, we discuss the experimental results.

Figure 5.7 summarizes the effect of silane partial pressure. In Figure 5.7, two nanowires are shown with a diameter of 100 nm, grown under equal growth conditions with the exception of the silane partial pressure. The growth temperature was 500 °C. At low partial silane pressure (0.0804 mbar, Figure 5.7A) gold clusters cover the facetted nanowire sidewalls. At high partial silane pressure (1.023 mbar, Figure 5.7B) most of the nanowire sidewall surface is free of gold clusters except a length $L \simeq 300$ nm situated near the catalyst particle. This observation will be discussed in the next paragraph. The magnified view shown in Figure 5.7C shows the transition from gold covered silicon to a clean wire surface. No faceting on the wire sidewall is observed. Clearly the partial silane pressure has an effect on the gold surface diffusion. Gold diffusion was observed at a partial pressure of 0.52 mbar (Figure 5.4), but was absent at a partial pressure of 1.023 mbar (Figure 5.7B-C). Somewhere between these two values the gold ceases to diffuse, however we do not know the exact value.

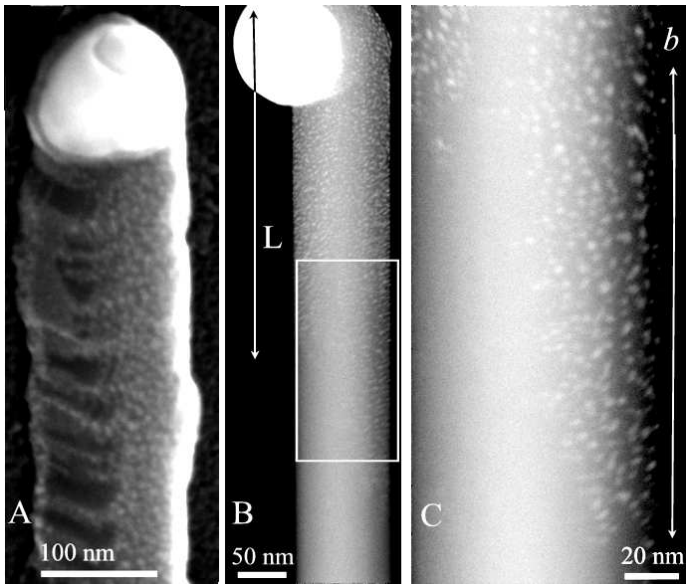

Figure 5.7: The effect of the partial silane pressure on the gold surface diffusion. Two silicon nanowires are shown with a diameter of 100 nm grown at 500 °C with different silane partial pressures. (A) SEM image of a wire grown at low partial silane pressure: 0.0804 mbar. Gold clusters can be observed all over the wire surface. (B) HAADF STEM image of a wire grown at a partial silane pressure of 1.023 mbar. Gold clusters can be observed on the 300 nm region L close to the catalyst particle. (C) Zoom of the marked region in (b) showing the end of the gold-covered zone. The difference in diffused distance is indicated by b and is approximately 150 nm. Samples 4738 4634

Figure 5.8 summarizes the effect of temperature. In panels A and B of Figure 5.8, two nanowires are shown with a diameter of 25 nm, grown under equal growth conditions with the exception of the temperature. The partial silane pressure was 0.19 mbar. The nanowire grown at 500 °C is covered with gold clusters and slightly tapered (the tapering angle is 1.2°) (Figure 5.8A), whereas the one grown at 430 °C has gold clusters only on a length $L \simeq 60$ nm near the catalyst

Table 5.2: Summary of the growth conditions to inhibit gold diffusion. *Gold diffusion was observed at a partial pressure of 0.52 mbar (Figure 5.4), but was absent at a partial pressure of 1.023 mbar (Figure 5.7B-C). Somewhere between these two values the gold ceases to diffuse and we chose to mention the upper limit.

Parameters to inhibit gold surface diffusion	
Temperature:	$\leq 500\,^{\circ}C$
Partial silane pressure*:	≥ 1 mbar
Nanowire diameter:	≤ 30 nm

particle (Figure 5.8B). A magnified view of the gold-covered region (Figure 5.8C) shows that the catalyst particle is not a perfect hemisphere. This will be discussed in the next paragraph.

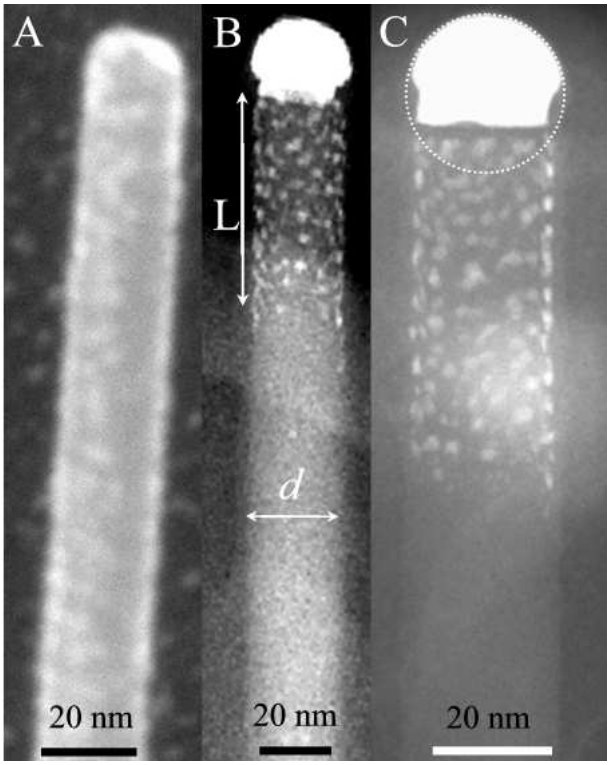

Figure 5.8: The effect of the temperature on the gold surface diffusion. Two nanowires are shown with diameters of 25 nm. Growth conditions were identical except for the temperature. The partial silane pressure was 0.19 mbar. (A) SEM image of a wire grown at 500 °C clearly covered by gold clusters and slightly tapered. (B) HAADF STEM image of a wire grown at 430 °C; gold clusters can be observed on the 60 nm region L close to the catalyst particle. (C) A magnified view of the wire shown in (b), a dotted circle is drawn around the catalyst particle to illustrate the deviation from a hemisphere. Samples 4717 4432

Figure 5.9 summarizes the effect of size on the gold surface diffusion. The nanowires of panels A and B of Figure 5.9 have been grown under the same conditions (T=430 °C P=0.19 mbar). The large diameter nanowire of Figure 5.8B (d $\simeq$ 300 nm) is covered with gold clusters and is clearly faceted, whereas the small diameter nanowire of Figure 5.8A (d $\simeq$ 25 nm) is not.

First let us analyze why gold-rich nanoclusters are always observed at the top part of the nanowires, on a length L (Figure 5.7B and Figure 5.8B). Many pieces of information concerning the gold surface diffusion will be extracted from this analysis. The presence of gold clusters near the catalyst is due to a transition regime when the nanowire growth is stopped, i.e., when the silane valves are closed and the heating of the substrate is switched off. This effect is par-

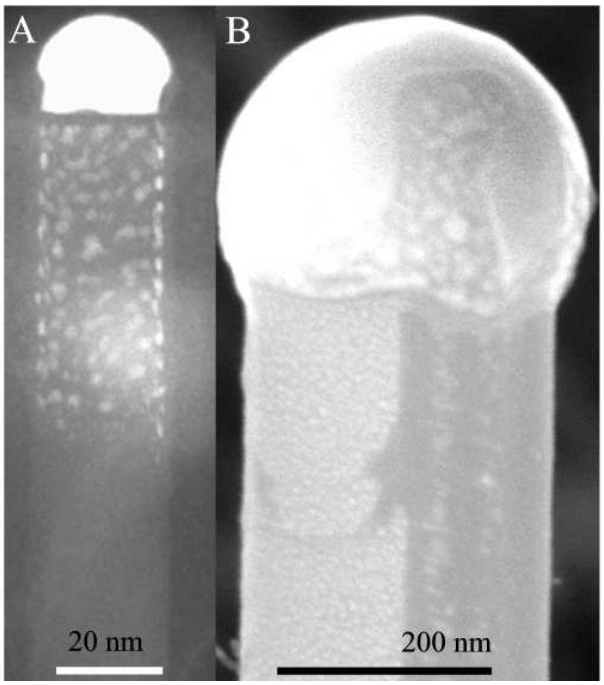

Figure 5.9: The effect of the nanowire size on the gold surface diffusion. Two nanowires are shown with diameters of 25 nm, (a) and 300 nm in (b). (A)HAADF STEM image of a wire grown at 430 °C. Gold clusters can be observed on the 60 nm region close to the catalyst particle. (B) SEM image of a Sinanowire also grown at 430 °C with a diameter of 300 nm. Gold clusters can be observed all over the wire surface. Samples 4432 4629

ticularly important in our growth chamber which has a large volume and high temperature inertia. Due to the large volume, it takes 5 min to change the gas composition of the growth chamber and 3 h to reach room temperature. Meaning that after the silane source has been closed, the partial silane pressure is ramping towards zero in 5 min, whereas the temperature remains fairly constant. During cooling down the sample is under constant flow of carrier gas (H_2). Of course the gold clusters can only come from the gold catalyst as the substrate is too far from this top part of the nanowire. Just after the silane source has been stopped, different mechanisms can happen:

1. nanowires continue growing by decomposing the last amount of silane in the chamber and incorporating the last amount of Si present in the catalyst.

2. Gold from the catalyst starts diffusing over the surface of the nanowires.

3. Gold starts forming clusters.

4. A silicon oxide layer is grown at the surface of the nanowire and the gold remains at the Si/SiO_2 interface.

Since cooling of the sample is done in a H_2 atmosphere, it seems impossible that mechanism (4) happens in the chamber in the few minutes after the closing of the silane source. So mechanism (4) clearly happens after the other mechanisms. Other facts indicate that mechanisms (2) and (3) are also separated in time. Diffusion is a random mechanism involving atom diffusion. Since the amount of gold present on the nanowire surface is approximately one monolayer, it seems probable that at high temperature (during growth) one or more liquid layers of Au or Au/Si are formed on the nanowire surface by atom diffusion. After a reduction in temperature, the gold starts to form clusters. If the clusters were formed already at high temperature, it would

be likely that they would start to form branches at the nanowire surfaces, each gold-rich cluster becoming a catalyst for a tiny nanowire that we call branch. Branches on nanowires can only be formed if the temperature of the wire is reduced, that is to say only if gold clusters are formed (Dhalluin et al., 2007). As far as mechanism (1) and (2) are concerned, the analysis of the STEM images (Figure 5.7B Figure 5.8B) indicate that they do not happen simultaneously but are separated in time. Indeed, if the gold cluster covered zone was growing during the 5 min necessary for the evacuation of silane, the catalyst would lose material in this last growth stage and this part of the wire would be slightly tapered as the diameter of the nanowire is adjusted to the diameter of the gold catalyst (Cui et al., 2001). Using a simple geometric model (Hannon et al., 2006), where the tapered part of the nanowire is supposed to have a conical shape characterized by its semiangle β, one finds that (see Appendix B.1)

$$\tan\beta = \frac{\Delta d}{2\Delta L} = \frac{d}{2L_{max}} = \frac{2e}{d} \qquad \Delta d = \frac{4e\Delta L}{d} \tag{5.1}$$

where L is the length of the nanowire grown during the tapered regime taken equal to the length of the covered zone (as indicated in Figure 5.8B), d is the nanowire diameter at the beginning of the tapered regime, and Δd is the variation of diameter after the growth of the length L. L_{max} is the maximum length of the nanowire if all the catalyst is consumed and if Δd is equal to d. e is the thickness of the gold layer. The last two equalities of Equation (5.1) come from the fact that the volume of the gold clusters is taken equal to the volume of the gold wetting layer. Assuming that the thickness e is equal to one atomic gold plane, $e \simeq 0.26$ nm, the decrease in wire diameter Δd can be estimated to be $\sim$2-3 nm (see Appendix B.1) for the nanowires of Figure 5.8B and Figure 5.7B that have diameters of 25 and 100 nm, respectively, and a hypothetical tapered length L equal to the length of the gold cluster covered zone, being 60 and 300 nm, respectively. Such variations of diameter should be visible, which is not the case as the nanowire diameter remains constant. Furthermore it can be seen in Figure 5.8C and Figure 5.11 that the catalyst particle is not a perfect spherical cap fitted to the nanowire diameter. This clearly indicates that gold surface diffusion (2) only starts after growth has finished (1).

Another indication to show that the sequence of events is indeed (1) followed by (2) can be obtained by taking into account the decay of the silane partial pressure after closing the silane source. We estimate an exponential decay of the silane partial pressure after closing of the source at time t= 1 min (see Figure 5.10). In our growth chamber the silane partial pressure goes to zero in five minutes. From our observations we know that at this temperature (500 °C) gold surface diffusion can occur for wires grown at a partial pressure of 0.5 mbar and lower (see Figure 5.4) (for a nanowire diameter of 50 nm or higher). Also the growth speed at the starting value for the partial pressure is known (1 μm/min). It was shown in (Kodambaka et al., 2006b) that the silane partial pressure can be directly related to the growth velocity (at a fixed temperature) since the sticking probability of the feed gas does not depend on the chemical potential of the catalyst particle. Now we can compare the gray surface (at constant growth velocity, being equal to 1 μm nanowire length) and the striped surface, being equal to the length the nanowire could grow during the transition regime when gold surface diffusion should occur. We can estimate the striped surface to be around 600 nm. This explanation implies that the last part of the nanowire ($\simeq$ 600 nm) should be tapered. As we have shown in the foregoing this is not the case.

So this shows that gold surface diffusion does not occur directly when the silane partial pressure is lowered at the end of growth. However during the decay of the silane partial pressure, values are present for which gold surface diffusion was observed at steady state growth condi-

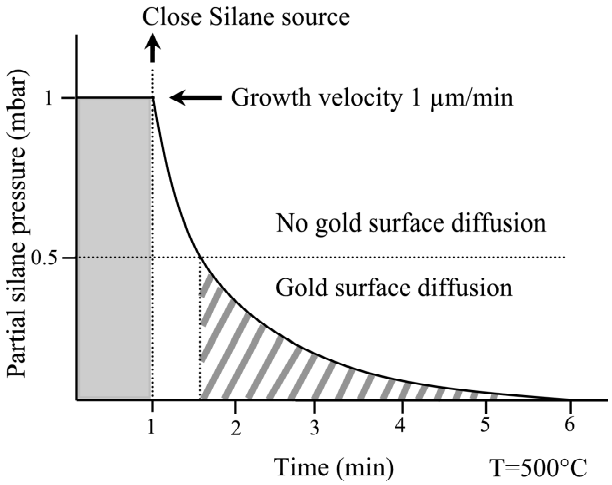

Figure 5.10: Estimated exponential decay of the silane partial pressure in the growth chamber. The silane flow is closed at time t= 1 min. The growth velocity at the starting partial pressure and the partial pressure below which gold surface diffusion can occur at this temperature (for a constant partial pressure value) are indicated. Comparison of the gray surface and the striped surface allows estimating the length the nanowire can grow, during which time gold diffusion can occur. Gold diffusion was observed at a partial pressure of 0.52 mbar (Figure 5.4), but was absent at a partial pressure of 1.023 mbar (Figure 5.7B-C). Somewhere between these two values the gold ceases to diffuse. The lower bound value is indicated in the figure.

tions (see Figure 5.10). If the nanowire would respond instantly to the new silane partial pressure value, we would expect gold diffusion as soon as the partial pressure reaches 0..52 mbar, which is not observed. As explained in the following this observation is attributed to the adsorption of silane on the nanowire sidewall, that can inhibit gold diffusion if the adsorbed silane quantity is sufficient, and reacts relatively slowly to a change in silane partial pressure.

A remark about the use of the term "diffusion" that is used to describe the liquid gold flow. For the described nanowire system the movement of the gold atoms is not entirely similar to a diffusion process where there is a gradient between the low and high concentration regions. The gold is diffusing from the gold catalyst (high gold concentration) to the nanowire sidewall (zero gold concentration) but on the nanowire sidewall no gold concentration gradient can be observed. For this reason we can also interpret the movement of the gold as a liquid flow over the nanowire surface. Indeed it was supposed in (Hannon et al., 2006) that during growth the gold is diffusing as a liquid layer. After or during growth the liquid film becomes unstable and breaks up in small clusters that are observed after growth. This seems a plausible explanation since the gold silicon eutectic is liquid and atom diffusion is energetically favorable over cluster diffusion, which was supposed to occur in (T.Kawashima et al., 2008). Therefore the gold is assumed to diffuse as a liquid layer. In the experiments where gold is present only near the catalyst particle, a zone covered by gold clusters next to a clean wire surface can clearly be observed. The separation between these two regions is fairly sharp and can be interpreted as the edge of the flow front. However we refer to the observed liquid flow as being a diffusion process in the following.

5.4.1 Model 1: Change in Chemical Potential of catalyst particle

To explain the observed influence of growth conditions on the gold surface diffusion, we can consider two explanations. The first hypothesis is described in this section, the second model

is described in the next section (Section 5.4.2).

Possibly the composition of the catalyst particle can be changed in such a way that gold surface diffusion can no longer occur because it becomes energetically unfavorable. We can express a change in chemical potential for gold when going from the liquid catalyst particle to a liquid (mono)layer on the wire surface. The chemical potential of the gold in the eutectic catalyst particle $\mu_{((Au))}(d)_{cat}$ as a function of diameter d, can be written as (Atkins, 1999) (see also Appendix B.2)[6]

$$\mu_{((Au))}(d)_{cat} = \mu_{((Au))^\circ} + RT\ln(\gamma^*_{Au}x^*_{Au}) + \frac{4\overline{V}_{((Au))}\sigma_{((AuSi))}}{d} \tag{5.2}$$

- where $\mu_{((Au))^\circ}$ is the standard chemical potential of pure liquid gold at standard conditions,
- x^*_{Au} is the gold fraction in the catalyst particle ($0 \leq x^*_{Au} \leq 1$ and 0.77 at 500 °C for the bulk eutectic at equilibrium, see Figure 2.2),
- $\overline{V}_{((Au))}$ is the molar volume of liquid gold (1.02x10^{-5} m^3 mol^{-1} without taking into account liquid contraction),
- $\sigma_{((AuSi))}$ is the surface energy of the eutectic particle (1.25 J m^{-2}) (Dhalluin et al., 2007) and
- d is its diameter (we assume the nanowire diameter $\sim$ catalyst diameter, taking into account the contact angle (see Appendix B.1) does not modify the result of the calculation).
- γ^*_{Au} is the gold activity coefficient and can be calculated by assuming that the liquid behaves as a regular solution:

$$\ln\gamma^*_{Au} = \frac{4\Delta_{mix}H(1-x_{Au})^2}{RT} \tag{5.3}$$

where $\Delta_{mix}H$ is the molar enthalpy of mixing, -10 kJ mol^{-1}, if x^*_{Au} = 0.5 (Hassam et al., 1983). More details can be found in Appendix B.2.3.

The chemical potential of a liquid gold layer $\mu_{((Au))}(d)_{wire}$ at the wire surface can be written as (see also Appendix B.2.2)

$$\mu_{((Au))}(d)_{wire} = \mu_{((Au))^\circ} + \frac{2\overline{V}_{((Au))}\sigma'_{(Si)}}{d} \tag{5.4}$$

where $\sigma'_{(Si)}$ is the surface energy of solid silicon covered by $\sim$ 1 monolayer of gold. Since the surface energy of solid silicon ($\sigma_{(Si)}$) and liquid gold ($\sigma_{((Au))}$) are 1.24 (Schmidt et al., 2004) and 1.25 J m^{-2} (Dhalluin et al., 2007) respectively, this value is taken to be 1.25 J m^{-2}.

The energy balance is now given by

$$\mu_{((Au))}(d)_{wire} - \mu_{((Au))}(d)_{cat} = \frac{-2\overline{V}_{((Au))}\sigma_{((AuSi))}}{d} - RT\ln(\gamma^*_{Au}x^*_{Au}) = \Delta\mu \tag{5.5}$$

[6] The double brackets (()) indicate the substance is liquid, single brackets () indicate solid, $^\circ$ indicates a pure substance and * indicates that this quantity is not at equilibrium.

If $\Delta\mu < 0$, gold surface diffusion can occur.

Let us study the effect of the nanowire diameter by setting the temperature to T = 430 °C, a value where the diameter is known to have an effect (Figure 5.9), and x^*_{Au} = 0.77 which is the bulk value at this temperature (Figure 2.2). For a nanowire with a diameter ranging from 1 to 300 nm, $\Delta\mu$ increases exponentially and is >0 for diameters >3 nm. Taking into account the effect of line tension that could modify the contact angle of the droplet with the nanowire for small diameters (Schmidt et al., 2004) (see also Section 5.6.2) does not change the calculated values for $\Delta\mu$, if we assume a line tension of $\sim$ -1 x10^{-9} J m^{-1} (Schmidt et al., 2004).

Now the effect of the gold fraction in the catalyst particle x^*_{Au} is studied at a fixed temperature of T = 500 °C, where an effect is expected (Figure 5.7). x^*_{Au} can be changed by modification of the growth parameters silane partial pressure and temperature. For $0.5 \leq x^*_{Au} \leq 0.999$, $\Delta\mu$ is positive and going through zero for $x^*_{Au} > 0.99$.

The effect of temperature is considered at fixed x^*_{Au} = 0.77. $\Delta\mu$ is positive and does not vary significantly for 430 °C $\leq T \leq$ 600 °C.

This analysis shows that gold surface diffusion is not favored energetically under all experimentally observed growth conditions, since $\Delta\mu$ can only become negative if the wire diameter becomes very small, indicating that gold diffusion is possible for very small nanowire diameters, contrary to the observed effect, or if the catalyst particle is purely gold. In this last case there is no eutectic and therefore no liquid phase. This solution seems physically highly unrealistic. Therefore it is clear that **we cannot explain the experimentally observed effects of growth conditions on the gold surface diffusion by taking into account a change in catalyst composition**.

This explanation is also unlikely because we observe the absence of gold surface diffusion for wire growth during the transition regime at and below a partial silane pressure that is known to cause gold surface diffusion at constant value. This indicates strongly that the observed effect is not related with the relatively fast response of catalyst composition to silane partial pressure (at this growth velocity) but is a slower process.

5.4.2 Model 2: Silane adsorption inhibits gold diffusion

A plausible explanation seems therefore that the wire surface can be changed in a reversible way due to a change in growth conditions, allowing or inhibiting the gold diffusion. The only component we actively add in larger or smaller quantities is the silane gas itself; therefore we propose that the adsorption of silane gas on the wire sidewall influences the gold diffusion.

This hypothesis is consistent with the observed effect of silane partial pressure. Indeed Le Chateliers principle states that (Atkins, 1999)

"A system at equilibrium, when subjected to a disturbance, responds in a way that tends to minimize the effect of the disturbance."

Therefore an increase of the silane partial pressure will naturally lead to a mechanism that counteracts the imposed change: in order to reduce the silane partial pressure more silane has to be adsorbed on the nanowire sidewall, and the gold diffusion is inhibited by this increased adsorption.

Now we consider the temperature effect. As we already showed in panels A and B of Figure 5.8, a decrease in temperature can completely block the gold surface diffusion. Furthermore we

performed experiments where the temperature was decreased during growth. The result is a nanowire only partially covered by gold clusters. A decrease in temperature thermodynamically favors adsorption as physisorption or chemisorption are exothermic processes (enthalpy of adsorption $\sim$ 20-100 kJ mol^{-1}) (Atkins, 1999). Again, using Le Chateliers principle, the system will favor mechanisms producing energy when the temperature is lowered (Atkins, 1999). So adsorption of silane will be favored when the temperature is lowered. Also a decrease in temperature will lower the mobility of the gold, possibly enhancing the before mentioned adsorption effect. It is evident that an adsorbed layer of silane molecules can exist only if silane decomposition on the wire sidewall (i.e., uncatalyzed growth) is extremely slow. Indeed we find that the uncatalyzed growth rate is negligible at temperatures below 600 °C.

Now we consider the effect of the wire diameter. The effect of wire diameter on gold diffusion might be explained by an increase of the chemical potential of the nanowire surface atoms. The chemical potential of a nanowire can be written (Dhalluin et al., 2007) (see also Appendix B.2.2)

$$\mu_{(Si)}(d) = \mu_{(Si)}(d = \infty) + \frac{2V_{(Si)}\sigma_{Si}}{d} \tag{5.6}$$

where $\mu_{(Si)}(d)$ is the chemical potential of silicon in the nanowire, $\mu_{(Si)}(d = \infty)$ is the chemical potential for bulk silicon, V_{Si} is the molar volume of silicon, and σ_{Si} is the surface energy of silicon. Actually the contribution of the nanowire surface was already included in Equation (5.5), however absorption of silane on the nanowire surface could modify the surface energy, which could not be taken into account in Equation (5.5).

Equation (5.6) allows comparison of the chemical potential of nanowire surface atoms for different nanowire diameters. The chemical potential will increase for decreasing diameter. However it is unclear if this will affect the silane adsorption (possibly a smaller wire diameter mimics the effect of a step edge on a crystal, which lowers the adsorption energy (Olsen et al., 2004)) or rather increases the gold-silicon interface energy, thereby inhibiting the gold surface diffusion.

It will be shown in Section 7.9 that the Mean Inner Potential (MIP, see Section 3.8) is increasing for decreasing nanowire size. This size effect was explained for gold clusters as an effect of surface strain (Popescu et al., 2007). The increase in MIP can be due to a redistribution of valence electrons, a change in lattice parameters (redistribution of nuclei) (Popescu et al., 2007) or a combination of both effects (Section 3.8). These effects could also modify the adsorption of silane (or the gold-silicon interface energy).

Interestingly, the edge of the gold cluster covered zone in Figure 5.7B,C is not straight (perpendicular to the growth direction), but inclined. This suggests anisotropy in the gold diffusion. We can observe a difference in diffused distance b (Figure 5.7C) to be approximately 150 nm (the nanowire diameter is 100 nm). A wire with a diameter of 30 nm grown under exactly the same growth conditions as the wire in Figure 5.7C (500 °C growth temperature with 1.023 mbar silane partial pressure), showed a difference in diffused distance of $\sim$ 60 nm (Figure 5.11). Since a nanowire can be regarded as a cylinder in a laminar gas flow, it can be seen intuitively that the larger the diameter, the more important will be the pressure drop when going from the flow side of the nanowire to the back side. The influence of the carrier gas (after the silane source has been closed) on the nanowire surface can possibly modify the layer of adsorbed silane molecules. This effect will be increasingly inhomogeneous for increasing diameters and might explain the anisotropy of gold surface diffusion and its size dependence. This indicates again that the gold surface diffusion can be modified by a change in the quantity of adsorbed silane on the nanowire surface, which in turn is influenced by the direction of the gas flow.

Also Figure 5.11 shows that the catalyst particle size decreased considerably with respect to the wire diameter. Clearly the nanowire diameter did not adjust to the catalyst size but remained constant. Confirming again that gold surface diffusion (mechanism (2)) only starts after nanowire growth has finished (mechanism (1)).

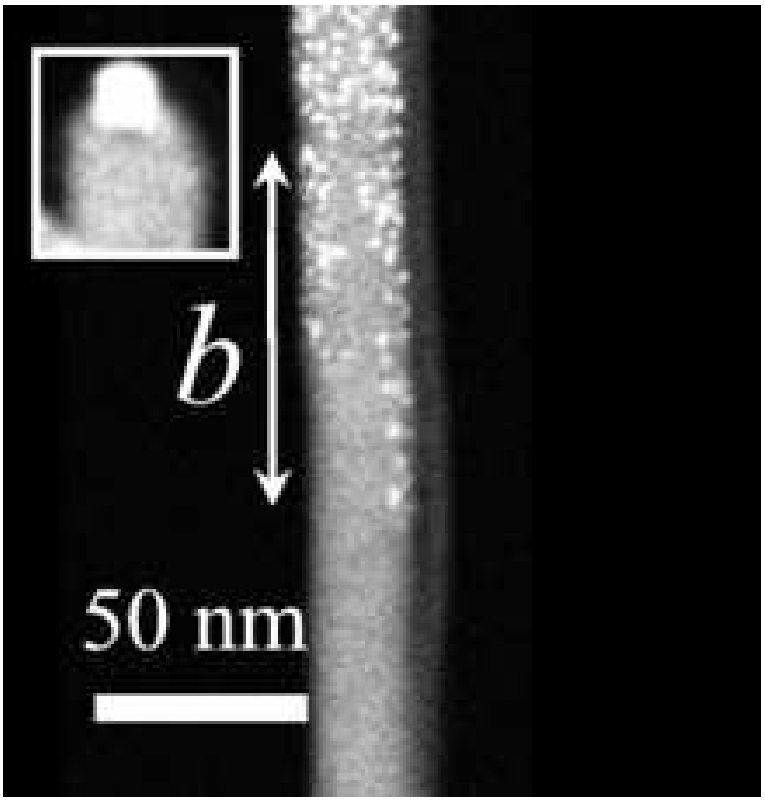

Figure 5.11: Magnified view of a nanowire with a diameter of $\sim$ 25 nm, grown under exactly the same conditions as the wire shown in Figure 5.7: a growth temperature of 500 °C with 1.023 mbar silane partial pressure. The difference in diffused distance of the gold is indicated by b and is approximately 60 nm. A magnified view of the catalyst particle is shown in the inset: the catalyst particle is considerably smaller than the wire radius. (The length of the gold covered region l close to the catalyst particle is $\sim$ 300 nm (comparable to the wire shown in Figure 5.7)). Sample 4631

Now let us consider the gold diffusion rate. Two particular nanowire growth experiments were realized under the same conditions as the wire shown in Figure 5.7B (500 °C growth temperature with 1.023 mbar silane partial pressure) except that, after the silane flow was closed, the sample was maintained at the growth temperature during a time τ_1 = 5 min in the first experiment and a time τ_2 = 15 min in the second one, after which the sample was cooled down to room temperature as usual. The length of the gold-covered zone near the catalyst particle was now found to be around l_1 = 600 nm and l_2 = 2500 nm in the respective experiments. Using the two-dimensional random walk expression for diffusion (Atkins, 1999) the mean traveled distance is $\sqrt{(D\tau)}$, where τ is the time interval during which the sample is maintained at the growth temperature and D is the diffusion coefficient. Taking into account that during cooling gold already diffused over a distance of 300 nm, we thus have for the first experiment l_1 - 300 = $\sqrt{(D\tau_1)}$ and a similar expression for the second one.

This gives diffusion coefficients D of 3x10^{-16} m^2 s^{-1} and 5.4x10^{-15} m^2 s^{-1} (at (500 °C) for the respective experiments indicating that the gold diffusion is slower just after the silane flow has been closed. This can be explained by the fact that the remaining silane molecules slow down the gold diffusion. In literature a value for D_0 of $\sim$ 1x10^{-12} m^2 s^{-1} can be found (Slezák

et al., 2000) for a monolayer or less of gold on Si(111) (at a slightly higher temperature). This again indicates that under our conditions gold diffusion is slower because it is perturbed by the remaining adsorbed silane molecules. The observation that the gold diffusion only starts after growth has finished indicates that the silane desorption is a rather slow process. The residence half-life of an adsorbed silane molecule can be estimated to be on the order of minutes. This means that the barrier for desorption is significantly higher than that for a physisorption process ($\sim 25\,\mathrm{kJ\ mol^{-1}}$), (Atkins, 1999) where the residence half-life is predicted around 10 ns at room temperature (Atkins, 1999). Possibly the adsorption process does involve a reversible chemical reaction where the silane molecule is decomposed into an intermediate state where it remains trapped a relatively long time. The observation of gold clusters on the doped regions of Si nanowires was explained by (Pan et al., 2005) as instabilities at the liquid/solid interface, caused by the addition of the dopant gas flow. Since we regard only undoped samples, this explanation is insufficient for our experiment. However since in their experiments the silane gas flow was lowered by 80% for growth of the doped region, this might be the same effect of an increase in silane partial pressure favoring silane adsorption and inhibiting gold diffusion on the undoped regions.

5.4.3 Discussion

Recently an influence of silane partial pressure on the critical wire radius was observed, (Dhalluin et al., 2007) indicating that small wires (diameter below 30 nm) cannot grow at low partial pressures ($<$0.05 mbar) for thermodynamical reasons. Two effects of high partial silane pressure on the growth of thin nanowires can therefore be identified:

1. High partial silane pressure favors very thin wire growth thermodynamically (Dhalluin et al., 2007)

2. High partial silane pressure inhibits gold surface diffusion and therefore favorizes thin wire growth, since thin wires cannot grow very long if they constantly lose catalyst material.

These two reasons that favorize thin wire growth at high partial silane pressure explain the different results regarding the absence or presence of gold on the wire sidewall found in literature (Cui et al., 2001; Wu et al., 2004; Hannon et al., 2006; Kodambaka et al., 2006b; Werner et al., 2006). Furthermore in most literature slightly higher partial silane pressure values are used (values of 0.1 mbar (Schmidt et al., 2005) to 6 mbar (Cui et al., 2001; Wu et al., 2004) can be found in recent literature) and growth is performed at relatively low temperature ($T \leq 500\,^{\circ}\mathrm{C}$). These are conditions that inhibit gold diffusion (see Table 5.2). On the other hand, most literature showing evidence of gold diffusion is performed at very low partial pressures since the growth is carried out under ultrahigh vacuum (Hannon et al., 2006; Kodambaka et al., 2006b; Werner et al., 2006).

In Section 5.4.1 the chemical potential of gold in the catalyst particle was compared to the chemical potential of gold on the nanowire surface, to see if a driving force for diffusion is present. What is not known and therefore not accounted for, is the influence of the nanowire surface energy without gold, that can be modified by silane adsorption (Section 5.4.2). An improved thermodynamic analysis of this system should take this effect into account.

Since gold is not desirable in electrical applications (Tavendale and Pearton, 1983), an attempt was made to remove the gold clusters. For this purpose the sample was dipped in an Hydrofluoric acid (HF) solution to remove the oxide layer covering the nanoclusters, then the sample was dipped in a mixture of nitric acid (HNO_3) and concentrated hydrochloric acid (HCl) (in a

volumetric ratio of 1:3 respectively, also known as "aqua regia") to etch the gold. This was followed by a last HF etch. In Figure 5.12 a STEM image is shown of a nanowire that had followed the treatment. Clearly very little gold has been removed. It seems therefore that the chemistry of these nanosized gold clusters is different with respect to the bulk. It has been reported that annealing the sample and a subsequent KI etch can more effectively remove the gold (Schmidt and Gösele, 2008).The principle of this procedure seems to be the increase in size of the gold clusters so that they can be etched chemically more efficiently. It is interesting to note here that nanosized gold clusters also have interesting size dependent optical properties (Wilcoxon et al., 1998), catalytical properties (Turner et al., 2008), a strongly size dependent melting point (Buffat and Borel, 1976) and Mean Inner Potential (Section 3.8) (Popescu et al., 2007). The relation between these interesting properties appears to be not entirely understood at present.

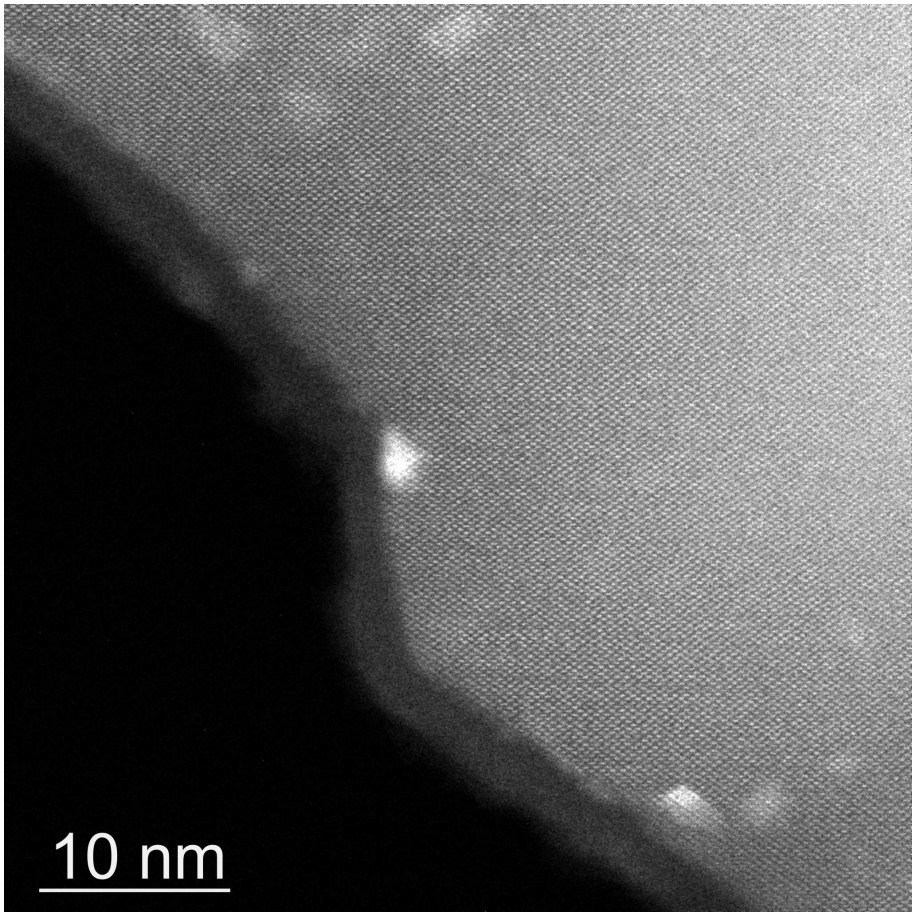

Figure 5.12: HRSTEM image of a nanowire that was chemically treated (as described in Section 5.4.3) to remove the gold clusters. Indeed the cluster density is slightly lower than in Figure 5.1, however the gold removal wasn't extremely successful. Sample 5062

A similar control of the gold diffusion can be obtained by introducing other gas types during growth: hydrogen-chloride (HCl) (Oehler et al., 2009b) or diphosphine (P_2H_6)(Section 7.1) (Björk et al., 2008). When HCl is used it seems that the amount of gold present on the nanowire sidewall can be tuned between one monolayer and zero by changing the HCl partial pressure.

5.5 Faceting of the nanowire sidewall

It was shown by (Ross et al., 2005) that the nanowire sidewall parallel to the growth direction is not flat but shows periodic sawtooth facets, as shown schematically in Figure 5.13. This

faceting could be due to the presence of gold on the wire sidewall, since gold is known to induce faceting on silicon surfaces (Hild et al., 2002; Minoda et al., 1999; Seehofer et al., 1995). The same sawtooth faceting can be obtained if gold is deposited on a $\langle 112 \rangle$ silicon substrate (the nanowire sidewall facets for the $\langle 111 \rangle$ growth direction) at elevated temperature (Wiethoff et al., 2008) The surface structure of nanowires is of particular importance for applications since transport properties will depend to a great extent on surface roughness and can be used to change thermoelectric properties (Hochbaum et al., 2008).

It will be shown that indeed faceting of the nanowire surface is observed only when gold is present. Interestingly, periodic sawtooth faceting of the nanowire sidewall as described in (Ross et al., 2005) was observed for the completely gold covered wires, but never on the wires showing gold clusters only on a short region near the catalyst particle. If the gold is diffusing during growth, the wire surfaces are maintained at the growth temperature until growth is terminated and surface reconstruction can occur, as shown in Figure 5.7 and Figure 5.9.

However if the gold is diffusing during cooling of the sample, the energy barrier for surface reconstruction cannot be overcome and no sawtooth faceting can be observed. The absence or presence of gold on the wire sidewall thus has an effect on the sidewall morphology.

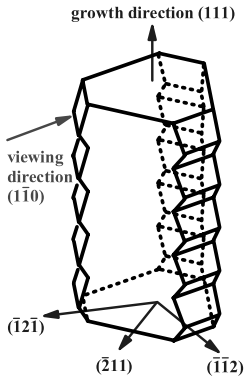

Figure 5.13: Schematic of the three dimensional structure of a wire. The cross section of each wire is a trigonal hexagon with three long and three short edges. One in two sidewall facets contains a periodic sawtooth faceting in the growth direction (Ross et al., 2005).

Here two different types of surface reconstruction are shown, that seem to depend on gold coverage or on the precursor gas-types. The second type was only observed if a second precursor gas (next to silane) was added.

When nanowires were grown under conditions that favourize gold diffusion, a faceting was observed as shown in Figure 5.14 (den Hertog et al., 2007). The alternating crystal planes are of $\{111\}$ and $\{113\}$ type. The angle between the facet planes is 150,5 ° degrees, close to the value found in (Ross et al., 2005) of 145,5 ° and coherent with the results presented by Wiethoff et al (Wiethoff et al., 2008).

The faceting of similar wires was studied using Grazing Incidence X-ray Diffraction (GIXRD) and Scattering (GISAXS) (David et al., 2008). Using this technique also inclined facets (with respect to the growth direction) could be studied, which is difficult using TEM. Here similar faceting was found, probably also for the inclined facets.

When nanowires were grown with the addition of HCl or diphosphine to the growth (Björk et al., 2008) a faceting was observed as shown in Figure 5.15, if gold clusters were present. The alternating crystal planes are of $\{111\}$ and $\{100\}$ type. The angle between both planes is 125,2 °.

The nanowires that were grown in the presence of HCl were grown in two or three consecutive

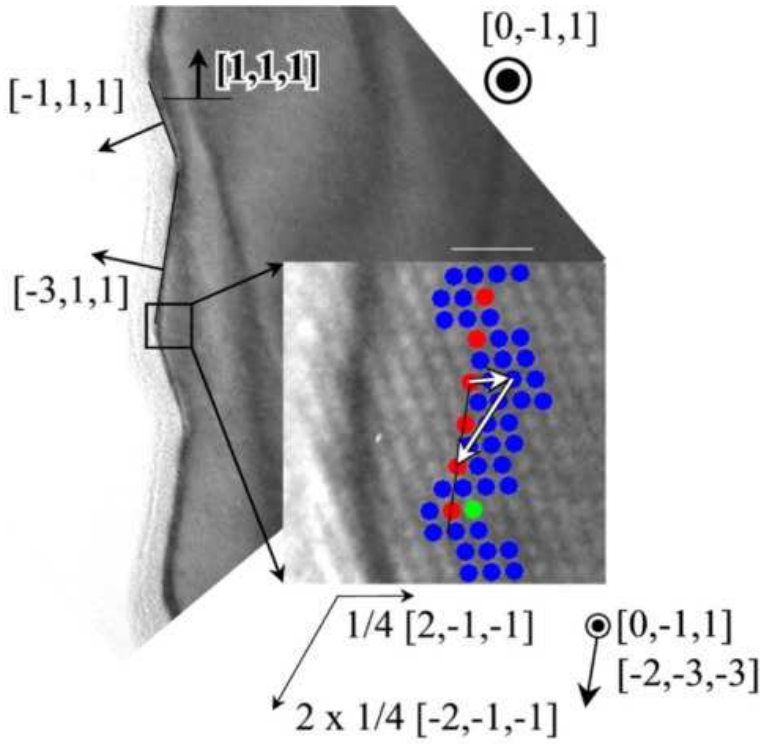

Figure 5.14: HRTEM image showing sawtooth faceting (Ross et al., 2005). The zoom of a small area allows identifying the alternating (-111) and (-311) planes using vector calculation as shown. The viewing direction is [0-11], the scale bar is 10 nm. Sample 4342

growth steps (Oehler et al., 2009b). The first growth step was performed at high partial HCl pressure ($> 0.1\,\mathrm{mbar}$), the second growth step at low HCl pressure ($< 0.1\,\mathrm{mbar}$) and the third growth step (if present) again at high partial HCl pressure ($> 0.1\,\mathrm{mbar}$) [7]. The nanowire growth was performed at 650 °C at silane partial pressures of 0.23-0.46 mbar.

We observed that for HCl partial pressures > 0.1 mbar no gold or faceting is observed on the nanowire sidewall (Oehler et al., 2009b). In Figure 5.16 a selection of images illustrates the effect of HCl on the nanowire surface in more detail. The HCl partial pressure is indicated for the different wire regions. Clearly a smooth wire surface without contrast from gold clusters and faceting is obtained at high partial HCl pressure (Figure 5.16A-B). The BF STEM image in Figure 5.16C shows a remarkably chaotic contrast in the region grown at low partial HCl pressure. In the HRTEM images relatively few crystallographic defects were observed (for example Figure 5.15C) in the faceted regions. This contrast is therefore attributed primarily to the faceting and the associated thickness changes.

In Figure 5.16D the transition region from low HCl partial pressure to high HCl partial pressure is shown. Clearly the density of gold clusters decreases when the HCl partial pressure is increased (towards the top of the image). When the gold cluster density is reduced, gold clusters tend to be present only on certain facets. When HCl is added to the nanowire growth the quantity of HCl is inversely proportional to the quantity of gold present on the nanowire surface. An example is shown in Figure 5.16E. This nanowire region was grown at low HCl pressure ($< 0.1\,\mathrm{mbar}$). Clearly the gold cluster density is lower than in Figure 5.1 or Figure 5.15D (bottom), however the cluster size remains approximately constant.

[7] The error in the quantity of HCl (in sccm) for the regions grown at low HCl pressure is relatively large, due to the mass flow meter. Therefore it is not possible to determine the amount of gold as a function of partial HCl pressure.

The diffusion of gold is inhibited if HCl is added to the growth system because, similar to silane (see Section 5.4.2), HCl can modify the surface energy (or occupy the crystal sites that enable the gold diffusion). The nanowire sidewall is chlorinated in the presence of HCl, which means that in this case the nanowire sidewalls are modified due to a chemical reaction. In Figure 5.16F a TEM image of the transition zone is shown. Clearly the nanowire region grown at low partial HCl pressure is faceted. A detail of the faceted part is shown in Figure 5.16G, interestingly this nanowire is faceted on both sides (different from the faceting shown in Figure 5.14 (see also Figure 5.13), where only one out of two parallel sidewall facets contains a sawtooth faceting in the growth direction (Ross et al., 2005)).

In Figure 5.17 the same sample is studied by SEM. Again a very faceted part is observed with some, but very few gold clusters (Figure 5.17A). In Figure 5.17B the smooth wire surface is visible. The wire section seems hexagonal and some contrast is visible, mostly on the ridges of the hexagon. This contrast is attributed to crystal steps.

Circumstantial evidence also suggest that HCl can completely block the gold diffusion. Thin wires ($d \leq 50\,\mathrm{nm}$) can grow very long in the presence of HCl, which is not possible if the catalyst is constantly losing a certain amount of catalyst material (see also Appendix B.1). Furthermore small branch growth is sometimes observed on the regions grown without HCl, which indicates the presence of a gold seed that can act as catalyst. Such branch growth was not observed on the regions grown in the presence of HCl.

It is clear that the gold surface diffusion can be modified and completely inhibited by increasing the HCl partial pressures. The nanowire regions grown at high HCl partial pressures are free of gold traces and do not exhibit a sawtooth-faceting. This means that for the same nanowire radius faceting is observed only on the nanowire regions where gold is present. For this reason faceting seems to be caused only by the presence of gold, and no effect of nanowire diameter on the faceting is to be expected.

Also nanowires were observed that were doped with Phosphorus by adding diphosphine (g) during growth. In this case, depending on growth conditions, gold clusters were present on the complete nanowire surface or only on the doped segments. Faceting similar to Figure 5.15 was observed on the regions where gold clusters were present.

In literature it can be found that the relative anisotropies of the surface free energies σ of different silicon planes is either $\sigma_{(111)} < \sigma_{(110)} < \sigma_{(100)}$ (Zhang, 2001) or almost the inverse $\sigma_{(111)} > \sigma_{(110)} > \sigma_{(113)} > \sigma_{(100)}$ (Bermond et al., 1995; Müller and Métois, 2008). Furthermore the presence of gold will modify the surface energy. The (111) plane exhibits different surface reconstructions in the presence of small gold coverages (Seehofer et al., 1995). Possibly the difference in surface free energy of the other observed facets ((113) and (100)) depends very sensibly on the amount of gold present. However it seems difficult to draw definite conclusions if literature on similar bulk samples, where surface reconstruction is studied under extremely well controlled conditions, does not seem coherent.

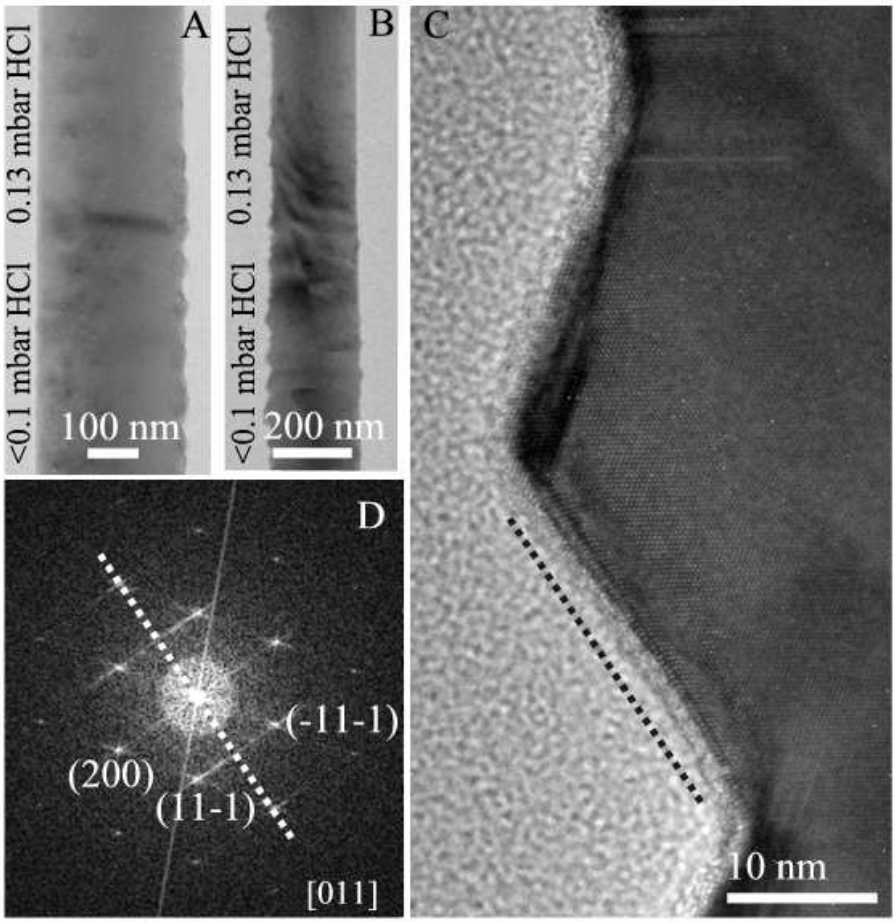

Figure 5.15: Faceting of a nanowire grown partly in the presence of HCl (g). (A) The transition of the faceted part to the smooth part (grown in the presence of HCl) (B) the more faceted part of the wire (C) High resolution image of the facets (D) Fourier Transform (FT) of (c), clearly the facets are alternating $\langle 111 \rangle$ and $\langle 100 \rangle$ planes. A dashed line follows one facet and is also present in the FT to show the facet is clearly a (100) plane. Sample 5666

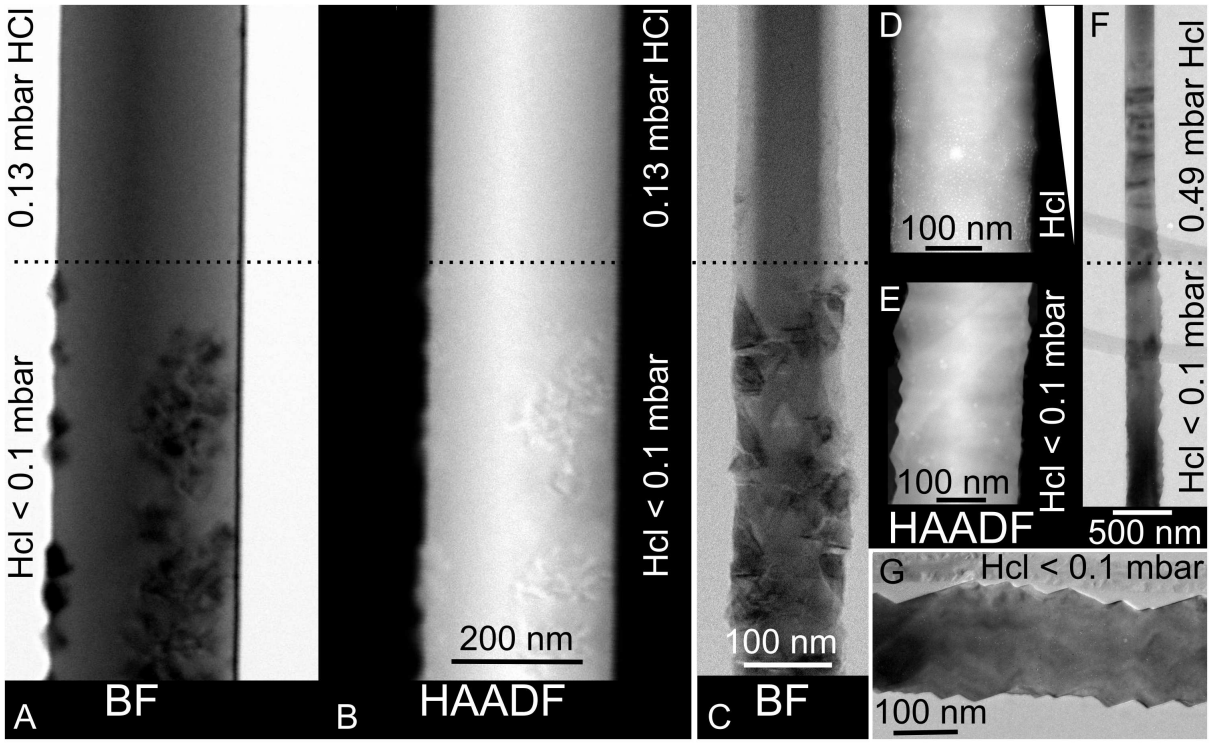

Figure 5.16: The influence of HCl on the presence of gold and the gold induced faceting. The HCl partial pressure is indicated for the different wire regions, separated by a dotted line. (A) BF STEM image at the transition zone. (B) Corresponding HAADF image. (C) BF STEM image at the transition zone. (D) HAADF STEM image at the transition zone, the HCl partial pressure is increasing towards the top of the image. (E) HAADF STEM image of a region grown at low HCl pressure. (F) TEM image of the transition zone. (G) TEM image showing the faceting in the region grown at low HCl partial pressure. Samples 5666 5738

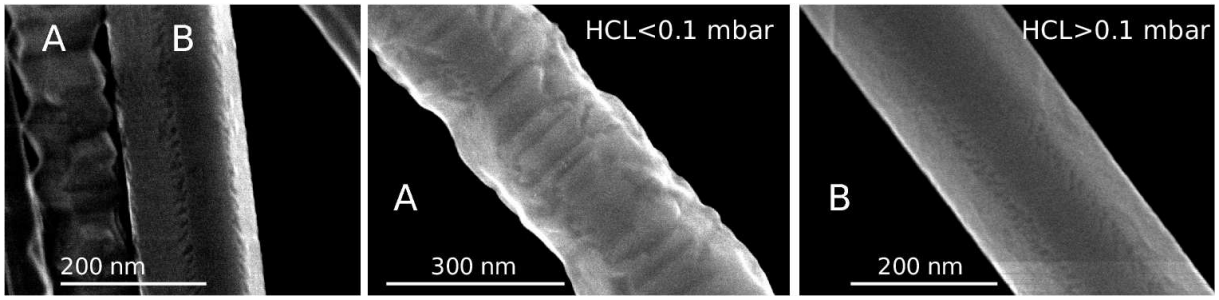

Figure 5.17: The influence of HCl on the presence of gold and the gold induced faceting studied by SEM. Two wires are shown side by side (A) Detail of a faceted wire, some gold clusters can be observed on the facets. (B) Detail of a smooth nanowire, no clear contrast of gold is observed, however the surface is not completely smooth possibly caused by crystal steps, especially on the corners of the hexagon. Samples 5738

5.6 Dewetting modelisation

In Section 5.3 the shape and dispersion of the gold clusters was described. The gold is diffusing as a liquid layer (Hannon et al., 2006) that becomes unstable during or after growth and breaks up in small clusters that are observed after growth. This seems a plausible explanation since the gold silicon eutectic is liquid and atom diffusion is energetically favorable over cluster diffusion, which was supposed to occur in (T.Kawashima et al., 2008). Therefore the gold is assumed to diffuse as a liquid layer. The oxide layer observed on the nanowire surface is grown after the dewetting of the gold layer has occurred, since at the end of the nanowire growth first the temperature is lowered to ambient temperature (dewetting of the liquid layer) and only then the nanowire sample is removed from the growth chamber and exposed to air (growth of the native oxide on the silicon surface) (Section 5.4). For this reason no effect of the oxide layer on the dewetting is expected.

Two simple models are proposed to describe the observed dewetting phenomenon, to determine the thickness of the liquid layer more precisely (than possible by estimation of the gold quantity present on the wire sidewall) and evaluate if size effects such as line tension are present. These models are based on the conservation of energy by introducing macroscopic constants to describe the dimensions of the system. Although these models are in principle valid only for macroscopic systems, which excludes the behavior of one liquid monolayer, they reproduce the experimental results surprisingly accurately.

5.6.1 Dewetting from multiple layers

We consider the dewetting of a liquid film of macroscopic thickness (several atomic layers). The initial state is a liquid film of certain thickness e on a substrate (Figure 5.18A).The thin liquid layer will dewet by forming a periodic network of clusters, which is the final state. We suppose that the 2D lattice is square [8], has a lattice parameter λ (Figure 5.18B) and after dewetting one cluster per unit cell is present. We suppose the clusters can be represented by a spherical cap with the radius of a sphere r, a height of the cluster h and a contact angle θ (Figure 5.18C). It can be easily seen that $r' = r\sin\theta$ and $h = r(1-\cos\theta)$. The surface S_{cap} and volume V_{cap} of a spherical cap are given by

$$S_{cap} = 2\pi rh = 2\pi r^2(1-\cos\theta) \qquad V_{cap} = \tfrac{1}{3}\pi r^3(2+\cos\theta)(1-\cos\theta)^2 \tag{5.7}$$

The surface energy of the film is given by σ_f, the surface energy of the substrate is given by σ_s and the interface energy between film and substrate is given by σ_{fs}. Now the change in free energy ΔF when going from the initial state to the final state can be expressed as:

$$\Delta F = \frac{S}{\lambda^2}[\pi r^2\sin^2\theta\sigma_{fs}] + \frac{S}{\lambda^2}[2\pi r^2(1-\cos\theta)]\sigma_f + \frac{S}{\lambda^2}[\lambda^2 - \pi r^2\sin^2\theta]\sigma_s - S\sigma_{fs} - S\sigma_f \tag{5.8}$$

where S is an arbitrary surface area. The first three terms correspond to the final state: the first term represents the film-substrate interface contribution, the second term represents the

[8] The same analysis can be performed for an hexagonal lattice, presented in Appendix B.3 and without the assumption of a periodic lattice presented in Appendix B.4 , which leads to the same results. For this reason it seems that the choice of 2D lattice is arbitrary.

surface of the truncated sphere contribution (use Equation (5.7)) and the third term represents the surface of the substrate contribution. The two final terms correspond to the initial state. Now we divide over S and obtain an energy change per surface

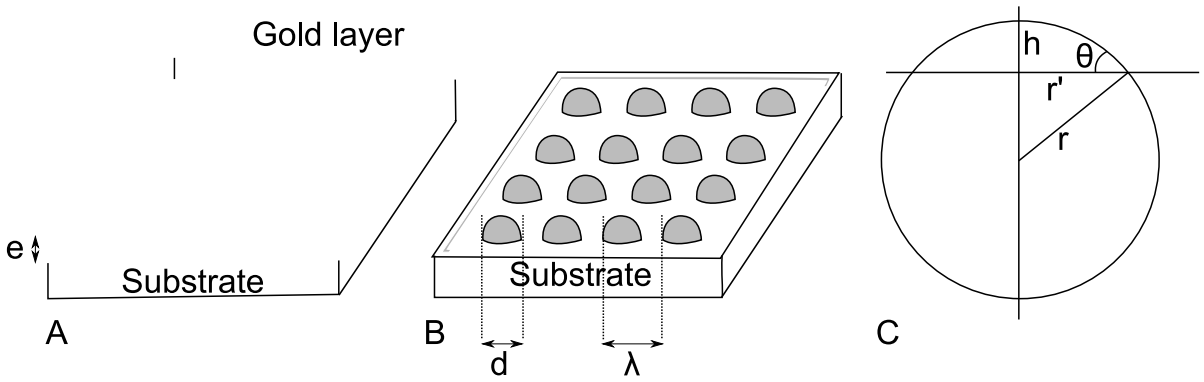

Figure 5.18: (A) Initial state: a liquid layer of gold on a silicon substrate (B) Final state, dewetting from a liquid layer results in a periodic network of clusters with a diameter d and a lattice parameter λ. (C) Schematic representation of a cluster that can be approximated by a truncated sphere with a radius r, a height of the cluster h and a contact angle θ.

$$\frac{\Delta F}{S} = \frac{\pi r^2 \sin^2\theta \sigma_{fs}}{\lambda^2} + \frac{2\pi r^2(1-\cos\theta)\sigma_f}{\lambda^2} - \frac{\pi r^2 \sin^2\theta \sigma_s}{\lambda^2} + \sigma_s - \sigma_{fs} - \sigma_f \tag{5.9}$$

which simplifies to

$$\frac{\Delta F}{S} = \frac{\pi r^2}{\lambda^2}[\sin^2\theta(\sigma_{fs}-\sigma_s) + 2(1-\cos\theta)\sigma_f] + \sigma_s - \sigma_{fs} - \sigma_f \tag{5.10}$$

The Young's Equation

$$\sigma_{fs} - \sigma_s = -\sigma_f \cos\theta \tag{5.11}$$

can be used to substitute the two last terms and we obtain

$$\frac{\Delta F}{S} = \frac{\pi r^2}{\lambda^2}[-\sin^2\theta\sigma_f\cos\theta + 2\sigma_f - 2\cos\theta\sigma_f] + \sigma_f\cos\theta - \sigma_f \tag{5.12}$$

We rewrite this and substitute $\sin^2\theta = 1-\cos^2\theta$ and use $2-3\cos\theta+\cos^3\theta = (2+\cos\theta)(1-\cos\theta)^2$

$$\frac{\Delta F}{S} = \frac{\pi r^2}{\lambda^2}[(2+\cos\theta)(1-\cos\theta)^2\sigma_f] - \sigma_f(1-\cos\theta) \tag{5.13}$$

Since each term contains σ_f we can divide both sides of the equation by σ_f to obtain a dimensionless expression. The thin layer will only dewet if

$$\frac{\Delta F}{S\sigma_f} \leq 0 \tag{5.14}$$

Now we use the conservation of matter before and after dewetting (use Equation (5.7)):

$$\lambda^2 e = \frac{\pi}{3} r^3 (1 - \cos\theta)^2 (2 + \cos\theta) \tag{5.15}$$

to substitute for λ^2. Critical values can be obtained by solving for $\Delta F = 0$

$$\frac{\Delta F}{S\sigma_f} = \frac{3e}{r} - (1 - \cos\theta) \qquad \text{which leads to} \qquad r_c = \frac{3e}{1 - \cos\theta} \tag{5.16}$$

and using Equation (5.15) to express the critical lattice parameter λ_c

$$\lambda_c = 3e\sqrt{\frac{\pi(2 + \cos\theta)}{1 - \cos\theta}} \tag{5.17}$$

A driving force for dewetting will be present only if $\lambda \geq \lambda_c$ and $r \geq r_c$.It is important to note that this critical radius is the radius of the complete sphere (r in (Figure 5.18b)), however the diameter we observe experimentally is the triple line diameter, being $2r'$ ($r' = r\sin\theta$). The critical cluster diameter d_c is given by

$$d_c = 2r_c \sin\theta = \frac{6e\sin\theta}{1 - \cos\theta} \tag{5.18}$$

In the following we refer to this diameter as the cluster diameter and this is the value we plot to allow direct comparison with experimental data.

In Appendix B.4 we show that the same analysis can be performed for dewetting of the liquid film without the assumption of periodicity. This approach illustrates that the important parameter is actually the density ρ and the critical value ρ_c is given by (see Appendix B.4)

$$\rho_c = \frac{1 - \cos\theta}{9e^2\pi(2 + \cos\theta)} \tag{5.19}$$

The values of the surface and interface energies are given in Table 5.3.

Table 5.3: Surface and interface energies

Material	Surface Energy (Jm^{-2})	Reference
Silicon (s) σ_s	1.24	(Schmidt et al., 2004)
Gold (l) σ_f	1.25	(Dhalluin et al., 2007)
Gold-silicon Interface σ_{fs}	0.33	Equation (5.11) (Ressel et al., 2003)

Experimentally we have observed a cluster density between 9.6x10^{15} and 1.1x10^{17} with an average of 3.4x10^{16} clusters m^{-2} (measured on eight images of different nanowires, grown at slightly different growth conditions, similar to Figure 5.3). The experimental cluster density should always be smaller than ρ_c ($\rho_{exp} < \rho_c$), otherwise no driving force for dewetting is present. In Figure 5.19 and Figure 5.20 the critical cluster density is compared to the average experimental cluster density for varying liquid layer thickness and varying contact angle. These graphs indicate that $e < 0.32$ nm and $\theta > 0.615$ rad.

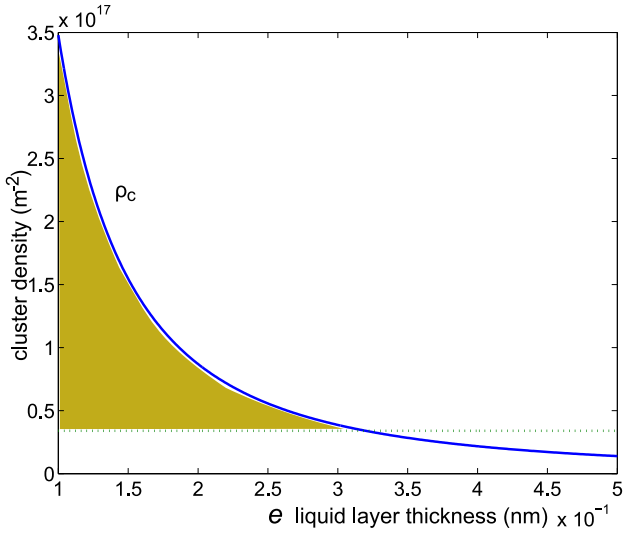

Figure 5.19: The critical cluster density (solid line) and the experimental cluster density (dotted line) are plotted for varying liquid layer thickness. The shaded area indicates the values where dewetting can occur. Dewetting can occur if $\rho_c > \rho_{exp}$ for $e < 0.32\,\mathrm{nm}$.

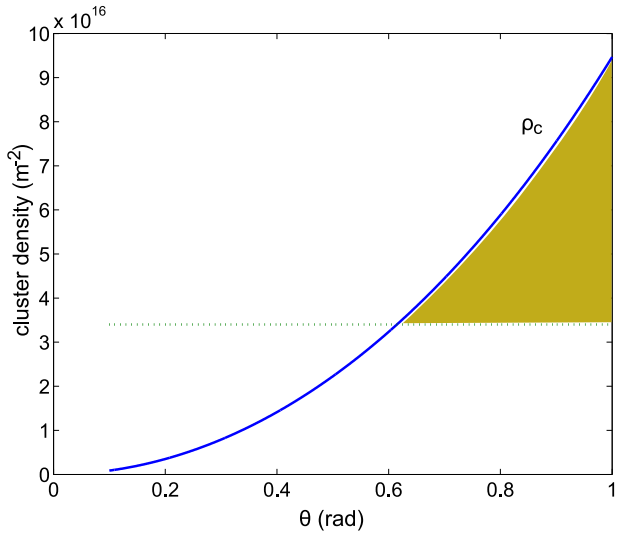

Figure 5.20: The critical cluster density (solid line) and the experimental cluster density (dashed line) are plotted for varying contact angle (θ)for the dewetting of several monolayers of liquid gold silicon on silicon. The thickness of the liquid layer is taken to be 0.26 nm. The contact angle of a gold droplet on silicon is $43° \approx 0.75$ rad. The shaded area indicates the values where dewetting can occur. Dewetting can occur if $\rho_c > \rho_{exp}$ for $\theta > 0.61\,\mathrm{rad}$.

The cluster diameter can be measured more precisely than the density (there is one order of magnitude difference between the highest and the lowest observed density) and is therefore considered as well. We also compare the calculated values for the lattice parameter with experimental values. This analysis is similar to the analysis of the cluster density. However since in reality no periodicity is observed, these values are of minor importance. Therefore the shaded areas in the graphs (Figure 5.21 and Figure 5.22) refer only to the cluster diameter. These shaded areas show the region where $d_c < d_{exp}$ and therefore dewetting can occur. In Figure 5.21 and Figure 5.22 the critical cluster diameter (d_c) and the critical lattice parameter (λ_c) are plotted for different layer thickness e and varying contact angle θ. Experimentally we measure a diameter of the clusters d_{exp} around 3 nm. The lattice parameter was found to be between 3.0 and 10.0 nm with an average of 6.5 nm, for example see Figure 5.1 (measured on eight images of different nanowires, grown at slightly different growth conditions, similar to Figure 5.3).

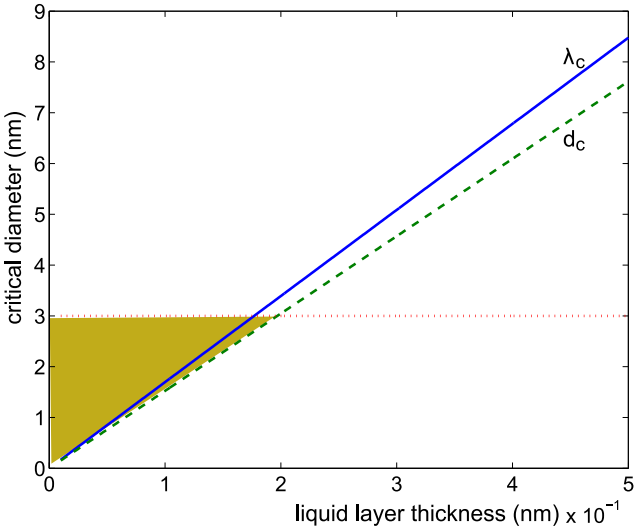

Figure 5.21: Critical cluster diameters (dashed line) and lattice parameters (solid line) are plotted for varying liquid layer thickness for the dewetting of several monolayers of liquid gold silicon on silicon. The contact angle is taken to be $43°$, the value for macroscopic liquid gold droplets on silicon. The experimental value of the cluster diameter is indicated (dotted line). The shaded area indicates the values where dewetting can occur. Dewetting can occur if $d_c < d_{exp}$ for $e < 0.2\,\mathrm{nm}$.

In Figure 5.21 the experimental value of the cluster diameter is indicated with a horizontal dotted line. This would indicate that the thickness of the liquid layer is below 2 Å. We should add that this simple model is in principle only valid for dewetting from several monolayers. In Figure 5.22 we can see that for a contact angle slightly larger than the contact angle found in the macroscopic system of a liquid gold droplet on silicon ($43° \approx 0.75$ rad), the critical cluster diameter is roughly the experimentally observed value.

Several assumptions are made in this approach:

1. As discussed before the gold is assumed to diffuse as a liquid layer.

2. The gold liquid layer could also be a gold silicon mixture, which seems probable as the catalyst particle is also a gold silicon mixture and the gold-silicon eutectic is particularly deep (Section 2.1). This could change the surface and interface energies and the amount of gold present on the nanowire would be merely a lower boundary to estimate the thickness of the liquid layer. The silicon present in the liquid layer would then oxidize after growth, explaining the fact that the gold clusters are covered by a relatively thick (2-3 nm) oxide layer (Figure 5.2). If silicon is present in the liquid layer the silicon will be more on

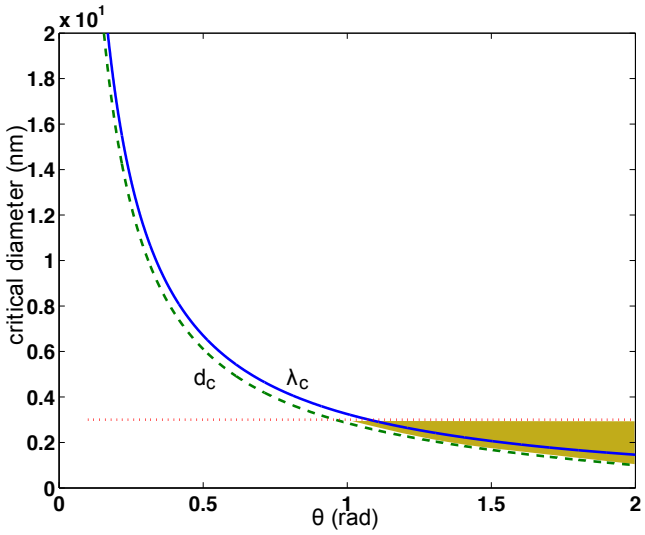

Figure 5.22: Critical cluster diameters (dashed line) and lattice parameters (solid line) are plotted for varying contact angle for the dewetting of several monolayers of liquid gold silicon on silicon. The thickness of the liquid layer is taken to be 0.26 nm. The contact angle of a gold droplet on silicon is $43° \approx 0.75$ rad. The experimental value of the cluster diameter is indicated (dotted line). The shaded area indicates the values where dewetting can occur. Dewetting can occur if $d_c < d_{exp}$ for $\theta > 1\,\mathrm{rad}$.

the surface since the surface energy of silicon is lower (Shpyrko et al., 2006). This will lower the surface energy of the liquid film (Brunet et al., 1976).

3. The gold clusters obtained after dewetting are described by a spherical cap, which is not necessarily true (Ressel et al., 2003).

4. The interaction of gold and silicon is not taken into account. In studies where the silicon surface reconstruction is studied as a function of gold coverage it is shown that the surface reconstructs due to the formation of a gold silicide phase at the surface (Hild et al., 2002; Minoda et al., 1999; Seehofer et al., 1995). More importantly it was shown in (Wiethoff et al., 2008) that a faceting similar to the faceting on the nanowire sidewall can be observed on a silicon $\langle 112 \rangle$ substrate with an excess of gold present as gold clusters on the reconstructed surface. In this work (Wiethoff et al., 2008) a lower limit for the gold coverage of 0.4-0.46 ML of gold is estimated on the silicon surface. This results in two limitations of our model. The surface energy of such a reconstructed gold-silicon surface is probably less than the surface energy of pure silicon (since a driving force is present to enable the surface reconstruction), however the value of the reconstructed surface energy is unknown and can therefore not be taken into account. Furthermore the conservation of matter cannot be expressed properly since a part of the gold will be incorporated in the reconstructed surface, however the quantity of gold on the nanowire surface cannot be measured very precisely and therefore the model is already approximative.

In the next section a variation of this approach is presented where the same four assumptions are made, to include the presence of line tension.

5.6.2 Dewetting from multiple layers including line tension

In this section we will review the simple model we constructed in the previous section but now include line tension. The possibility of line tension was first proposed by (Pethica, 1961) and (Widom, 1995) and implicates a change in contact angle for nanometer-sized droplets. The line tension is a one dimensional surface energy that acts on the triple line diameter of nanometrically sized droplets, thereby modifying the contact angle θ. The effect of the line tension τ (in Jm^{-1}) on the contact angle is given by the modified Young's equation (Pethica, 1961) (Widom, 1995)

$$\sigma_f \cos\theta = \sigma_s - \sigma_{ls} - \frac{\tau}{r'} \tag{5.20}$$

This equation is just an equilibrium of forces on the triple line point. The effect of line tension on the droplet shape is explained schematically in Figure 5.23 for a positive line tension.

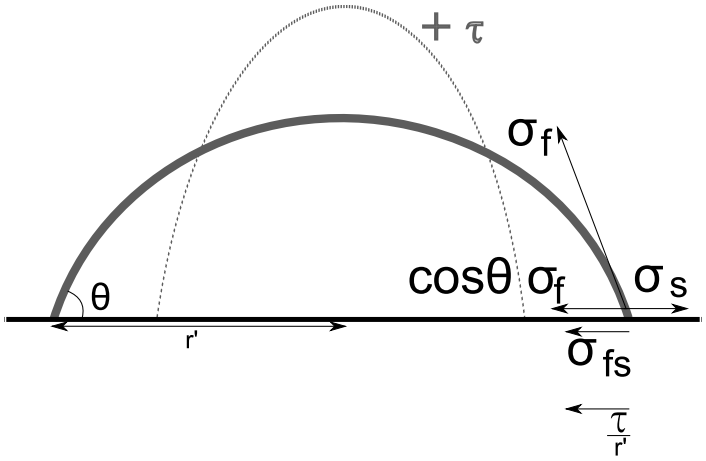

Figure 5.23: Droplet on a surface. On the right all forces are indicated working on the triple line point. The equilibrium of these forces is given by the Young's equation (Equation (5.11)), or by the modified Young's equation (Equation (5.20)), including the effect of line tension. The effect of a positive line tension on contact angle and the droplet shape is indicated by a dashed line.

Since the clusters we observe are in the nanometer size range, line tension could have an effect on the cluster shape. It was proposed by (Schmidt et al., 2004) that the line tension effect can actually be observed at the beginning of nanowire growth, and explains the size of the nanowire basis. They found a line tension of $\tau \approx -1x10^{-9}\, Jm^{-1}$. A positive line tension increases the contact angle (Figure 5.23) and a negative line tension flattens the droplet.

The equations relating the contact angle and thickness of the liquid layer e with r_c and λ_c including the influence of line tension can be found using a similar analysis as described in the previous section. Details are shown in Appendix B.5.

It is found that

$$r_c = \frac{3e + \tau"}{2(1-\cos\theta)} \pm \frac{\sqrt{(3e+\tau")^2 + 12e\tau" \frac{1+\cos\theta}{(2+\cos\theta)}}}{2(1-\cos\theta)} \tag{5.21}$$

$$\lambda_c = (1-\cos\theta)\sqrt{r_c^3}\sqrt{\frac{\pi(2+\cos\theta)}{3e}} \tag{5.22}$$

where τ" = $\frac{\tau}{\sigma_c \sin\theta}$

However the results of these calculations are difficult to interpret. Boundary values for the line tension can be determined by expression of the line tension as a function of theta and the critical cluster radius using the modified Young's Equation (5.20).

In Figure 5.24 the line tension τ is plotted as a function of the contact angle θ for different values of the critical cluster diameter (d_c is 1 nm (solid line), 2 nm (dashed line), 3 nm (dotted line) and 4 nm (dashed dotted line). Since experimentally the critical cluster diameter is around 3 nm, this figure tells us that for this system the line tension can be between -0.5x10^{-9} and 3x10^{-9} J m^{-1}. It is clear from Figure 5.24 that if a line tension as found in (Schmidt et al., 2004) would be present in this system, the cluster diameter should be larger than the experimentally observed value.

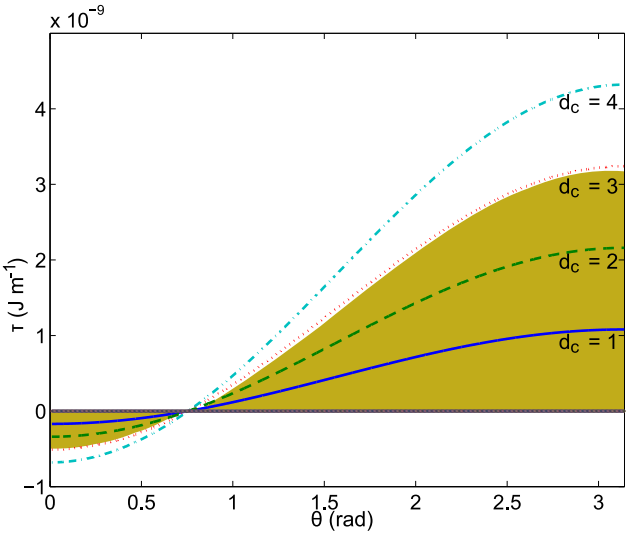

Figure 5.24: The contact angle theta is plotted for the line tension at different critical cluster diameters: 1 nm (solid line), 2 nm (dashed line), 3 nm (dotted line) and 4 nm (dashed dotted line). The shaded area indicates the values where dewetting can occur ($d_{exp} \sim 3\,\mathrm{nm}$).

5.7 Conclusion

The presence or absence of gold clusters on the silicon nanowire sidewall can be controlled by three growth parameters being silane partial pressure, temperature and catalyst size. The gold clusters have a rather uniform diameter around [3]nm. It is assumed that during growth gold can diffuse over the nanowire sidewall as a liquid layer, as suggested by (Hannon et al., 2006). We propose a qualitative model based on an increased silane adsorption on the wire sidewall, which effectively blocks the gold diffusion. The growth conditions to inhibit gold diffusion are summarized in Table 5.2 Section 5.4.

An effect of wire diameter on gold diffusion was observed which might be due to an increase in chemical potential of surface atoms as the diameter decreases.

Control of the surface diffusion of gold provides a tool to fabricate long, uniform diameter structures with flat sidewalls and no gold clusters decorating the nanowire sidewall. Also the possibility exists to modify the sidewall morphology after growth by performing a post-growth anneal during which the gold can diffuse over the wire sidewalls. In this way gold clusters can be deposited on the nanowire sidewall, or a part of it, in a controlled and reproducible way,

allowing direct functionalization of the nanowire. Applications like the realization of nanowire web's (Cimalla et al., 2007), could benefit from the presence of gold clusters on the nanowire surface or a specified part of it, as it would avoid the additional deposition of gold nanoclusters at the nanowire surfaces.

The presence of gold on the nanowire sidewall introduces faceting. Two different types of faceting were observed that seem to depend on gold coverage.

Two models were considered to explain the dewetting of the liquid film during or after growth, that results in the observation of gold clusters on the nanowire sidewall. A model valid for the dewetting of several layers of liquid on a surface (section Section 5.6.1) and the same model but this time including line tension (section Section 5.6.2). Taking into account all calculations we can say that

- The liquid layer seems to be on the order of one monolayer, this is indicated by the results from section Section 5.6.1. Also this amount corresponds to the estimated quantity of gold on the wire surfaces. This amount was estimated using the number and average size of the gold clusters.
- Size effects (in the form of line tension) that could modify the contact angle of small gold or gold silicon droplets do not appear very important for the dewetting of this system, contrary to the results presented by Schmidt et al (Schmidt et al., 2004). This is illustrated in Figure 5.24.

Part III

THE NANOWIRE VOLUME: DOPANT AND DEFECT DETECTION

6

CRYSTALLOGRAPHY: DETERMINATION OF THE GROWTH DIRECTION AND DEFECTS IN SILICON NANOWIRES

In this chapter the focus lies on the crystalline structure of the nanowires. Several nanowire growth systems were studied with the aim to improve the control over growth characteristics.

Firstly the characterization of the crystallographic growth direction in several nanowire growth systems, including nanotrees, is presented.

Secondly the crystallographic defects that could sometimes be present are characterized.

If gold was used as the catalyst few defects were present in the nanowire volume and the defects could be identified easily using TEM images or diffraction patterns (DPs).

However in other nanowire growth systems, inclined defects (with respect to the electron beam) or complicated series of defects were present.

Diffraction resulting from the superposed crystal grains can create TEM images/DPs that can be confused with an hexagonal crystal structure. In Section 6.4 the observed incidental defects and recurring defects are shown and very clear evidence is presented that no other crystal structure than diamond cubic silicon is present in the observed nanowires[1] [2].

6.1 Introduction

In this chapter the crystalline properties of several different nanowire growth systems are described. In this section the aim of these experiments is introduced.

Nanowires were studied grown with the gold catalyst and trimethylalumina (TMA) was added to the growth process with the goal to p-dope the silicon nanowire. Doping of nanowires is important since applications of nanowires such as transistors and solar cells make use of a p-n

[1] This work was performed in collaboration with Cyril Cayron (CEA/LITEN). Some of the presented results were published in (Cayron et al., 2009).

[2] The studied nanowires were grown by Fabrice Oehler (CEA/DSM/INAC/SP2M/SINAPS), Florian Dhalluin (CNRS UMR 5129), Thomas David (CEA/DSM/INAC/SP2M/SINAPS), Heinz Schmid (IBM Zurich) and Pascal Gentile (CEA/DSM/INAC/SP2M/SINAPS), Grenoble.

junction (see also Appendix A.4). Diphosphine was also added to the growth to n-dope certain regions of the nanowires.

Accidently nanotrees were grown due to the addition of TMA. Nanotrees could also be grown without TMA in a two step growth process (Dhalluin et al., 2007). In literature growth of nanotrees was shown by redeposition of catalyst material (Dick et al., 2004). Such tree like nanostructures are mostly interesting for their large surface area and could be used for example in nanoreactors as proposed by (Cimalla et al., 2007) or as anodes in lithium batteries (Chan et al., 2008).

Nanowires that were grown in a template of nanoporous alumina with a gold catalyst were also observed. The template of nanoporous alumina is interesting because localized growth is possible and the pores guide the nanowire growth direction (Buttard et al., 2008). Therefore nanowires could be grown perpendicular on a $\langle 100 \rangle$ oriented silicon wafer, which is compatible with microelectronics applications. Something that is at the moment not possible using normal VLS growth.

Although gold is a very successful catalyst material, it is not compatible with microelectronics since gold is known to create deep traps (Tavendale and Pearton, 1983). As shown in Chapter 5 gold can diffuse over the nanowire sidewall and create a surface reconstruction, the saw-tooth faceting. Both the gold and the surface reconstruction will modify the electronic properties of the nanowire. Even if gold is not diffusing over the nanowire sidewall, single gold atoms can be present in the nanowire volume (Allen et al., 2008). For this reason other catalyst materials were tested, being nickel (Ni), platina (Pt) and copper (Cu), that are more compatible with microelectronics. The aim is to find a nanowire growth system were nanowire dimensions, surface properties, growth direction and doping can be carefully controlled and combined with a high crystalline quality.

Hydrochloric acid gas (HCl) was sometimes added to the growth process. It was already described in Section 5.5 that HCl seems to modify the gold diffusion (Oehler et al., 2009b). HCl seems to be beneficial for the nanowire growth, especially if a solid catalyst is used[3].

6.2 Experimental details

The detailed growth conditions of the observed nanowire samples presented in this section are described. Different catalyst materials (Au, Cu, Ni and Pt) were used and other gas types (TriMethylAlumina (TMA), diphosphine and HCl) were added to the growth process.

6.2.1 Gold catalyst

The nanowires were grown using gold as the catalyst as described in Section 5.2.

One sample was studied where nanowires were grown in a membrane of nanoporous alumina. The growth conditions were 0.13 mbar silane partial pressure and 450 °C growth temperature.

Nanowires were observed that were grown by two consecutive growth steps. In the first step nanowires were grown at conditions that favourize gold diffusion. The second growth step was carried out at lower temperature and sometimes at a higher silane partial pressure. During the

[3] Nanowire growth with a Ni or Cu catalyst is more successful if HCl is added to the growth process, the exact role of the HCl is unclear at present.

second growth step the gold clusters present at the wire sidewall can nucleate to grow a branch. Using this approach very thin wires (d<25 nm) can be grown on the larger trunk wire (Dhalluin et al., 2007), and a tree-like structure (so called nanotrees) are obtained.

6.2.2 Gold catalyst & TriMethylAlumina

TMA was added to the growth system with the aim of growing p-doped nanowires [4]. A gold film with a thickness of 2 nm was used to form the catalyst particles using an annealing treatment at 900 °C. The nanowires grown in the presence of TMA described in this chapter were grown on a silicon $\langle 111 \rangle$ oriented wafer, at the following growth conditions: total reactor pressure 20 mbar, 3.7 l min^{-1} hydrogen (carrier gas), 40 min growth duration. Two particular samples are observed, with very different properties.

The first sample was grown using 0.1 mbar silane partial pressure, 650 °C growth temperature and 1.5% of TMA. This lead to the growth of nanotrees and no crystalline defects were observed (Section 6.3.2).

The second sample was grown using 0.26 mbar silane partial pressure, 500 °C growth temperature and 3% of TMA. The nanowires on this sample were relatively short and contained many crystalline defects, which are described in Section 6.4.2. A complete SEM study of the effect of TMA in combination with the growth temperature on the wire morphology can be found in (Oehler et al., 2009a).

6.2.3 Gold catalyst & Diphosphine

Two nanowire samples A and B were studied, that were grown in the presence of diphosphine to grow phosphorus doped regions[5]. These samples will be described in more detail in the next chapter. The growth conditions for the nanowires with phosphorus doping were as follows: Sample A was grown at 440 °C in He at 67 mbar with a silane partial pressure of 0.267 mbar. Sample B was grown at 460 °C in H_2 at 33 mbar with a silane partial pressure of 0.133 mbar.

6.2.4 Nickel, Copper and Platinum catalysts

When Ni and Cu were used as a catalyst, the metal was evaporated on a silicon wafer, the growth was performed at a temperature of 800 °C for the Ni catalyst and 750 °C for the Cu catalyst. The partial silane pressure was 0.13 mbar, with H_2 as the carrier gas and HCl was added to the growth. The melting point of either Ni and Ni-Si is above the growth temperature, therefore the Ni catalyst is solid during growth. The Cu-Si eutectic has two eutectic points at 802 °C and 820 °C (Hansen and Anderko, 1958), and is therefore probably solid during growth (size effects on the eutectic temperature are not expected since the catalyst particle is generally large ($> 100\,\mathrm{nm}$)(Kodambaka et al., 2007)).

Also nanowires were grown with platina (Pt) as the catalyst. The growth conditions for these nanowire were identical to the conditions for a Ni catalyst, however no HCl was added to the growth chamber. The catalyst is probably solid since a silicon-platina eutectic can form only

[4] Transport measurements performed by Fabrice Oehler and Nicolas Pauc (CEA/DSM/INAC/SP2M/SINAPS) showed that the as-grown nanowires were undoped. p-doping could be activated by annealing the samples at or above 800 °C.

[5] Grown by Heinz Schmid, IBM Zurich.

at 830 °C (Massalski, 1990). X-ray diffraction (XRD) was performed on the deposited catalyst after the anneal step and showed the present phases were PtSi and Pt_2Si (Dhalluin, 2009).

6.3 Crystallography

In this section some crystallographic features of the studied nanowire systems are investigated. The focus lies on the determination of the crystallographic growth direction, since this is of interest for applications. Furthermore the sidewall facets parallel to the nanowire axis were studied of nanowires grown with the Cu catalyst.

6.3.1 The crystallographic growth direction

In Section 2.3 some potential applications of silicon nanowires were already introduced. Since device features have been shrinking for over 40 years, following Moore's law, new architectures are proposed were nanowires play a key role. Devices that make use of nanowires have already been reported (Cho et al., 2007; Singh and et al., 2006; Xiang and et al., 2006; Cohen and et al., 2007; Thelander et al., 2008; Björk et al., 2008), however nanowires are not yet integrated in devices produced on a large scale.

An important aspect for the integration of bottom up syntesized nanowires (see Section 2.1) is the control of the crystallographic growth direction, since the electronic structure of silicon is highly anisotropic especially in nanowires as the bulk crystal symmetry is not preserved (Wang et al., 2005), for this reason the transport properties of nanowires depend on growth direction. It was shown by tight binding simulations that for small silicon and germanium nanowire FETs (diameter $\sim 3\,\text{nm}$) the $\langle 110 \rangle$ orientation is preferable (Wang et al., 2005). For this reason determination of the nanowire growth direction is very important. Experimentally it is not trivial to couple transport properties and the crystallographic growth direction of a single nanowire, as the sample for transport measurements is generally not suited for TEM measurements. If the electrical connections to the nanowire are fabricated on a thin membrane transparent to electrons (for example Si_3N_4) as shown in (Peng et al., 2008), transport properties and the crystallographic growth direction can be measured on a single nanowire, which allows a correlation.

In the following we present the nanowire growth direction of several nanowire growth systems and we show how the growth direction can be determined accurately. A summary of the results can be found in Table 6.1.

Table 6.1: Summary of the observed growth directions depending on nanowire system. A general direction $\langle\rangle$ indicates that several wires with that growth direction were observed, a particular direction [] indicates that this growth direction was a single observation.

Catalyst	NW diameter (nm)	Growth direction	Remarks
Au	$> 100\,\text{nm}$	$\langle 111 \rangle$	
Au	$< 50\,\text{nm}$	$\langle 111 \rangle$, $\langle 110 \rangle$, $\langle 112 \rangle$	
Cu	$> 100\,\text{nm}$	$\langle 111 \rangle$, $\langle 110 \rangle$, $\langle 112 \rangle$	$\langle 112 \rangle$ direction favourized, twins
Ni	$> 100\,\text{nm}$	$\langle 111 \rangle$, $\langle 110 \rangle$, $\langle 112 \rangle$	$\langle 112 \rangle$ direction favourized, twins
Pt	$> 100\,\text{nm}$	$\langle 111 \rangle$, $\langle 110 \rangle$, $\langle 112 \rangle$, $[\bar{5}12]$	

For nanowires grown with gold as the catalyst (see Section 5.2) the crystallographic growth

direction of large wires (diameter $> 100\,nm$) was found to be the $\langle 111 \rangle$ direction. In smaller wires (diameter $< 50\,nm$) the growth direction was found to be either $\langle 111 \rangle$ or $\langle 110 \rangle$. One very small nanowire (diameter $\sim 6\,nm$) was observed to grow in the $\langle 112 \rangle$ direction and contained a single vertical twin defect (see Figure 6.9). These results are coherent with (Schmidt et al., 2005), where it was shown that large silicon nanowires have a tendency to grow in the $\langle 111 \rangle$ direction, whereas small silicon nanowires (diameter $< 50\,nm$) grow in the $\langle 110 \rangle$ or $\langle 112 \rangle$ direction.

Nanowires containing phosphine doped sections with a diameter of 60 nm that were not in epitaxy with the silicon $\langle 111 \rangle$ substrate (sample A) were growing either in the $\langle 111 \rangle$ or the $\langle 112 \rangle$ direction, in the last case they often contained vertical twins. Wires growing in epitaxy on the silicon wafer (sample B) were growing in the $\langle 111 \rangle$ direction.

Large nanowires (diameter $\geq 100\,nm$) that were grown with Cu or Ni as the catalyst were also growing in these three favourised growth directions ($\langle 111 \rangle$, $\langle 110 \rangle$ and $\langle 112 \rangle$), however the $\langle 112 \rangle$ direction occurred more frequently. Very often wires that grow in the $\langle 112 \rangle$ direction contain vertical defects (this will be described in more detail in Section 6.4).

Determination of the growth direction should be performed with care, since the nanowire should be perpendicular to the electron beam. This is an easy task if the nanowire is growing in epitaxy on a substrate of known orientation (in the case of a cross section or cleaved sample) and is not bended, however if the nanowire is deposited on a holey carbon film it does not necessarily lie exactly in the plane of the TEM grid [6].

The growth direction can be determined either from a single HRTEM image (Figure 6.1) or by an association of diffraction patterns (Figure 6.2). In the following an example of both methods is given.

Figure 6.1 shows the case of a nanowire grown with PtSi as the catalyst and illustrates how a single HRTEM image can be used to obtain the growth direction. The fundamental assumption of this method is that the catalyst interface is perpendicular to the growth direction. This method can be used only if the wire-catalyst interface is visible in the HRTEM image. From the Fourier transform of the HRTEM image in Figure 6.1B, one can see that the nanowire is observed along the [112] direction (Figure 6.1C). The growth direction can be calculated using vector calculation as shown using the perpendicular trace of the wire-catalyst interface (Figure 6.1D). In Figure 6.1D it is shown that the [112] and $[02\bar{1}]$ directions are both perpendicular to the growth direction. The growth direction is therefore given by $[112] \times [02\bar{1}] = [\bar{5}12]$. The problem of this method is that if the assumption (catalyst interface $\perp$ growth direction) is not true, as is the case in Figure 6.2F for example, we do not find the true growth direction but a projection of the growth axis perpendicular to the observation axis. However the angle between the projection and the growth axis should be small. In the case of Figure 6.1 it can be verified that there is no low index direction close to the $[\bar{5}12]$ direction (the $[\bar{1}00]$ and $[\bar{1}01]$ directions make an angle with the $[\bar{5}12]$ direction of 24 and 25 ° respectively). Other nanowires grown using PtSi as the catalyst were growing in the $\langle 111 \rangle$, $\langle 110 \rangle$ or $\langle 112 \rangle$ directions.

The growth direction can also be determined using an association of diffraction patterns. In Figure 6.2[7] the same nanowire is observed along different directions. Respective stereograms, diffraction patterns and BF TEM images are shown for each direction. The nanowire was grown using a Ni catalyst and the sample was prepared by cleaving. Care was taken to tilt

[6] It seems best to prepare dispersion samples on a plane carbon film if the goal is to determine the growth direction. However in this work a holey carbon grid was used most frequently.

[7] The DP in Figure 6.2E is strange, as it does not exist in normal diamond cubic silicon. For this reason only the {111} planes of the grain observed along the [132] direction are indexed. This DP will be explained in more detail in Section 6.4.2.

the nanowire around its vertical axis and to maintain the catalyst-wire interface perpendicular in the TEM image (in the edge-on position).

All three images and corresponding DPs seem to indicate the $[31\bar{3}]$ direction as the growth direction, because the diffraction spot of the $(31\bar{3})$ plane appears to be perpendicular to the wire-catalyst interface. However in Figure 6.2E the $[1\bar{1}1]$ direction is perpendicular to the nanowire sidewall and should therefore be perpendicular to the growth direction. This means that the dot product of the growth direction $\overrightarrow{a}$ and $[1\bar{1}1]$ is zero, which is not true for $\overrightarrow{a} = [31\bar{3}]$. In Figure 6.2B the $[\bar{3}1\bar{3}]$ direction is perpendicular to the nanowire sidewall and the growth direction. The growth direction $\overrightarrow{a} = [a_x b_y c_z]$ can therefore be described by two equations (see Figure 6.2B,E)

$$\overrightarrow{a} \cdot [1\bar{1}1] = a_x - b_y + c_z = 0 \qquad \overrightarrow{a} \cdot [\bar{3}1\bar{3}] = -3a_x + b_y - 3c_z = 0 \tag{6.1}$$

It follows that $b_y = 0$ and $a_x = -c_z$, and therefore **the growth direction is the** $[10\bar{1}]$ **direction**, which seems also coherent with the third direction of observation (Figure 6.2G-I). Using a stereogram it can be seen more easily if the true growth direction is found or only the projection. The direction of the nanowire sidewall is indicated in the respective stereograms (Figure 6.2B,E,G) to illustrate that the projection of the growth direction passes through the true growth direction, the $[10\bar{1}]$ direction, but is not perpendicular to the true growth direction.

In this example the direction of observation is not perpendicular to the nanowire growth direction, however using two projections the growth direction can be calculated.

The wire-catalyst interface seems slightly inclined with respect to the wire axis Figure 6.2F,I. Therefore in this particular example the assumption that the catalyst interface is perpendicular to the growth direction is not true.

For most of the observed nanowires only one HRTEM image was used for determination of the growth direction. It was assumed that if the wire-catalyst interface is in the edge-on position and a low index plane is found as the growth direction, little ambiguity is present.

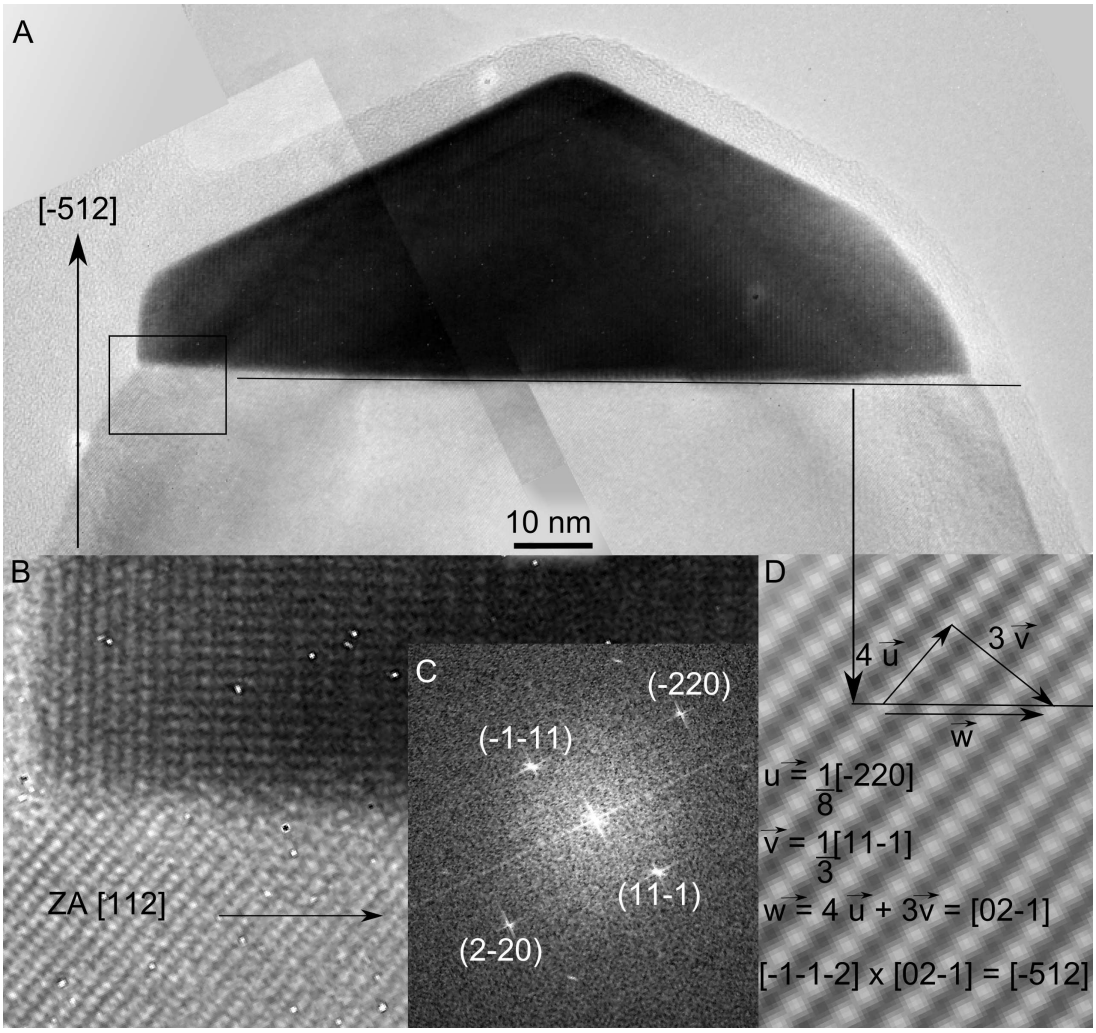

Figure 6.1: A silicon nanowire grown with a Pt catalyst observed along the [112] direction. (A) Combination of three HRTEM images to show the complete catalyst particle. The wire-catalyst interface is slightly curved. The growth direction is $[\bar{5}12]$. (B) HR zoom and (C) corresponding FT with indexed planes. (D) Filtered HR image to show how the growth direction can be calculated using vector calculation. Sample 4454

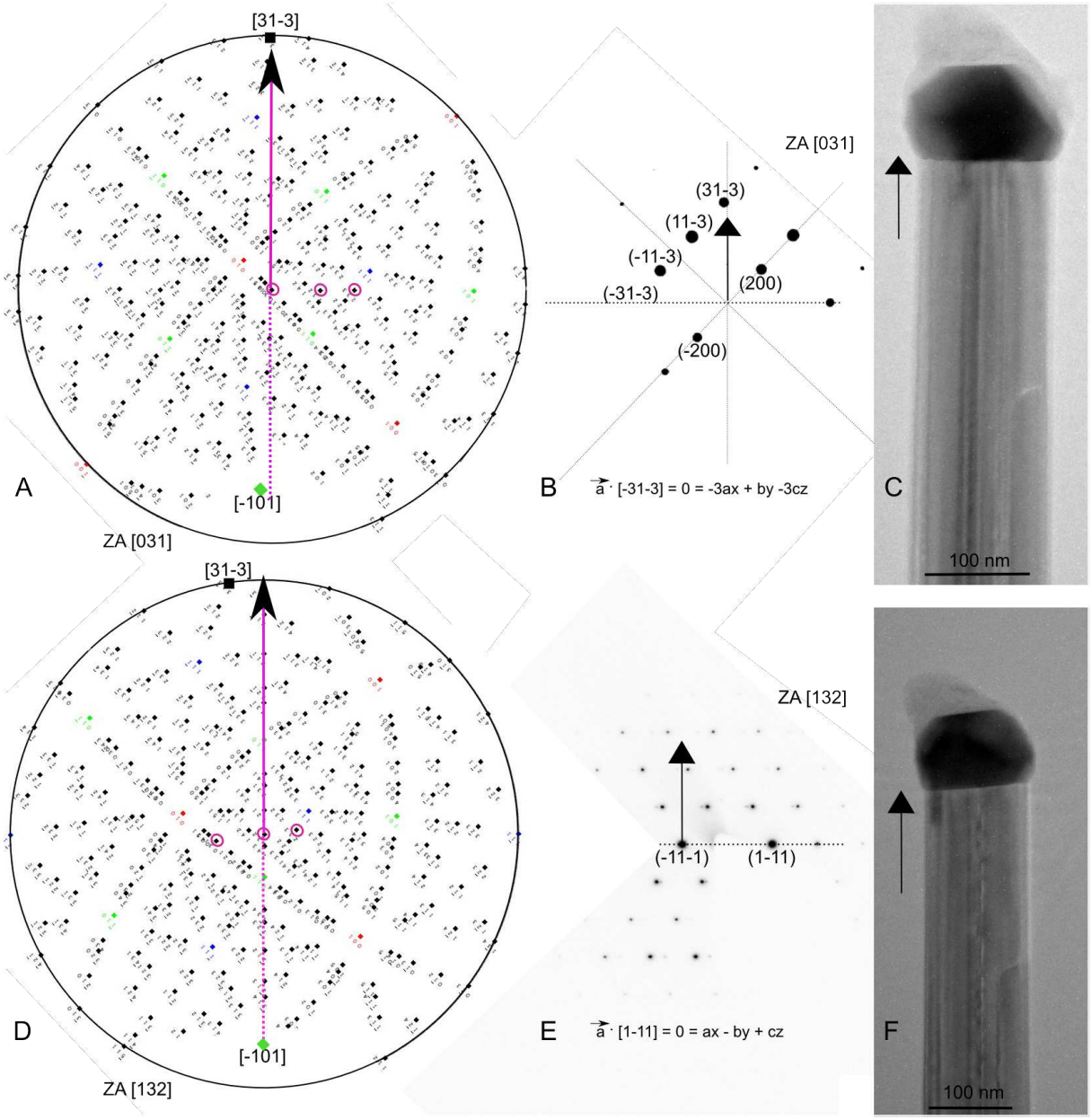
[31-3]
A
[-101]
ZA [031]
ZA [031]
(31-3)
(11-3)
(-11-3)
(200)
(-31-3)
(-200)
B
a · [-31-3] = 0 = -3ax + by -3cz
C
100 nm
[31-3]
D
[-101]
ZA [132]
ZA [132]
(-11-1)
(1-11)
E
a · [1-11] = 0 = ax - by + cz
F
100 nm

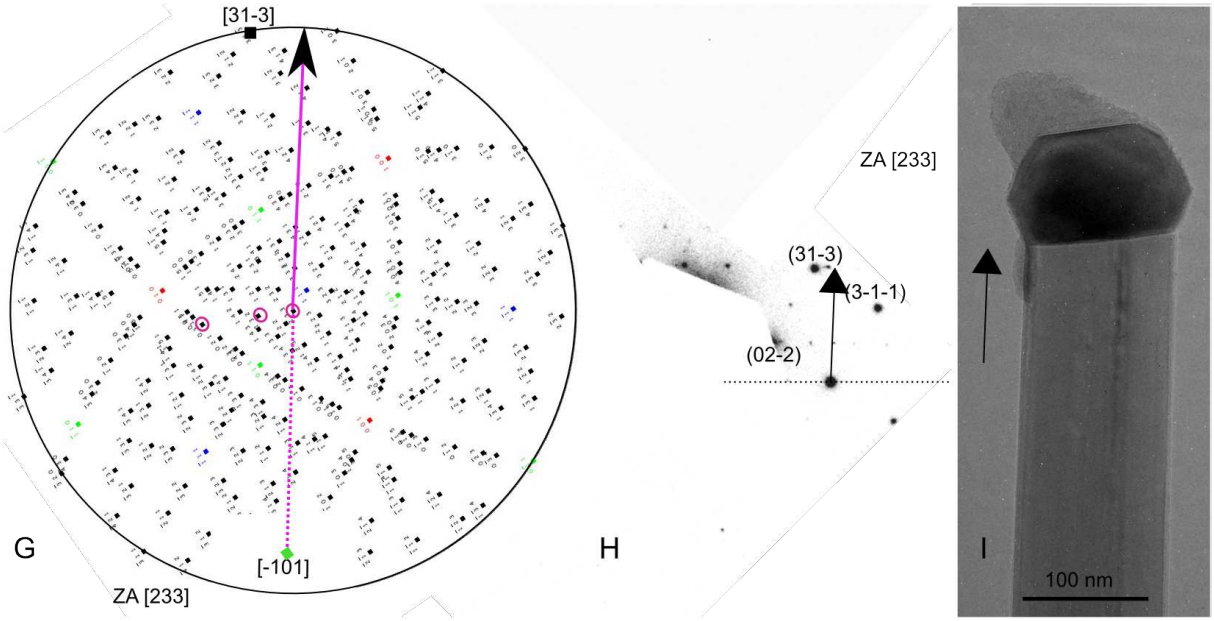

Figure 6.2: Silicon nanowire grown with a Ni catalyst, the corresponding diffraction pattern and the stereogram. The nanowire was observed along three different directions, that are indicated in each stereogram. (A) Stereogram of the [031] ZA. (B) The indexed diffraction pattern (DP) (C) TEM BF image. (D) Stereogram of the [132] ZA. (E) Indexed DP (F) TEM BF image. (G) Stereogram of the [233] ZA. (H) Indexed DP (The nanowire could not be tilted completely on the ZA due to the microscope's tilt range, which caused the reduced quality of the DP). (I) TEM BF image. Sample 4530

One sample was studied where nanowires were grown in a nanoporous membrane of aluminum-oxide. Figure 6.3 shows an energy filtered TEM (EFTEM) image of the nanowire in the nano-pore. EFTEM was used in this case as better contrast between the pore and the nanowire can be obtained than in a conventional BF TEM image. Figure 6.3B-C show an HRTEM image and the corresponding FT. The nanowire growth plane is as usual a {111} plane. However the growth direction is imposed by the nano-pore and in a different direction. This example illustrates clearly that although the favourized growth direction is the ⟨111⟩ direction, guided growth in another direction is possible[8].

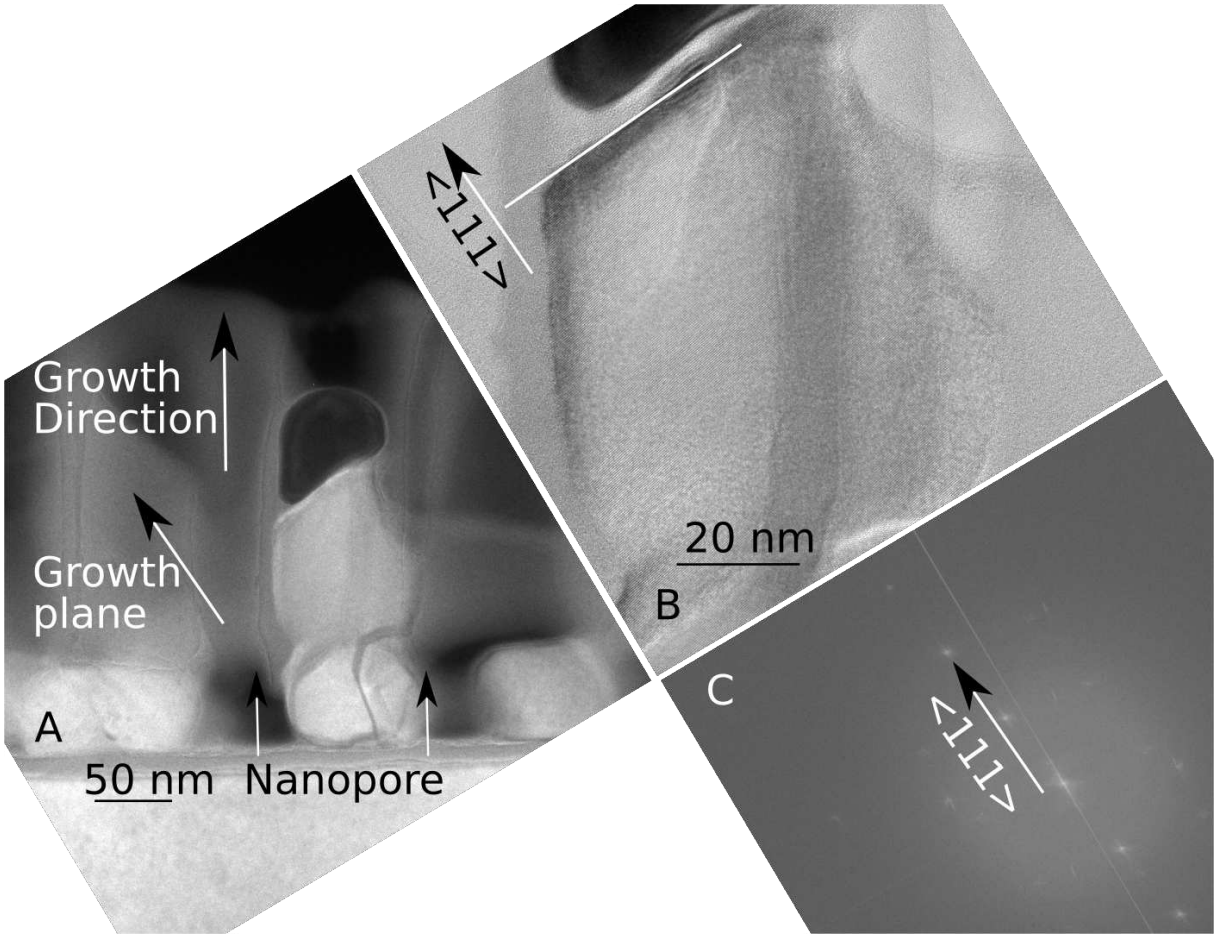

Figure 6.3: A nanowire grown in a aluminum-oxide nanopore with a gold catalyst. (A) Energy Filtered TEM image (acquired at the silicon plasmon energy loss (17 eV)) (B) HR TEM image (C) FT of (b). Sample 5066

6.3.2 Nanotrees

Is was already mentioned in Section 6.2 that nanotrees can be obtained if TMA is added to the growth chamber at certain growth conditions. Here the crystallographic characteristics of these nanotrees are described.

In Figure 6.4A-B topview SEM images of the nanotrees are shown. Most nanotrees grow perpendicular to the substrate, in the ⟨111⟩ direction. This was also observed in TEM. The branches extend out from the large trunk wire in six symmetrical directions. In Figure 6.4C a BF TEM image is shown. Branches are growing mostly in ⟨111⟩ directions. Three upward ⟨111⟩ direc-

[8] This image was published in (Buttard et al., 2008).

tions and three downward ⟨111⟩ directions are present. An example of a branch growing in the downward ⟨111⟩ direction is shown in Figure 6.5. No defects were observed at the trunk-branch interface (or at other parts in the nanotree). One branch was observed to change growth direction from the ⟨111⟩ to the ⟨100⟩ direction without a defect (see Figure 6.6).

Nanotrees could also be grown without the addition of TMA (see Section 6.2 and (Dhalluin et al., 2007)). In (Section 6.4.1) we will comment on the crystalline quality of some of the branches.

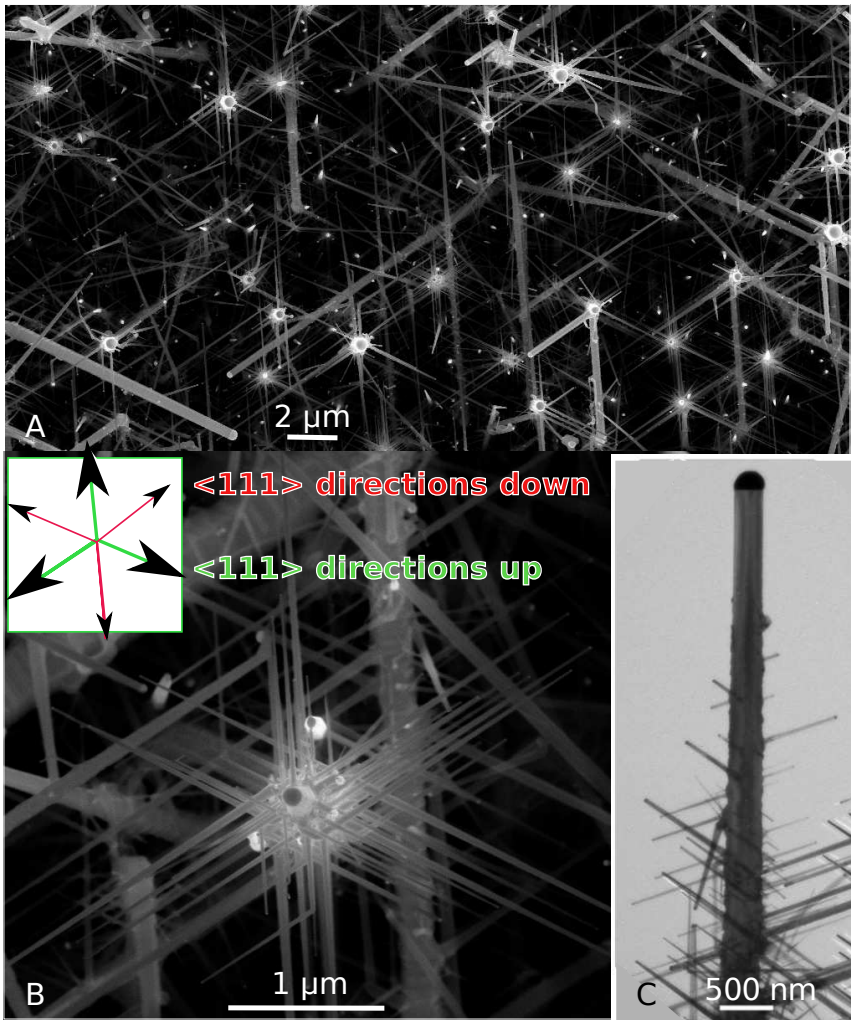

Figure 6.4: (A) Top view SEM image of an ensemble of nanotrees grown with TMA and a gold catalyst. (B) Top view SEM image of a nanotree. The three upward and downward ⟨111⟩ directions are indicated in the inset. (C) TEM BF image of a nanotree. Sample 4913

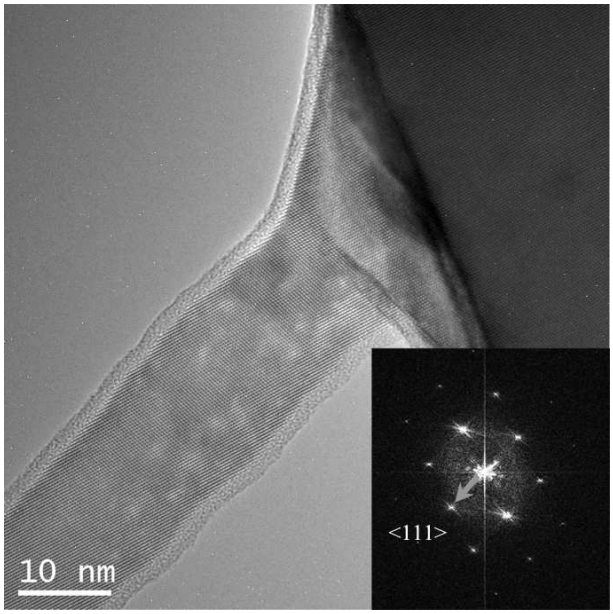

Figure 6.5: HR TEM image of a branch in epitaxy with the trunk-wire. The FT is shown in the inset, clearly indicating that no crystallographic defects are present and the branch is growing in the $\langle 111 \rangle$ direction. Sample 4913

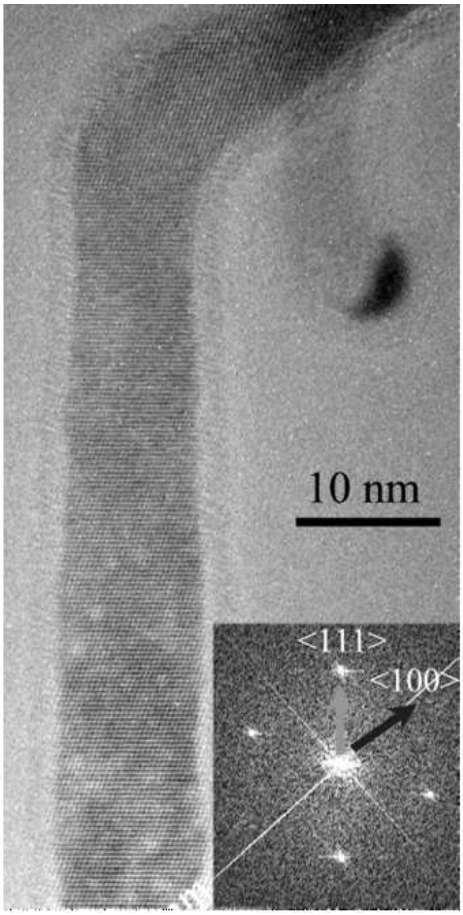

Figure 6.6: HRTEM image of a branch changing direction without a crystallographic defect. The FT is shown in the inset to illustrate the change in growth direction from $\langle 111 \rangle$ to $\langle 100 \rangle$. Samples 4913

6.3.3 Sidewall facets in Cu catalysed nanowires

In Section 5.5 an aspect of faceting was already discussed. The focus was placed on a periodic sawtooth-faceting that can be present on the nanowire sidefacet. In this section the wire sidefacets (parallel to the nanowire axis) of nanowires grown with copper (Cu) as the catalyst are described[9].

In literature it can be found that the shape of a wire section of a VLS grown silicon nanowire is a hexagon (T.Kawashima et al., 2008; Ross et al., 2005; Wu et al., 2004). For very large nanowires ($d > 300\,\mathrm{nm}$) also a dodecagonal cross section was reported (David et al., 2008) . The sidefacets of a nanowire with the $\langle 111 \rangle$ growth direction are all $\{112\}$ planes (Figure 5.13) (Ross et al., 2005). It was shown in (Wu et al., 2004) that the sidefacets of a nanowire with the $\langle 110 \rangle$ growth direction are $\{111\}$ and $\{100\}$ planes.

The wire sections were obtained as described in Section 4.4. Only a limited number of wire sections were observed. In Figure 6.7 three wire sections are visible. Interestingly two different hexagons are observed, either with two large facets and four small facets or with three large facets and three small facets, similar to (T.Kawashima et al., 2008). Both larger nanowires are growing in the $\langle 112 \rangle$ direction. The corners of the wire sections are slightly rounded, especially the smallest wire in the middle is very rounded and better described by a triangle with very rounded corners. The growth direction of this wire could not be determined.

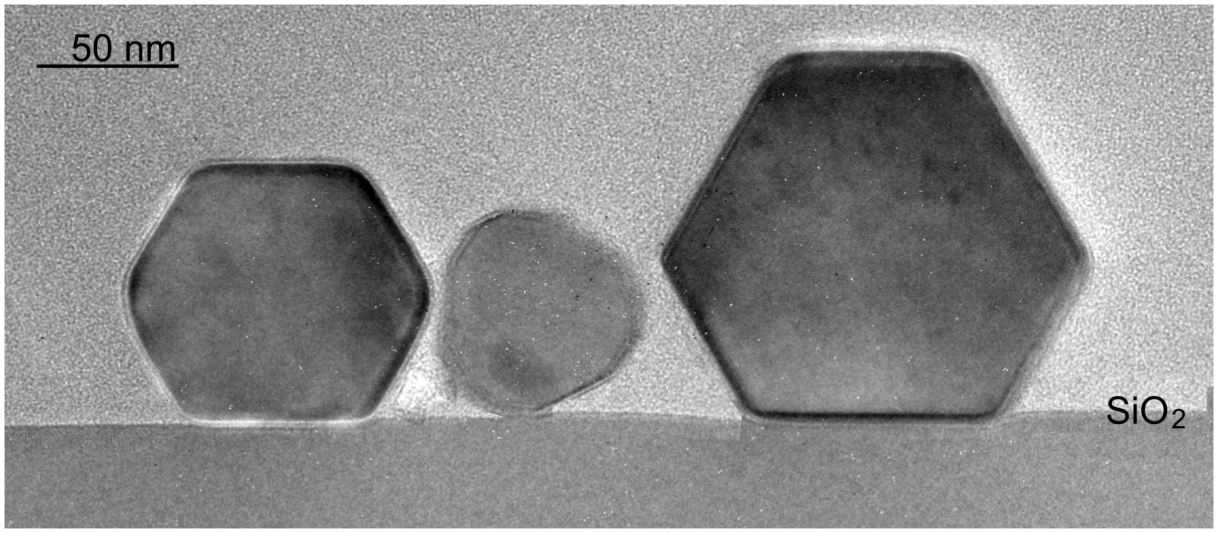

Figure 6.7: TEM BF showing three wire sections. The nanowires were grown using a Cu catalyst. Both the left and the right wire grow in the $\langle 112 \rangle$ direction. The growth direction of the thin wire in the middle could not be determined. Sample 5356

Two different growth directions were observed: the $\langle 112 \rangle$ and the $\langle 110 \rangle$ direction. Two nanowire sections were observed along the $\langle 110 \rangle$ direction, that both contained one or a series of twin defects in the middle, dividing the wire section in two symmetrical parts. The facets present for different growth directions and the angles between facets are shown in Figure 6.8. The angles between the facets were the same as expected for bulk silicon. For the $\langle 112 \rangle$ growth direction the sidewall facets are $\{111\}$ and $\{113\}$ planes. The facets were $\{111\}$ and $\{115\}$ planes for the $\langle 110 \rangle$ growth direction containing a single twin. The facets of the other wire section observed

[9] Wires with a Cu catalyst were used to test the wire section sample preparation method (Section 4.4) because the wire density on the growth substrate is high and the wires are long ($80\,\mu m$). Due to time restrictions not all nanowire growth systems could be studied along the growth direction.

along the ⟨110⟩ direction[10] appeared to be {111} and {110} planes, coherent with (Wu et al., 2004). It seems that the presence of one, or a rapid succession of vertical twins, dividing the nanowire section in two equal parts, is quite a common phenomenon for nanowires grown with a Cu catalyst.

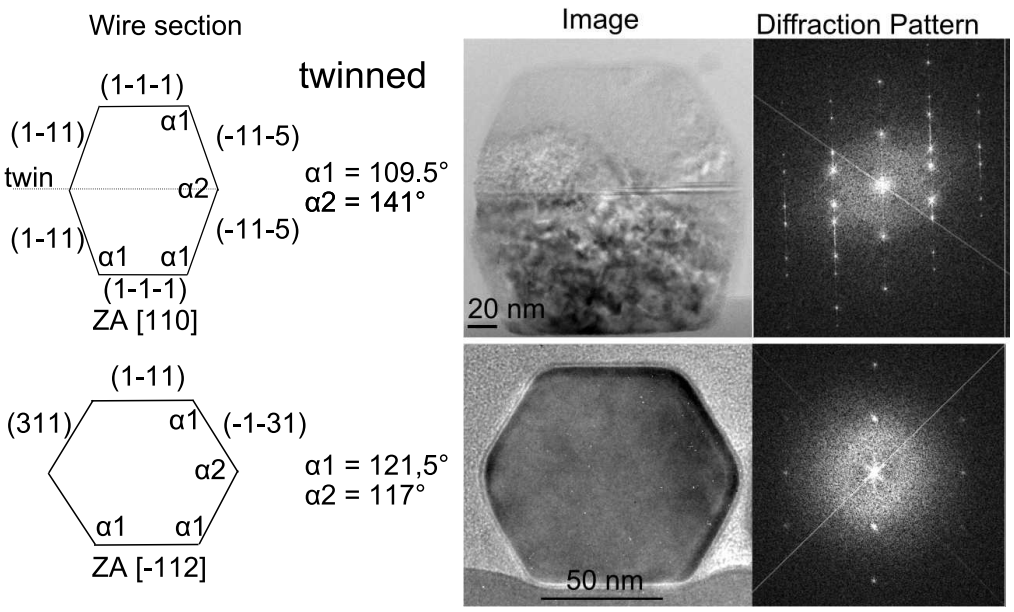

Figure 6.8: TEM BF images and schematic of the wire sections of nanowires grown using a Cu catalyst. (A) The growth direction is ⟨110⟩ and the nanowire contains a twin on a {111} plane. (B) The growth direction is ⟨112⟩. Sample 5356

[10] The wire was damaged by the sample preparation and therefore not shown.

6.4 Defects

In the study of silicon NW's, defects are of large interest. For one reason because defects can modify the electronic properties locally since the periodicity of the crystal is locally disturbed (Thibault et al., 1996) and also since defects can act as accumulation centers for impurities (Thibault et al., 1996; Blavette et al., 1999; Allen et al., 2008). Therefore defects should either be avoided or carefully controlled.

First defects that were observed in wires grown using a gold catalyst (Chapter 5) are described. Then defects will be shown that were observed if TMA was added to the growth chamber or a Ni catalyst was used.

6.4.1 Incidental defects in silicon nanowires grown with a gold catalyst

Generally the crystalline quality of the wires was high and few defects were observed.

Most observed defects were so called Σ=3 twin grain boundaries on a $\{111\}$ plane (Σ =3 indicates that 1 in 3 lattice points in both grains coincide), coherent with literature (Korgel et al., 2006; den Hertog et al., 2007; Johansson et al., 2006; Zhou and Zhang, 1998; Zhou et al., 1999; Carim et al., 2001). The energy for a twin defect is relatively low and due to the high symmetry between both grains, the electronic properties are hardly affected. Two types of twin defects were observed, being vertical and horizontal twins.

One other type of defect was observed, a 90° grain boundary, which was limited to a single observation.

In literature a vertical twin was reported (Korgel et al., 2006) (Carim et al., 2001). Similar twin defects were observed in this work, an example is shown in Figure 6.9 on the left. The Fourier Transform (FT) of both nanowires is also shown. Both grains of the twin defect on the left are indicated in the inset and indexed in the FT and the angle between two $\{111\}$ planes in grain I is indicated. For the branch on the right two spots are visible in the FT at an angle of 61° and with an interplanar spacing close to $0.31\,\mathrm{nm}$, the spacing between $\{111\}$ planes, which will be explained in detail in the next section. NWs growing in the $\langle 112\rangle$ direction often contain a vertical twin defect.

A twin defect on a $\{111\}$ plane can also be associated with a change of growth direction. In Figure 6.10[11] (den Hertog et al., 2007) this is illustrated. Large wires (diameter>50 nm) grow along $\langle 111\rangle$ directions (Schmidt et al., 2005), and can sometimes contain twins near the base, Figure 6.10A, or at a kink, Figure 6.10E. In Figure 6.10A a weak beam image of a wire is shown with a series of horizontal twin faults at the base. In Figure 6.10B a high resolution zoom is shown. The three equivalent $\langle 111\rangle$ directions are indicated for both grains: family I of equivalent $\langle 111\rangle$ directions in grey and family II of equivalent $\langle 111\rangle$ directions in black. An atomic model of the twin is shown in Figure 6.10C. In Figure 6.10D a SEM top view image is shown. Normally only 3 upward equivalent $\langle 111\rangle$ directions should be observed. The fact that 6 directions are observed can be explained by the presence of a twin at the base of the wire, Figure 6.10A, which flips the first 3 equivalent $\langle 111\rangle$ directions (family I indicated by white arrows in Figure 6.10B) to another set of 3 equivalent upward $\langle 111\rangle$ directions (family II indicated by grey arrows inFigure 6.10B). In Figure 6.10E a typical example of a kinked nanowire is shown. The kink is caused by a twin grain boundary on a $\langle 111\rangle$ plane. After the kink, growth continues in a different $\langle 111\rangle$ direction. A reconstruction of the lattice, shown in Figure 6.10E,

[11] The TEM images in A and B were made by C. Ternon

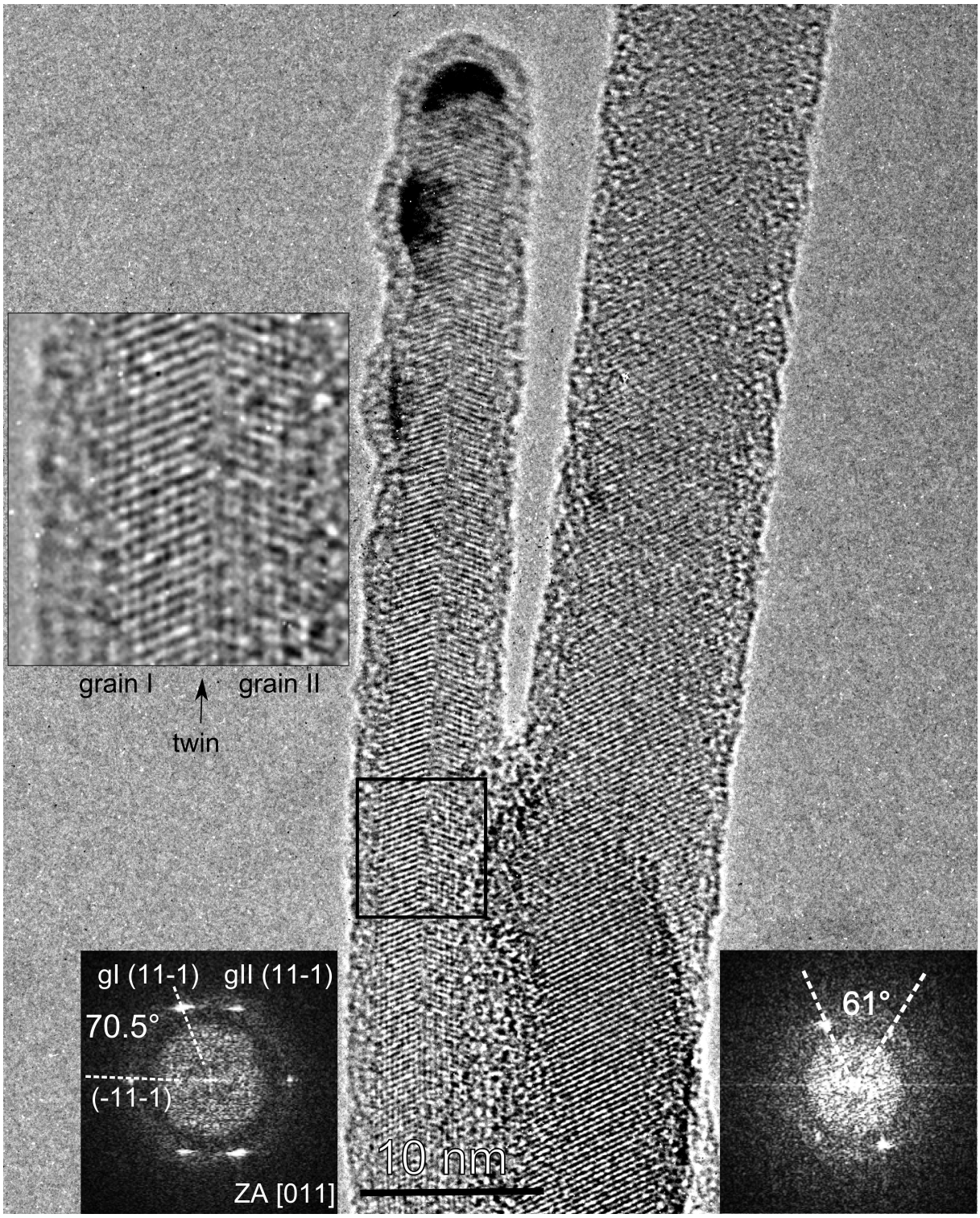

Figure 6.9: HRTEM image of a NW containing a vertical twin (left). The growth direction of the NW is ⟨112⟩. The NW is a 'branch' growing on the 'trunk' of a larger NW, similar to (Dick et al., 2004) (Nam and Fischer, 2008). The NW on the right probably contains a twin as well, that is inclined with respect to the electron beam, this situation will be described in Section 6.4.2. The angle between two families of planes is indicated in the FT. Sample 4629

demonstrates that the kink is caused by a twin fault. The three equivalent $\langle 111 \rangle$ directions are shown in grey. In Figure 6.10D the density of kinks is relatively high. Such a high kink density was observed at relatively high growth temperature (550-600 °) and low silane partial pressure ($\leq 0.13\,\mathrm{mbar}$).

Faceting caused by a regular series of twin faults was shown to be a quite common phenomenon for GaP wires (Johansson et al., 2006). Twin planes have been observed in silicon nanowires made by laser ablation (Zhou and Zhang, 1998; Zhou et al., 1999). To our knowledge, a series of horizontal twins has not been observed before in silicon nanowires controllably grown in the $\langle 111 \rangle$ direction, following the epitaxial orientation of the substrate. It is supposed that the sequence of kinks observed in Figure 6.10A-B are caused by instabilities at the beginning of growth, caused by a change in partial pressure of silane (under our growth conditions it takes five minutes to change the gas composition of the growth chamber). Clearly, the energy barrier for twin nucleation (Johansson et al., 2006) is sufficiently high in silicon, that under our growth conditions twinning is unlikely to happen, when steady state growth is accomplished. One kink was observed without a grain boundary. In this case, the kink was caused by growth along one of the three inclined $\langle 111 \rangle$ direction.

Incidentally a 90 ° grain boundary was observed Figure 6.11. This type of defect is characterized by the fact that a rotation of the first grain around the growth direction by 90 ° results in the second grain. The interface plane between both grains is either parallel to the direction of observation or slightly inclined. The $[1\bar{1}0]$ direction in the first grain is parallel to the $[00\bar{1}]$ direction of the second grain (Figure 6.11). As the ratio of the norms of these two directions is equal to $\sqrt{2}$, it is mathematically impossible to have a common period along these directions and the GB is said to be incommensurate (Lancon et al., 2000). Therefore this type of defect is also called an incommensurate$\sqrt{2}$ Si(100)/Si(0$\bar{1}$1) domain.

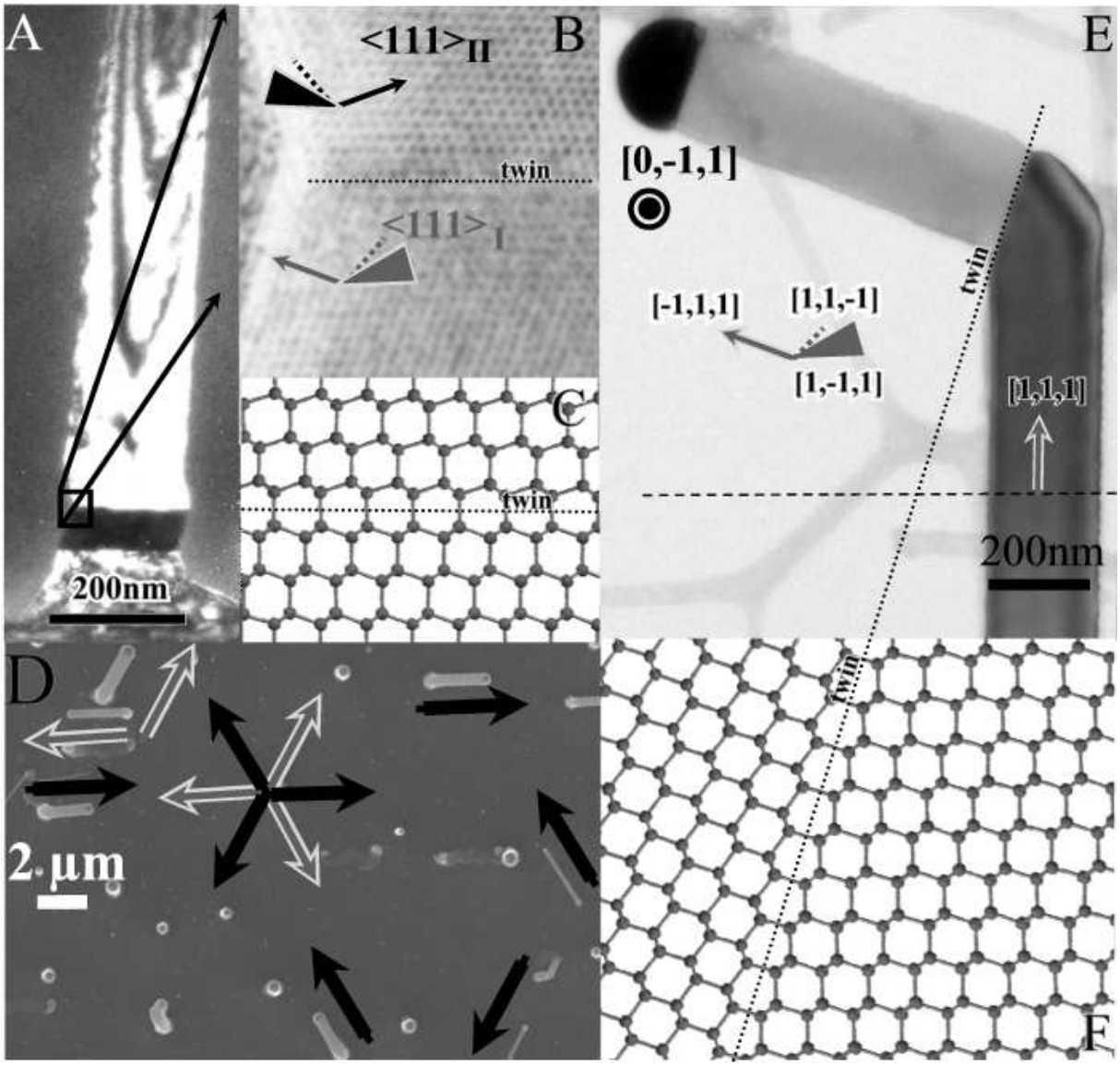

Figure 6.10: Silicon nanowires grown with a gold catalyst at 575 °C and a silane partial pressure of 0.08 mbar (A) TEM weak beam image having horizontal (111) twin faults at its base. (B) HRTEM image zooming on the fault in (a). The upward nearly horizontal {111} plane normals are represented by arrows, when they are in the plane, by triangles when the normal points out of the plane, and by dotted lines when it points into the plane. I corresponds to the upper grain, II to the lower one. (C) Atomic model of the {111} $\Sigma = 3$ defect. (D) SEM top view image showing a few kinked wires. The arrows indicate the 6 possible ⟨111⟩ directions of growth after the kink. Family I is in grey surrounded by white. Family II is in black. (E) Conventional two beam TEM image of a kinked wire. (F) Atomic model of the {111} $\Sigma = 3$ fault at the kink. Samples 4342 4255

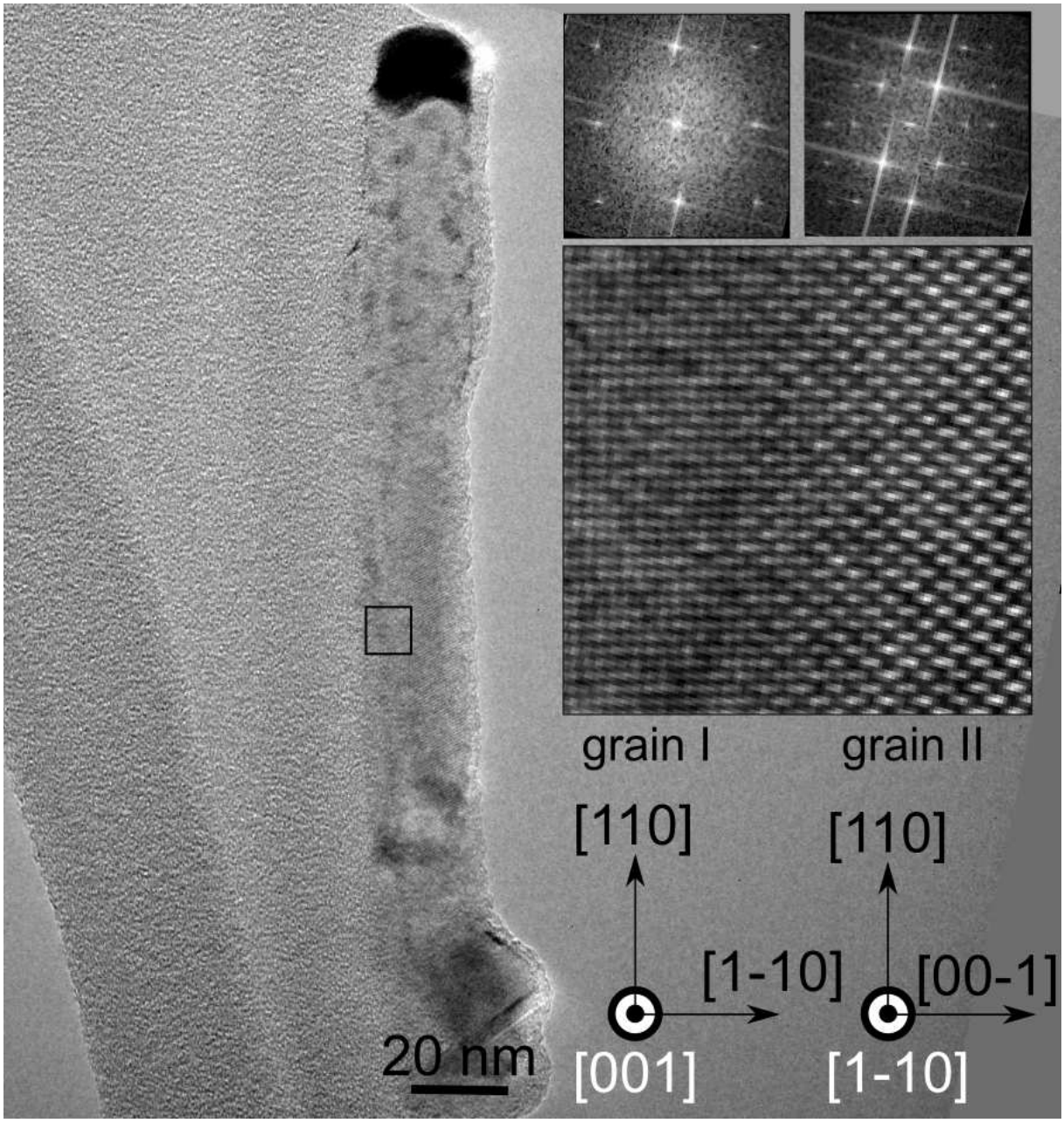

Figure 6.11: TEM image of a NW containing an 90 ° grain boundary. The growth direction is [110] for both grains however the left grain is on the [001] ZA and the right grain is on the [1-10] ZA. FT's of both grains are shown. Sample 4432

6.4.2 Recurring defects in silicon nanowires

In this section defects observed in silicon nanowires grown with a Ni catalyst and wires grown in the presence of TriMethylAlumina with gold as the catalyst are presented. It will be shown that in these wires many twins on {111} planes are found. The high defect density complicates the identification of the defects due to superposition of different crystal grains.

In silicon thin films and silicon under high pressure more than twelve forms of silicon have been reported (Wentorf and Kasper, 1963; Besson et al., 1987), among others the 2H wurtzite structure. Hexagonal structures were also found in silicon and germanium thin films deposited by laser ablation (Zhang et al., 1999a; Zhang et al., 2000) and recrystallization by an electron beam (Parsons and Hoelke, 1984). The existence of silicon polytypes was demonstrated and confirmed using x-ray diffraction (Hendriks et al., 1984), HRTEM (Dahmen et al., 1989) and Raman studies (Bandet et al., 2002). However in these studies the polytypes appear as a sequence of stacking faults and twin defects, locally ordered on a few nanometers, but no long range order on tens of nanometers exists.

Furthermore silicon NW's and cones have been reported with the hexagonal crystal structure (2H wurtzite and 6H) (Fontcuberta i Morral et al., 2007; Cao et al., 2005; Miyamoto and Hirata, 1978; Arbiol et al., 2008).

HRTEM images as shown in (Fontcuberta i Morral et al., 2007) and (Arbiol et al., 2008) were observed on NW's synthesized with a Ni catalyst and NW's with gold as the catalyst, where TMA gas was present as a dopant precursor during growth.

An example of these HRTEM images with corresponding DPs is shown in Figure 6.12. Figure 6.12A-B show the NW observed along the [011] direction with an extra period of 1 nm. Figure 6.12C-D show the NW observed along a different direction. The HRTEM/DP shows crystal planes with an interplannar spacing ~ 0.31 nm and angles between the crystal planes of 56° and 62° degrees (similar to the diffraction pattern shown in Figure 6.2E). This direction does not exist in diamond cubic silicon.

It was argued by (Fontcuberta i Morral et al., 2007; Arbiol et al., 2008) that the HRTEM/DPs shown in Figure 6.12A-D can be indexed as a 2H hexagonal structure with an error of less than 5%. A plane view was made using FIB milling on a NW catalyzed with Ni to verify this hypothesis. The sample preparation was described in Section 4.4. In Figure 6.13 STEM images of this sample are shown.

Clearly no hexagonal phase with long range order is present in this nanowire, but many twin defects and four twin variants can be observed. Most defects are present on {111} planes, however defects on {112} (Figure 6.13B) and {100} planes (Figure 6.13F) can also be observed. Also a series of defects on alternating {111} and {112} planes can mimic a defect on a {110} plane (Figure 6.13B). It is clear that when the NW is studied from the side (in a dispersion sample (Section 4.1), cross section sample (Section 4.2) or cleaved sample (Section 4.3)) the different crystal grains will superpose in the image/DP. The structure of the {112} grain boundaries seems similar to (Thibault et al., 1996). The resolution at the grain boundary is limited due to the sample thickness ($\sim 250\,\mathrm{nm}$) and amorphous surface layers due to the FIB sample preparation. Such complicated twinning in nanowires has been observed in a more elegant form in silver NW's (Chen et al., 2004), where a fivefold twin separates the wire in five equal parts. A mild form of vertical twinning was already shown in Section 6.3.3 for wires grown with Cu as the catalyst.

It might be argued that the defects are created or modified during the FIB sample preparation.

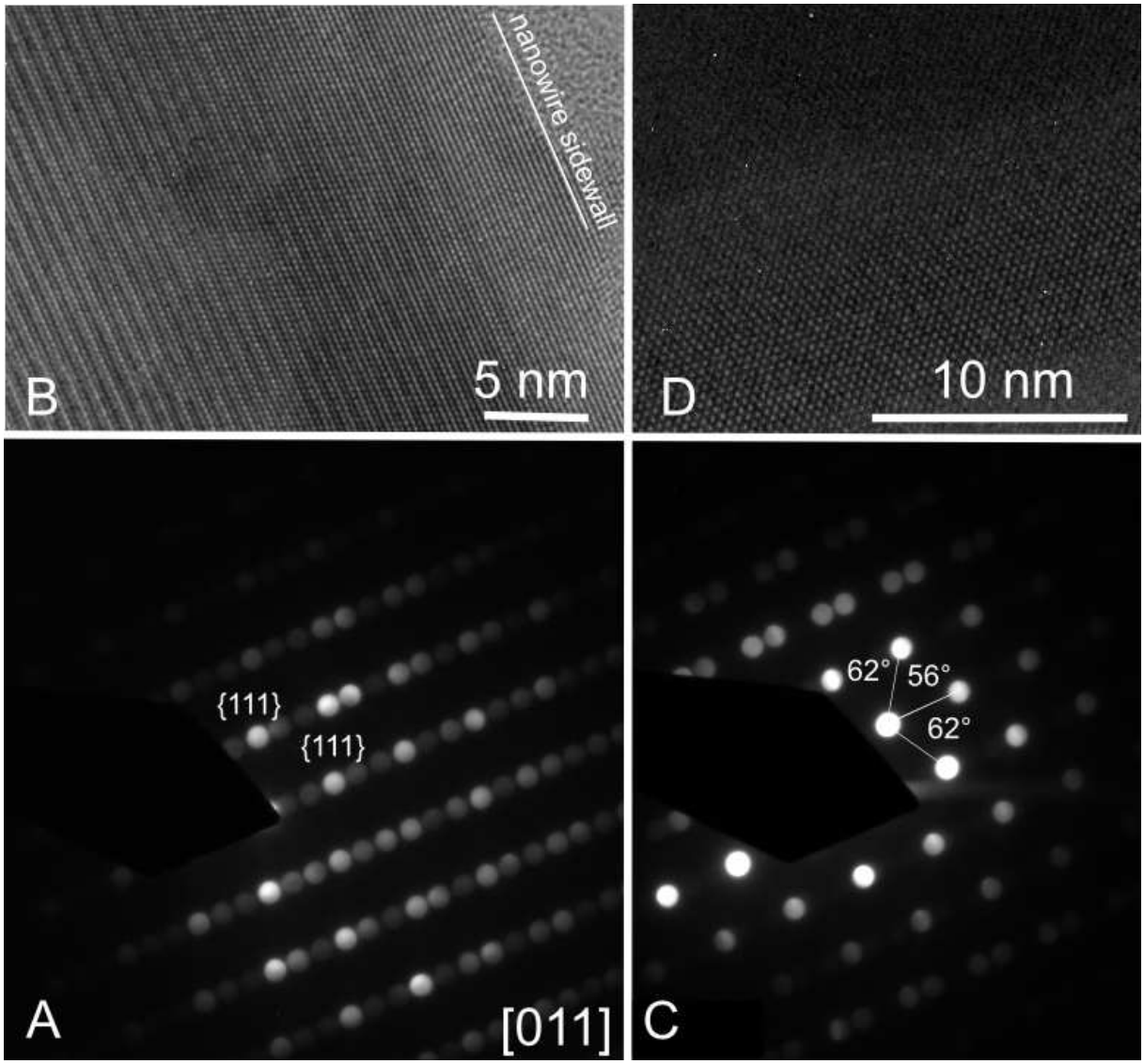

Figure 6.12: The same NW on two different ZA's. (A) Diffraction pattern of a NW on the [011] ZA, however an extra period of $\sim 1\,\text{nm}$ is present. (B) HRTEM image of the same zone. (C) DP on another ZA, the angles are indicated and the distances are close to the interplanar distance of a $\{111\}$ plane. (D) HRTEM image of the same zone. Sample 4530

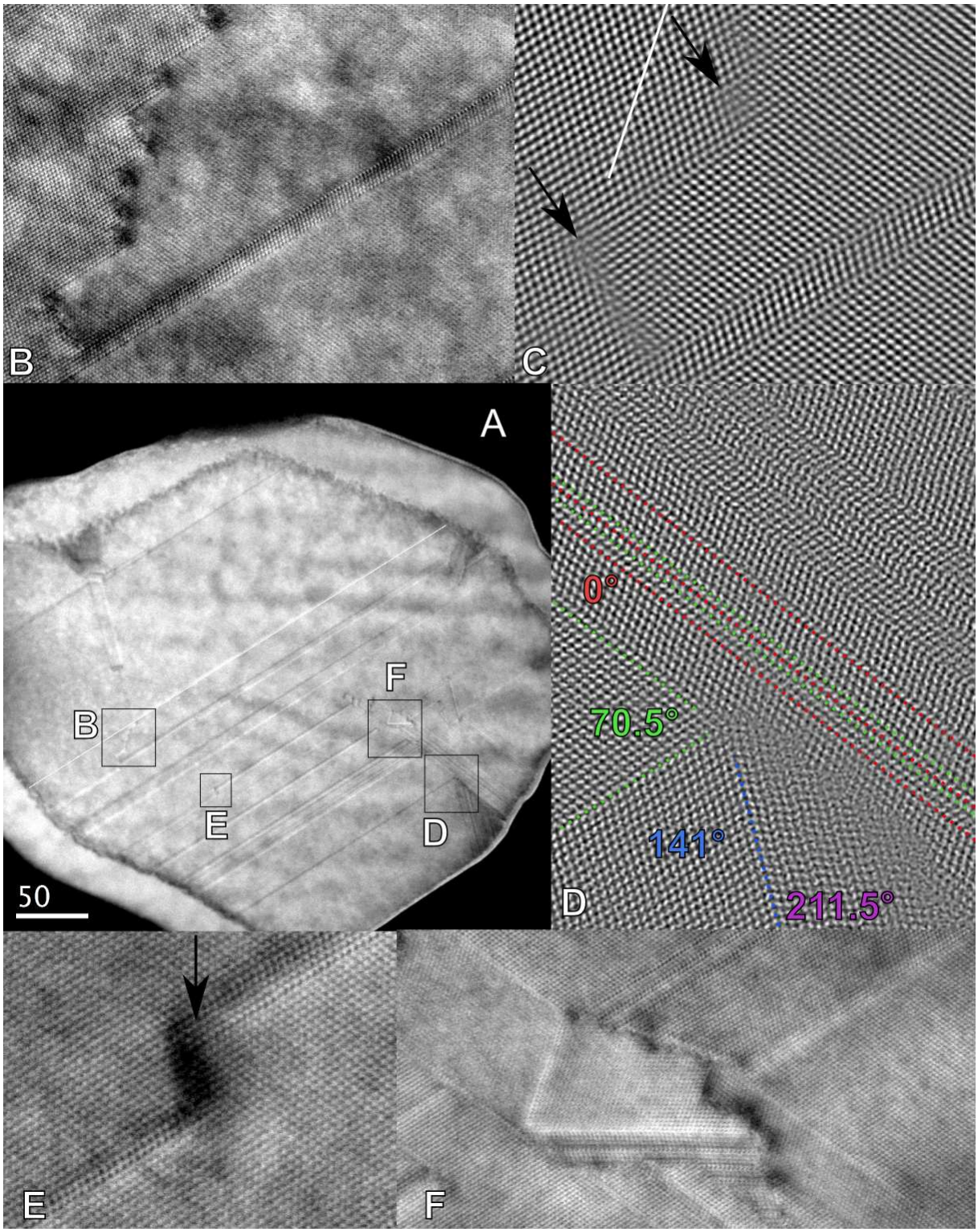

Figure 6.13: (A) bright field (BF) STEM image of a plane view of a nanowire observed along the [011] direction (grown with solid NiSi catalyst). Numerous defects can be observed. Damage due to FIB milling has formed a damaged layer of $\sim 50\,\mathrm{nm}$ around the nanowire core. (B) BF STEM Zoom of a series of alternating twin defect on $\{111\}$ and $\{112\}$ planes. (C) (Filtered) HAADF STEM zoom of the defect shown in B: the $\{112\}$ defect planes are indicated by black arrows. The $\{110\}$ plane is indicated by a white line in the left grain, showing that the series of defects can mimic a grain boundary on a $\{110\}$ plane. (D) (Filtered) HAADF STEM zoom showing 4 different twin variants. The angle between respective grains is indicated. The interface between the $0°$ tilted grain and the $211.5°$ tilted grain seems to consists of a series of point defects and dislocations. (E) BF STEM zoom showing a defect on a $\{100\}$ plane indicated by an arrow. (F) BF STEM zoom of a complicated ensemble of defects. Three twin variants can be identified as well as numerous twin defects on $\{111\}$ planes and other defects. Sample 4530

However in dark field and two beam TEM images (Figure 6.14) contrast changes already indicate the presence of defects. These images were obtained on a nanowire sample prepared by cleaving, by tilting the sample off the [110] orientation while keeping the {111} plane excited. Furthermore the FIB is regularly used for preparation of silicon samples that do not show a high twin density.

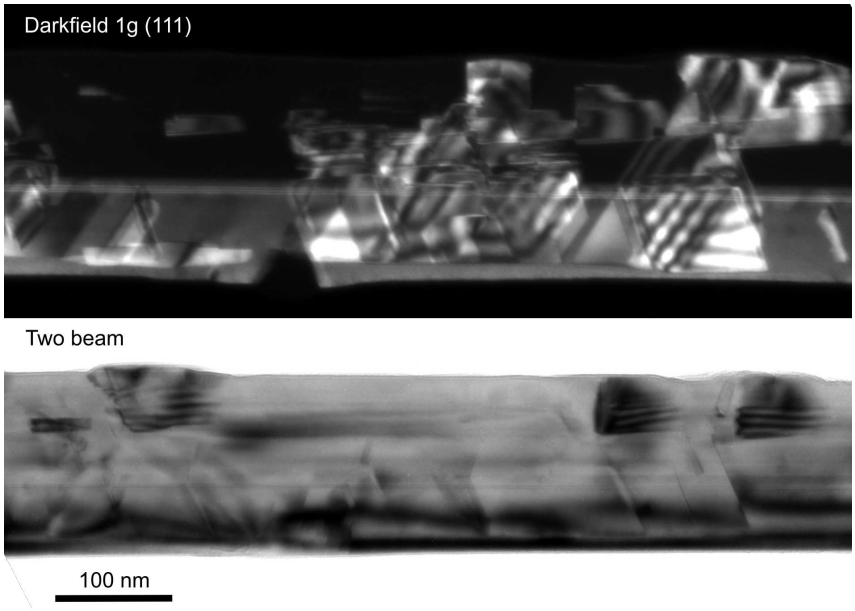

Figure 6.14: (A) Darkfield image of a nanowire grown using a Ni catalyst, made using the 1g (111) excitation. (B) Two beam image of the same nanowire. Sample 4530

The diffraction patterns and HRTEM images shown in Figure 6.13A-D can all be explained by the presence of a twin defect.

The diffraction pattern observed in Figure 6.13A is explained schematically in Figure 6.15. A [110] DP is shown corresponding to the first crystal grain (Figure 6.15A). The second crystal grain is rotated over 70.5° around [110] with respect to the first grain due to a twin defect and creates a rotated [110] DP (Figure 6.15B). An overlay of the combined DPs on the experimental data shows that some spots are explained, however the spatial frequency of 3 times the {111} interplanar distance is not explained. In Figure 6.15D an atomic model of a twin defect on a {111} plane is shown. If these two crystal grains are superposed Figure 6.15E is obtained and a spatial frequency 3 times the {111} interplanar distance appears. What we have just shown is that indeed two grains separated by a twin boundary have a coincidence lattice of one in three lattice points, which is why a twin defect is also called a $\Sigma = 3$ grain boundary.

The schematics in Figure 6.15F-G illustrate how the two crystal grains could superpose. In Figure 6.15F a top view of the $[\bar{1}12]$ oriented wire section is shown. If the two twin defects on {111} planes do not extend entirely to the other side of the wire, the [110] DP is a superposition of grain I and II. The four $\langle 111 \rangle$ directions are indicated (Figure 6.15F) to show no other {111} plane is contained in the growth direction. Therefore the interface between the two grains could be a (110) plane, it is also possible that this interface contains steps or facets in the growth direction, as shown schematically in Figure 6.15G, where the wire is observed from the side.

If the nanowire grows in the $\langle 110 \rangle$ direction (for example the wire in Figure 6.13), superposition of two grains can be caused by twin defects only on {111} planes, because two {111} planes are contained in the growth direction.

Multislice simulations of HRTEM images were performed using JEMS (Stadelmann, 2008) to

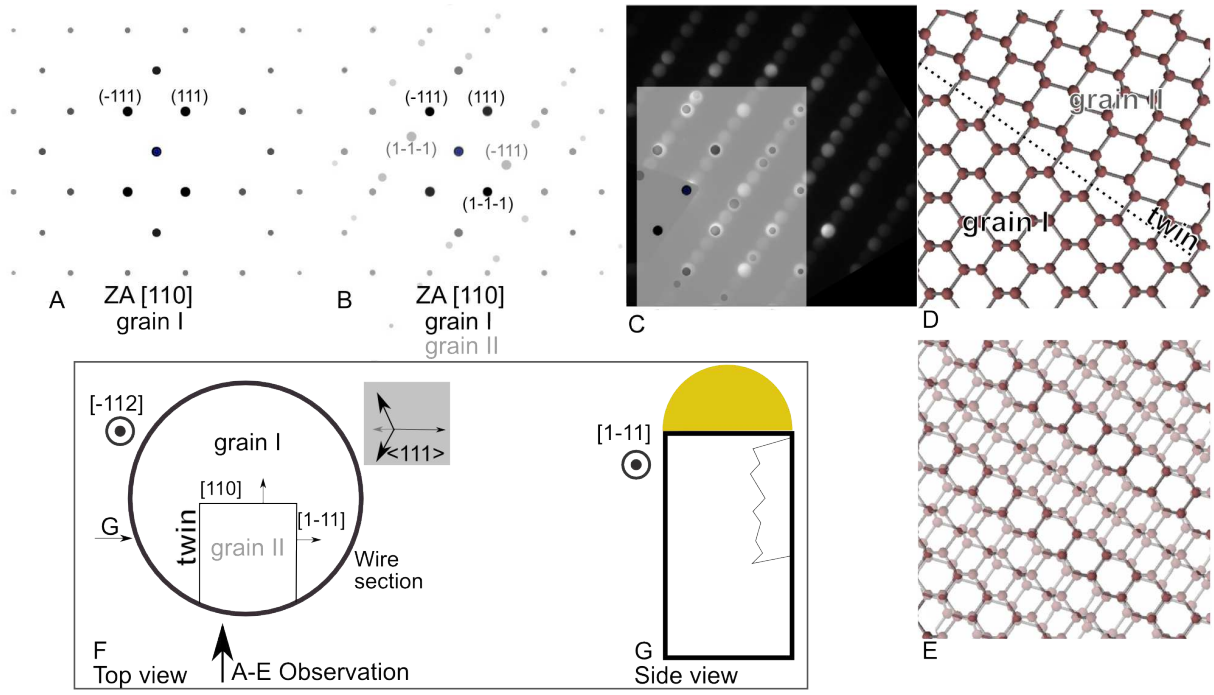

Figure 6.15: (A) [110] DP of grain I. (B) [110] DP of grain I and grain II, that is rotated 70.5 ° around [110] with respect to grain I. (C) Both DPs overlaid on an experimental DP. (D) Atomic model of a twin boundary with grain I and grain II. (E) Overlay of the crystal grains I and II shown in (d) shows a spatial frequency of 3 times the {111} interplanar distance. (F) Top view. Schematic of a wire section on the $[\bar{1}12]$ ZA, which is the growth direction. The interface plane between both grains can be near a (110) plane, but might contain steps or facets. The four $\langle 111 \rangle$ directions are indicated for this orientation, to illustrate that only one {111} plane is present parallel to the nanowire growth direction. (G) Side view of the wire as indicated in (f) on the $[1\bar{1}1]$ ZA. The interface seen from this direction might contain steps and facets caused by defects on alternating planes, for example {112} and {111} planes.

allow comparison with the HRTEM image in Figure 6.12B. In the simulation the twin defect is placed on the {110} plane perpendicular to the direction of observation. In Figure 6.16A-B two TEM images of regions with odd contrast are shown and compared to JEMS multislice simulations (Figure 6.16C-G). The spatial frequency of 3 times the {111} interplanar distance, that was already observed in the diffraction pattern (Figure 6.15) is also clearly observed in the HRTEM simulations. The multislice simulations were performed at Scherzer defocus and two other focus values. The complete crystal thickness was between 50 and 60 nm. The plane wave first propagated through a crystal thickness $t1$, followed by the twinned crystal with a thickness $t2$. The TEM image in Figure 6.16A would correspond best to the simulations in Figure 6.16F at Scherzer defocus (as shown in the inset in Figure 6.16A) and the TEM image in Figure 6.16B resembles the simulation in Figure 6.16D at Scherzer defocus (as shown in the inset in Figure 6.16B). Also in STEM a similar moiré pattern is observed (Figure 6.17).

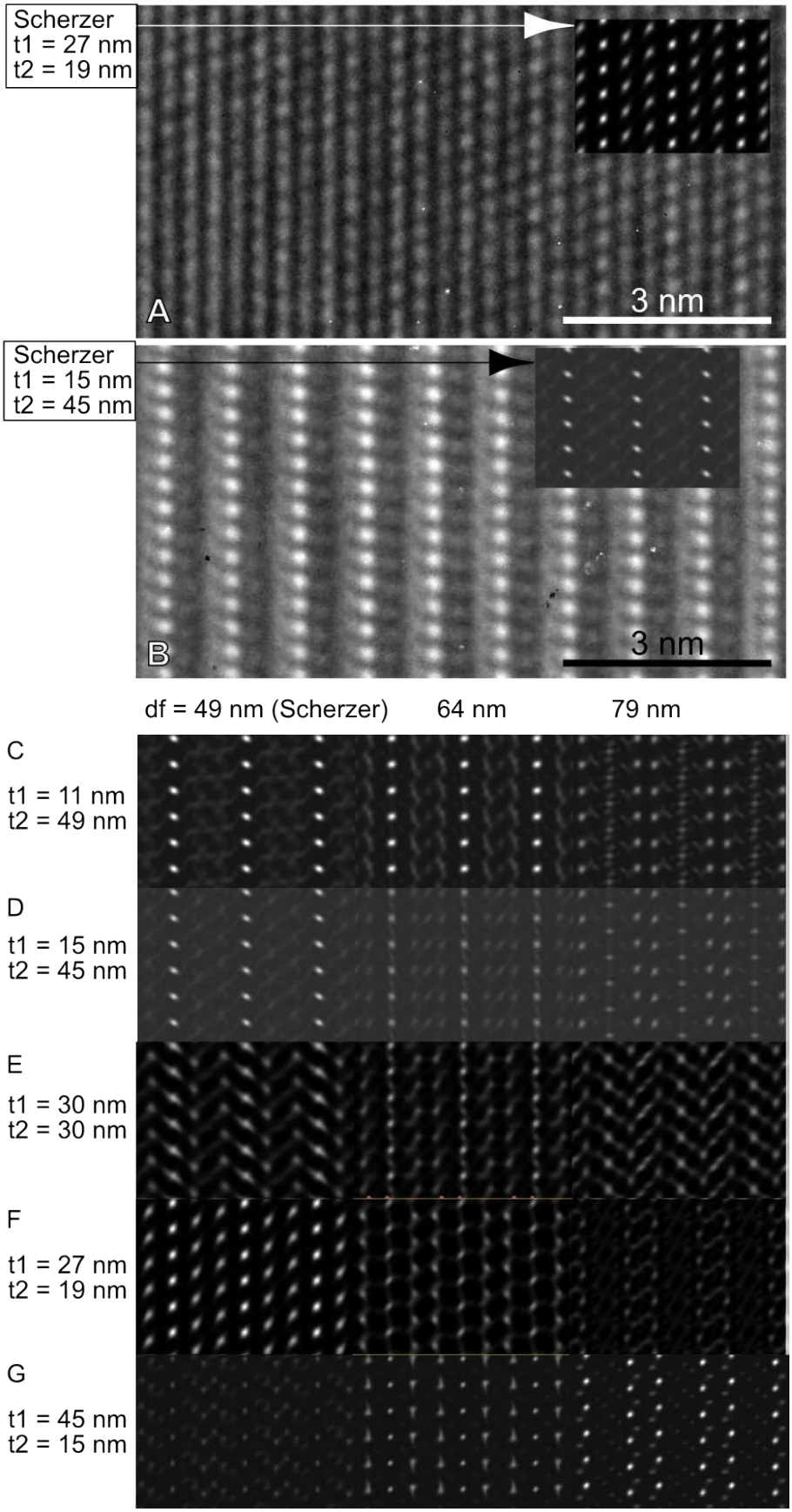

Figure 6.16: (A-B) HRTEM images of a defect zone on the [110] ZA, acquired on the JEOL 4000 EX. The best match with simulation is shown in the inset. (D-G) Multislice simulations of two superposed crystal grains related by a twin defect placed on a {110} plane. The thickness of both crystal grains was varied and three different defocus values as indicated were used. The total crystal thickness was between 50 and 60 nm. The characteristics of the JEOL 4000 EX were included in the simulations. Sample 4967

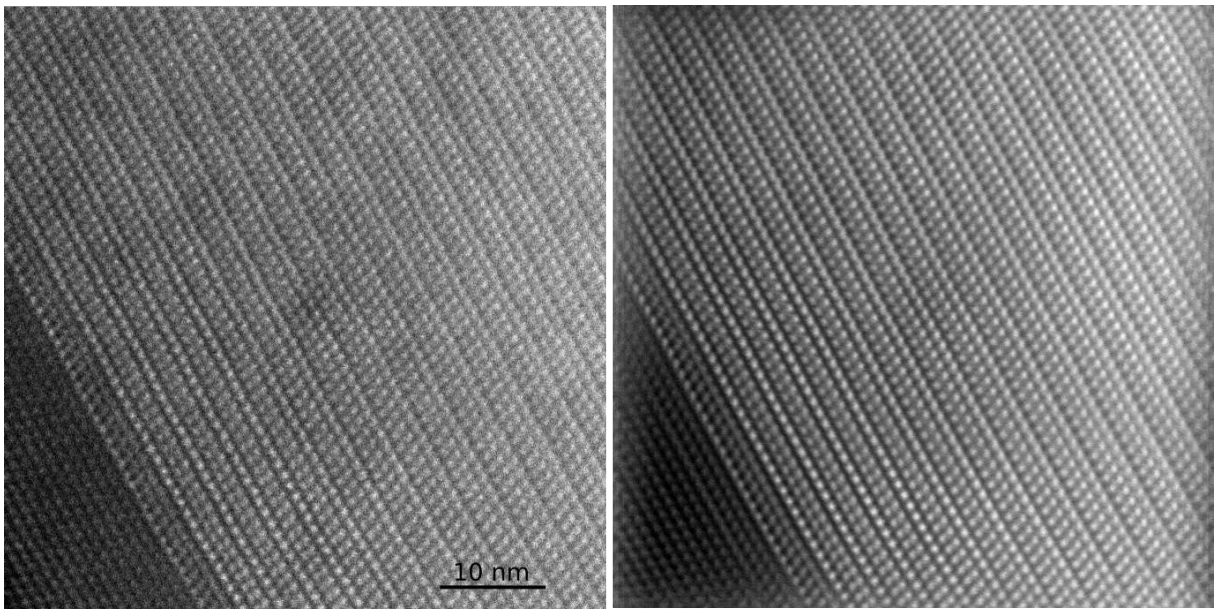

Figure 6.17: HAADF STEM image of the defect also shown in Figure 6.12B. On the left the original image, on the right a filtered image. A similar beat frequency or moiré, as observed in TEM images (Figure 6.16) is visible. Sample 4530

The DPs in Figure 6.12C and Figure 6.2E are also explained by superposition of two crystal grains, which is illustrated schematically in Figure 6.18.

The matrices representing the transformations from a primary cubic crystal into its four $\Sigma 3$ variants as given by (Cayron, 2007)[12]

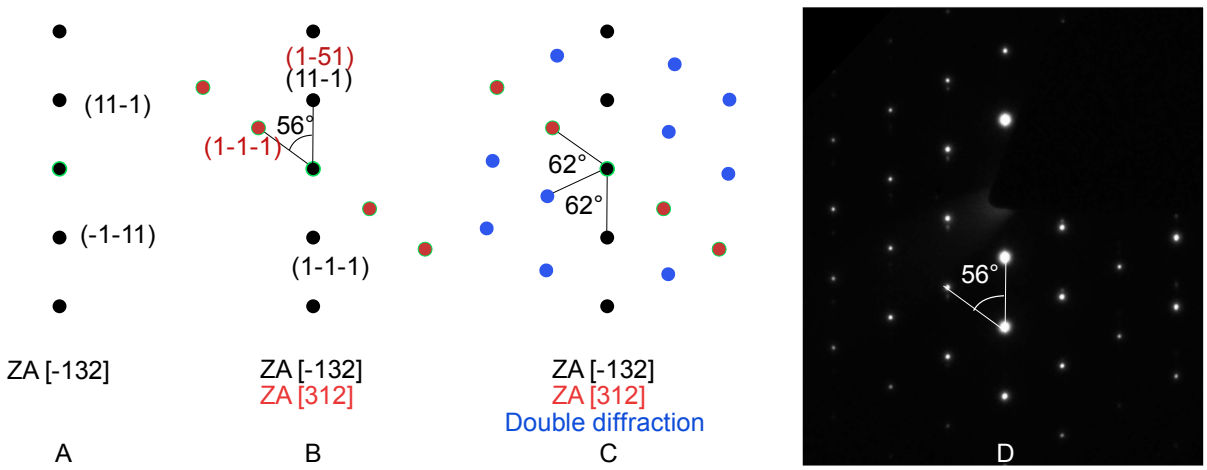

Figure 6.18: (A) The diffraction spots of {111} planes in the first crystal grain on the $[\bar{1}32]$ ZA. (B) The diffraction spots of {111} planes in the first grain (black) and the diffraction spots of {111} planes in the second twinned grain (red), that is on the [312] ZA. The angle between the diffracting {111} planes in respective grains is $56°$. (C) A third row of diffraction spots (blue) is caused by dynamical diffraction. (D) Experimental diffraction pattern.

[12] It should be noted that in (Cayron, 2007) the transposed of the presented matrices are given.

$$T_0 = \frac{1}{3}\begin{pmatrix} 1 & -2 & -2 \\ -2 & 1 & -2 \\ -2 & -2 & 1 \end{pmatrix} \qquad T_1 = \frac{1}{3}\begin{pmatrix} 1 & 2 & 2 \\ -2 & -1 & 2 \\ -2 & 2 & -1 \end{pmatrix} \tag{6.2}$$

$$T_2 = \frac{1}{3}\begin{pmatrix} -1 & -2 & 2 \\ 2 & 1 & 2 \\ 2 & -2 & -1 \end{pmatrix} \qquad T_3 = \frac{1}{3}\begin{pmatrix} -1 & 2 & 2 \\ 2 & -1 & -2 \\ 2 & 2 & 1 \end{pmatrix} \tag{6.3}$$

can be used to calculate the orientation of the second twinned crystal with respect to the first grain.

The first crystal is observed along the $[-1, 3, 2]$ direction Figure 6.18A). Using the transformation matrices it is found that the second crystal is observed either along the $1/3[\bar{1}1, 1, \bar{2}]$, [3,1,2], $1/3[\bar{1}, 5, \bar{1}0]$ or $1/3[11, \bar{9}, 6]$ direction.

We suppose the second grain is observed along the [3,1,2] direction. Using the matrix $T1$ (Equation (6.2)), the $(11\bar{1})$ plane in the first grain can be calculated to be the $1/3(1, \bar{5}, 1)$ plane in the second grain . The angle between the $(1\bar{5}1)$ plane and the $(1\bar{1}\bar{1})$ plane in the second grain is $56°$ (Figure 6.18B), which is exactly the experimentally observed value (see Figure 6.12C and Figure 6.18D). The diffraction pattern can therefore be interpreted as a superposition of two diffracting grains. The third row of diffraction spots is created by double diffraction in the two superposed grains (Figure 6.18C).

This superposition occurs if both grains are $\langle 123 \rangle$ oriented. This kind of HRTEM images/DPs created by the presence of a twin and superposition of two crystal grains were already observed for gold nanoparticles (Buffat et al., 1992).

These results are coherent with literature where odd diffraction patterns (DPs)[13] obtained on thin silicon and gold films and silicon nanowires have been attributed to double diffraction between superposed twinned crystals (Dickson and Pashley, 1962; Pashley and Stowell, 1963; Carim et al., 2001; Buffat et al., 1992). In addition to this explanation some of the diffraction spots have been attributed to streaking effects caused by very thin defect sequences (Kohno et al., 2003). A very thin crystal grain bounded by defects will diffract as a very thin sample with a consequently very long reciprocal lattice rod that easily intersects with the Ewald sphere and creates a streaking effect. For very thin samples of fcc films it has been proposed that at the surface the ABCABC cubic stacking is incomplete, therefore some of the crystal can be described by the 2H wurtzite phase, creating extra diffraction spots (Cherns, 1974). This idea was also used for nanowires (Korgel et al., 2006).

It was shown that the presence of twin defects can create anomalous diffraction patterns. A complete study of the twin defect rich nanowires viewed at many different ZA's, compared to simulations, is presented in (Cayron et al., 2009). It is shown that indeed a 12H hexagonal structure could explain many different DPs, however only the presence of twin defects can explain all the experimentally observed diffraction patterns[14].

[13] These DPs are called odd because they cannot be explained by diffraction on the perfect crystal of the diamond cubic structure (for silicon) or face centered cubic structure (for gold).

[14] A distinction is made between micro and nano-twins. As the crystal grain of a nano-twin is only several atomic planes thick, its associated reciprocal lattice rod is very long, and will cut the Ewald sphere at a large range of tilt angles. This effect creates extra diffraction spots that are relatively insensitive to the tilt angle.

6.4.3 Raman analysis

In (Fontcuberta i Morral et al., 2007) Raman analysis was used as evidence that the crystal structure of the nanowires was the 2H hexagonal wurtzite structure and not diamond cubic. Indeed it has been shown in literature that the Raman spectrum of the silicon wurtzite structure contains a peak around 503-506 cm^{-1} (Zhang et al., 1999b; Bandet et al., 2002; Prades et al., 2007), whereas this peak is found at 520 cm^{-1} in normal diamond cubic silicon, since the phonon resonance frequency depends on the crystal structure.

For this reason Raman spectra were obtained on the nanowires grown with a Ni catalyst. The nanowires were either dispersed on a glass microscope slide (Section 4.1) or a silicon nanowire TEM sample prepared by cleaving (Section 4.3) was used.

Raman experiments were realized on an InVia Renishaw spectrometer allowing measurements in the visible and the near Infra-Red spectral ranges, equipped with an air-cooled CCD detector, a microscope, and a 50 (NA = 0.95) objective. Raman spectra were obtained using the 514,5 nm line of an Argon-Krypton ion laser resulting in a probe size diameter of around 1 μm.[15]

The majority of the wires showed a Raman spectrum similar to that of silicon with the diamond cubic structure. However in some rare cases a vibrational mode was observed at 517 cm^{-1}, 510 cm^{-1} and 504 cm^{-1}. In this last case the spectra obtained on the extremities and middle of the nanowire were different (Figure 6.19). At one end the vibrational mode was relatively broad and observed around 484 cm^{-1}, which could be attributed to amorphous silicon (Iqbal and Veprek, 1982). In the middle a peak at 504 cm^{-1} was observed, whereas the other wire extremity showed a peak close to the value of diamond cubic silicon (519 cm^{-1}). Since all TEM evidence (as presented in the previous section) suggests that no other crystal structure than diamond cubic silicon was present, a possible explanation is that a series of defects can mimic locally an hexagonal crystal structure and correspondingly cause a shifted Raman signal around 503-506 cm^{-1}. However a long range order of this crystal structure is absent. Indeed it can be observed in Figure 6.13D that at a scale of several atomic planes hexagonal crystal structures can be present due to the high twin density.

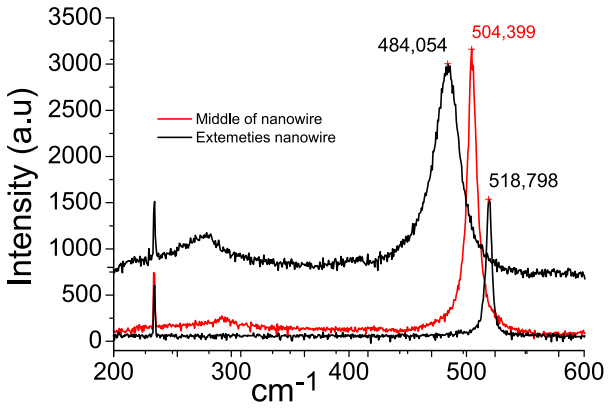

Figure 6.19: Example of three Raman spectra made on the same nanowire in the middle and on both ends of the nanowire. Sample 4530

[15] Raman spectra were obtained in the group of Michel Mermoux (LEPMI, CNRS-INPG-UJF, BP75, 38402 Saint Martin d'Hères cedex, France) with the help of Eddy Romain-Latu (LETI, Grenoble) and Dennis Rouchon (LETI, Grenoble).

6.4.4 Cause for twins?

Clearly the twin density can be different from one nanowire sample to the next. What can cause this difference? It is suspected that the twin probability depends on the quantity of impurities. For example it has been shown that twinning can be induced during MBE (Molecular Beam Epitaxy) growth by deposition of submonolayer quantities of boron (Fissel et al., 2006)[16].

The nanowire sample grown in the presence of TMA was analyzed using EDX (Section 3.4) to see if a detectable quantity of Alumina would be present in the nanowires, that could in principle cause the high defect density. In Figure 6.20 the results of the EDX analysis are shown. Using the automatic EDX quantification software present in TIA (by FEI) the aluminum concentration in the catalyst was found to be between 4 and 9 at.% [17]. In the nanowire hardly any signal of Al was present. In some spectra (Figure 6.20) a very small peak could be observed at the Al position, however the signal is not sufficiently strong to clearly distinct it from the noise. Therefore it seems that the alumina content in the nanowire is below the detection limit of the technique and < 1 at. %.

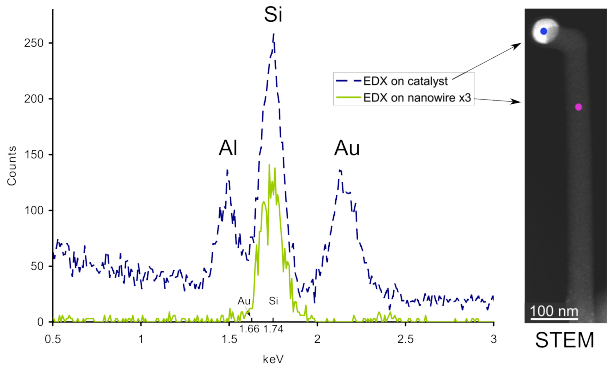

Figure 6.20: EDX spectra made on the gold catalyst particle and on the nanowire. An alumina signal can be detected in the catalyst particle, but not in the nanowire. Sample 4967

6.4.5 Are Cu, Pt or Ni promising catalyst materials?

So far mostly HRTEM images were shown, either to determine the growth direction or show the presence of defects. Ni, Cu and Pt were tested as catalyst materials to see if good control over nanowire dimensions, surface properties and growth direction can be combined with a high crystalline quality, and because these metals are a bit more compatible with microelectronics applications than gold.

In this section some more observations are shown of these nanowire growth systems to evaluate if these are promising catalyst materials. SEM images of a large number of nanowires are shown, to illustrate the efficiency of a catalyst in terms of nanowire density and length.

In Figure 6.21A a SEM image of wires grown with a Cu catalyst are shown. The diameter dispersion is relatively small, the wire density is high and most wires are straight and long. Near the growth substrate surface a dense and chaotic layer of nanowires is visible.

[16] Alumina is directly below boron in the periodic table of elements, for this reason the electronic structure of both elements is relatively similar and might cause a similar reaction.

[17] In this particular spectrum the Al concentration was determined to be 28 at.%, which seems not coherent with the rest of the data. Without the use of a reference sample these measurements are not quantitative but merely indicate an approximate concentration.

In Figure 6.21B a SEM image of nanowires grown with a Pt catalyst is shown grown on a $\langle 001 \rangle$ oriented silicon substrate. These nanowires are relatively short and thick with respect to the wires grown with a Cu catalyst. The nanowires have a conical shape and sometimes change growth direction. One favourized growth direction seems to be present, but also other growth directions can be observed. The angles of the $\langle 011 \rangle$, $\langle 111 \rangle$ and $\langle 125 \rangle$ direction with the substrate normal $\langle 001 \rangle$ are indicated. Since the SEM image is made at an unknown angle with respect to the substrate, the observed favourized growth direction could be either an $\langle 011 \rangle$ or $\langle 111 \rangle$ direction. TEM measurements did not show a particularly favourized growth direction.

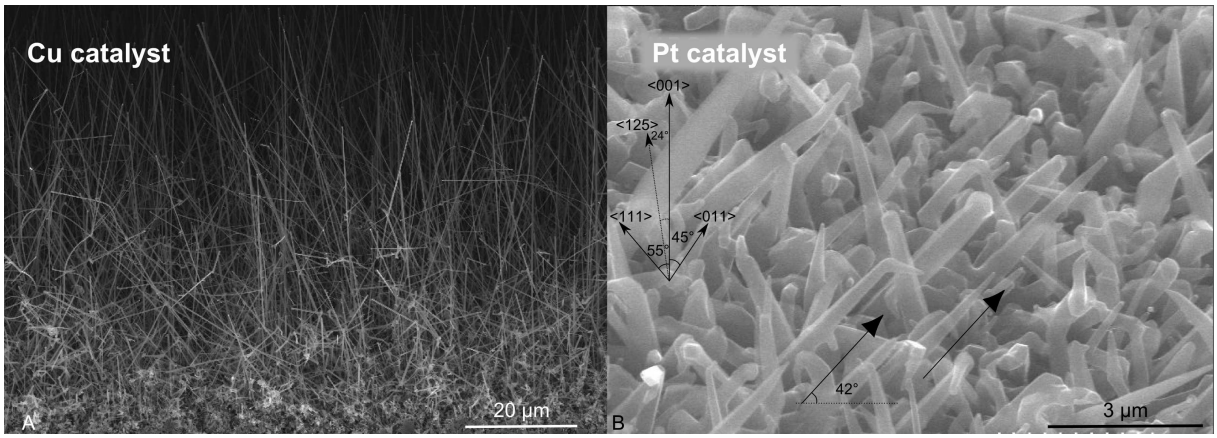

Figure 6.21: SEM image of nanowire grown with (A) a Cu catalyst on a silicon $\langle 111 \rangle$ substrate, and (B) a Pt catalyst on a silicon $\langle 100 \rangle$ substrate. Samples 5356 4454

The observed nanowire's grown with a Ni catalyst contain an impressive amount of twin defects (Figure 6.13). In metals and alloys the mechanical properties can be changed and improved by tuning of the defect density (Watanabe, 1985). In semiconductor nanowires a remarkable control over horizontal twinning was shown recently for InP and GaP nanowires that allows growth of twinning superlattices. The periodicity of the twins can be tuned using temperature, nanowire diameter (Caroff et al., 2008) and impurity dopants (Algra et al., 2008). Twinned superlattices can be used to tune the electronic and thermoelectric properties of the nanowire due to phonon scattering on the superlattice.

However in silicon nanowires grown with a Ni catalyst no control over twin boundary formation was observed. Therefore Ni does not seem a promising catalyst material, as the twin defect density cannot be controlled. Furthermore the Ni nanowires did not grow in epitaxy with the (100) silicon substrate (see Figure 6.22) and the nanowire density was low. In Figure 6.23 a SEM image of an ensemble of nanowires grown with Ni as the catalyst is shown, it seems that wires are growing in all directions, regardless of the substrate orientation. Few straight and long nanowires are observed on a background of short and bended nano-objects.

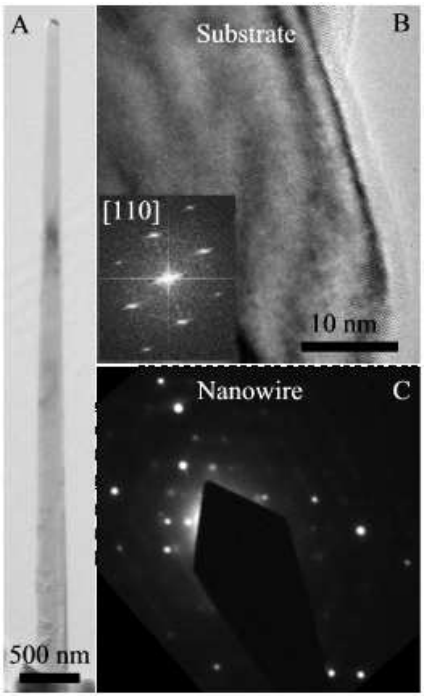

Figure 6.22: TEM images and DP to illustrate that nanowires grown with a Ni catalyst are not in epitaxy with the silicon substrate. (A) BF TEM image of a nanowire. (B) HR TEM image of the substrate and the corresponding FT. The substrate is on the [110] ZA. (C) DP pattern obtained on the nanowire (at the same tilt settings). Clearly the orientation of the substrate and the nanowire are different, which means that the nanowire was not grown in epitaxy with the substrate. Sample 4530

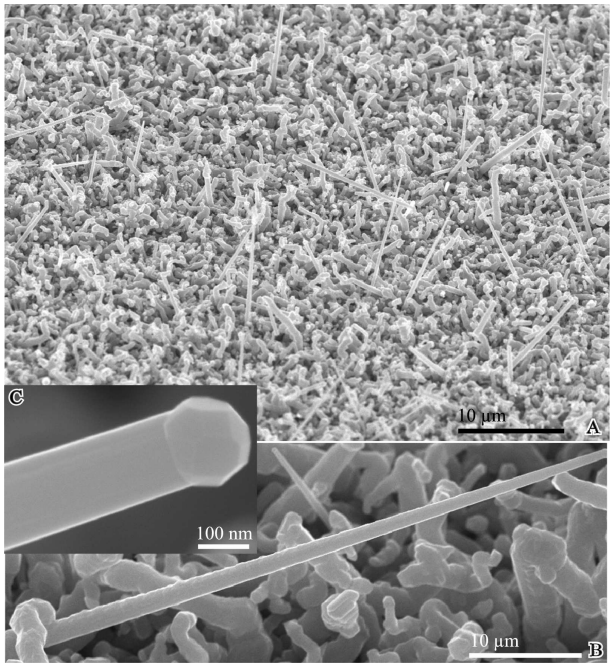

Figure 6.23: SEM images of nanowires grown with a Ni catalyst. (A) Global view of the sample. (B) Zoom of a nanowire.(C) Zoom of the catalyst particle showing facets. Sample 4530

6.5 Conclusion

In this chapter a synthesis of all observed defects and crystallographic characterizations was reported. Parts of this synthesis are rather catalog-like, however it seemed valuable to leave a trace of these observations. Here a summary of these observations is presented.

In the observed silicon nanowires three favourised growth directions ($\langle 111 \rangle$, $\langle 110 \rangle$ and $\langle 112 \rangle$) have been observed, coherent with literature (Schmidt et al., 2005). However the $\langle 112 \rangle$ direction was also frequently observed in relatively large nanowires (diameter$>$100 nm), generally if vertical defects were present.

Nanowires grown with a gold catalyst in a matrix of nanoporous alumina grow in the direction of the pores. The $\{111\}$ plane is the growth plane, that can be different from the growth direction. In nanowires grown with a Pt catalyst one wire was observed to grow in the $[\bar{5}12]$ direction. Nanotrees grown with a gold catalyst in combination with TMA grow in the $\langle 111 \rangle$ direction as well as the branches.

In nanowires grown with a Ni catalyst and with a gold catalyst in combination with TMA, many vertical twin defects are present, as observed in an FIB prepared wire section sample. Therefore the different grains can superpose in the TEM image/DP, which can be falsely interpreted as a wurtzite hexagonal crystal structure. Clear evidence shows that in the observed nanowires no hexagonal phase (with long range order) was present, but a high twin defect density can mimic a hexagonal structure on a length of a few atomic planes.

In this chapter several different nanowire growth systems were studied with the aim to achieve better control over nanowire dimensions, surface properties, growth direction and doping, combined with a high crystalline quality, and to avoid contamination due to the gold catalyst ((Allen et al., 2008; Hannon et al., 2006)). Of the tested catalyst materials (Cu, Ni, and Pt), only Cu seems relatively promising since a high density of straight and long nanowires can be obtained with a small diameter dispersion.

A gold catalyst in combination with TMA[18] or diphosphine[19] was used to p- or n-dope the nanowires. The aluminum doping was activated only if the sample was annealed at 800 °C and no junctions could be grown. Using diphosphine n-doped regions could be grown, that create p^- - n^+ junctions (the intrinsic silicon is slightly p-type). In the next chapter active dopant detection is presented in nanowires with modulated doping.

[18] Grown at CEA Grenoble.
[19] Grown at IBM Zurich.

7

ELECTRON HOLOGRAPHY

In this chapter the experimental results using off-axis holography (see Section 3.8) obtained on nanowires with axially modulated doping and intrinsic nanowires are described and compared to potential simulations.

We show that active dopants can be detected quantitatively in silicon nanowires as well as the position of the junction. Charges at the wire-oxide interface have a large influence on the measured potential and can be estimated by comparison of experimental data with simulations. Also the abruptness of the junction can be estimated. Phase modulations in the vacuum at the side of the nanowire, so-called fringing fields, were observed and compared to simulations.

7.1 Experimental details

Two types of nanowires have been studied using electron holography: undoped nanowires (growth is described in Section 5.2 and Section 6.2 in the presence of TMA) and two samples of nanowires with axially modulated doping, called hereafter sample A and B[1].

The SiNWs on sample A contained five 200-nm-long n-doped segments (10^{20} at. cm^{-3}) separated by equally long intrinsic regions (Figure 7.1A). In this sample gold clusters were present predominantly on the doped regions and small thickness changes could sometimes be observed at the junctions.

The SiNWs on sample B were grown epitaxially on a lightly doped (10^{15} at. cm^{-3} p-type) $\langle 111 \rangle$ silicon wafer and contained three 150 nm long n-doped (phosphorus) regions with N_D of 10^{20}, 10^{19} and 10^{18} at. cm^{-3} separated by intrinsic segments (Figure 7.1B). All doping concentrations were determined from electrical transport measurements on individual homogenously doped wires for each respective carrier concentration (Björk et al., 2009). In sample B, a uniform distribution of small gold clusters was present everywhere on the SiNW surface and no abrupt thickness changes at the junction were observed.

The diameter of the nanowires was 56-63 nm. Both SiNW samples were studied with the native oxide (3 nm) left on the surface.

The doped silicon nanowires were grown using the vapor-liquid-solid mechanism in a cold

[1] The studied unnanowires were grown by Florian Dhalluin (CNRS UMR 5129), Fabrice Oehler (CEA/DSM/INAC/SP2M/SINAPS) and Pascal Gentile (CEA/DSM/INAC/SP2M/SINAPS), Grenoble. The nanowires containing doped segments were grown by Heinz Schmid (IBM Zurich).

wall chemical vapor deposition tool using Au metal particles with a diameter of 60 nm as catalysts. Silane (SiH_4) was used as the precursor gas and phosphine (PH_3), 0.3% in He, as the n-type doping source. The gas phase ratio of Si:P used to grow the doped segments were according to (Schmid et al., 2009) 66:1, 414:1 and 1667:1. Sample A was grown at 440 °C in He at 67 mbar with a silane partial pressure of 0.267 mbar. Sample B was grown at 460 °C in H_2 at 33 mbar with a silane partial pressure of 0.133 mbar.

Remark that less gold is present on sample A, that was grown at higher partial silane pressure, in accordance with Chapter 5.

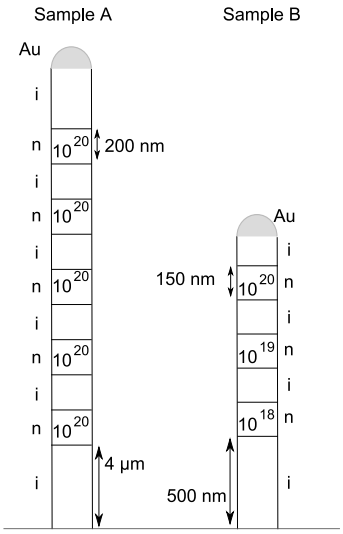

Figure 7.1: Schematics of the two studied nanowire samples A and B, containing n-doped regions alternated with intrinsic regions.

Most samples were prepared using cleaving (Section 4.3), such that holograms of nanowires that are still attached to the growth substrate could be acquired. This sample preparation technique has several advantages:

- The specimen is electrically connected to the wafer so artefacts due to charging are reduced (Cooper et al., 2008).
- The specimen is observed completely surrounded by vacuum and therefore not influenced by the structure of for example a carbon support film.
- If the nanowires are grown in epitaxy on the substrate, then all nanowires on the substrate are oriented similar with respect to the electron beam.

Diffraction contrast has to be minimized to reduce dynamical diffraction effects since Equation (3.22) is valid only in the absence of dynamical diffraction effects. Therefore the specimen is tilted $\sim 4^\circ$ degrees off the zone axis, while the junction is tilted no more than 2° off the edge-on position to prevent a spread of the interface region in the reconstructed phase image. The disadvantage of this sample preparation is that thin nanowires will vibrate slightly under the electron beam far away from the substrate. In sample A the first intrinsic region was 4 μm in length, therefore no detailed BF or HRTEM images could be made of the doped regions of cleaved specimens. In sample B the first intrinsic region was only 500 nm long, which eliminated the vibrations at the top of the nanowire almost completely. Incidentally wires from sample A were therefore studied dispersed on a plain carbon film (this is indicated in the figure caption).

Calibration of the phase image was performed using calibrated bright field (BF) images of the same nanowire and the diameter of the nanowire as measured in the amplitude image. This is very important since magnification of the Lorentz lens can depend on defocus (Formanek, 2004) and the holograms were not obtained at the same defocus values [2].

For some holographic experiments nanowires were treated chemically or physically, and this treatment had an effect on the visibility of the doped regions.

7.2 Electric potential simulations

Simulations were performed for a cylindrical nanowire using Technology Computer Aided Design (TCAD) (Silvaco International, 2007) software to calculate the potential everywhere in the structure using a cylindrical Poisson solver. These simulations were also performed to estimate the expected phase signal in the vacuum depending on surface charge.

In this section we describe the simulated structure and method that was used to "translate " the results of potential simulations to a phase shift measured by holography. We show already some results that illustrate the theoretical dopant detection limit as a function of interface charge. Direct comparison of experiment and simulation is shown in the experimental sections.

7.2.1 Description of the simulation

The exact geometry of the wire was obtained from TEM images (the thickness of the oxide layer on the wire surface was 3 nm) and the doping concentrations were taken from transport measurements (Björk et al., 2009; Schmid et al., 2009) (Figure 7.2). We assume that these estimated doping concentrations are approximately correct. Therefore the doping concentrations were not varied in the simulations. To obtain an agreement between experiment and simulation we have only varied the charge at the oxide-silicon interface and we have compared two different methods to apply the interface charge.

Simulations were performed with different charge quantities present at the oxide-silicon interface and in the presence of interface trap states. This is illustrated schematically in Figure 7.3. A fixed density of charges (sheet charge) was added at the oxide-silicon interface, that was varied from 0 to -2x10^{12} e.c. (electron charges) cm^{-2}. Similar densities of interface traps were added at different energy levels within the silicon bandgap. For simplicity only the results obtained by simulations with fixed charges are presented in this section. Simulations using fixed charges and interface traps give similar results (if the resulting interface charge is similar) and will be compared in Section 7.7.2 Figure 7.19.

The silicon substrate was connected to earth (since the sample is connected to the microscope during the experiment). A current boundary condition was specified at the gold catalyst particle as the nanowire is not connected at the top. The work function WF of the gold catalyst particle was 5 eV (Eastman, 1970). A Schottky contact is specified at the nanowire-gold interface, where the surface potential of the contact V_s is given by (Silvaco International, 2007)

[2] If the Lorentz lens is used it is more difficult to see if the sample is in focus on the phosphor screen, therefore it is convenient to fine tune the focus using the image on the CCD camera. Since the image moves if the focus is adjusted using the sample stage, it is convenient to use the lens defocus. However for reproducibility and comparison of results, and to avoid calibration uncertainties, holograms should have been obtained at the same defocus and diffraction lens settings

$$V_s = WF - af - \frac{E_g}{2e} - \frac{kT}{2e} \ln \frac{N_C}{N_V} \tag{7.1}$$

where af is the electron affinity of the semiconductor material, e is the charge of an electron, E_g is the bandgap, N_C is the conduction band density of states, N_V is the valence band density of states, and T is the ambient temperature. This equation is explained in Appendix A.5. The gold-silicon contact is assumed to be an ideal contact. However surface states can be present at the contact that lead to so-called Fermi level pinning, which was not taken into account. However since the potential signal close to the catalyst particle is not interpreted[3], this is not a problem.

Around the simulated nanowire a vacuum region of 5 μm was included to simulate the structure more truthfully and avoid artifacts due to the boundary conditions (see Figure 7.2). Along the outer edges of the simulated structure, homogeneous (reflecting) Neumann boundary conditions are imposed so that current can only flow out of the device through the contacts. In the absence of surface charge along the outer edges of the simulated structure, the normal electric field component becomes zero. Current is not permitted to flow from the semiconductor into an insulating region. At the interface between two different materials, the difference between the normal components of the respective electric displacements must be equal to any surface charge according to:

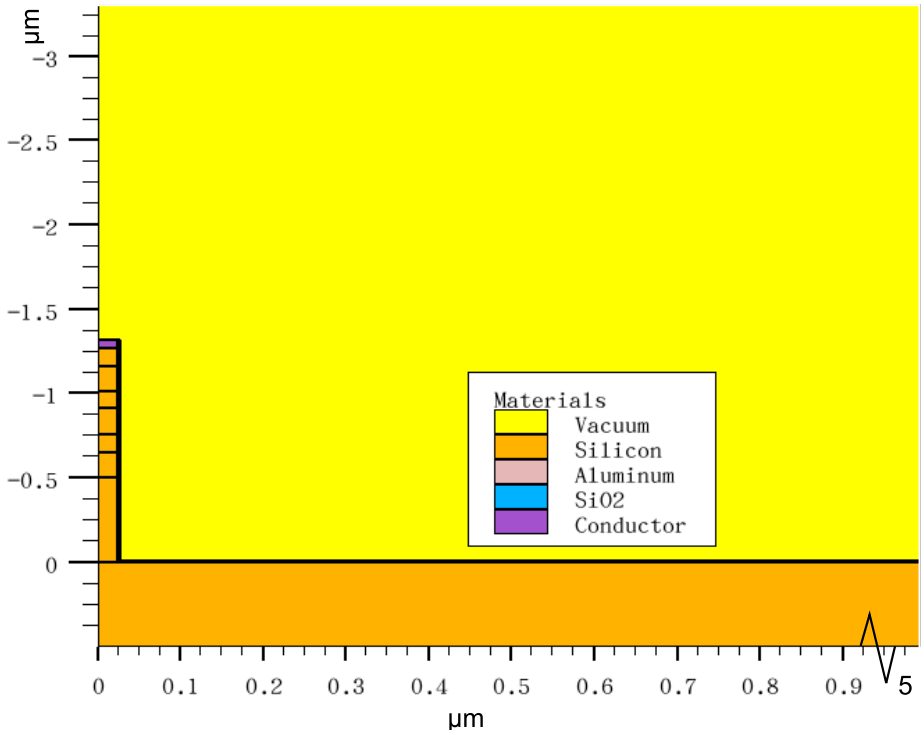

Figure 7.2: Schematic of a 2D cylindrical simulation. Half of the nanowire is visible with the different regions. Around the nanowire vacuum is defined. The catalyst was simulated by using another metal, being alumina, with the workfunction of gold. 3 nm silicon oxide was present on the nanowire sidewalls.

[3] It would actually be interesting to interpret the potential variations close to the gold particle since it could give information about the Schottky contact. The problem is that apparently the workfunction of gold in the catalyst particle is not necessarily the same as the workfunction of bulk gold (Bailly et al., 2008), surface states at the interface could be present leading to Fermi level pinning, and sample induced noise is present on the experimental signal.

$$\hat{n} \cdot \epsilon_1 \nabla V_1 - \hat{n} \cdot \epsilon_2 \nabla V_2 = \rho_s \tag{7.2}$$

where $\hat{n}$ is the unit normal vector, ϵ_1 and ϵ_2 are the permittivities of the materials on either side of the interface and ρ_s is the sheet charge at the interface.

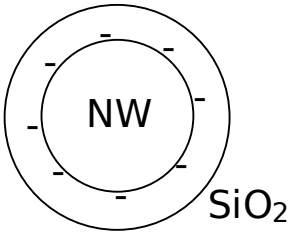

Figure 7.3: Schematic of the nanowire section with charge at the silicon-silica interface.

7.2.2 Simulation Results

The built-in potential of a p-n junction can be calculated using the classical formula using Equation (3.32) (Sze, 1985), in the absence of other charges, as they will modify the location of valence and conduction bands with respect to the Fermi level. In the presence of other charges the built-in potential V_{bi} and the resulting step in phase can be found from simulations using several possible approaches:

1. V_{bi} can be supposed to be constant throughout the specimen thickness, implying that the potential found at the center of the structure is assumed to describe also the potential at the surface. The calculated phase change using this approximation is plotted in column 4 of Table 7.1

2. V_{bi} can be found by integration of the simulated potential profile over the thickness of the specimen as suggested in Equation (3.22), which takes into account the variation of the potential near the surfaces due to surface depletion. The step in phase can be calculated using the difference in integrated potential between the intrinsic and the n-doped region (Equation (3.22)). The calculated phase change using this approximation is shown in column 5 of Table 7.1

3. V_{bi} can be found by integration of the simulated potential profile over the complete width of the simulation, since according to the simulation a potential profile is expected also in the vacuum outside the structure (Figure 7.17) which should contribute to the phase signal. This approach would predict larger phase shifts (maximum 1 rad for the considered doping concentrations) which is not coherent with the observed quantities. For this reason this approach was discarded. The experimentally observed phase signal in the vacuum due to doping modulation was in all cases less than predicted by simulation.

The difference in potential between the n and p-type region at the center of the structure (column three of Table 7.1) gives the same result as integration of the potential profile over the thickness of the structure (column 4 of Table 7.1). This justifies direct comparison of phase profiles extracted from measurements and simulated potential profiles that have been converted from volts to radians (for example Figure 7.9).

The intrinsic region was assumed to be lightly p-doped (10^{15} at. cm^{-3}), which could be attributed to the presence of ionized acceptor type interface traps (Nicollian and Brews, 1982).

Table 7.1: Phase step over junctions with different doping concentration (at.cm^{-3}). The phase step (rad.) is calculated for a NW with a diameter of 60 nm (including 3 nm oxide at the surface) using Equation (3.32) and calculated using the integral of the simulated potential profile. The simulation was performed using four different charge quantities at the oxide-wire interface: 0 e.c. cm^{-2}, -1x10^{11} e.c. cm^{-2}, -1x10^{12} e.c. cm^{-2} and -2x10^{12} e.c. cm^{-2}.

Charge quantity (e.c. cm^{-2})	p-n (at. cm^{-3})	$\Delta\phi$ (rad) Equation (3.32) Center nanowire	$\Delta\phi$ (rad) Simulation Center nanowire	$\Delta\phi$ (rad) Simulation Integration
0 Charge	10^{15} - 10^{20}	0.39	0.39	0.39
	10^{15} - 10^{19}	0.37	0.36	0.37
	10^{15} - 10^{18}	0.34	0.33	0.34
	10^{15} - 10^{17}	0.31	0.32	0.32
-1x10^{11} Charge	10^{15} - 10^{20}		0.43	0.43
	10^{15} - 10^{19}		0.40	0.40
	10^{15} - 10^{18}		0.38	0.38
	10^{15} - 10^{17}		0.33	0.33
-1x10^{12} Charge	10^{15} - 10^{20}		0.44	0.45
	10^{15} - 10^{19}		0.41	0.42
	10^{15} - 10^{18}		0.39	0.38
	10^{15} - 10^{17}		0.01	0.00
-2x10^{12} Charge	10^{15} - 10^{20}		0.44	0.46
	10^{15} - 10^{19}		0.42	0.43
	10^{15} - 10^{18}		0.10	0.06
	10^{15} - 10^{17}		0.01	0.00

A charged nanowire can be approximated by an infinite line charge. The analytical formula to relate the line charge density λ with the potential $V(r)$ is given by (Tipler, 1999)

$$V(r) = -2\lambda k_C \ln r + V_0 \tag{7.3}$$

where k_C is the Coulomb constant (8.99x10^9 N m^2 C^{-2}) and V_0 is chosen such that the potential is zero at convenient place in the structure. However in holography the projected potential along the beampath is measured, therefore the integrated potential, given by

$$\int_{-\infty}^{\infty} -2\lambda k_C \ln\left(x^2 + y^2\right) dx \tag{7.4}$$

should be calculated, which is impossible since the integral goes to infinity.

For this reason simulations were also used to simulate the expected signal in the vacuum for an intrinsic nanowire with a certain quantity of charge present in the oxide layer. This can be achieved either by defining a series of cutplanes (2D potential maps) at increasing distance from the nanowire. The integral of a line profile perpendicular to the nanowire axis is made in each cutplane and the difference between the integrated values in two planes (multiplied by C_E, see Equation (3.22)) determines the simulated phase change between two points at increasing distance from the nanowire. Or a potential profile perpendicular to the nanowire axis starting in the nanowire center can be extracted from the simulation. This radial profile was exported to Digital Micrograph^{TM} (DM), where the cylindrical potential was reconstructed by

symmetry. The integration along the beam direction (for instance y) was then realized in DM. Multiplication with C_E again gives the phase. Both methods give the same result, which should be the case. The different steps for the simulation of holograms from potential simualtions will be illustrated more clearly in Figure 7.21.

Several problems were encountered for accurate simulation of potential maps as obtained by holography:

1. The Device Simulator Software (Silvaco International, 2007) is a powerful tool to simulate microelectronic devices, however it is not optimized to simulate potential maps obtained by holography. Off-axis electron holography measures the projected potential in the direction of the electron beam which is an integration in the beam direction (Equation (3.22)). The phase difference can therefore be calculated either using the simulation software or by exporting the data (as described). Calculation of the entire phase image from simulation is therefore possible, but slightly more tedious since each point in the image represents an integration[4].

2. Another problem was the simulation of the contacts. As already mentioned the nanowire substrate is connected to the microscope, which provides one contact. At the top of the nanowire the gold catalyst particle is present. If this particle is defined as a metal in the simulation, the software expects the gold particle to be a contact. For this reason a current boundary condition was defined for this contact, however when the Poisson equation is solved for the complete structure all contacts are set to zero applied bias (or zero volts) which is not necessarily an accurate simulation of the gold particle. Solving for the structure with only the substrate contact is not possible as the calculation does not converge. It seems difficult to choose accurate boundary conditions for the gold particle also since it is not unlikely that the gold particle acts as a reservoir of charges and/or becomes charged due to the electron beam. In addition the influence of the electron beam cannot be taken into account in the simulation.

3. The mesh of the simulated structure was chosen such that an increase in mesh size did not result in a change of the simulated result. For 2D cylindrical simulations typical mesh sizes at the junctions, oxide interfaces and surfaces were $\sim 1\,\text{nm}$. However for 3D cylindrical simulations the same mesh sizes were often not possible as the maximum number of nodes would be reached. Therefore the results of 3D cylindrical simulations have to be compared to 2D cylindrical simulations to avoid meshing artifacts.

7.3 Influence of thickness changes

The theory describing off-axis holography was already described in Section 3.8. We recall that using electron holography the phase difference of the electrons that traversed the sample with respect to a reference wave can be measured. The phase difference is related to the Mean Inner Potential (MIP) and the sample thickness t by a linear formula (Equation (3.22)). The difference in MIP between regions of different doping is equal to the built-in potential, related to the respective doping concentrations (Equation (3.32)).

The phase signal that is measured is therefore influenced by the thickness of the sample, and thickness variations will result in phase variations. In this section we will show results on nanowires with axially modulated doping that contained thickness variations at the junction

[4] Due to time restrictions we did not calculate entire phase images including doped regions

(sample A, Figure 7.1). Although the thickness variations influence the phase measurement it is shown that most of the phase signal is due to doping contrast

In Figure 7.4A a TEM BF image and a high resolution image (Figure 7.4B) on the transition of the intrinsic to the doped region of a nanowire of sample A is shown. Clearly a thickness change can be observed. The thickness change was not the same on each transition and varied between 1 and 5 nm. Sample A was also studied using STEM. A typical image is shown in Figure 7.4C. Clearly gold clusters are present on the thicker, doped region. The gold clusters are not distributed homogeneously over the wire substrate but appear progressively towards the top of the nanowire and stop suddenly at the transition to the next intrinsic region.

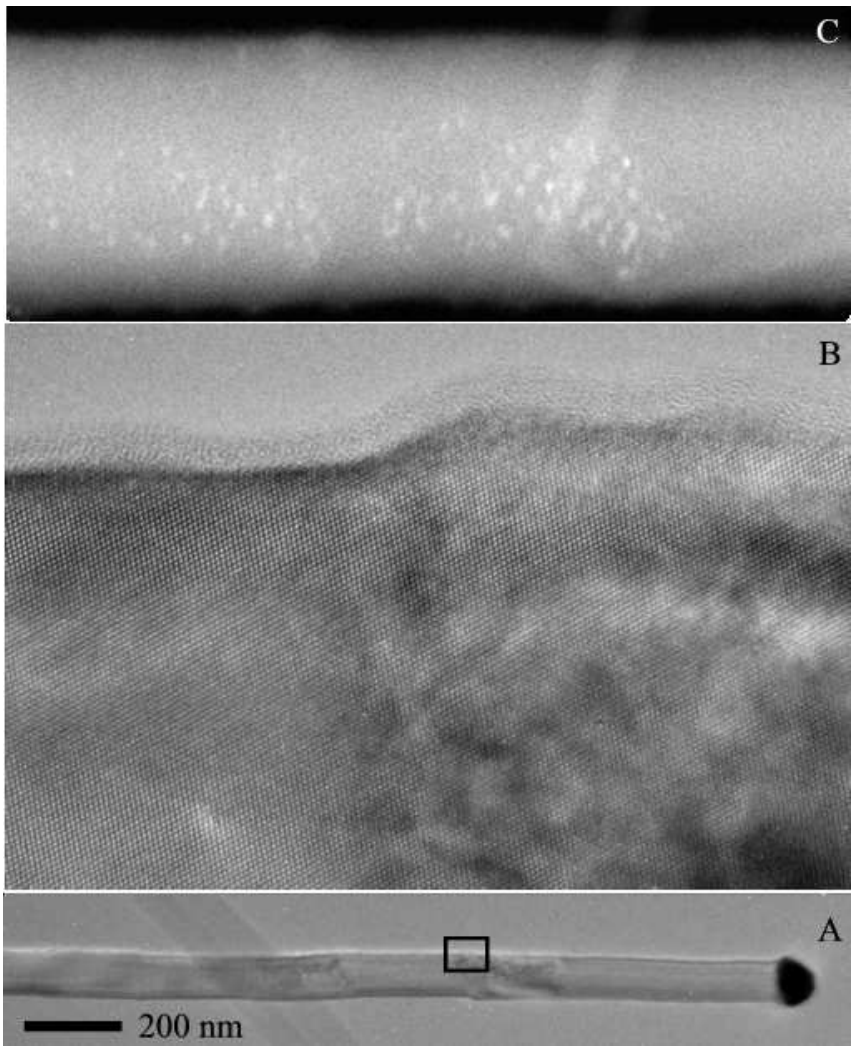

Figure 7.4: (a) TEM bright field image. (b) HRTEM image of the region marked in a. A thickness change can be observed. (c) STEM image of a doped region. Gold clusters can be observed, inhomogeneously dispersed over the (doped) nanowire surface. IBM sample A

In Figure 7.5A-D a schematic illustration of a nanowire from sample A with the hemispherical gold tip on the left side and the axially n-doped segments is shown, together with the corresponding HAADF STEM image, the reconstructed amplitude and phase images with enhanced contrast levels for better visibility and a phase profile made at the dotted line. The image and phase profile clearly reveal the structure of the silicon nanowire showing four segments of higher phase shift that correspond to the four doped segments, alternated by intrinsic segments. A closer look at the phase profile shows that the four peaks do not have the same

intensity as would be expected. In particular the peak closest to the tip shows a markedly reduced phase shift (a dotted line is drawn to guide the eye) which suggests that the proximity of the Au tip might affect the potential distribution. The phase jumps seem to increase linearly going from left to right. This is attributed to an increasing thickness contribution at each junction.

The amplitude image is sensitive to thickness variations, this is described by

$$\frac{t}{\lambda_i} = -2 \ln \frac{A_{obj}}{A_{ref}} \tag{7.5}$$

where λ_i is the mean free path for inelastic scattering, A_{obj} is the energy-filtered amplitude and A_{ref} corresponds to the amplitude of the unscattered reference wave (Völkl et al., 1999). However no variations are visible in a line profile made at the center of the nanowire in the amplitude image (Figure 7.5F). This is certainly due to the fact that Equation (7.5) is not very sensitive to small thickness variations (≤ 5 nm).

However slight variations in diameter are visible by looking at the edge of the wire. In Figure 7.5C a line is drawn to aid visualization of the diameter variations. The diameter is smaller in the intrinsic regions of the wire, as indicated by arrows. It was shown in Figure 3.6 that the width of an object with two abrupt interfaces can be measured in the phase image independent of mask size. Therefore it seemed that the diameter of the nanowire can be measured accurately in the amplitude image. Because the obtained diameter changes using the calibrated amplitude image appeared rather large, we have simulated holograms of a nanowire with varying diameter and measured the apparent diameter in the amplitude image. The simulation assumes the nanowire is a cylinder with a MIP of 12 V, the nanowire was sampled with a similar number of fringes as used in the experiment. The results of the simulation are shown in Figure 7.6. The procedure for hologram simulation will be explained in more detail in Figure 7.21. It appears that due to the cylindrical shape the measured diameter in the amplitude image is not linear with the diameter and that the amplitude image cannot be used to measure the nanowire thickness accurately.

In the presence of thickness variations a correct interpretation of the data is possible only if calibrated bright field (BF) images are made, to accurately measure the diameter change along the nanowire, that is supposed to be equal to the thickness change[5]. In general BF and high resolution images were acquired of all of the observed nanowires to account for the influence of thickness variations on the phase image.

In Figure 7.7C the phase image of a nanowire, with doped segments as indicated in the schematic (Figure 7.7A) is shown with enhanced color scale. The diameter of the nanowire at each segment is 63.8, 63.1 and 64.7 nm respectively, as obtained from the BF image (Figure 7.7B). The two highly doped regions are clearly visible. In Figure 7.7D a phase profile extracted across the nanowire (indicated by the dotted line in Figure 7.7C) is shown (solid line). The phase signal that would be due to the thickness change as measured and shown in Figure 7.7B-C has been calculated (◯), which can be used to correct the phase change for thickness variations (□) by simple subtraction. It is clear that thickness variations are present, however Figure 7.7 suggests that the observed phase signal is primarily due to doping contrast.

Determination of the nanowire thickness is not as straightforward as it might seem, since the nanowire cross section is not a cylinder but a hexagon (Ross et al., 2005). For this reason the

[5] This was not possible in the case of Figure 7.5 since the TEM sample was prepared by cleaving. Because the doped regions were too far away from the substrate the wire vibrated slightly.

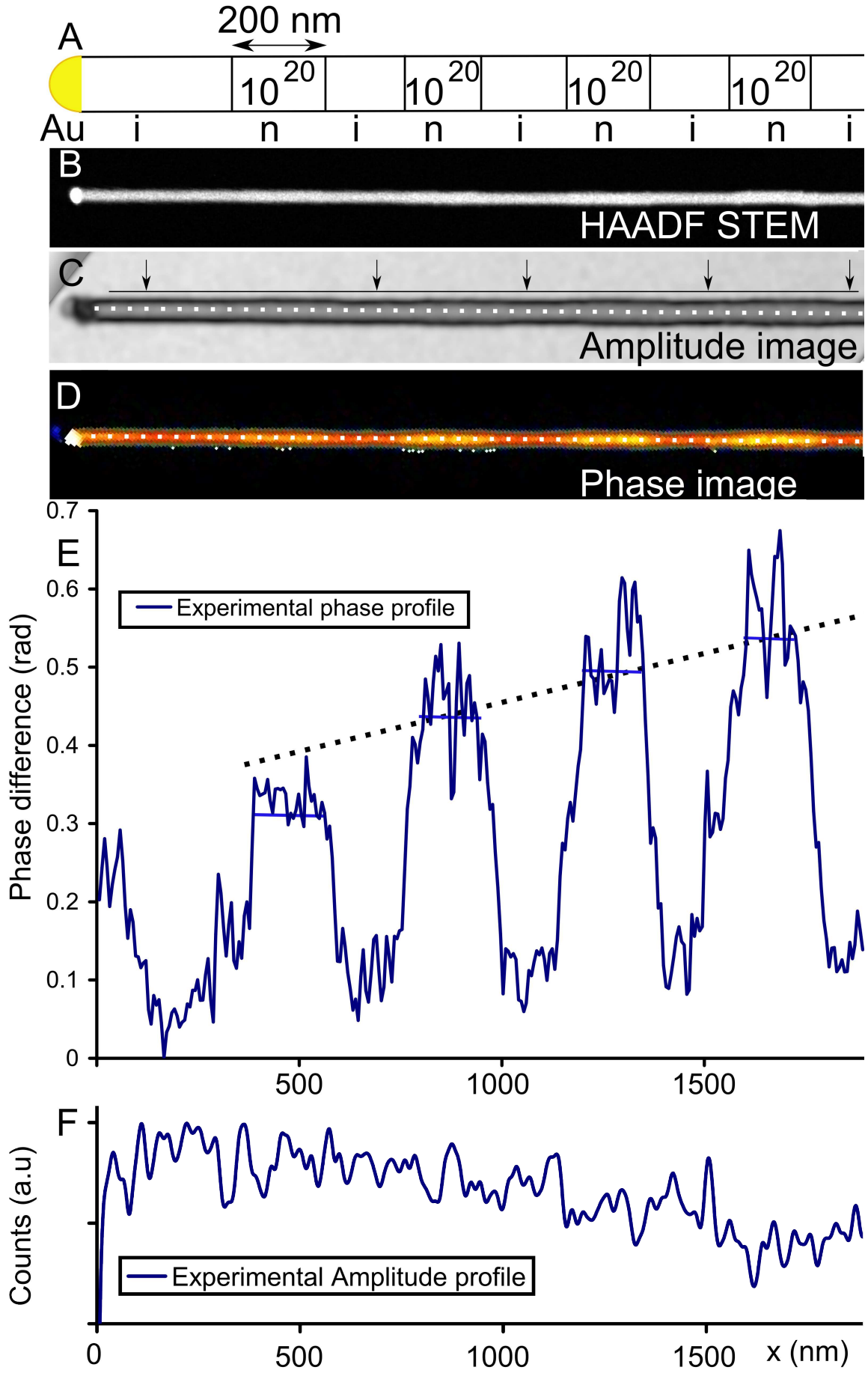

Figure 7.5: (A) Schematic of a nanowire from sample A. (B) HAADF STEM image. (C) Amplitude image. A line near the wire side is drawn to aid visualization of small diameter changes. Arrows mark the thinner intrinsic regions. (D) Phase image (E) Line profile made at the dotted line in (c). The average of the four peaks was estimated and used to draw a dotted line to guide the eye relating the four doping peaks. (F) Line profile made at the dotted line in (c) showing that no variations are present in the amplitude image. IBM sample A

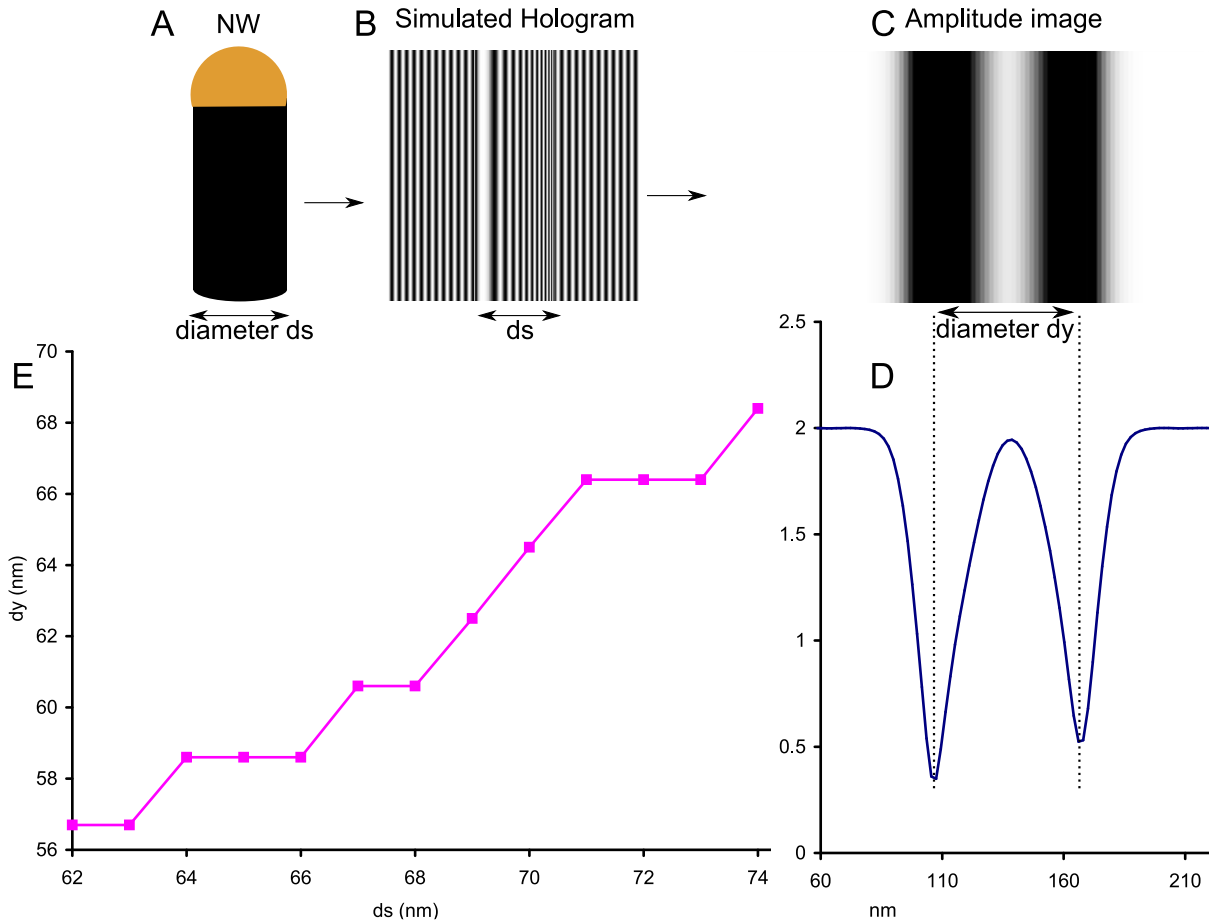

Figure 7.6: (A-D) Flow scheme to illustrate the x and y axis in the graph in (E). (A) Simulated nanowire with diameter ds. (B) Simulated hologram of the nanowire in (a). (C) Reconstructed amplitude image. (D) Line profile over the amplitude image. The apparent diameter as measured in the amplitude image dy is indicated. (E) Graph showing the imprecision if the nanowire diameter is measured in the amplitude image. On the x-axis the nanowire diameter ds used to create the hologram. On the y-axis the diameter measured in the amplitude image dy obtained by reconstruction of the simulated hologram.

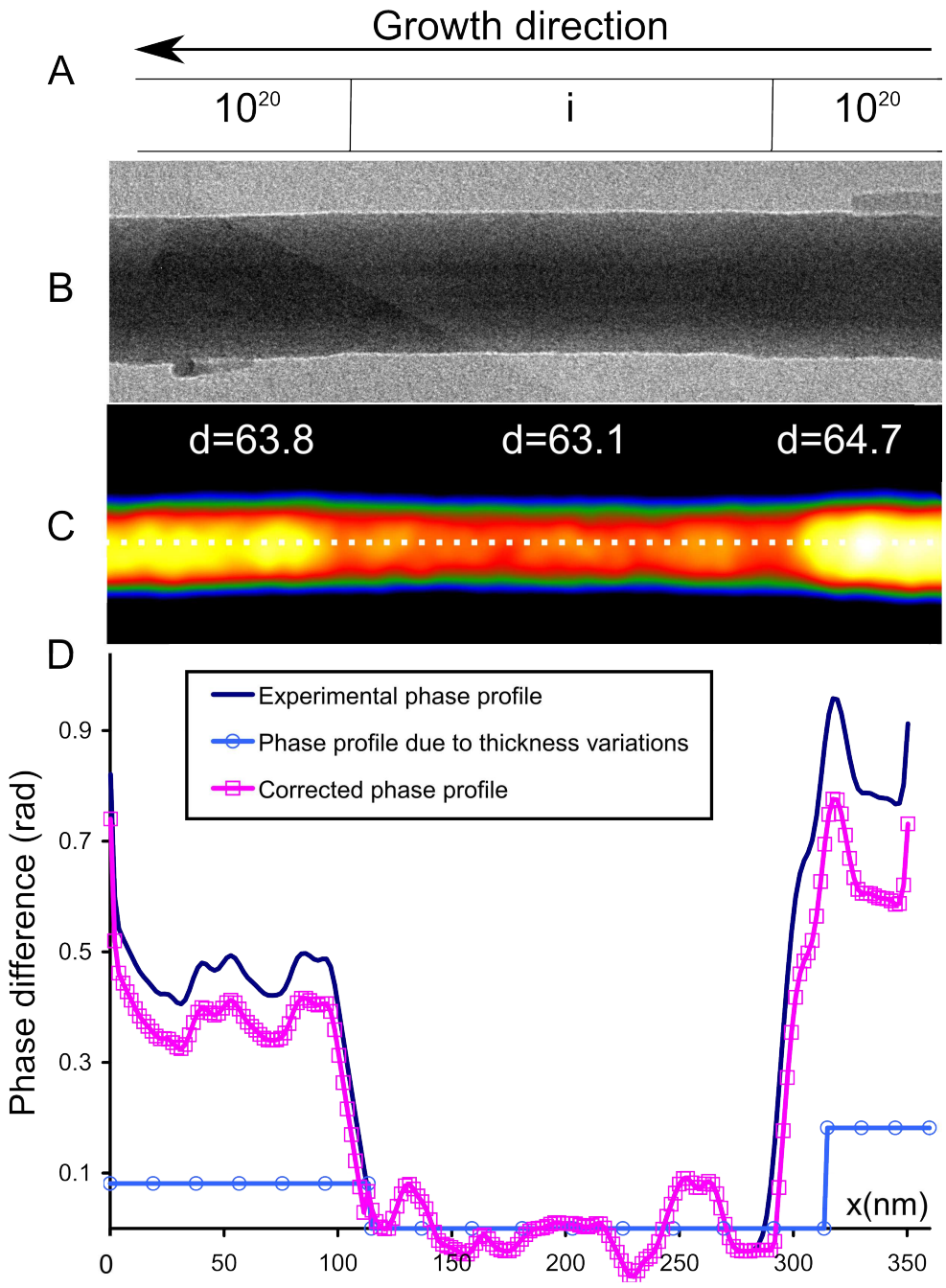

Figure 7.7: (A) Schematic of a detail of a nanowire. (B) BF image showing thickness changes. (C) Phase image with amplified color scale. Three segments are visible that are all 200 nm long: n-doped 10^{20} (Phosphorus), intrinsic and 10^{20} at. cm^{-3} (Phosphorus) respectively. The segments vary slightly in diameter and the diameter as obtained from the BF image is indicated. (D) Phase profile made at the dotted line (solid line), the phase signal that would be due to the thickness change as indicated in (c) (◯) and the phase change corrected for the measured thickness changes (□). The nanowire was studied on carbon film. The crystallographic growth direction of the nanowire was ⟨112⟩. IBM sample A

diameter is not necessarily equal to the thickness, however the same diameter was found in two bright field images taken 60° apart. Other approaches to measure the thickness such as Energy Filtered TEM (EFTEM) or Convergent Beam Electron Diffraction (CBED) did not improve the thickness measurement in this case because the resolution is $\geq 3\,\text{nm}$ for this sample thickness ($\sim 60\,\text{nm}$), which is not sufficient to detect these thickness variations.

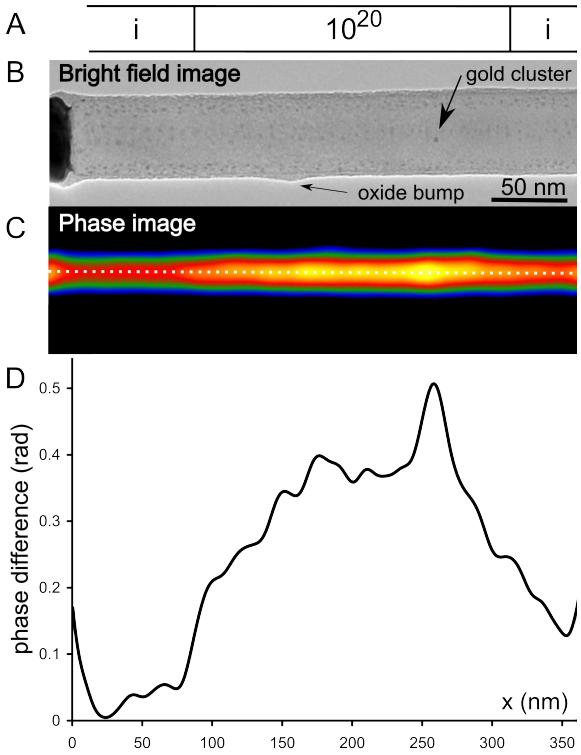

Figure 7.8: (A) Schematic of a detail of a nanowire from sample B. (B) Bright field image. No thickness changes were observed and gold clusters are present on a faceted surface. A larger gold cluster and a small thickness change of the oxide shell can be observed. The crystallographic growth direction of the nanowire was ⟨111⟩. (C) Phase image with amplified color scale showing one doped region. (D) Extracted phase profile across the phase image shown in (c).
IBM sample B

7.4 Dopant detection limit

In sample B doped regions of different doping concentrations were present, to assess the dopant detection limit. Experimental results are compared with potential simulations (Section 7.2).

Sample B did not contain thickness variations, as illustrated by the bright field image of a nanowire shown in Figure 7.8B. The nanowire surface is facetted and a homogeneous distribution of gold clusters is present, coherent with (Ross et al., 2005; den Hertog et al., 2008). A schematic illustrating the doping concentrations, the phase image with amplified color scale and the extracted phase profile across the nanowire are shown in Figure 7.8A-D to illustrate clearly that no thickness variations are present that could cause the observed step in phase.

In Figure 7.9B a hologram of a nanowire from sample B is shown. In Figure 7.9C the phase image is shown with modified contrast levels to show more clearly the differently doped regions. In Figure 7.9D a phase profile extracted across the phase image is shown, indicated by a dotted line in Figure 7.9C, as well as the simulated potential profile, converted from volts to radians using Equation (3.22) (the nanowire diameter is 56 nm). A fixed density of charges (sheet charge) was added at the oxide interface, that was varied from 0 to -2x10^{12} e.c. (electron charges) cm^{-2}. The simulated potential profile was used to calculate the expected step in phase using Equation (3.22). The simulation shows that without charges in the oxide the expected phase step will be below 0.1 rad between each of the alternating segments, due to the large depletion width in the intrinsic region ($\sim 1\,\mu$m (Sze, 1985)). However the phase signal in the experimental data is much larger than suggested from simple calculations and corresponds

well to simulations that use a sheet charge at the oxide interface of -1x10^{12} e.c. cm^{-2}. Due to the negative charges in the oxide layer the electrons are repelled from the intrinsic segment, effectively reducing the depletion width. Interestingly the visibility of the lowest doped segment (10^{18} at. cm^{-3}) depends very sensitively on the amount of charge present at the oxide interface. This is due to the fact that the amount of charge present in the oxide (-1.8x10^{7} e.c. in a length of 1 cm) becomes approximately equivalent to the doping concentration (2.5x10^{7} at. in a length of 1 cm). It should be noted that the region with 10^{18} at. cm^{-3} doping was not equally well visible in all observed nanowires. The regions with 10^{20} at. cm^{-3} and 10^{19} at. cm^{-3} doping were visible in all observed nanowires, but the 10^{19} at. cm^{-3} region systematically caused a larger step in phase. The comparison of the experimental data with simulation aids the estimation of the quantity of charge at the oxide-nanowire interface, given that the doping concentrations have been estimated from transport measurements (Björk et al., 2008; Björk et al., 2009; Schmid et al., 2009).

Table 7.1 shows the step in phase that can be expected for the phosphorus doping concentrations with respect to lightly p-doped silicon (10^{15} at. cm^{-3}) for nanowires of similar diameter and independent of the depletion width. Table 7.1 suggests that doping concentrations as low as 10^{17} at. cm^{-3} could be detected if no surface charges were present. However the depletion width for this doping concentration is similar to the field of view of the hologram. Therefore it will be difficult to detect doping concentrations as low as 10^{17} at. cm^{-3}, even if no surface charges are present. If surface charges of -1x10^{12} e.c. cm^{-2} are present, it is clear that doping concentrations of 10^{18} at. cm^{-3} can still be detected, however lower doping concentrations are below the detection limit.

It is clear from Table 7.1 that it is difficult to derive the exact dopant concentrations from the phase profiles extracted across highly doped regions, as the differences in simulated phase change are quite small with respect to the fluctuations in the experimental phase profiles.

The observed fluctuations in the experimental phase profiles are partly noise. An estimation of the noise contribution was made by reconstruction of two reference holograms acquired directly after one another (see also Section 3.8.5). A phase profile was traced in the empty phase image (see Figure 7.9D solid line at the bottom of the graph). The fluctuations of the phase signal in the epxerimental data exceed the expected noise contribution. It seems therefore that contributions from the sample are present in the fluctuations of the phase signal such as:

1. Slight thickness changes of ~ 1 nm, which would change the phase signal by ≤ 0.09 rad for silicon (if the nanowire surface is faceted very small thickness changes are difficult to detect but likely, due to the faceting).

2. Slight variations in the oxide thickness can also be present, an example is shown in Figure 7.8D.

3. Also the presence of gold clusters can modify the phase locally by 0.1 rad, for the presence of one monolayer of gold (Popescu et al., 2007). In reality gold clusters are present with a thickness of approximately 2 nm and diameter of 3 nm (den Hertog et al., 2008) (see Chapter 5).

However due to the spatial resolution of ~ 10 nm the signals of small thickness changes and gold clusters will be spread out in the reconstructed phase image. The influence of the gold clusters can be seen both in Figure 7.7 and Figure 7.8. In Figure 7.7 the step in phase measured across the junction on the left (the side of the catalyst particle) is clearly smaller than the step in phase across the junction on the right. This could be due to the presence of gold clusters on the doped region on the right, since STEM images have shown that the density of gold clusters

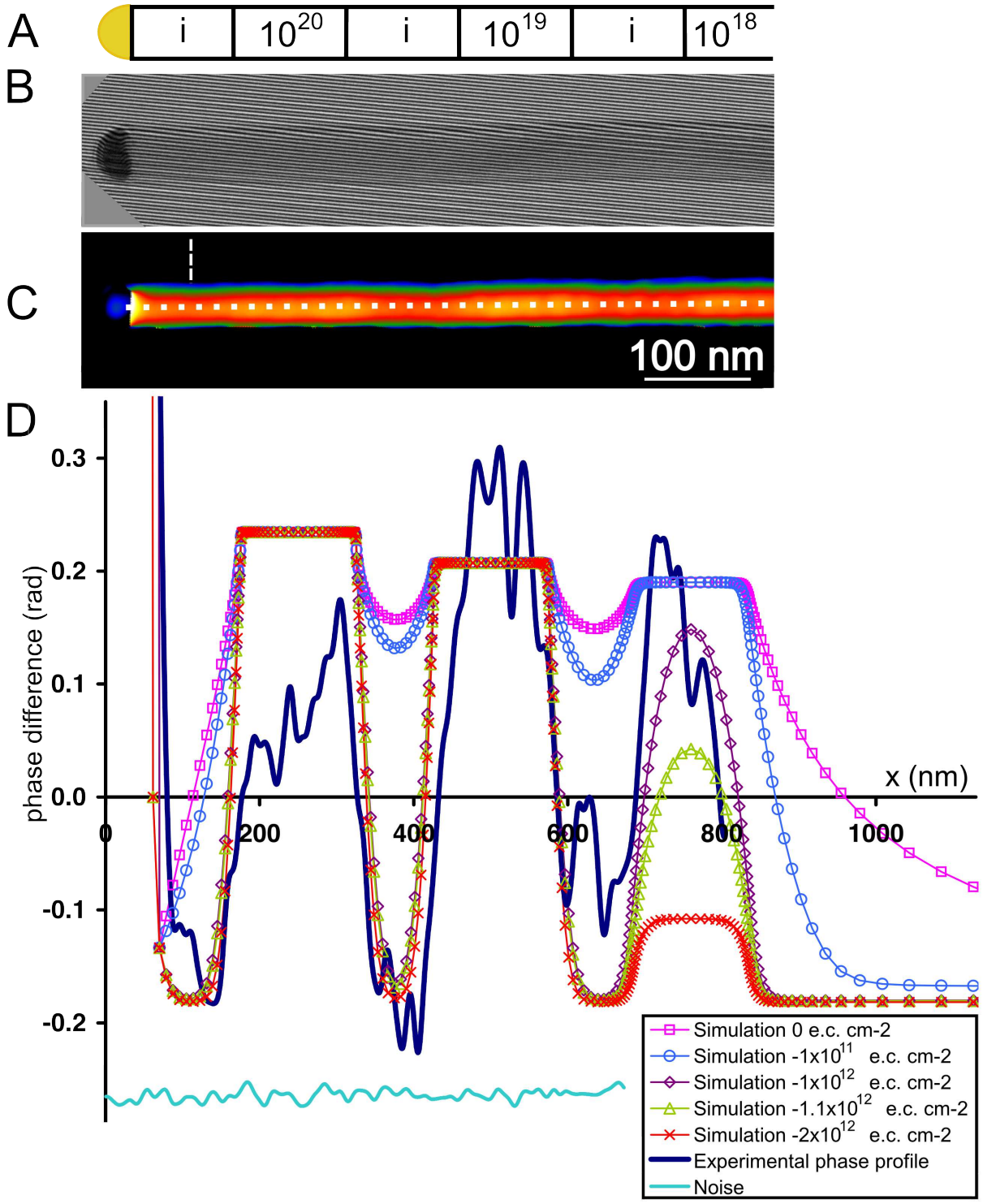

Figure 7.9: (A) Schematic of a nanowire from sample B that contains three n-doped (Phosphorus) regions of varying doping concentration: 10^{20}, 10^{19} and 10^{18} at. cm^{-3} . The doped regions are separated by intrinsic regions. All segments are $\sim$ 150 nm long. (B) Hologram of the nanowire. (C) Phase image with amplified color scale. (D) Phase profile (solid line) made at the dotted line, averaged over 3.5 nm. Simulations of the phase-profile at the center of this structure with zero charge at the wire oxide-interface (□), with -1x10^{11} e.c. cm^{-2} charge at the interface (◯), with -1x10^{12} e.c. cm^{-2} charge (◊), with -1.1x10^{12} e.c. cm^{-2} charge (△) and with -2x10^{12} e.c. cm^{-2} charge (×) are plotted for comparison. The phase difference was obtained from simulation by multiplying the potential with t and C_E (Equation (3.22)). The noise level as obtained from reconstruction of two reference holograms and tracing a phase profile in the obtained empty phase image (averaged over 0.3 nm) is plotted at the bottom of the graph (solid line). The crystallographic growth direction of the nanowire was ⟨111⟩. IBM sample B

is increasing towards the end of a doped region (see Figure 7.4). As already mentioned the quantity of gold present is approximately equal to 1-1.5 monolayers (Hannon et al., 2006; den Hertog et al., 2008), which can cause an additional step in phase $\sim$ 0.1-0.15 rad. However the observed step in phase over the junction is much larger and $\sim$ 0.4 rad, which clearly shows once more that the observed phase signal in Figure 7.7 is primarily due to doping contrast. In Figure 7.8B-C a sharp peak is present on the doped region. At this location a slightly larger gold cluster can be observed in the bright field image (Figure 7.8D). The additional step in phase due to this gold cluster is $\sim$ 0.1 rad, very similar to the phase signal that could be expected from one monolayer of gold.

7.5 Width of the p-n junction

The spatial region where the potential changes over a junction is called the depletion width, W (Sze, 1985). In Figure 7.10B the experimental phase profile across the 10^{19} at. cm^{-3} doped region (Figure 7.9) is shown, compared to the simulated potential profile over an abrupt junction and a non-abrupt junction including a length L of low n-doped (10^{18} at. cm^{-3}) silicon between the heavily doped segment and the intrinsic segment. A sheet charge of -1x10^{12} e.c. cm^{-2} was present at the oxide interface. Due to the fluctuations on the experimental phase profile the comparison of the profiles is not directly evident. However the slope of the potential and the depletion width W seem to correspond best to a non-abrupt junction with L=30 nm. Since it seems more realistic to have a dopant concentration that is gradually increasing at the junction, also simulations were performed were various low n-doped segments were included (10^{16} , 10^{17} and 10^{18} at. cm^{-3} respectively) between the intrinsic and highly n-doped region. However these lowly doped zones are depleted due to the surface charges (see Table 7.1) and therefore the simulated step in phase over a n^{+}-n junction (n 10^{19} -n 10^{17} at. cm^{-3}) and an n^{+}-p^{-} (n 10^{19} -p 10^{15} at. cm^{-3}) are the same. Combining the uncertainty on the number of decades over the junction (two to four decades) with the uncertainty on the length L, that is 30-60 nm, an abruptness of the junction of 7.5-30 nm/decade is estimated.

The mask used during the reconstruction procedure of the holograms has also the effect of spreading an interface region. This effect was investigated in Figure 3.6 for a simulated abrupt interface. The spreading of an abrupt interface in the phase image is approximately equal to the spatial resolution, which is much smaller than the width of the junction in the phase image, which means that the phase variation over a junction can in principle be interpreted in terms of doping concentration gradient. It should be noted that W depends both on the doping concentrations and the surface charges. Therefore estimation of the concentration gradient using simulation is possible only if both parameters are approximately known, or one parameter is precisely known (which is difficult with current measurement techniques).

Such a non-abrupt junction seems probable for nanowires grown by VLS, and could be caused both by the effective switching time of the gas flow at the level of the nanowire, and the liquid catalyst particle whose composition lags behind the gas composition of precursors in the growth chamber.

The growth of the nanowires was performed with the aim of growing all the regions of the same length, being 150 nm in sample B (Figure 7.9 and Figure 7.8) or 200 nm in sample A (Figure 7.7), however the intrinsic segments appear slightly shorter in the phase images. For example the simulations in Figure 7.9 correspond well to the experimental phase profile if the intrinsic segment length was approximately 105 nm. This would suggest that the growth of the doped regions is slower and should be better calibrated. However it was shown in (Schmid

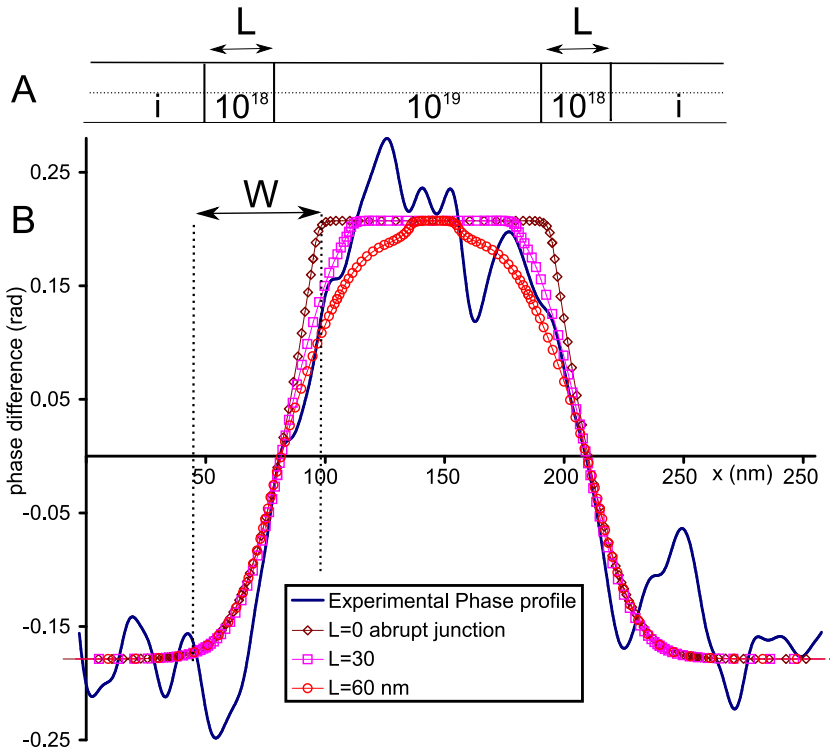

Figure 7.10: (A) Schematic of the simulated non-abrupt junction. (B) Simulations of the phase profile at the center of the nanowire structure shown in (a) compared with an experimental profile of the junction (solid line). The simulation was performed with -1x10^{12} e.c. cm^{-2} sheet charge. A simulated phase profile of the abrupt junction (◊), of a non-abrupt junction including L= 30 nm of 10^{18} at. cm^{-3} doped silicon (□) and a non-abrupt junction including L=60 nm of 10^{18} at. cm^{-3} between the highly doped and the intrinsic silicon are shown (◯). IBM sample B

et al., 2009) that the growth speed of doped and intrinsic regions is almost the same. Another explanation is therefore that, as shown in the foregoing, a concentration gradient is present at the junction. Due to the concentration gradient the depletion width is longer and the highly doped region appears shorter.

7.6 Surface charges and the electron beam

We have shown that the experimental data agree well with simulations where negative charges are present at the silicon-oxide interface. In this section the origin of such negative charges is discussed.

The simulation assumes that fixed charges are present at the oxide interface. In reality there are three possible contributions to the charge density at the oxide interface (Nicollian and Brews, 1982), as illustrated in Figure 7.11. (i) the fixed oxide charges in the oxide, (ii) interface trapped charges and (iii) electron beam induced oxide trapped charges (Fazzini et al., 2005; Nicollian and Brews, 1982), due to the generation of electron hole pairs by the high energy electron beam (Houben et al., 2004).

The estimated number of charges at the oxide interface of -1x10^{12} e.c. cm^{-2} is in excellent agreement with the value found by transport measurements (Björk et al., 2009). Transport measurements (Björk et al., 2009) do not allow to distinguish fixed charges from interface trapped charges, however it is generally accepted that this order of magnitude of charge densities is

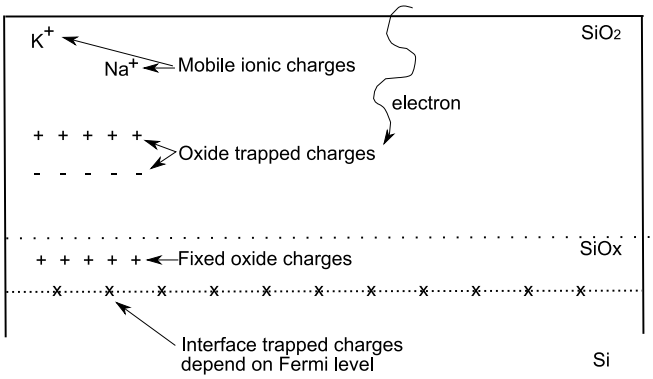

Figure 7.11: Schematic illustrating the different possible types of charges that can be present in the oxide or at the oxide-silicon interface (Nicollian and Brews, 1982).

due to interface traps (Schmidt et al., 2007b). Futhremore interface traps seem physically more realistic because the charges are supplied by the dopants and therefore a dipole is present and the object is globally neutral[6].

Interface traps can be either acceptor or donor-type, depending on the position of the Fermi level with respect to the valence and conduction band (Schmidt et al., 2007b; Sze, 1985). Therefore negative charges would be expected mostly at the surface of the n-doped segments (Björk et al., 2009; Schmidt et al., 2007b; Sze, 1985). However the comparison of holography experiments and simulation shows that negative charges are also present at the surface of the intrinsic regions. This could be due to the complicated nature of the nanowire surface, that is faceted and can be covered with gold clusters (den Hertog et al., 2008; Hannon et al., 2006). The crystal planes present are {111} {112} and {100} (den Hertog et al., 2007; Ross et al., 2005) (see Section 5.5), partially different from the well studied case of interface traps at the silicon-silica interface of {100} and {110} oriented silicon wafers. Another possibility is the influence of the electron beam on the occupation level of acceptor type interface trap states.

It seems likely that in the experiment such interface traps can be negatively charged due to the influence of the electron beam in the lightly p-doped intrinsic region, since it was found by simulations (Houben et al., 2004) that especially the minority carrier concentration is modified by the electron beam during the holography experiment. Furthermore an influence in the acquired potential map is expected only for lowly doped silicon ($\leq 10^{17}$ at. cm^{-3}). Indeed this effect could modify the observed potential profile in the intrinsic regions.

The influence of the electron beam could not be taken into account in the simulation. It was verified that the results were reproducible with a lower beam current (the beam current was decreased from 3 to 0.7 nA nm^2), coherent with the observations in (Cooper et al., 2008). Probably the specimen reaches a steady state of charging due to the electron beam already at a lower beam current value.

If the effect of the electron beam on the charge density was known, this could be included in the simulation, because apparently the specimen reaches a steady state of charging already at low beam current. However it seems that the interaction of the electron beam with such a relatively complicated nanostructure cannot be understood using a simple model but has to be simulated, which should be done for future experiments.

[6] If such a density of fixed charges was present a nanowire aray of one by one cm with one nanowire per micron, of length 5 μm and diameter 60 nm, would carry a charge of 150 nC.

7.7 Fringing fields in the vacuum

So far we have compared experiment and simulation inside the nanowire. In this section we discuss the phase signal in the vacuum at the side of the nanowires and we compare the results with simulations. First we present results obtained on undoped nanowires, followed by the results on nanowires with axially modulated doping.

The interpretation of phase signals in the vacuum is possible only if a reference hologram of good quality and obtained directly after the first hologram is obtained, and if a suitable reference region has been defined. In this condition distortions or imaging artifacts can be surpressed.

7.7.1 Undoped nanowires

In Figure 7.12 a phase image of an intrinsic nanowire is shown, with a phase profile made across the dotted line. In the vacuum at the side of the nanowire the phase signal decreases gradually going away from the nanowire. The MIP is a positive quantity (Williams and Carter, 1996)[7]. In the crystal a nucleus is never far away and therefore the average crystal potential is positive as well as the MIP, as shown schematically in Figure 7.13. For this reason a positive phase change is associated with a positive charge and a negative phase change with a negative charge, this is shown schematically in Figure 7.13C-D. A decreasing phase gradient in the vacuum therefore indicates a positive charging of the sample[8].

Such a phase profile made perpendicular to the nanowire axis was similar on all intrinsic nanowires, however the slope in the vacuum could vary. In Figure 7.14 the slope of the phase signal in the vacuum is plotted for varying wire diameter as well as the simulated phase signal in the vacuum (see Section 7.2) for an intrinsic nanowire with different amounts of charges at the oxide-wire interface. There is quite some dispersion in the experimental data, however it seems that an increasing slope in the vacuum is observed for increasing wire diameter. This is coherent with simulations, however the experimentally observed increase in phase gradient in the vacuum for increasing wire diameter seems larger than predicted by simulation.

In Figure 7.15 the phase profile at the side of the intrinsic nanowire also shown in Figure 7.12 is compared with simulations of the phase profile in the vacuum. A positive charge quantity of $2x10^{10}$ e.c. cm^{-2} would cause an approximately similar phase gradient in the vacuum.

7.7.2 Nanowires with axially modulated doping

In Figure 7.16 one side of a phase profile made perpendicular to the nanowire growth direction is shown, as indicated by the dashed line in Figure 7.9C, and compared to simulations. Clearly the phase signal increases in the vacuum when going away from the nanowire, indicating electric fields in the vacuum that could be caused by the negative charge present in the oxide (Figure 7.13D). Similar phase profiles made perpendicular to the nanowire axis were obtained on all nanowires containing n-doped regions [9]. They are clearly different from the phase

[7] In (Völkl et al., 1999) the MIP is described as a negative quantity, however this discrepancy is due only to the use of different conventions of sign.

[8] The sign of the phase change can be inverted by selecting the other sideband during the reconstruction procedure. For this reason the argument is only true if the sideband is chosen such that the phase profile made perpendicular to a nanowire also shows a positive phase shift (profile comparable to Figure 7.12).

[9] Except for one nanowire were the profile shape was similar to Figure 7.12

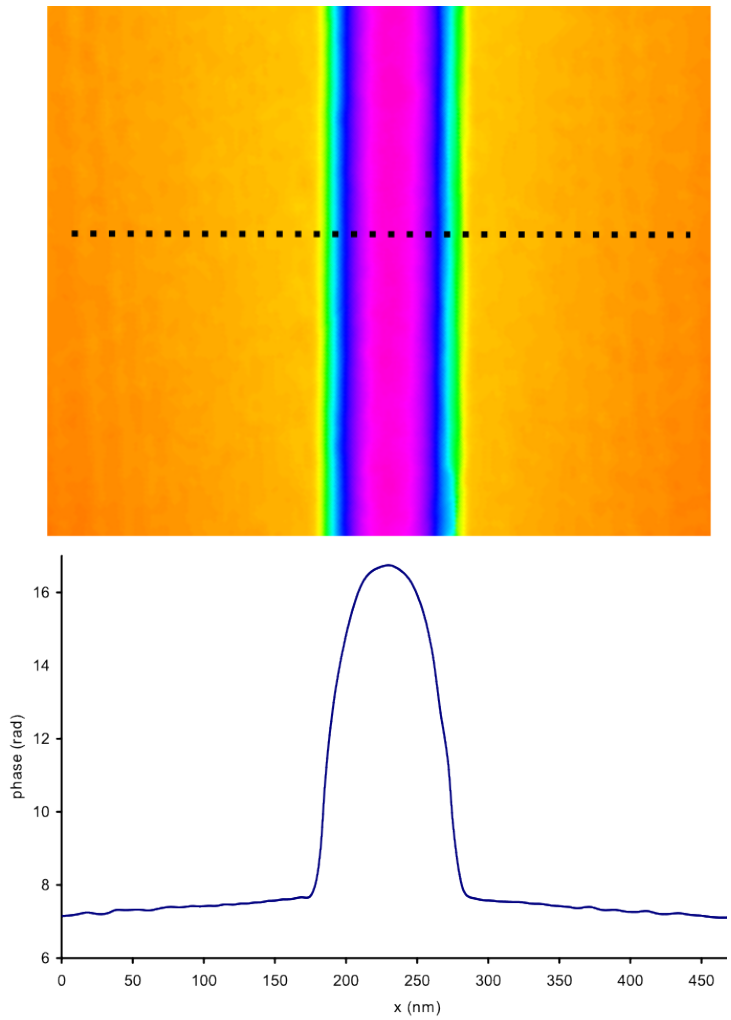

Figure 7.12: Phase image of an intrinsic nanowire and phase profile across the nanowire made at the dotted line. Sample 4634

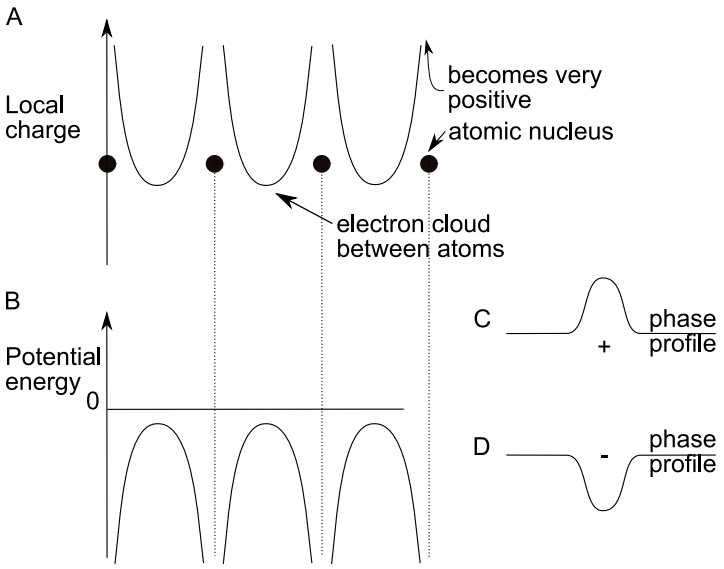

Figure 7.13: (A) Local charge in a 1D crystal. On the nucleus the charge becomes very positive (B) The potential energy of the electron, which is always negative when a (negatively charged) electron enters the positive crystal potential (see also Section 3.8.4). Adapted from (Williams and Carter, 1996). (C) The phase profile over a positive charge. (D) The phase profile over a negative charge.

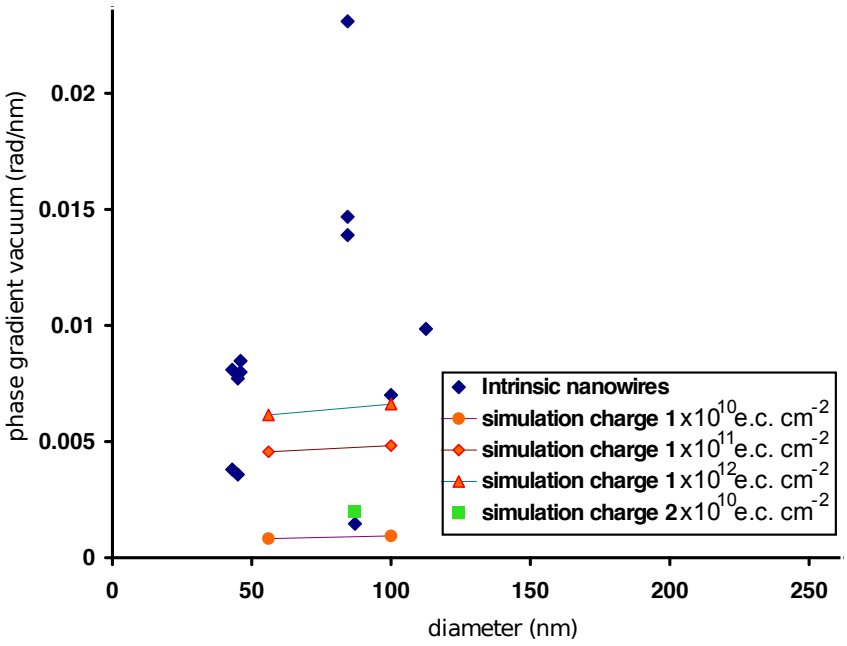

Figure 7.14: Gradient in the vacuum at the side of intrinsic nanowires (blue ◊) and simulation of the gradient in the vacuum for a charged nanowire with a sheet charge of $1x10^{10}$ e.c. cm^{-2} (orange ◯), $2x10^{10}$ e.c. cm^{-2} (green □), $1x10^{11}$ e.c. cm^{-2} (orange ◊) and $1x10^{12}$ e.c. cm^{-2} (orange △). Lines are drawn between simulations of different wire diameters to guide the eye.

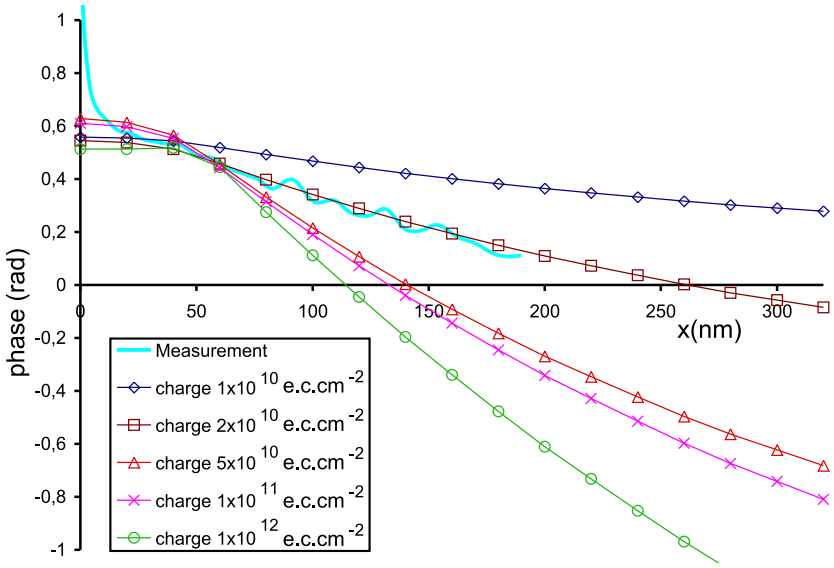

Figure 7.15: The phase signal in the vacuum of an intrinsic nanowire (also shown in Figure 7.12) is compared to the simulated phase signal in the vacuum at the side of the nanowire if different quantities of positive sheet charge are present: 1x10^{10} e.c. cm^{-2} (◊), 2x10^{10} e.c. cm^{-2} (□), 5x10^{10} e.c. cm^{-2} (△), 1x10^{11} e.c. cm^{-2} (×) and 2x10^{12} e.c. cm^{-2} (◯). Sample

signal in the vacuum obtained on intrinsic wires (Figure 7.12).

Clearly the experimental phase profile corresponds well to the simulation with a negative sheet charge of -1x10^{12} e.c. cm^{-2}. However the simulation was performed for an entirely intrinsic nanowire. If the simulation is performed for an entirely n-doped nanowire (10^{19} at. cm^{-3}), a lower gradient of the phase signal in the vacuum is found. According to simulations, the gradient in the vacuum should be different around the doped regions. This is illustrated more clearly in Figure 7.17 were a series of 2D potential profiles is extracted from a 3D cylindrical simulation. Potential variations are present in the vacuum around the doped regions. In the experimental phase images a significant phase signal in the vacuum around the doped region was rarely observed. However in some cases the phase in the vacuum was modulated around the doped regions. An example is shown in Figure 7.18. Using the simulation shown in Figure 7.17 made 60 nm to the side of the nanowire center, the expected phase change in the vacuum for this junctions (10^{20} at. cm^{-3} n-doped - 10^{15} at. cm^{-3} p-doped) can be calculated by integration as described in Section 7.2 to be $\sim$ 0.4 rad. However in the experimental phase image (Figure 7.18) the phase variation is $\sim$ 0.1 rad.

The potential simulation is coherent with the experimental results inside the nanowire structure. However according to simulation a larger phase signal would be expected in the vacuum around the nanowire (Figure 7.17), as already mentioned in Section 7.2.

This discrepancy could be caused by the fixed charges at the wire-oxide interface in the simulation, that result in the simulation of a charged object. Therefore simulations were performed with interface traps at the wire-oxide interface of the same density (1x10^{12} cm^{-2}). If interface traps are present the negative charge trapped at the oxide interface would come from an ionized donor forming a dipole. In this case the structure is electrically neutral, which seems physically more realistic. An agreement with the experimental results inside the nanowire is obtained only if the acceptor type interface traps are ionized (and therefore negatively charged) almost equally on the doped and the intrinsic regions. In the simulation this can be accomplished artificially by definition of the interface traps close to the valence band (i.e. 0.9 V below

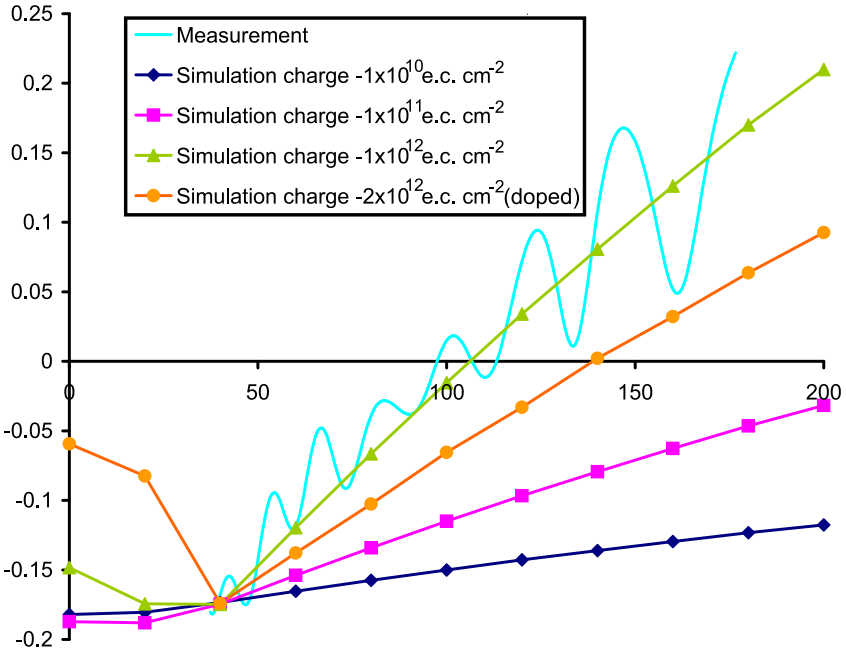

Figure 7.16: Phase signal at the side of the nanowire shown in Figure 7.9, compared to simulations of an intrinsic nanowire (p-type 10^{15} at. cm^{-3}) with varying amount of sheet charge at the oxide-wire interface: -1x10^{10} e.c. cm^{-2} (◇), -1x10^{11} e.c. cm^{-2} (□), -1x10^{12} e.c. cm^{-2} (△) and -2x10^{12} e.c. cm^{-2} (◯). This last simulation (△) was performed for an entirely n-doped nanowire (10^{19} at. cm^{-3}).

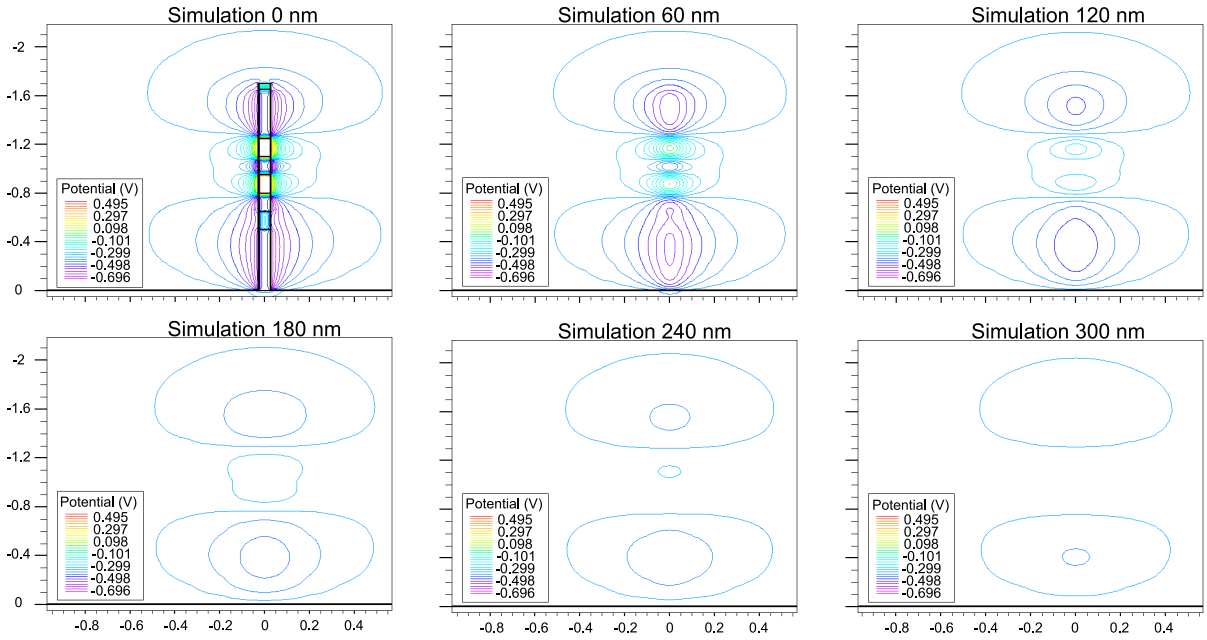

Figure 7.17: 2D potential profiles made at the center of a 3D cylindrical simulation of sample B (see Figure 7.1B): 0 nm, and at increasing distance at the side of the nanowire. The simulation was performed with a sheet charge of -1x10^{12} e.c. cm^{-2}. All axes are in μm.

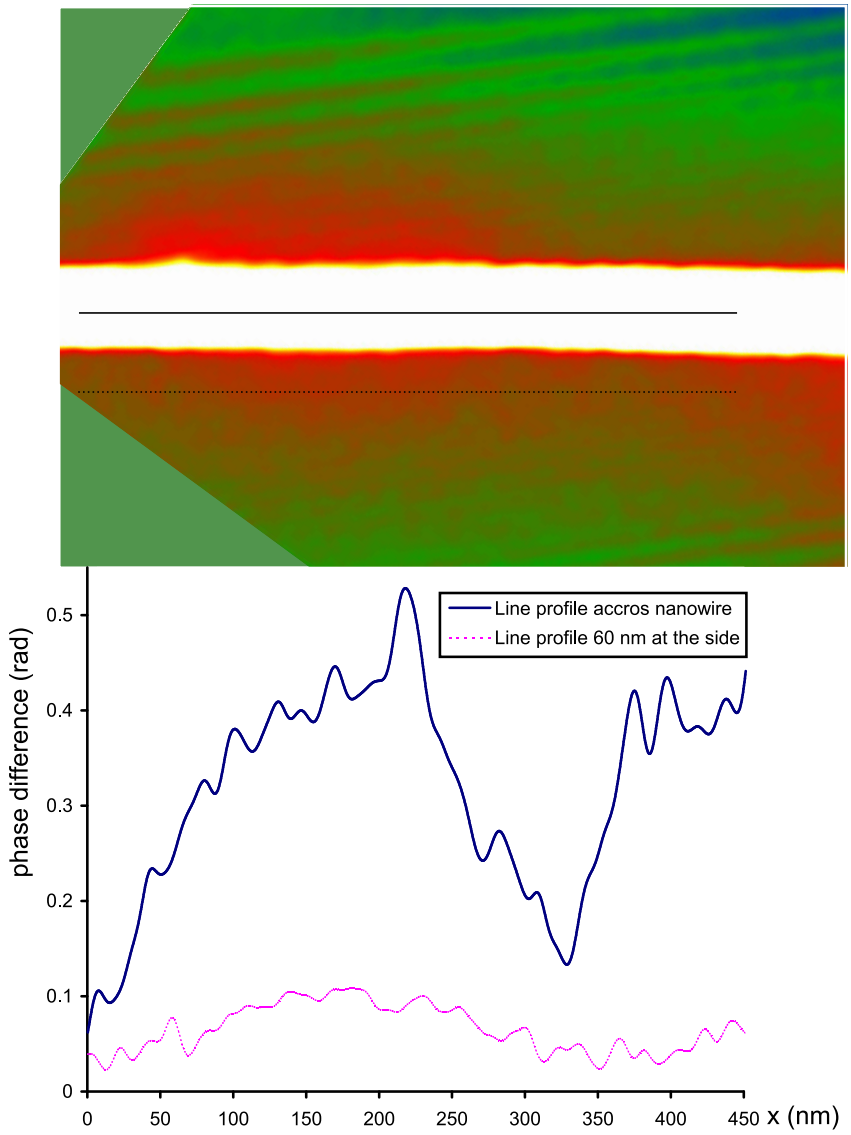

Figure 7.18: A phase image of the same nanowire as shown in Figure 7.8 with modified color scale to show fluctuations in the vacuum. Below a phase profile made across the solid line at the center of the nanowire (solid line) and a phase profile made across the dotted line in the vacuum 60 nm at the side of the center of the nanowire (dotted line). IBM sample B

the conduction band (the silicon bandgap is 1.12 V (Sze, 1985))) [10]. However almost similar potential profiles as obtained using fixed charges can be simulated inside the nanowire and in the vacuum if acceptor type interface traps are defined at the wire-oxide interface 0.9 V below the conduction band with a density around 1x10^{12} cm^{-2} (Figure 7.19) .

Therefore the absence of fringing fields in the vacuum could be caused by the beam-specimen interaction that was not accurately included in the simulation.

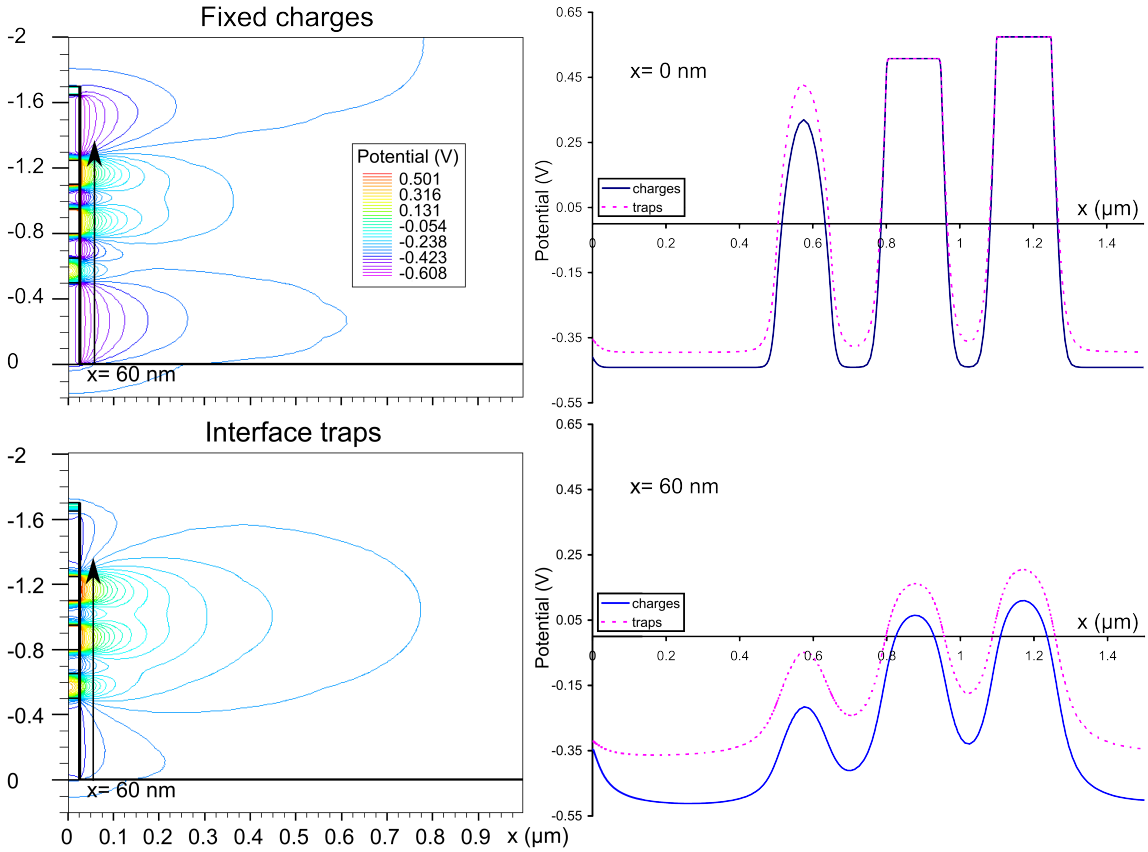

Figure 7.19: On the left, potential profiles obtained by 2D cylindrical simulations either with negative fixed charges at the wire oxide interface (top) or with interface traps 0.9 V below the conduction band (bottom). A nanowire from sample B is simulated (see Figure 7.1B). The density of charges and traps is 1x10^{12} cm^{-2}. On the right, the potential profiles made across the center of the nanowire (x=0 nm, top) and made at 60 nm, as indicated by the arrow (bottom) in both simulated potential profiles.

In literature phase signals, or so called fringing fields, were observed in the vacuum when a bulk specimen containing a p-n junction was prepared by cleaving and in-situ biased in the microscope (Twitchett et al., 2002). Apart from (Twitchett et al., 2002), no literature can be found were the expected fringing fields are observed in the vacuum, and even here they are only observed for a biased specimen. Experiments compared to simulation of connected p-n junctions have suggested that positive charges in the surface oxide created by the electron beam are responsible for the absence of fringing fields in the vacuum (Fazzini et al., 2005; Beleggia et al., 2008). They found a positive sheet charge density around 1.5-3x10^{13} e.c. cm^{-2}. It should be noted that simulations including such high positive charge densities on the surface of the studied nanowires result in hardly any potential variations at the junctions, since the complete nanowire volume is depleted.

[10] In literature it is generally agreed that acceptor type interface traps are located in the upper half of the bandgap (Sze, 1985; Schmidt et al., 2007b).

We have shown in this section that it seems the nanowires are charged, which creates a field in the vacuum. The experimental phase gradient in the vacuum at the side of the nanowire was compared to potential simulations in the vacuum at the side of a charged nanowire. If a charged nanowire creates a potential gradient in the vacuum, the reference wave will be perturbed by this potential, as is shown schematically in Figure 7.20.

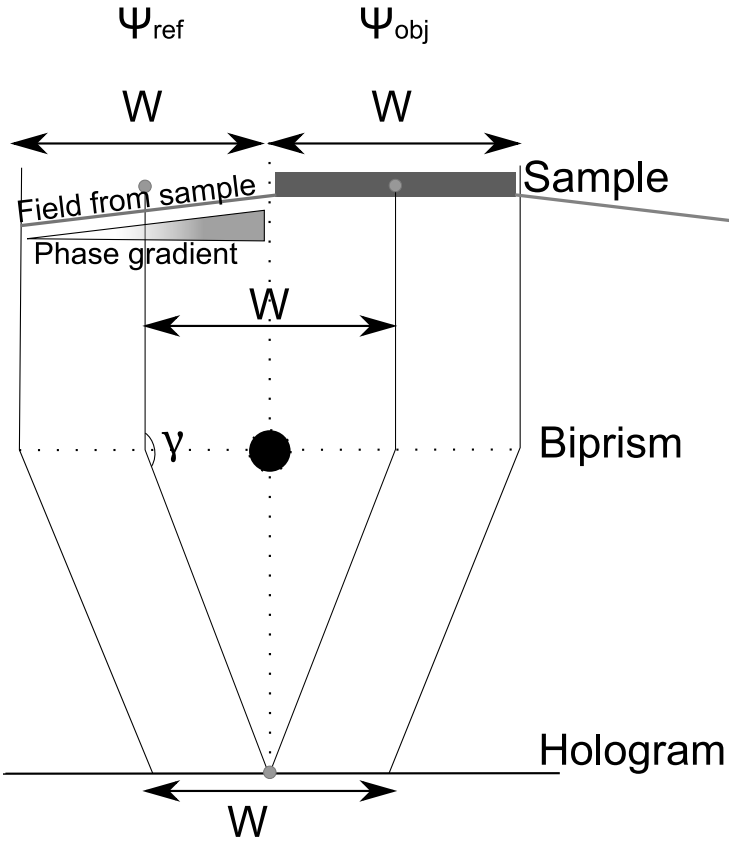

Figure 7.20: Schematic of the hologram formation. The points in the middle of the reference wave and the object wave are superposed in the hologram. If fields extend out from the object in the reference region, the reference wave will be perturbed. The perturbation is in first approximation equal to a linear phase gradient on the reference wave.

Simulations were performed to evaluate the effect of a field on the reference wave as follows. A radial potential profile was made in the simulated potential map perpendicular to the nanowire axis (Figure 7.21A-C). The radial profile was imported in Digital Micrograph, the 2D cylindrical profile was reconstructed from this radial profile and the MIP of the silicon wire was added (Figure 7.21D). A projection of the potential along the electron beam (y-axis) was realized using DM (Figure 7.21E). The obtained projected potential (in V nm) was converted to radians (Equation (3.22)) and used as the phase $\phi(x)$ of the object wave to simulated the hologram using Equation (7.6) (Figure 7.21F). In Figure 7.20 it can be seen that two points superpose in the hologram that are a distance W apart. Therefore $\Psi_{obj} = \exp i\phi(x+\frac{W}{2})$ and $\Psi_{ref} = \exp i\phi(x-\frac{W}{2})$ and the intensity in the hologram can be written as (Matteucci et al., 1991)

$$I_{holo}(x) = \mid \exp i\phi(x+\frac{W}{2})\exp(i\gamma x\frac{2\pi}{\lambda}) + \exp i\phi(x-\frac{W}{2})\exp(-i\gamma x\frac{2\pi}{\lambda}) \mid^2 \tag{7.6}$$

where $\exp(i\gamma x\frac{2\pi}{\lambda})$ is the dephasing of the wave due to the action of the biprism (Yamamotoa et al., 2000), where γ is the deflection angle of the electron wave given by

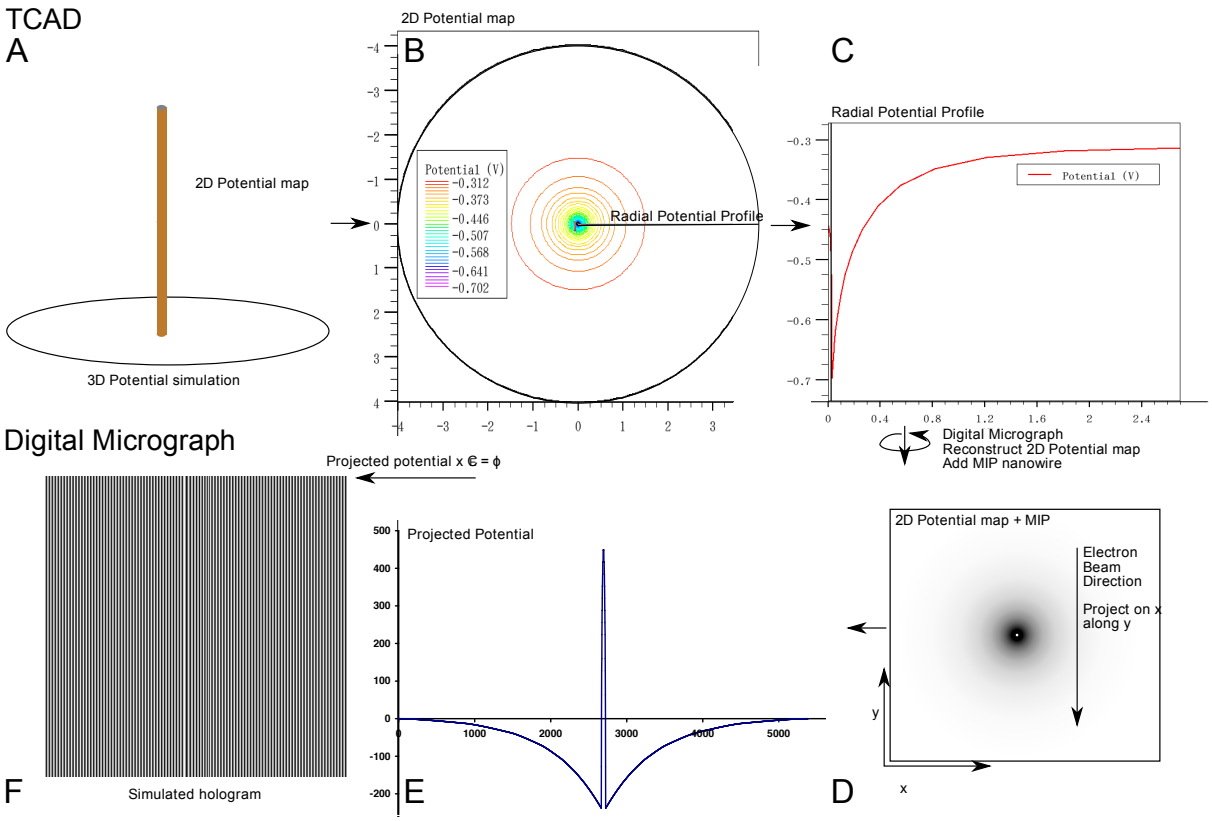

Figure 7.21: The simulation of a hologram from a TCAD potential simulation is graphically illustrated. (A) A 2D potential map is extracted from a 3D cylindrical simulation. (B) A line trace is made in the 2D potential map. It is also possible to start with a 2D potential simulation. (C) Obtained radial potential profile. (D) The radial potential profile is exported to DM and reconstructed including the addition of the MIP of the silicon nanowire (the MIP was taken 12 V). The potential was projected along the beam direction y to obtain (E) the projected potential. (F) The projected potential can be converted to the phase by multiplication with C_E (Equation (3.22)). The hologram is simulated using the phase $\phi(x)$ and Equation (7.6).

$$\gamma = \frac{e\pi}{2E \ln\left(\frac{R}{f_{bp}}\right)} U_b \tag{7.7}$$

where f_{bp} is the distance between the filament and the grounded electrodes of the electron biprism and the other parameters were already defined (Section 3.8.1). The approach used for Equation (7.6) is an approximation, as the size of the biprism and the effects of Fresnel fringes are not taken into account.

The simulations show that the phase gradient at the side of the simulated nanowire was independent of the presence of the field in the reference wave. This is due to the use of two reference regions, defined symmetrically with respect to the nanowire axis to obtain a symmetrical phase image with respect to the nanowire (see Section 3.8.3). Because the phase gradient at the side of a charged nanowire is linear in first approximation over a few hundred nm (see Figure 7.12 and Figure 7.16), a linear gradient is present in the reference wave which would create a linear phase ramp in the phase image. Such a linear phase ramp can be removed easily with the use of suitable reference regions.

7.8 Influence of the gold catalyst

The nanowire is capped with a gold catalyst, that is expected to form a Schottky barrier with silicon, and has a different workfunction than silicon. Also traces of the catalyst can be present on the nanowire sidewall (Chapter 5). In this section we assess the influence of the gold catalyst and gold clusters on the experimental results.

We have already mentioned that the surfaces of nanowires with axially modulated doping are covered by gold clusters only on the doped regions (sample A) or on the complete wire surface (sample B). Also charges appear to be present at the oxidized interface, caused either by interface traps or fixed charges. It should be noted here that gold is known to create deep electron traps (Tavendale and Pearton, 1983). Therefore the possibility exist that the interface charges are (partially) due to the presence of gold.

Undoped wires were studied with and without gold clusters on the nanowire sidewall. The gold clusters are too small to see in either the phase or amplitude image because they are distributed homogeneously and the spatial resolution is not sufficient. On the intrinsic nanowires, no difference was observed if phase profiles made perpendicular to the nanowire axis were compared, obtained at regions with or without gold clusters on the nanowire surface (the phase profiles always have a shape as shown in Figure 7.12). This would indicate that the gold has actually little influence on the wire-oxide interface charge density in the intrinsic nanowires.

It is unclear why the 10^{19} at. cm^{-3} doped region systematically shows a larger step in phase than the 10^{20} at. cm^{-3} doped region (Figure 7.9C-D). A similar effect was observed in Figure 7.5, where the doped region close to the gold catalyst particle shows a decreased phase signal. An explanation could be that carriers present in the first doped region flow into the gold catalyst or create a buildup of charge near the catalyst interface, due to the difference in work function, effectively reducing or masking the dopant related potential. The gold catalyst may also charge under the influence of the electron beam and act as a reservoir of charges, which partially deplete the first doped region. In the potential simulations no effect of the presence of gold on the doped region next to it is observed. The effect of gold can therefore be attributed either to the beam-specimen interaction, or to inaccurate boundary conditions in the simulation (Section 7.2).

7.9 The mean inner potential

The holography data obtained on intrinsic and doped nanowires was also used to measure the MIP of silicon. The MIP can be calculated simply by measuring the phase shift over a nanowire using a phase profile made perpendicular to the nanowire axis (e.g. Figure 7.12) and the nanowire thickness by Equation (3.22). In literature values for the silicon MIP can be found ranging from 9 to 12 V (Völkl et al., 1999), which is quite a large dispersion, especially if these variations are compared to variations that can be caused by doping contrast (~ 1 V in bulk samples, see also Table 7.1). Indeed a large dispersion in MIP was found experimentally. In Figure 7.22 the MIP is plotted as a function of nanowire radius [11]. In Figure 7.22 it can be seen that the MIP of the nanowires varies from 11 to 20 V with an average around ~ 16 V, much higher than generally found in literature. Most data points indicate a trend of increasing MIP for decreasing wire radius, although some scatter is present. This effect of sample size on the measurement of the MIP has been reported in literature for gold clusters (Popescu et al., 2007), where it was attributed to surface strain. In Section 3.8 possible reasons for the increase of the MIP as a function of size were already indicated. It was not observed that the lattice distances gradually increased at the surface for decreasing nanowire size (within the precision of HRTEM measurements). For this reason a redistribution of nuclei (due to strain) seems improbable. Possibly an increasing delocalization and redistribution of valence electrons for decreasing nanowire size causes the increase in MIP. Quantum confinement is not expected for these nanowire diameters, although electro-statical effects can be expected (Niquet et al., 2006). It has been suggested that the increase in MIP for decreasing specimen size is due to the definition of the MIP, that is no longer valid for thin specimens (Lichte, 2008a).

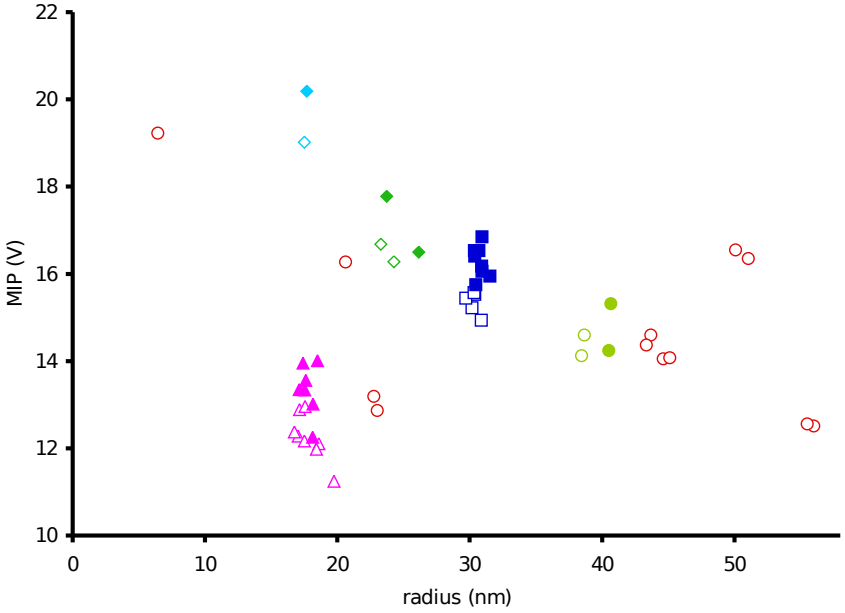

Figure 7.22: The MIP of the nanowires is plotted as a function of the nanowire radius. Intrinsic nanowires, or nanowire regions are indicated by open symbols, n-doped nanowire regions (10^{20} at. cm^{-3}) are indicated by filled symbols. Color coding is used for nanowires that contain doped segments, where the results obtained on one nanowire are indicated by the same symbol of the same color. Samples IBM A 5122 4633 4634 4967

It seemed possible that the dispersion in the measured values for the silicon MIP was caused by charging of the sample. For this reason the MIP is plotted as a function of the gradient in the vacuum at the side of intrinsic nanowires in Figure 7.23. As no correlation is visible it seems

[11] The nanowire radius was determined by fitting a cylinder to the phase profile, that was calibrated by BF images.

that the measured MIP is independent of charging of the sample. However it is known that the step in phase measured over a p-n junction can be influenced by charging of the sample (Cooper, 2009; Cooper et al., 2007b; Cooper et al., 2008).

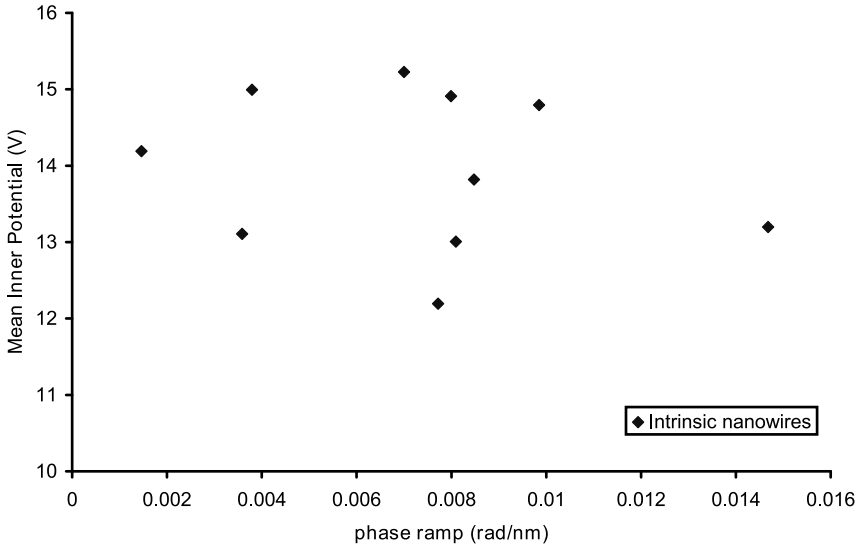

Figure 7.23: MIP of intrinsic nanowires plotted as a function of the phase gradient in the vacuum at the side of the nanowire (with a diameter ranging between 43 and 112 nm). Samples 4633 4634 4967

7.10 Dopant deactivation

Several treatments were realized on the doped nanowires (Samples A and B, Section 7.1) that resulted in a suppression of doping contrast in the phase images. The treatments were:

- A hydrofluoric acid (HF) -vapour etch of 2 min (49%)
- Irradiation with 400 kV electrons
- Removal of gold clusters using potassium iodide (KI)

After these treatments no phase contrast at all was observed in the nanowire. There seem to be two possible explications for this phenomenon. The dopants are either deactivated or chemically removed from the sample. Possibly the surface of the nanowire is damaged during the process in such a way that the amount of surface defects becomes equal to the doping concentration. Due to these defect trap states the doping is deactivated. For a wire diameter of 60 nm the density of surface defects should be $1.5\text{x}10^{14}$ cm^{-2} to deactivate a doping concentration of 10^{20} at. cm^{-3}.

When an HF-vapour etch was performed, the phase signal in the doped regions seemed slightly noisier. The HF vapour is supposed to attack only the oxide and not destroy the surface, and the native oxide that was regrown should be grown under the same conditions as the original native oxide (at room temperature (RT) and ambient conditions). Possibly the phosphorus dopant atoms are removed entirely from the nanowire during the HF step. This is possible if HF is highly reactive with phosphorus at the nanowire surface and the diffusion rate of the phosphorus in silicon is sufficient to diffuse over 30 nm (the nanowire radius) in 2 min (the length of the HF vapour step) at room temperature, or the dopants are mostly close to the nanowire surface (M. Fernández-Serra and Blase, 2006). Movement of heavy antimony (Sb) atoms in silicon was already observed in HRSTEM experiments (Yamasaki et al., 2007), al-

though these experiments were performed at RT, they are also performed under a high energy electron beam, that might favourise itself the dopant diffusion. It was found that an Sb atom can hop to another site in 11 sec. This would mean that the dopant atom can be displaced maximally by 12 Si bond lengths (2.33 Å) in 2 min, not sufficient to diffuse over the nanowire radius in 2 min, however the phosphorus atom is much smaller, but the experimental conditions are less energetic. In literature it can be found that the phosphorus diffusion does indeed depend on the extent of free surface (Ghostagore, 1970), and nanowires of this size have an exceptional surface to volume ratio. Also it was found that pile up phosphorus close the the silicon- silica interface can be removed in a HF dip (Kalkofen et al., 2005). If the diffusivity found in (Ghostagore, 1970) is extrapolated, a diffusion coefficient of 10^{-41} cm^2 s^{-1} is found. Using the random walk equation $\sqrt{(D\tau)}$, where τ is the time interval, the average diffused distance in 2 min is $1x10^{-12}$ nm. **Therefore it seems improbable that the dopant atoms are chemically removed from the nanowire during either one of this treatments.**

An increase in surface defect states seems the more probable explanation (for HF vapour etch or KI gold etch).

When the nanowire was irradiated using 400 kV electrons, dopants were possibly deactivated by creation of defects due to beam damage. It was observed during the TEM experiment that defects were created only in the doped regions, the contrast changes and defects appeared only in the doped regions, Figure 7.24.

7.11 Conclusion & Outlook

Holography of doped and undoped nanowires is not yet entirely understood. Our work shows some of the problems that are present for the (quantitative) interpretation of holography data, and might help to solve these problems, such as the absence of fringing fields in the vacuum.

In conclusion doping concentrations as low as 10^{18} at. cm^{-3} can be detected with respect to intrinsic silicon in nanowires as thin as 60 nm, as well as the position of the junction.

It has been shown that the MIP of silicon nanowires increases for decreasing wire diameter, however a relatively large spread in the measured values for the MIP was present. Therefore the doping concentration can only be estimated if a junction is present and holography on a homogeneously doped nanowire seems not promising at present to estimate the doping concentration.

The amount of charge at the oxide interface strongly influences the observed potential profile. For this reason correct interpretation of the data is possible only by comparison with simulated potential profiles. The abruptness of the junction was estimated between 7.5-30 nm/decade doping concentration. The phase gradient in the vacuum at the side of nanowires containing doped segments indicates negative charging of the wires of the same order of magnitude as the negative surface charges. The phase gradient in the vacuum at the side of intrinsic nanowires indicates positive charging of the wires of varying importance, possibly due to the electron beam (Fazzini et al., 2005; Beleggia et al., 2008). Fringing fields in the vacuum around the doped regions were only rarely observed and smaller than predicted by simulations.

The influence of the electron beam on the acquired potential profiles is complicated and not completely understood. For this reason the influence of the electron beam on the charge density in the sample should be simulated and taken into account in future simulations.

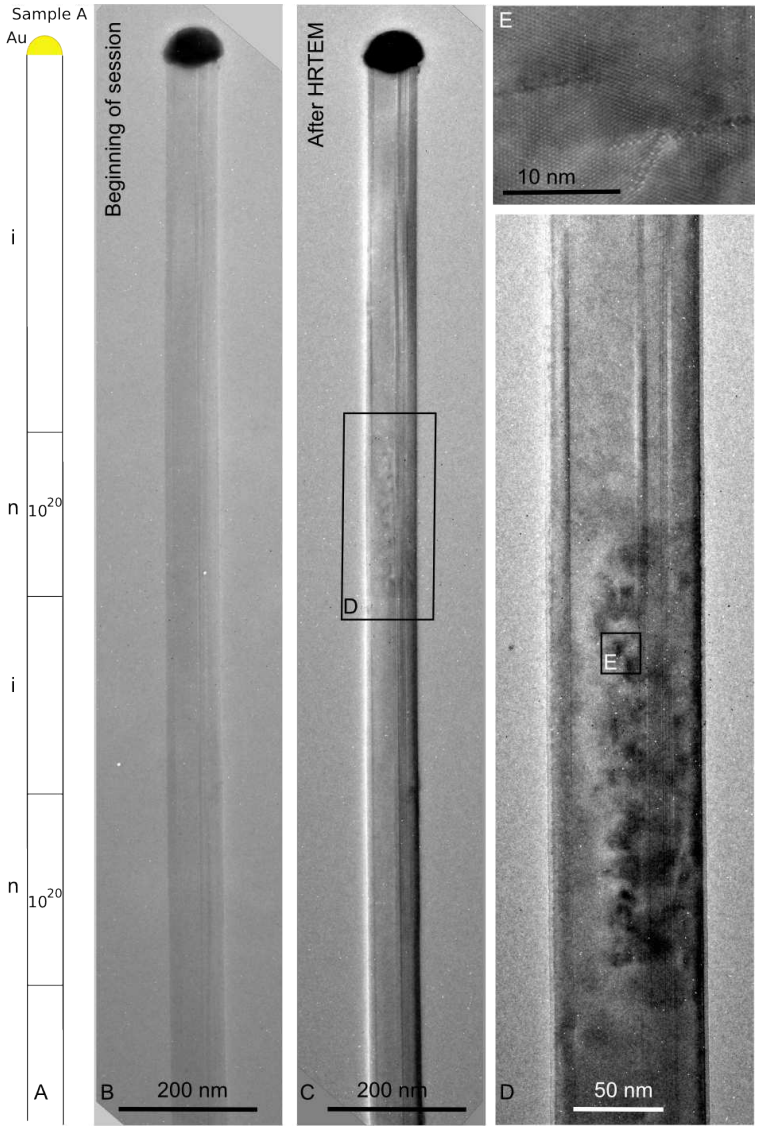

Figure 7.24: BF images and HRTEM image that illustrate the apparition of beam damage in the doped zone. The wire grows in the ⟨111⟩ direction, the vertical streaks are caused by numerous vertical twin defects. Sample A

Quantitative measurement of the doping concentration in nanostructure seems possible in the near future if variations due to gold clusters and faceting can be removed. An improved experiment to extract quantitative dopant concentrations from semiconductor samples would be to bias the specimen in-situ in the TEM (Twitchett et al., 2004). The electrical connections to the nanowire would also remove the carriers generated by the electron beam more effectively (Cooper et al., 2008; Cooper et al., 2007b).

A stable and high performance microscope is indispensable for the study of such nano-objects as well as suitable sample preparation.

8

CONCLUSION

The goal of this thesis was to better understand and control nanowire growth by means of structural, chemical and electronic characterization of nanowires by transmission electron microscopy.

Control over surface properties is a very important point for the integration of nanowires in devices. The surface can be modified due to the chemical composition e.g. gold clusters, the crystallographic facets (sawtooth faceting) and the quality of the surface oxide, since defect states or trapped charges can be present. Furthermore the electrical properties of nanowires have to be controlled using dopant atoms. During this PhD many nanowire samples were studied and some aspects of nanowire growth have been clarified. Three central themes have been studied:

- The behavior of the gold catalyst.
- Crystallographic properties.
- Active dopant detection.

In the following a conclusion for each topic is presented and compared to literature.

8.1 Control of gold diffusion

In literature it was already shown that gold can diffuse over the wire sidewall (Hannon et al., 2006) and gold clusters can be present on the wire surface (Werner et al., 2006). In other publications no gold could be observed on the nanowire sidewall (Cui et al., 2001; Allen et al., 2008). However the influence of growth parameters on the gold diffusion was not clear.

We have shown in Chapter 5 that control can be obtained over gold diffusion from the catalyst particle over the nanowire sidewall, by changing the growth parameters, that in turn influence the nanowire sidewall properties. The quantity of absorbed silane at the nanowire sidewall seems to be the important parameter, that depends both on silane partial pressure and temperature, and also an effect of nanowire size was observed[1]. It was already shown in (Kodambaka et al., 2006a) that the sidewall properties are determining for the gold diffusion, but they used low quantities of oxygen to modify the wire sidewall. In this work we have shown that in ad-

[1] These results have been published in (den Hertog et al., 2008). A patent was constructed using findings related to the article.

dition to oxygen, the silane gas itself can modify the sidewall properties and thereby the gold diffusion, by adsorption on the wire sidewall. In most nanowire growth experiments addition of oxygen is impossible due to the explosive nature of the silane gas. Control of gold diffusion using silane (and the temperature) is therefore a method that can be more easily applied in most growth experiments.

The gold appears to diffuse as a thin film of liquid gold or liquid Au/Si eutectic over the nanowire sidewall. During or after growth this layer dewets and gold clusters are observed on the nanowire sidewalls. Calculations were performed to explain the observed dewetting phenomenon.

Control of the surface diffusion of gold provides a tool to fabricate long, uniform diameter structures with flat sidewalls and no gold clusters decorating the nanowire sidewall. Also the possibility exists to modify the sidewall morphology after growth by performing a post-growth anneal during which the gold can diffuse over the wire sidewalls and surface reconstruction can occur resulting in a saw-tooth faceting. In this way gold clusters can be deposited on the nanowire sidewall, or a part of it, in a controlled and reproducible way, allowing direct functionalization of the nanowire. Furthermore the possibility exist to grow tree-like structures by using the deposited clusters as catalysts to grow nanobranches. Applications like the realization of nanowire web's (Cimalla et al., 2007), could benefit from such nano-trees, as it would avoid the additional deposition of gold nanoclusters at the nanowire surfaces.

8.2 The crystal structure and defects in the nanowire volume

Several different nanowire growth systems were studied with the aim to achieve better control over nanowire dimensions, surface properties, growth direction and doping, combined with a high crystalline quality, and to avoid contamination due to the gold catalyst ((Allen et al., 2008; Hannon et al., 2006)). Of the tested catalyst materials (Cu, Ni, and Pt), only Cu seems relatively promising since a high density of straight and long nanowires can be obtained with a small diameter dispersion, and copper is slightly more compatible with microelectronics applications.

In the observed silicon nanowires three favourised growth directions ($\langle 111 \rangle$, $\langle 110 \rangle$ and $\langle 112 \rangle$) have been observed, coherent with literature (Schmidt et al., 2005). However the $\langle 112 \rangle$ direction was also frequently observed in relatively large nanowires (diameter$>$100 nm), generally if vertical defects were present.

In general the crystalline quality of wires grown with a gold catalyst using silane was high. If other catalyst materials or precursor gasses were used more defects were observed. Especially in nanowires grown with a Ni catalyst and with a gold catalyst in combination with TMA, many vertical twin defects are present, as observed in an FIB prepared wire section sample (Figure 4.3 and Figure 6.13). Therefore the different grains can superpose in the TEM image/DP, which can be falsely interpreted as a wurtzite hexagonal crystal structure. Clear evidence shows that in the observed nanowires no hexagonal phase (with long range order) was present, but a high twin defect density can mimic a hexagonal structure on the length of a few atomic planes.

8.3 Doping characterization

In electron holography literature of active dopant detection in semiconductor samples mostly thick (100-500 nm) FIB prepared samples are studied (Twitchett et al., 2004; Cooper et al., 2007b; Rau et al., 1999).

Here we show for the first time doping contrast in thin (60 nm) nanowires with axially modulated doping (Chapter 7). This was possible due to an excellent microscope, nanowires with well controlled doping level[2] and suitable TEM sample preparation.

Using off axis electron holography the electrical properties of nanowires with axially modulated doping were studied, with the goal to determine the active dopant concentration. We show that active dopant detection is possible in nanostructures such as nanowires. Doping concentrations as low as 10^{18} at. cm^{-3} can be detected with respect to intrinsic silicon in nanowires as thin as 60 nm. Potential simulations have been performed to better understand the experimental results. Comparison of experiments and simulations showed that the surface properties of these nanostructures, and more specifically the amount of charge present at or near the surface, are extremely important for the potential distribution in the structure. The estimated amount of charge present at the wire-oxide interface is -1x10^{12} e.c. cm^{-2}, which is in excellent agreement with the amount of charge estimated from transport measurements (Björk et al., 2009).

The phase ramp in the vacuum at the side of intrinsic and axially modulated doped nanowires was compared to simulations of intrinsic nanowires with charge at the oxide interface. A positive charge of 2x10^{10} e.c. cm^{-2} or higher was estimated to be present on intrinsic nanowires. A negative charge around -1x10^{12} e.c. cm^{-2} was found on nanowires with axially modulated doping, coherent with the previous results.

According to simulations, fringing fields around the doped regions should be present in the phase image, however they were only rarely observed and smaller than according to simulation. In literature such fringing fields were observed only once with an applied bias voltage (Twitchett et al., 2002), and their continuous absence was explained by the presence of positive charges in the surface oxide, caused by the electron beam (Fazzini et al., 2005). They estimate an amount of charges around 1.5-3x10^{13} e.c. cm^{-2}. If such a high positive charge density was present, no potential variations would be expected in the studied nanowires in this work. Indeed it seems that also in our case simulations are not coherent with the experimental results in the vacuum due to the influence of the electron beam. The effect of the electron beam on the charge distribution in the sample should be simulated and included in the potential simulations.

8.4 Outlook

Valuable information for nanowire growth was obtained using TEM characterization. The study of new nanowire growth systems will always require TEM analysis. Some TEM based techniques such as HRTEM and EDX can be routinely used. Others, such as holography, should be further developed. This work shows that we are not so far from quantitative holography.

Doping characterization in nanowires seems a very promising subject, because for the application of nanowires in devices the doping has to be understood and controlled on the nm length

[2] These nanowires were supplied by IBM Zurich.

scale. Holography is the only tool that can probe active dopant atoms in the nanowire volume and could therefore in principle play a key role in the study of dopants in nanostructures. As shown in this work several problems have to be resolved to allow quantitative holography, such as the influence of the electron beam and the sample induced noise. In-situ biasing of a nanowire during the holography experiment should be realized for more quantitative results.

It is not only the doping concentration that is of interest but also the abruptness of the junction, especially for devices based on tunneling such as tunneling field effect transistors (Reddick and Amaratunga, 1995). Therefore the concentration gradient at the junction was estimated to be 7.5-30 nm/decade by comparison with simulations. The precision of this comparison is limited mostly by noise introduced by the specimen, and could be improved. Possibly in-situ biasing coupled with simulations could give more quantitative information also on this point.

We have started to study the effects of chemical (HF and KI etch) and physical (400 kV electron irradiation) treatments on the doping contrast, that is strongly related to the surface properties of the nanowire. More insight into the effects of the surfaces and defect states at the wire-oxide interface can possibly be obtained using known methods to passivate such defects, for example a low pressure atomic hydrogen plasma or a molecular hydrogen anneal (Tavendale and Pearton, 1983). Possibly such a treatment could "reactivate" the doping in the examples shown in Section 7.10, where after particular treatments no doping contrast was observed. If the deactivation of dopants is due to an increased level of defect states, it should be reversible if the defects can be passivated. These experiments could give more insight into the origin of the negative charges that seem to be present at the wire-oxide interface, clarify the dopant deactivation mechanism and provide tools to design the physical properties of the wire-oxide interface at the same time. Also it would be interesting to compare the surface properties of etched nanowires with the VLS grown nanowires, that have been studied here.

9

RÉSUMÉ EN FRANÇAIS

Ce chapitre présente un résumé en français de cette thèse. Ceci est demandé par l'Université Joseph Fourier, parce que cette thèse a été réalisée en France, mais a été redigée en anglais.

Le but de cette thèse a été, de mieux comprendre les mécanismes de croissance des nanofils de silicium faits par le procédé Vapeur Liquide Solide (VLS), et de contrôler la structure cristalline, la composition chimique et les propriétés électroniques grâce à la microscopie électronique en transmission (MET). Il est important d'avoir une bonne connaissance et un bon contrôle de tous ces aspects des nanofils afin qu'ils puissent être introduits avec succès dans des dispositifs. Les nanofils sont des objets quasi cylindriques ayant un diamètre de taille nanométrique (en pratique, les fils observés ont eu des diamètres allant de 6 à 500 nm) et d'un grand rapport longueur sur largeur. Pour cette raison, ces objets sont considerés comme des objets unidimensionnels et peuvent avoir des propriétés physiques intéressantes et différentes du matériau massif.

Le manuscript comporte quatre parties principales. L'introduction présente le but, les méthodes et les moyenes mis en œuvre pour réaliser ce travail. Ensuite les trois thèmes principaux étudiés dans cette thèse sont présentés: la diffusion du catalyseur d'or, les défauts cristallins et la mesure des dopants par holographie.

9.1 Introduction sur les Nanofils, la Microscopie électronique en Transmission et la Préparation des échantillons MET

9.1.1 Introduction

Le chapitre 1 (Chapter 1) situe le travail scientifique de cette thèse : il explique l'intérêt de l'étude et résume les résultats obtenus de façon à ce qu'une peronne non-scientifique puisse en apprécier le travail.

9.1.2 Nanofils, croissance, histoire et applications

Le chapitre 2 (Chapter 2) donne un peu plus de détails sur les nanofils : les différentes façons de les élaborer, quelques définitions se rapportant à ce type de nano-objets, les premières publications et les applications.

9.1.3 La Microscopie électronique en transmission

Le chapitre 3 (Chapter 3) décrit rapidement les différentes techniques de microscopie électronique en transmission qui ont été utilisées dans cette étude et la raison pour laquelle une technique spécifique a été employée. Après quelques rappels de base, l'holographie électronique est décrite plus précisément car cette technique est relativement nouvelle au CEA-Grenoble. À la fin du chapitre, les caractéristiques des microscopes utilisés sont rappelées. En particulier, la résolution de phase et la résolution spatiale du microscope FEI TITAN en holographie électronique sont données en fonction du grandissement du microscope et du voltage du biprisme.

9.1.4 Préparation des échantillons

Le chapitre 4 (Chapter 4) décrit les méthodes classiques de préparation d'échantillons pour la microscopie électronique en transmission. Pendant la thèse trois méthodes de préparation rélativement innovantes ont été développées. La première méthode utilise le clivage du substrat de silicium sur lequel les nanofils ont poussé afin de pouvoir étudier les nanofils perpendiculaires à la direction de croissance. Cette méthode est expliquée dans la Figure 4.2. Ce type de préparation permet d'observer le nanofil attaché à son substrat de croissance, sans que le nanofil ait subi un traitement chimique ou physique. La deuxième méthode a pour but d'observer le fil le long de l'axe de croissance. Pour obtenir une section du fil, il y a deux possibilités. Si le diamètre du nanofil est important ($\geq 200\,\text{nm}$) et la densité des fils sur le substrat de croissance est faible, il est souhaitable de préparer une section du fil par FIB (Focussed Ion Beam). Les étapes de préparation sont décrites dans la Figure 4.3 et l'échantillon obtenu dans la Figure 6.13. Si les nanofils sont de petits diamètres, une deuxième méthode pour préparer une section du fil est possible. Les fils sont d'abord déposés de façon alignée sur un substrat propre. Puis un autre substrat propre est collé au premier, de façon à obtenir un collage classique de "cross-section". Les méthodes classiques de préparation sont alors appliquées : tronçonnage, polissage et amincissement par bombardement ionique pour obtenir des images le long de la direction de croissance des nanofils (Figure 6.7).

9.2 Contrôle de la diffusion d'or

Dans le chapitre 5 (Chapter 5) le comportement du catalyseur d'or pendant la croissance des fils est étudié. Nous avons démontré que, pendant la croissance, l'or peut diffuser sur les flancs des nanofils. Nous avons déterminé les paramètres de croissance qui permettent d'annihiler cette diffusion: la pression partielle du silane et la température (voir Table 5.2). Nous avons expliqué que cette absence de diffusion est dûe à l'absorption de silane sur les flancs des nanofils. Le diamètre du nanofil influe également sur ce phénomène de diffusion. Nous montrons également que la présence d'or semble modifier le facettage des nanofils. Si l'or est présent sur les flancs, deux types de facettes alternent dans la direction de croissance (apellés dans la littérature facettage en dents de scie (Ross et al., 2005)). Sans or, la circonférence du fil est toujours hexagonale mais le facettage en dents de scie le long de la direction de croissance est absent. Dans la littérature, il est connu que l'or peut diffuser sur les flancs (Hannon et al., 2006), et que des clusters d'or peuvent être présents sur les flancs (Werner et al., 2006). Dans d'autres publications, les observations montrent qu'il n'y a pas d'or en surface (Cui et al., 2001; Allen et al., 2008), mais ceci n'est pas commenté dans le texte de ces papiers. Un effet de l'oxygène sur la diffusion d'or a déjà été observé (Kodambaka et al., 2006a), mais nous sommes les premiers

à mettre en evidence un effet dû au silane lui-même. Cet effet a été publié dans Nanoletters (den Hertog et al., 2008).

9.3 Cristallographie: détermination de la direction de croissance et des défauts dans certains nanofils de silicium

Le deuxième grand thème de cette thèse, présenté dans le chapitre 6 (Chapter 6), est l'étude des propriétés cristallographiques des nanofils, c'est à dire essentiellement la détermination de la direction de croissance des nanofils et de leur qualité cristalline : présence de défauts linéaires ou plans. La caractérisation structurale a montré que trois directions de croissance sont favorisées ($\langle 111 \rangle$, $\langle 110 \rangle$ et $\langle 112 \rangle$) ce qui est cohérent avec la littérature (Schmidt et al., 2005). En général, peu de défauts sont présents dans les fils élaborés avec un catalyseur d'or et avec du silane comme précurseur. Lorsque d'autres métaux catalytiques ou gaz précurseurs sont introduits, la densité des défauts, surtout celle des macles, peut augmenter considérablement. Pour cette raison, des grains différents présents dans le cristal peuvent se superposer dans l'image TEM ou dans le cliché de diffraction, ce qui est interprété dans la littérature comme étant une phase hexagonale. Grâce à une section de fil préparée par FIB et à l'analyse des clichés de diffraction et d'images expérimentales, nous démontrons clairement qu'il n'y a pas de phase hexagonale mais qu'une haute densité de macles peut imiter une phase hexagonale. Ces résultats ont été publié dans Journal of Applied Crystallography (Cayron et al., 2009).

9.4 Caractérisation des dopants par holographie électronique

Le troisième grand thème de cette thèse est l'étude des dopants actifs par holographie électronique (Chapter 7). Nous montrons pour la première fois un contraste de dopants dans les nanofils fins non uniformément dopés (diamètre de 60 nm). Nous montrons qu'il est possible de déterminer une concentration de 10^{18} at. cm^{-3} par rapport au silicium intrinsèque dans des fils de 60 nm de diamètre. La comparaison entre expériences et simulations du potentiel montre que l'état de surface, et plus précisément la quantité de charge sur ou proche de la surface, est extrêmement important et influence énormément la mesure finale. Pour rendre la simulation cohérente avec l'expérience, une quantité de charges sur l'interface fils-oxyde de l'ordre de -1x10^{12} e.c. (charge électronique) cm^{-2} est nécessaire. Cette valeur est en parfait accord avec la quantité de charges trouvées par des mesures de transport électrique (Björk et al., 2009). De même, le signal de phase à côté du nanofil dans le vide a été comparé à la simulation. Nous observons que la pente de la phase dans le vide observée expérimentalement pour un fil avec des régions dopées est cohérente avec la quantité de charge sur l'interface fils-oxyde (-1x10^{12} e.c. cm^{-2}). Pourtant, selon la simulation, des variations de phase devraient être présentes autour des régions dopées, ce qui était rarement observé expérimentalement. Pour cette raison, nous supposons que le faisceau d'électrons modifie la densité de charges dans l'échantillon, ce qui n'est pas pris en compte dans la simulation. Ces résultats sont accepté pour publication dans Nanoletters et les proceedings de MSM 2009.

9.5 Conclusion & Avenir

Beaucoup d'échantillons ont été étudiés au cours de cette thèse, fourni par deux équipes de croissance (SINAPS et IBM). Ce travail en équipe et en collaboration a été très motivant et

constructif. En quelques mots, nous résumons les trois thèmes principaux de cette thèse:

1. Le contrôle de la diffusion d'or de la particule catalyseur sur les flancs du fil. Ce contrôle permettra de faire crôitre des nano-architectures plus originales comme par exemple un réseau de nanoarbres (Cimalla et al., 2007).

2. La caratérisation structurale et l'analyse des défauts cristallins. D'un point de vue général, la maîtrise de la direction de croissance et de la qualité cristalline sont des élements importants pour l'intégration des nanofils dans des dispositifs.

3. La mesure des dopants actifs par holographie électronique. Bien que ces mesures ne soient pas encore quantitatives, elles ont permis d'identifier les problèmes et les artéfacts qui devraient être résolus: l'influence des charges en surface, l'influence du faisceau sur la distribution de charges, le bruit introduit par l'échantillon et l'influence du catalyseur d'or sur le signal de phase de la région dopée voisine. Une mesure de dopage plus quantitative semble possible si les deux extrémités du fil sont portés à un potentiel différent, c'est à dire si le fil est connecté. Cette méthode a déjà été appliquée aux échantillons massifs avec succès (Twitchett et al., 2002). L'application de contacts au nanofil a comme avantage supplémentaire d'obtenir des conditions limites bien définies ce qui permet une meilleure comparaison entre expérience et simulation. Ces contacts peuvent également faciliter l'évacuation des charges introduites par le faisceau.

NOMENCLATURE

α	semi convergence angle
Δf	the defocus
δ	semi illumination angle
ϵ_o	the permittivity of the vacuum,
γ	deflection of electron wave due to the action of the biprism
κ	Boltzmann constant $1.3806504 \times 10^{-23}\,\mathrm{JK}^{-1}$
λ	the lattice parameter of a 2D lattice in Chapter 5
λ	the wavelength of the electron
λ_i	the mean free path for inelastic scattering
$\mho$	the potential energy
μ_{sc}	spatial coherence
$\overrightarrow{q}$	spatial frequency
$\phi(r)$	the electron phase
Ψ	the image wavefunction
ψ	the object wavefunction
σ	the surface tension
σ_c	The atomic cross section for coherent scattering
σ_f	the gold surface energy
σ_s	the silicon surface energy
σ_{fs}	the gold-silicon interface energy

σ_{ic}	the atomic cross section for incoherent scattering
θ	the half scattering angle
θ_B	the Bragg angle
$A(r)$	image electron amplitude
a_o	the bohr radius
C	Fringe contrast
c	the speed of light in vacuum
C_s	spherical abberation
d	a constant to calculate the phase resolution Section 3.8.2
E	the energy of the incoming electron beam
e	the charge of an electron
E_0	the rest energy of an electron
f	Atomic scattering factor electrons
f_x	the scattering factor for x-rays
h	planck's constant ($6.6262x10^{-34}$ Js)
I	Intensity
$i(r_s)$	Fourier-transform of the source intensity distribution
k	wave vector $1/\lambda$
k_C	the Coulomb constant (8.99x10^9 N m^2 C^{-2})
M	the Debye-Waller factor
m_o	the rest mass of the electron
N_A	acceptor concentration
N_D	donor concentration
n_i	intrinsic carrier concentration
N_{av}	the number of avogadro ($6.02\ 10^{23}$ at. mol^{-1})

R	the radius of the electron biprism
t	Sample thickness
U_b	the distance between the filament and the grounded electrodes of the electron biprism
V	the electrostatic potential
ADF	Annular Dark Field
BF	Bright Field
CTF	Contrast Transfer Function
DFT	Density Functional Theory
DP	Diffraction Pattern
EDX	Energy Dispersive X-ray Spectroscopy
FEG	Field Emission Gun
HAADF	High Angle Annular Dark Field
HRTEM	High Resolution TEM
ML	monolayer
Observed along a [011] direction	$\equiv$[011] DP
sccm	standard cubic centimeters per minute
silica	silicon oxide
STEM	Scanning Transmission Electron Microscopy
TEM	Transmission Electron Microscopy
VLS	Vapour Liquid solid (method)
ZA	Zone Axis

Appendices

A

COMPLEMENTARY INFORMATION FOR CHAPTER 3

A.1 History of Transmission Electron Microscopy

In the following two sections the development of TEM and some very basic theory is described for readers unfamiliar with TEM.

Historically electron microscopes were developed because of the limited resolution of light microscopes, since the spatial resolution δ depends on the wavelength λ used, according to the Rayleigh criterion

$$\delta = 0.61 \frac{\lambda}{\mu \sin \beta} \tag{A.1}$$

where μ is the refractive index of the viewing medium and β is the semiangle of collection of the magnifying lens(Williams and Carter, 1996). Since the wavelength of an electron is much smaller than the wavelength of light it seemed possible to attain much higher resolution. The idea of an electron microscope was first proposed by Knoll and Ruska in 1932, five years after the demonstration that an electron had wave like properties (Davisson and Germer, and Thmopson and Reid). Within one year the concept was put into practice, and four years later Transmission Electron Microscopes (TEM's) were commercially available. Later on it was realized that electron microscopy is not only interesting because of the resolution. Since the specimen is bombarded with negatively charged particles with a wave like character all sorts of interactions can occur that allow structural, chemical, electrical and magnetic analysis of the sample. A summary of all the signals generated when a high energy electron beam hits a specimen is shown in Figure A.1 (Williams and Carter, 1996)

The electrons traversing the sample can be scattered by the electrons in the crystal or by the atom core. We can distinguish two scattering processes: elastic scattering (the electron doesn't lose energy during the scattering process) and inelastic scattering (the electron loses energy). If the electrons are scattered in a particular direction this is called diffraction, which is both due to the wavelike nature of the electrons, their coherence and the periodic spacings present in the crystal. This will be shown in more detail in Appendix A.2.2. The wavelength of the electron depends on its acceleration energy:

$$\lambda = \frac{h}{\sqrt{2 m_0 e E}} \tag{A.2}$$

where m_0 is the restmass of the electron (9.1095x10^{-31} kg), e is the elemental unit of charge

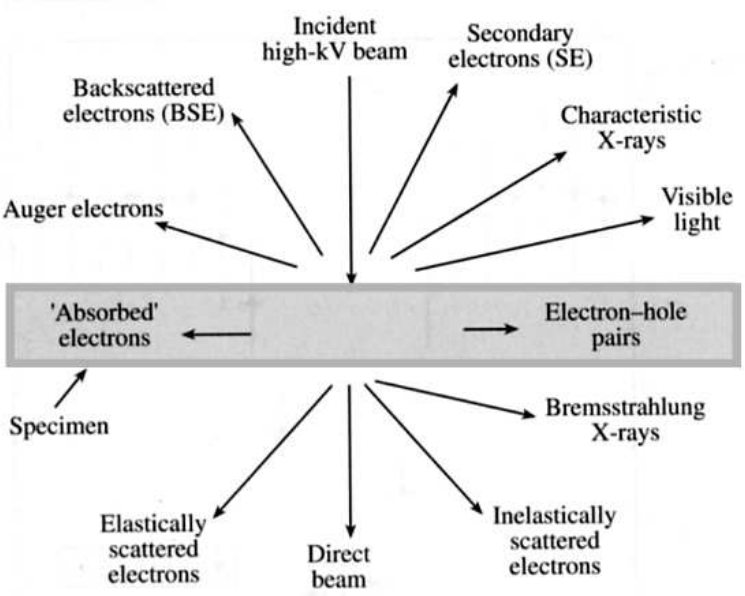

Figure A.1: Schematic illustration of all signals that are generated in the sample when it is bombarded by a high energy electron beam (Williams and Carter, 1996).

($1.6021765 \cdot 10^{-19}$ C) and E is the acceleration voltage. This formula doesn't take into account relativistic effects, that will become more and more important at higher acceleration voltages. The most important consequence of this formula is that the wavelength of an electron decreases for increasing acceleration voltages. Since the resolution depends on the wavelength, Equation (A.1), one way of increasing the resolution of the microscope is to increase the acceleration voltage. This was the approach to surmount resolution limits in the seventies and eighties. Microscopes with 1 to 3 MeV acceleration voltage were build. The drawback of bombarding the specimen with these very high energy electrons is that there is a lot of specimen damage (for comparison: the threshold for knock on damage (the energy needed to knock an atom off its lattice site) is 150 kV for silicon (Stoddard et al., 2005). Also the acceleration voltage becomes unstable at such high acceleration voltages which degrades the resolution (due to the chromatical aberrations of the lens system). For this reason another approach to surmount resolution limits appeared around 1970 (Hardy, 1967), with the aim to improve the resolution by correcting the aberrations of the electron lenses. Electron lenses suffer from chromatic aberrations (meaning that the focal point of the lens is not the same for different wavelengths). This can be corrected by ensuring that the spread in wavelengths of the electrons is as small as possible, by introducing a monochromator (an energy filter) that reduces the energy spread (Hely, 1982) (Hardy, 1967) (Koops et al., 1977). Modern monochromators can reduce the energy spread to $<$ 0.2 eV at 200 kV (Matijevic et al., 2007). However the most important aberration is the spherical aberration (meaning that the focal point of the lens is not the same for electrons that enter in the center and electrons that enter near the edges of the lens). One of the first successful examples of correcting this aberration was shown by (Haider et al., 1995). Now the resolution limit of a state of the art aberration corrected microscope is 0.5 Å (TEAM, 2008) and most modern microscopes are operated between 200 and 300 kV. There is a trend to go to lower voltages to increase the specimen-electron interaction and decrease the damage of the specimen, while maintaining high resolution imaging capabilities, which is possible due to aberration correction.

A.2 Basic theory of Transmission Electron Microscopy

In conventional TEM the wavelike character of electrons is mostly employed to form images on the screen. How is this done? Any electron microscope has an electron gun to emit electrons, several types exist that differ in brightness and coherence. After the gun there is one or a series of electromagnetic lenses that form the electron probe: the condenser system. The probe passes trough the sample, which is very thin since it has to be transparent to electrons and passes through the objective lens that is directly behind the specimen. These two are so close that the specimen is actually in the magnetic field of the objective lens (which can be a problem if one tries to study magnetic properties of the sample). The objective lens is the most important lens of the microscope since its performance determines most of the performance of the microscope. The reason is that electron lenses suffer from chromatic and spherical aberrations much more than light lenses. Since the objective lens is the only lens in the system that has to deal with electrons entering over a large range of angles, the aberrations in this lens will influence the image most and determine the resolution (Rodenburg, 2008). The objective lens is followed by the projector system that magnifies the image, which is projected onto a phosphor screen to give the user a global view. The image on the center of the phosphor screen can then be projected on film or onto a charge coupled device (CCD) to record the image. The electrons are first converted to photons because until now the devices to detect photons are more effective then the ones to detect electrons, but manufacturers are putting an effort into direct detection of electrons to increase detection efficiency. The final goal is obviously to detect a single electron. In Figure A.2 a schematic of a TEM column is shown. The lens system can be used to form a parallel beam on the sample (TEM), or to form a very punctual probe that is scanned over the sample. In this last case the intensity collected by a detector at each probe position will make up one pixel of the image (STEM). This is basically the same idea as in Scanning Electron Microscopy (SEM). Most modern microscopes can be operated in both modes but also machines dedicated to one of the two modes are used. At each level of the microscope: condenser system, objective lens and projector system, apertures of different sizes can be inserted. These are used to modify the incoming electron beam (condenser aperture), choose which region of reciprocal space we want to study and limit spherical abberations (objective aperture) and choose which spatial region of the sample we want to study in reciprocal space (selected area aperture in the projector system). The electromagnetic lenses consist of copper coils placed in soft iron polepiecies. This is the basis of each TEM. Depending on what one wants to study with the particular microscope other units can be added to allow a certain technique, this will be described in Section 3.3 to Section 3.8. The principle of (coherent) imaging in the TEM is described in (Section 3.2). In Appendix A.2.1 the resolution limit of TEM is described in some more detail.

A.2.1 The Contrast Transfer Function

In the following the relation between object and image wave is explained in more detail, which leads us to the resolution limits of the microscope. This section is complemetary to Section 3.2.

The microscope can be regarded as a linear system, the consequence is that the action of objective and projector lenses can be described by a transfer function in Fourier space (Williams and Carter, 1996)

$$\Psi(r) = F^{-1}(T(\overrightarrow{q}).F\psi) \tag{A.3}$$

where F (F^{-1}) denotes the Fourier (inverse Fourier) transform and $T(\overrightarrow{q})$ denotes the transfer

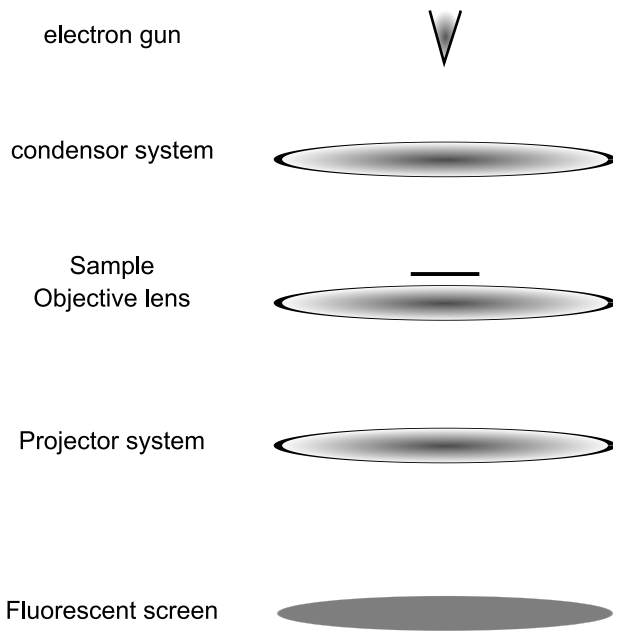

Figure A.2: Schematic of a TEM column.

function (CTF) depending on a spatial frequency $\overrightarrow{q}$. The effect of the transfer function is that the object wave is modified by the microscope system and for this reason the image wave that arrives at the detector is modified and contains aberrations. $T(\overrightarrow{q})$ can be written as (Williams and Carter, 1996)

$$T(\overrightarrow{q}) = A(\overrightarrow{q})E(\overrightarrow{q})\exp(i\chi(\overrightarrow{q})) \tag{A.4}$$

for weak phase objects $T(\overrightarrow{q})$ reduces to (valuable in the Weak Phase Object Approximation (WPOA))

$$T(\overrightarrow{q}) = A(\overrightarrow{q})E(\overrightarrow{q})2\sin\chi(\overrightarrow{q}) \tag{A.5}$$

where $A(\overrightarrow{q})$ is the aperture function, $E(\overrightarrow{q})$ is the envelope function and $\chi(\overrightarrow{q})$ is the phase distortion function, generated by aberrations. The aperture function and the envelope function have the same effect, high spatial frequencies are damped. $\chi(\overrightarrow{q})$ is given by (Williams and Carter, 1996)

$$\chi(\overrightarrow{q}) = \frac{2\pi}{\lambda}\left(C_s\frac{\lambda^4\overrightarrow{q}^4}{4} + \Delta f\frac{\lambda^2\overrightarrow{q}^2}{2}\right) \tag{A.6}$$

where C_s is the spherical aberration of the objective lens and Δf is its defocus. The CTF depends on parameters that characterize the microscope and mainly the objective lens (C_s and $E(\overrightarrow{q})$), and parameters that be changed by the user (λ, $A(\overrightarrow{q})$ and Δf). Abberation can be compensated by defocus and an optimal transfer function is obtained: the Scherzer defocus (Williams and Carter, 1996)

$$\Delta f_{sch} = -1.2\sqrt{C_s\lambda} \tag{A.7}$$

The effect of the transfer function is that not all spatial frequencies are equally well transmitted by the optical system. The contrast transfer function of the JEOL 4000EX is shown as an exam-

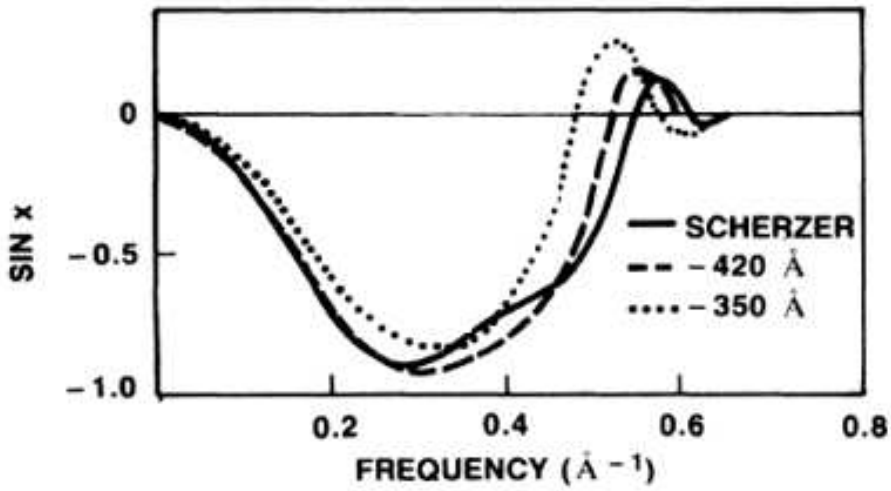

Figure A.3: Contrast Transfer function of the JEOL 4000 EX (Ourmazd et al., 1986) including the envelope function. The microscope parameters are E_a = 400 kV, C_s = 1 mm, C_c = 1.4 mm, Δf_{sch} = -49 nm and ΔE = 1.6 eV. The CTF is also indicated for two other values of Δf

ple in Figure A.3 at Scherzer defocus and two other focus values. For higher spatial frequencies (which correspond to smaller distances in real space) the contrast transfer function oscillates around zero. This means that for these high frequencies the contrast in the image can no longer be interpreted relatively intuitively (Williams and Carter, 1996). Due to the contrast transfer function we can observe an inversion of contrast for changing defocus and between different spatial frequencies.

A.2.2 Wave interference and diffraction

Waves can only interfere coherently if their phase difference is an integral multiple of 2π. The phase can also be written as $2\pi kr$ where k is the magnitude of the wave vector ($k = \frac{1}{\lambda}$) and r is the distance the wave has propagated. In a crystal atoms are arranged in a regular pattern that creates planes with different interplanar spacings. An example of the unit cell of the silicon crystal can be found in (Stokes, 2008). Now in order for two waves that scatter on different but parallel planes to interfere coherently there is a relation between the angle of incidence onto the plane in question, and the interplanar distance d, to create a path distance that generates a phase difference equal to an integral multiple of 2π. This is Bragg's Law

$$n\lambda = 2d \sin \theta_B \tag{A.8}$$

where n is an integer and θ_B is the Bragg angle. This process is extremely important in TEM since high resolution images are in fact created by coherent scattering and interference on the crystal lattice planes. A crystal has different planes, with different interplanar distances. A reciprocal lattice point can be attributed to each family of planes. In reciprocal space a family of planes, which have the same interplanar distance, is a spot (the corresponding spatial frequency). Each crystal therefore has a lattice in real space, and we imagine its lattice in reciprocal space to be able to understand diffraction phenomena. Because the TEM sample is very thin, each reciprocal lattice point is relaxed in the direction perpendicular to the sample surface and therefore it becomes a rod. Now a sphere can be constructed that cuts through this lattice of reciprocal lattice rods with a radius of $\frac{1}{\lambda}$: the Ewald sphere. The sphere always cuts through the origin O of the reciprocal lattice, and the vector from its center to O represents the wave vector

of the incident electron beam. Where the sphere cuts a reciprocal lattice rod a diffraction spot is observed, even when the Bragg condition isn't entirely fulfilled (Williams and Carter, 1996). If we look at a high resolution TEM image we most often see white (or black) dots on a black (or white) background. What we see is an interference pattern, but because the image looks so much like a direct image of the crystal lattice, with the dots being the atoms, it is tempting to interpret the image in this way. The important advantage of the TEM technique is that an image and its corresponding diffraction can be obtained of the same region on the sample.

A.2.3 Phase information

Here a simple analysis is shown to illustrate that the phase difference between an electron that traversed the specimen and an electron that traversed the vacuum can be related to the crystal potential (Williams and Carter, 1996) in the absence of dynamical diffraction effects (kinematical approximation), to obtain Equation (3.22). It was shown in Appendix A.1 that the wavelength of an electron is related to the acceleration voltage and described by Equation (A.2). Inside the crystal the wavelength will be modified by the crystal potential $V(x, y, z)$, the modified wavelength λ' is given by

$$\lambda' = \frac{h}{\sqrt{2me(E + V(x, y, z))}} \tag{A.9}$$

Therefore if the electron has passed through a slice of material with a thickness dz, the electrons experience a phase shift given by (Williams and Carter, 1996)

$$d\phi = 2\pi\frac{dz}{\lambda'} - 2\pi\frac{dz}{\lambda} = 2\pi\frac{dz}{\lambda}\left(\frac{\lambda}{\lambda'} - 1\right) \tag{A.10}$$

$$d\phi = 2\pi\frac{dz}{\lambda}\left(\sqrt{\frac{E + V(x, y, z)}{E}} - 1\right) \tag{A.11}$$

Since $V/E \ll 1$ (E is 200000 V and V is $\sim$ 10 V) this gives a first order approximation of

$$d\phi \simeq \frac{\pi}{\lambda E}V(x, y, z)dz \tag{A.12}$$

$$d\phi \simeq C_E V(x, y, z)dz \tag{A.13}$$

Here C_E is given by $\pi/\lambda E$ which is valid if the electron wavelength is not influence by relativistic effects. The value of C_E including relativistic effects is given in Equation (3.21).

A.3 Coherence and holography

It was mentioned in Section 3.8 that increasing the biprism voltage has the effect of increasing the distance between the virtual sources and increasing the width W of the hologram. This will also decrease the fringe spacing, which allows a higher spatial resolution but also decreases the contrast since the coherence of the virtual sources is decreased. This can be seen easily by

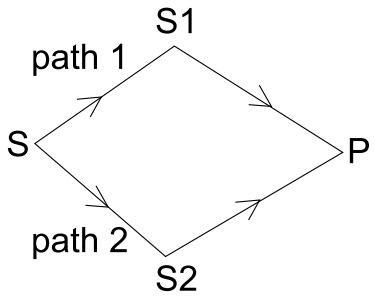

Figure A.4: Schematic diagram that illustrates the generalized ray paths in an interference experiment (Fowles, 1989).

comparison with the classical Young's fringes experiment found in any optics textbook, e.g. (Fowles, 1989). Here we show briefly the relevant equations adapted from (Fowles, 1989) to illustrate the influence of biprism voltage on the loss of coherence.

The spatial coherence distribution is associated with the size of the electron source. The spatial coherence is therefore determined by the real size of the source and the electrons emitted by the source that illuminate the specimen, the effective size of the source, that is influenced by the beam convergence angle α.

Using the Young's fringes analysis, two rays emanate from the slit S (the FEG source in the TEM) to illuminate the apertures S1 and S2 (the virtual sources in off axis holography) and interfere on a screen at the point P (see Figure A.4). At the point P the two fields E1 and E2 are added and the intensity I is given by

$$I = \langle E \cdot E^* \rangle = \langle (E_1 + E_2) \cdot (E_1^* + E_2^*) \rangle = \langle \mid E_1 \mid^2 + \mid E_2 \mid^2 + 2Re(E_1 \cdot E_2^*) \rangle, \tag{A.14}$$

$$I_1 = \langle \mid E_1 \mid^2 \rangle, \qquad I_2 = \langle \mid E_2 \mid^2 \rangle, \tag{A.15}$$

$$I = I_1 + I_2 + 2Re(E_1 E_2^*). \tag{A.16}$$

The * denotes the complex conjugate, $\langle\rangle$ the time average and Re the real part. All quantities are assumed to be stationary which means the time average is independent of the choice of the origin of time.

The time of flight for path 1 is called t_f and $t_f + \tau$ for path two, as the path lengths differ. The interference term $2Re(E_1 E_2^*)$ may be written as

$$2Re\Gamma_{12}(\tau) \tag{A.17}$$

where

$$\Gamma_{12}(\tau) = \langle E_1(t_f) E_2^*(t_f + \tau) \rangle \tag{A.18}$$

$\Gamma_{12}(\tau)$ is the mutual coherence function or the correlation function.

A normalized correlation function can be defined called the "degree of partial coherence" $\gamma_{12}(\tau)$

$$\gamma_{12}(\tau) = \frac{\Gamma_{12}(\tau)}{\sqrt{\Gamma_{11}(0)\Gamma_{22}(0)}} = \frac{\Gamma_{12}(\tau)}{\sqrt{I_1 I_2}} \tag{A.19}$$

where $\Gamma_{11}(0)$ $\Gamma_{22}(0)$ are the self-coherence or autocorrelation functions, and by definition equal to I_1 and I_2 respectively. The intensity I can now be written

$$I = I_1 + I_2 + 2\sqrt{I_1 I_2} Re\gamma_{12}(\tau) \tag{A.20}$$

An interference pattern results if $\mid \gamma_{12}(\tau) \mid$ is nonzero. $0 < \mid \gamma_{12}(\tau) \mid < 1$ indicates partial coherence ($\mid \gamma_{12}(\tau) \mid = 1$ corresponds to complete coherence).

Using Equation (A.20) I_{max} and I_{min} can be expressed:

$$I_{max} = I_1 + I_2 + 2\sqrt{I_1 I_2} \mid \gamma_{12} \mid \qquad I_{min} = I_1 + I_2 - 2\sqrt{I_1 I_2} \mid \gamma_{12} \mid \tag{A.21}$$

The fringe visibility or contrast (defined in Equation (3.17)) depends on I_{min} and I_{max} (since the intensity I on the CCD detector is read out as the number of electron counts N) and can therefore be written as

$$C = \frac{2\sqrt{I_1 I_2} \mid \gamma_{12} \mid}{I_1 + I_2} \tag{A.22}$$

If $I_1 = I_2$ the fringe visibility is given by

$$C = \mid \gamma_{12}(\tau) \mid \tag{A.23}$$

The fringe visibility is equal to the modulus of the degree of partial coherence, and therefore a direct measure of the partial coherence. However other contributions to the fringe visibility are also present (see Equation (3.18)).

The FEG source is only partially coherent due the finite source size and instabilities (see Section 3.2) and therefore the electron wave has a finite coherence length and time.

If the biprism voltage voltage is increased, the two virtual sources $S1$ and $S2$ are pushed further apart. Because the path length from the FEG source to the virtual sources increases, the size of the virtual sources is magnified due to the finite size of the FEG source, degrading the mutual coherence and the fringe visibility. Generally it is assumed that the loss of spatial coherence is the most important factor that degrades the fringe visibility for increasing biprism voltage (Midgley, 2001; Völkl et al., 1999). For longer acquisition times the temporal coherence also becomes important.

However determination of the spatial coherence at the level of the specimen is slightly more complicated than this simple analysis shows.

At this point it is important to differentiate between the semi convergence angle α and the illumination angle δ[1]. This is illustrated schematically in Figure A.5.

[1] In literature (Völkl et al., 1999) the illumination angle is often referred to as β, however this is confusing as the collection angle is also generally called β (Figure 3.1). 2δ is also referred to as the full angular width of the electron source as seen from the object plane (Lehmann, 2004), where it is called Θ_c.

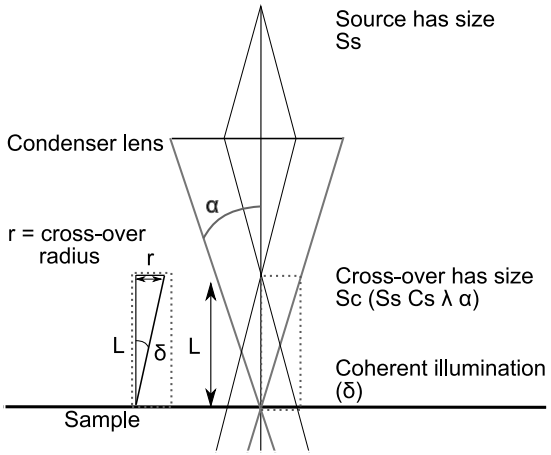

Figure A.5: Schematic describing the difference between the beam convergence angle α and the illumination angle δ. The region in the dotted box is shown magnified on the left. Here the raypaths are shown for an overfoccused condenser lens, the analysis is similar for the underfocussed case. Adapted form (Völkl et al., 1999).

In a TEM microscope with a thermionic emitter the beam is generally focused on the specimen for high resolution images, to have sufficient electron counts in a relatively short acquisition time (to minimize sample drift). In this case the illumination angle experienced by the specimen (δ) is the same as the convergence semi angle α. However if the electron source is a FEG the source size is smaller and the brightness (number of electrons or current density per unit solid angle (Williams and Carter, 1996)) is higher. For this reason the size of the beam cross-over ($2r$, as indicated in Figure A.5) is very small. Therefore the cross-over can be placed below or above the specimen plane to illuminate a larger part of the specimen. The beam convergence angle remains unchanged, however the angle of illumination on the specimen δ is now defined by the cross-over size $2r$, and the height L between the specimen plane and the cross-over.

Clearly the spatial coherence of the electrons that reach the sample is influenced by many parameters. The important parameter is the illumination angle that determines the coherence at the level of the sample. The illumination angle is determined by other parameters of the microscope.

We start at the gun (Figure A.5), which has a finite size Ss. The beam convergence angle α (that can be modified by an aperture) influences the effective size of the source that is used to illuminate the specimen. For this reason the size of the cross-over above (or below) the specimen is influenced by Ss, α, the spherical aberrations of the lens system C_s and the wavelength λ. The size of the cross over and the height L in turn determine the illumination angle and the spatial coherence at the level of the specimen.

The mutual coherence function (Equation (A.23)), or fringe visibility due to the partial spatial coherence C_{sc} (Equation (3.18)), can therefore be described using the illumination angle δ (that contains all other contributions as described) and the width of the hologram W that contains the action of the biprism, by (Lehmann, 2004)

$$C_{sc} = \exp\left(-\left(\pi k \delta W\right)^2\right) \tag{A.24}$$

The spatial coherence can be improved by reducing δ, by increasing L (under or overfocus of the beam) to achieve nearly parallel illumination or by decreasing the effective source size by reducing the beam convergence angle α by inserting a smaller condenser aperture, at the cost

of reducing the number of electrons. As mentioned earlier the electron beam is made highly astigmatic to achieve nearly parallel illumination perpendicular to the biprism to have a high spatial coherence in the direction of superposition of the virtual sources, however the beam is more focussed in the direction parallel to the biprism to increase the number of electron counts and the phase resolution (Equation (3.23)).

It should be noted that coherence is not a property of the system, but can be defined for a certain plane in an optical system (Schattschneider et al., 2000). More detailed information on coherence can be found in (Verbeeck et al., 2005; Potapov et al., 2007).

A.4 The p-n junction: calculation of the built-in potential

The derivation of Equation (3.32) is shown, adapted from (Sze, 1985). A p-n junction is created if a piece of semiconductor doped with p-type dopants is connected to a piece of semiconductor doped with n-type dopants. The p-type dopants take an electron from the available valence electrons (which is similar to the donation of a hole to the crystal lattice) and become negatively ionized (see Figure A.6A). The n-type dopants donate an electron to the crystal lattice and become positively ionized (see Figure A.6B). When the p and n-doped parts of semiconductor are connected, the large gradient in carrier concentration at the junction causes carrier diffusion (see Figure A.6C). Holes from the p-side diffuse into the n-side and electrons from the n-side diffuse into the p-side. The holes that leave the p-side leave a negatively charged donor ion behind and the electrons that leave the n-side leave a positively charged ion behind, which are left uncompensated since these ionized donors/acceptors are not mobile but fixed to the crystal lattice. This process creates a positive space charge layer on the n-side and a negative space charge layer on the p-side. The space charge regions creates an electric field pointing from the positive charges to the negative charges (as indicated in Figure A.6C). The electric field is in the direction opposite to the diffusion current for each type of charge carrier. For this reason a thermal equilibrium is reached (for a given temperature without any external excitations) where the net current flow over the junction is zero. Therefore the drift current must equal the diffusion current for each carrier. The total current for holes J_p can be written as

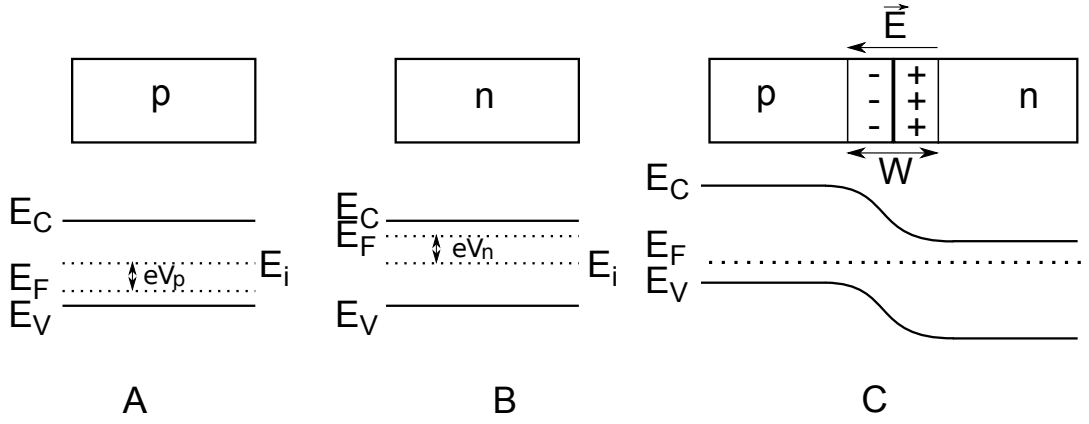

Figure A.6: (A) Uniformly doped p-type semiconductor and the band structure. (B) Uniformly doped n-type semiconductor and the band structure. (C) The p-n junction if the p and n-type parts are brought together and the energy band diagram of in thermal equilibrium. The electric field E due to the space charge region and its direction as well as the depletion width W over the junction are indicated (Sze, 1985).

$$J_p = J_p(drift) + J_p(diffusion) = 0 \tag{A.25}$$

which can be written as

$$J_p = e\mu_p P\left(\frac{1}{e}\frac{dE_i}{dx}\right) - kT\mu_p\frac{dp}{dx} = 0 \tag{A.26}$$

where μ_p is the hole mobility, related by the Einstein relation to the diffusivity D_p as

$$D_p = \left(\frac{kT}{e}\right)\mu_p \tag{A.27}$$

and E_i is the energy value at half the value of the bandgap. The hole concentration can be expressed as

$$p = n_i e^{\frac{E_i - E_F}{kT}} \tag{A.28}$$

where n_i is the intrinsic carrier concentration. The constant Fermi level required at thermal equilibrium results in a unique space charge distribution at the junction, given by Poisson's equation (Equation (3.29)). In regions far from the junction charge neutrality is maintained, therefore

$$N_D - N_A + p - n = 0 \tag{A.29}$$

and Equation (3.29) simplifies to

$$\frac{d^2V}{dx^2} = -\frac{\rho}{\epsilon} = -\frac{e}{\epsilon}(N_D - N_A + p - n) = 0 \tag{A.30}$$

where N_D and N_A are the acceptor and donor concentrations and p and n are the hole and electron concentrations respectively.

In the p-doped region far from the junction we suppose that $N_D = 0$ and $p \gg n$. From the definition of the electric potential (the potential energy change per unit charge) it follows that the hole potential V_p is given by

$$V_p = -\frac{1}{e}(E_i - E_F) \tag{A.31}$$

We use $N_D = n = 0$ and $p = N_A$ in Equation (A.29) and substitute the result in Equation (A.28) to obtain an expression for V_p

$$V_p = -\frac{1}{e}E_i - E_F \quad = -\frac{kT}{e}\ln\frac{N_A}{n_i} \tag{A.32}$$

Similarly for an n-type neutral region the electric potential with respect to the Fermi level is given by

$$V_n = -\frac{1}{e}(E_i - E_F) \quad = \frac{kT}{e} \ln \frac{N_D}{n_i} \tag{A.33}$$

The built-in potential V_{bi} is given by $V_n - V_p$, therefore

$$V_{bi} = \frac{kT}{e} \ln \frac{N_A N_D}{n_i^2} \tag{A.34}$$

Clearly this formula is valid only if the location of valence and conduction bands with respect to the Fermi level is determined only by the doping concentrations (N_A and N_D) and no external charges are present. Also this analysis supposes that the length of both n- and p-doped regions is longer than the depletion width W in the respective regions. In an experimental situation this is not always the case.

A.5 Schottky contact

A Schottky contact is specified at the nanowire-gold interface Section 7.2, where the surface potential of the contact V_s is given by (Silvaco International, 2007)

$$V_s = WF - aff - \frac{E_g}{2e} - \frac{kT}{2e} \ln \frac{N_C}{N_V} \tag{A.35}$$

where aff is the electron affinity of the semiconductor material, E_g is the bandgap, N_C is the conduction band density of states, N_V is the valence band density of states, and T is the ambient temperature. We will briefly recall the meaning of the different parts of this equation adapted from (Sze, 1985).

In Figure A.7 a Schottky contact between gold and silicon is schematically shown. The silicon is intrinsic. If the two materials are brought together the Fermi levels of the two metals must be equal in thermal equilibrium and the vacuum level must be continuous. For the ideal metal semiconductor contact the barrier height for electrons is given by $WF - aff$. The surface potential V_s is given by the energy difference between the conduction band at equilibrium and the conduction band at the contact (see Figure A.7B).

The Fermi level in an intrinsic semiconductor is given by

$$E_F = E_i = \frac{E_C + E_V}{2} + \frac{kT}{2} \ln \frac{N_C}{N_V} = \frac{E_g}{2} + \frac{kT}{2} \ln \frac{N_C}{N_V} \tag{A.36}$$

At room temperature the second term is generally much smaller than the bandgap and therefore the Fermi level of an intrinsic semiconductor lies very close to the middle of the bandgap. The potential at the surface of the contact is therefore given by

$$V_s = WF - aff - \frac{E_F}{e} = WF - aff - \frac{E_g}{2e} - \frac{kT}{2e} \ln \frac{N_C}{N_V} \tag{A.37}$$

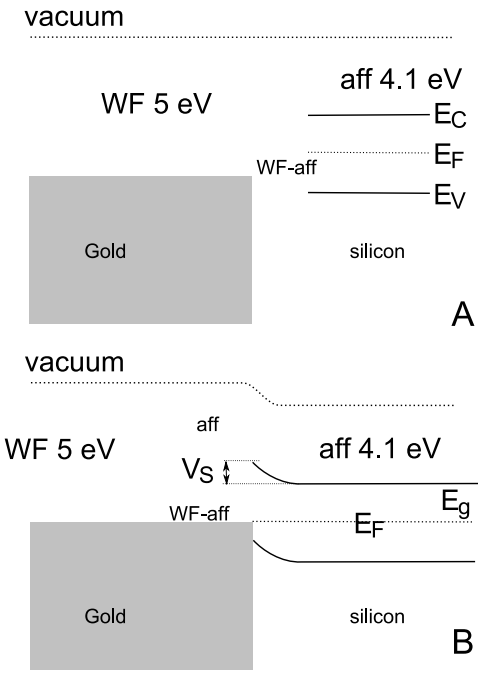

Figure A.7: (A) Energy diagram of isolated gold adjecent to intrinsic silicon. (B) Energy band diagram of the gold-silicon contact in thermal equilibrium.

B

COMPLEMENTARY INFORMATION FOR CHAPTER 5

B.1 Tapering of a nanowire due to gold loss

A geometrical analysis is performed to relate the tapering of a nanowire due to a constant gold loss, as a complement to Section 5.4

The catalyst particle can be considered a spherical cap with volume V_{cap} (see Equation (5.7)). The volume of the catalyst particle can be calculated either by assuming that the catalyst is a hemisphere, Figure B.1A, $\theta = 90°$, or θ can be calculated using the surface energies as defined in Table 5.3 and the Neumann quadrilateral relation (Chen et al., 1996)

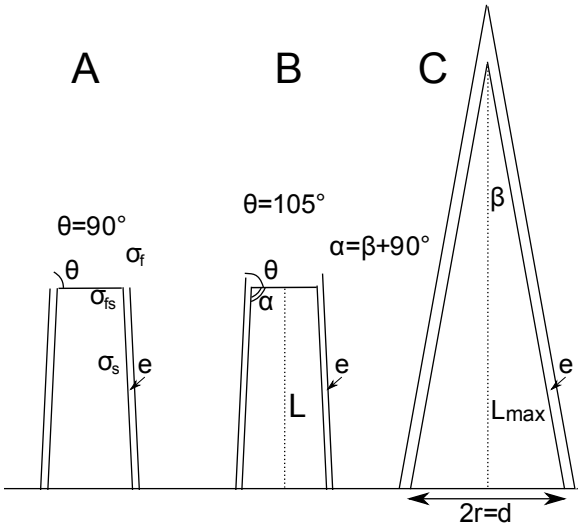

Figure B.1: (A) Schematic of a nanowire with a hemispherical catalyst. Respective angles and surface energy values are indicated. (B) The same nanowire with the contact angle θ as defined by Equation (B.1) (C) Nanowire where the complete catalyst particle is consumed due to gold diffusion, which results in a cone with semi opening angle β, radius r and length L_{max}.

$$\sigma_f \cos\theta = \sigma_s \cos\alpha - \sigma_{fs}, \tag{B.1}$$

where the constants are indicated schematically in Figure B.1A[1]. Since α is close to 90°, this term is close to zero and not taken into account. Using Equation (B.1) and the surface energies (Table 5.3) θ is calculated to be $\sim 105°$ (Figure B.1B).

[1] Obviously the surface energy of silicon σ_s will be modified by the gold liquid layer, but the effect is unknown.

The nanowire can be considered a cone with semi opening angle β (see Figure B.1C), length L and radius r. The thickness of the liquid layer e is indicated. We could develop a more sophisticated model to describe the effect of gold loss on the nanowire shape based on the equations presented in (Schmidt et al., 2004), however experimentally a cone is observed. The volume of a cone is given by

$$V_{cone} = \frac{1}{3}\pi r^2 L \tag{B.2}$$

If the catalyst particle loses material the radius will decrease and the radius of the nanowire will adjust to this new radius, that causes the wire to grow tapered. The gold in the initial catalyst particle and the amount of gold present on the nanowire surface determine the maximum length L_{max} the nanowire can grow (Figure B.1C). Due to the conservation of matter (the gold in the catalyst particle equals the gold on the wire sidewall) we can write for a hemispherical catalyst particle ($\theta = 90°$ in Equation (5.7) Figure B.1A)

$$\frac{2}{3}\pi r^3 = \frac{1}{3}\pi(r+e)^2 L - \frac{1}{3}\pi r^2 L \tag{B.3}$$

where e is the liquid layer thickness.

This can be rewritten

$$L_{max} = \tfrac{2r^3}{e^2+2re} \qquad L_{max} = \tfrac{r^2}{e} = \tfrac{d^2}{4e} \tag{B.4}$$

Since $e^2 \ll 2re$.

The nanowire can be regarded as a cone, therefore

$$\tan\beta = \frac{\Delta d}{2\Delta L} = \frac{d}{2L_{max}} \tag{B.5}$$

We substitute Equation (B.4) into Equation (B.5) to obtain

$$\tan\beta = \frac{2e}{d} \qquad \Delta d = \frac{4e\Delta L}{d} \tag{B.6}$$

Now we take into account the more accurate value of the contact angle θ (Figure B.1B). If $\theta = 105°$, the volume of the catalyst particle is given by a hemispherical cap (Equation (5.7)) the same analysis gives

$$L_{max} \simeq \frac{r^2\sqrt{2}}{e} \tag{B.7}$$

and we substitute in Equation (B.5) to obtain

$$\tan\beta = \frac{\sqrt{2}e}{d} \qquad \Delta d = \frac{2\sqrt{2}\Delta L e}{d} \tag{B.8}$$

The amount of gold on the nanowire sidewall is approximately equal to one monolayer (see Section 5.3) and therefore e is approximately 0.26 nm (Hannon et al., 2006). If the expected tapering is calculated for a nanowire with diameter d of 100 nm and ΔL is taken equal to the length of the gold covered zone near the catalyst particle (Section 5.4 Figure 5.7) using Equation (B.6) Δd is calculated to be 3.1 nm, using Equation (B.8), that is the more accurate equation, Δd is calculated to be 2.2 nm.

Equation (B.6) differs by a factor $1/2$ from the result presented in (Hannon et al., 2006). If we assume the equation given by (Hannon et al., 2006) is wrong, this means that the tapering is twice as small and the thickness of the liquid layer is around 2 monolayers in (Hannon et al., 2006). The results presented in (Hannon et al., 2006) were obtained under ultra high vacuum, therefore an increased gold diffusion does not seem unlikely.

B.2 The chemical potential

In this section we present some classical thermodynamics, adapted from (Atkins, 1999; McQuarrie and Simon, 1997), to illustrate the use of the chemical potential to gain insight into the gold diffusion mechanism (Section 5.4.1). First, we recall the definition of the chemical potential and derive the Laplace equation to show the effect of surface curvature on the chemical potential. Second, we remind how the chemical potential of a solution containing both gold and silicon (the catalyst particle) can be described. The derivation of the equations used in Section 5.4.1 and Section 5.4.2 is presented.

B.2.1 The chemical potential

The chemical potential describes how the Gibbs energy of a system changes as a substance is added to it. For pure substances the chemical potential is the same as the molar Gibbs energy (Atkins, 1999). For substances in a mixture the chemical potential μ is defined as being the partial molar gibbs energy

$$\mu_J = \left(\frac{\partial G}{\partial n_J}\right)_{p,T,n'} \tag{B.9}$$

The chemical potential is the slope of a plot of Gibbs energy against the amount of the component J, with pressure[2], temperature and the amounts of other substances n' held constant.

The variation of the chemical potential with pressure p is given by

$$\left(\frac{\partial \mu}{\partial p}\right)_T = V_m \tag{B.10}$$

where V_m is the molar volume. For an incompressible substance this reduces to

$$\Delta\mu = V_m \Delta p \tag{B.11}$$

[2] The nomenclature is adapted from (Atkins, 1999). p refers to pressure and P refers to an applied pressure, that additions to the pressure p already present, for instance the vapour pressure. The double brackets (()) indicate the substance is liquid, single brackets () indicate solid, $^\circ$ indicates a pure substance and * indicates that this quantity is not at equilibrium.

B.2.2 The Laplace equation

We calculate the vapour pressure p of a pressurized liquid (see Figure B.2). If we have a liquid (with μ(l)) in equilibrium with its vapour (with μ(g)) the chemical potentials are equal: μ(l)=μ(g). For this reason for any change that preserves equilibrium the resulting change in μ(l) must be equal to the change in μ(g), therefore $d\mu$(l)= $d\mu$(g). When the pressure P on the liquid is increased by dP, the chemical potential of the liquid changes by $d\mu(l) = V_m(l)dP$ and the chemical potential of the vapour changes by $d\mu(g) = V_m(g)dp$, where dp is the change in vapour pressure. If the vapour is treated as a perfect gas, the molar volume can be replaced by $V_m(g) = {}^{RT}/_{p}$, to obtain

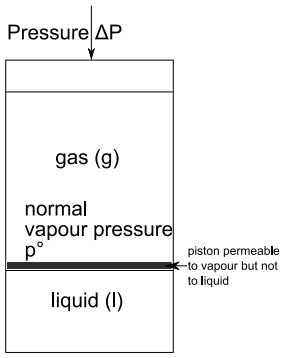

Figure B.2: Schematic of a liquid in equilibrium with its vapour, with a normal vapour pressure p°. Pressure P can be applied to the liquid using a piston that is permeable to the gas but not the liquid.

$$\frac{RT\,dp}{p} = V_m(l)dP \tag{B.12}$$

where p is the vapour pressure we would like to calculate. If no additional pressure is acting on the liquid, P (the pressure experienced by the liquid) is equal to the normal vapour pressure p°, therefore if $P = p^\circ$, $p = p^\circ$. If an additional pressure ΔP is present on the liquid $P = p + \Delta P$. The effect of pressure on vapour pressure is so small that $p \sim p^\circ$. Therefore p in $p + \Delta P$ is replaced by p°. The limits of the integration can now be set as follows

$$RT \int_{p^\circ}^{p} \frac{dp}{p} = \int_{p^\circ}^{p^\circ+\Delta P} V_m(l)dP \tag{B.13}$$

if $V_m(l)$ is constant throughout the small range of pressures this leads to

$$RT \ln\left(\frac{p}{p^\circ}\right) = V_m(l)\Delta P \tag{B.14}$$

This formula is valid for an ideal system only. Substitution of Equation (B.11) into this relation gives

$$\Delta\mu(l) = RT \ln\left(\frac{p}{p^\circ}\right) \tag{B.15}$$

When pressure is applied to a condensed phase, its vapour pressure rises.

Whenever there is a non-flat surface, the pressure on the concave side is always greater than the pressure on the convex side because of the additional pressure created by the surface tension (see Figure B.3). The relation between these two pressures is known as the Laplace equation, which is derived in the following.

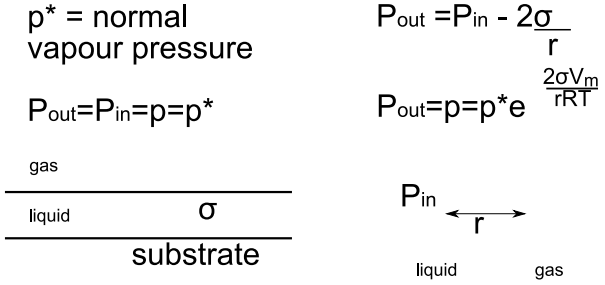

Figure B.3: Schematic of the vapour pressure above a flat liquid surface and around a liquid droplet, that is determined by the Laplace equation.

Now we consider the vapour pressure around a small spherical droplet with radius r. The droplet is in equilibrium when the force on the inside F_{in} is equal to the force on the outside F_{out}. The outward force is pressure $\times$ area and given by

$$F_{out} = p_{in} 4\pi r^2 \tag{B.16}$$

where p_{in} is the pressure on the inside of the droplet. The inward force is determined similarly, but including a contribution from the surface tension σ. The change in surface area dA when the radius of a sphere changes from r to $r + dr$ is given by

$$dA = 4\pi(r + dr)^2 - 4\pi r^2 = 8\pi r dr \tag{B.17}$$

where dr^2 is ignored. The work w done if the surface of the sphere is stretched by an amount dA is given by

$$dw = \sigma 8\pi r dr \tag{B.18}$$

Since the work is defined force $\times$ distance, the force for a displacement over dr is

$$F = \sigma 8\pi r \tag{B.19}$$

Therefore F_{in} is given by

$$F_{in} = p_{out} 4\pi r^2 + 8\pi\sigma r \tag{B.20}$$

where p_{out} is the pressure on the outside of the droplet. $F_{out} = F_{in}$ gives the Laplace equation:

$$p_{in} 4\pi r^2 = p_{out} 4\pi r^2 + 8\pi\sigma r \qquad p_{in} = p_{out} + \frac{2\sigma}{r} \qquad p_{in} - p_{out} = \Delta P = \frac{2\sigma}{r} \tag{B.21}$$

Similar analysis for a surface curved in only one direction, a cylinder of length L, gives for $F_{out} = F_{in}$

$$p_{in}2\pi rL = p_{out}2\pi rL + L\sigma 2\pi \qquad p_{in} = p_{out} + \frac{\sigma}{r} \qquad p_{in} - p_{out} = \Delta P = \frac{\sigma}{r} \tag{B.22}$$

We substitute ΔP from Equation (B.21) into Equation (B.14) and rewrite to obtain the Kelvin equation

$$\ln\left(\frac{p}{p^\circ}\right) = \frac{2\sigma V_m}{rRT} \tag{B.23}$$

Substitution of Equation (B.15) into the kelvin equation results in an additional term to describe the chemical potential of a (liquid) spherically curved surface $\Delta\mu_{sphere}$

$$\Delta\mu_{sphere} = \frac{2\sigma V_m}{r} = \frac{4\sigma V_m}{d} \tag{B.24}$$

and a cylindrically curved surface $\Delta\mu_{cylinder}$

$$\Delta\mu_{cylinder} = \frac{\sigma V_m}{r} = \frac{2\sigma V_m}{d} \tag{B.25}$$

B.2.3 Raoult's law and mixed solutions

The catalyst particle is actually a solution that contains both gold and silicon. For this reason an extra term is necessary to describe the chemical potential of the gold in the catalyst particle. First the mixing term in Equation (5.2) is derived, second Equation (5.3) is explained, following the analysis presented in (Desré, 2006).

Again we consider a liquid phase in equilibrium with its vapour Figure B.2.

The chemical potential of a perfect gas can be described

$$\mu = \mu^\ominus + RT\ln\frac{p}{p^\ominus} \tag{B.26}$$

where $\mu^\ominus$ is the standard chemical potential, the molar Gibbs energy of the pure gas at 1 bar and $p^\ominus$ is the standard pressure of 1 bar. The chemical potential of a substance $A(g)$ is therefore

$$\mu_A^\circ = \mu_A^\ominus + RT\ln\frac{p_A^\circ}{p^\ominus} \tag{B.27}$$

If another substance is present in the solution the vapour pressure is p_A and the chemical potential μ_A

$$\mu_A = \mu_A^{\ominus} + RT \ln \frac{p_A}{p^{\ominus}} \tag{B.28}$$

Combining these two equations gives

$$\mu_A = \mu_A^{\circ} + RT \ln \frac{p_A}{p_A^{\circ}} \tag{B.29}$$

Raoult's law states that the ratio of the partial vapour pressure of each component to its vapour pressure as a pure liquid, p_A/p_A°, is approximately equal to the mole fraction of A, x_A, in the liquid mixture

$$\frac{p_A}{p_A^{\circ}} = x_A \tag{B.30}$$

For an ideal solution, a solution that obeys Raoult's law, the chemical potential is therefore given by

$$\mu_A(l) = \mu_A^{\circ} + RT \ln x_A \tag{B.31}$$

For a solution that does not obey Raoult's law x_A is replaced by the activity, a_A of the substance A. Activity can be considered an "effective mole fraction". The activity is related to the mole fraction as $a_A = \gamma_A x_A$ where γ_A is the activity coefficient. The chemical potential for a real solution can therefore be written

$$\mu_A(l) = \mu_A^{\circ} + RT \ln \gamma_A x_A \tag{B.32}$$

The molar enthalpy of mixing for an ideal solution $\Delta_{mix}H^{id}$ is given by

$$\Delta_{mix}H^{id} = \Delta_{mix}G^{id} + T\Delta_{mix}S^{id} = 0 \tag{B.33}$$

and the molar Gibs energy of mixing $\Delta_{mix}G^{id}$ and molar entropy of mixing $\Delta_{mix}S^{id}$ by

$$\Delta_{mix}G^{id} = RT(x_A \ln x_A + x_B \ln x_B) \qquad \Delta_{mix}S^{id} = -R(x_A \ln x_A + x_B \ln x_B) \tag{B.34}$$

Indeed it follows $\Delta_{mix}H^{id}$ = 0 for an ideal solution. For a regular solution $\Delta_{mix}H \neq 0$. For a regular solution $\Delta_{mix}G$ is given by

$$\Delta_{mix}G = RT(x_A \ln x_A + x_B \ln x_B + x_A \ln \gamma_A + x_B \ln \gamma_B) \tag{B.35}$$

To focus on the effect of nonideality the excess molar Gibbs energy of mixing $\Delta_{mix}G^{xs}$ is defined

$$\Delta_{mix}G^{xs} = \Delta_{mix}G - \Delta_{mix}G^{id} \tag{B.36}$$

Substitution of Equation (B.34) and Equation (B.35) in Equation (B.36) shows that

$$\frac{\Delta_{mix}G^{xs}}{RT} = x_A \ln \gamma_A + x_B \ln \gamma_B \tag{B.37}$$

$\Delta_{mix}G^{xs}$ can be decomposed into contributions from the respective fractions x_A and x_B present in the solution using the Euler rule (Desré, 2006)

$$\Delta_{mix}G^{xs} = x_A\overline{G}_A^{xs} + x_B\overline{G}_B^{xs} \tag{B.38}$$

and therefore it follows that

$$\overline{G}_A^{xs} = RT \ln \gamma_A \qquad \overline{G}_B^{xs} = RT \ln \gamma_B \tag{B.39}$$

Now we write the internal energy change ΔU_m due to mixing in a binary solution composed of the constituents A and B, which is determined by three pair energies ϵ_{AA}, ϵ_{BB} and ϵ_{AB} that represent the energy contributions between two nearest neighbours of the solute atoms A and B

$$\Delta U_m = N_{av} z \left(\epsilon_{AB} - \frac{\epsilon_{AA} + \epsilon_{BB}}{2} \right) x_A x_B = \lambda x_A x_B \tag{B.40}$$

where z is the number of nearest neighbours and λ is an interaction parameter depending on the different pair energies. In the model of Bragg and Williams, or a strictly regular solution, it is supposed that the mixture is random and λ is temperature independent.

Because the enthalpy H is given by $H = U + PV$ and the change in volume upon mixing (ΔV_m) is considered negligable it follows that the molar enthalpy change of mixing $\Delta_{mix}H$ is given by

$$\Delta_{mix}H = \lambda x_A x_B \tag{B.41}$$

Since $\Delta H = \Delta G - T\Delta S$ (see also Equation (B.33)) it follows that for a regular solution, for which $\Delta_{mix}S^{xs} = 0$,

$$\Delta_{mix}H = \Delta_{mix}G^{xs} = \lambda x_A x_B \tag{B.42}$$

Since $x_B = 1 - x_A$, a plot of G^{xs} and $\Delta_{mix}H$ against x_A is a parabola that is symmetric about the vertical line at $x_A = 1/2$ with the maximum equal to the enthalpy of mixing (Equation (B.42)), leading to $\lambda = 4\Delta_{mix}H$.

Futhermore

$$\Delta_{mix}\overline{H}_A = \Delta_{mix}H + (1 - x_A)\frac{\partial \Delta_{mix}H}{\partial x_A} \tag{B.43}$$

This formula can be derived for a general state function X, such as internal energy U, free energy G, enthalpy H, entropy S or volume V. Suppose $\overline{X}_A$ and $\overline{X}_B$ are the molar quantities of a general state for the pure components A and B, and X_m describes the quantity of this state for one mole of the mixture of A and B. Using the Euler relation

$$X_m = \sum_i x_i \overline{X}_i \tag{B.44}$$

which was also used in Equation (B.38) (Desré, 2006), this can be written

$$X_m = x_A\overline{X}_A + x_B\overline{X}_B \tag{B.45}$$

The total derivative of this equation is given by

$$dX_m = (\overline{X}_A dx_A + \overline{X}_B dx_B) + (x_A d\overline{X}_A + x_B d\overline{X}_B) \tag{B.46}$$

The Gibbs-Duhem relation states that at constant temperature and pressure $x_A d\overline{X}_A + x_B d\overline{X}_B = 0$, therefore Equation (B.46) reduces to $dX_m = \overline{X}_A dx_A + \overline{X}_B dx_B$. Because $x_A + x_B = 1$ and $dx_A = -dx_B$ it follows

$$\overline{X}_A = \overline{X}_B - \frac{\partial X_m}{\partial x_B} \tag{B.47}$$

Substitution into Equation (B.45) gives

$$\overline{X}_B = X_m + (1 - x_B)\frac{\partial X_m}{\partial x_B} \qquad \text{and by analogy} \qquad \overline{X}_A = X_m + (1 - x_A)\frac{\partial X_m}{\partial x_A} \tag{B.48}$$

which proves Equation (B.43).

Combination of Equation (B.39), Equation (B.42) and Equation (B.43) shows that

$$\Delta\overline{H}_A = \Delta\overline{G}_A^{xs} = \lambda(1 - x_A)^2 = 4\Delta_{mix}H(1 - x_A)^2 = RT\ln\gamma_A \tag{B.49}$$

which is Equation (5.3).

B.3 Dewetting to form an hexagonal 2D lattice of clusters

We show the same analysis as presented in Section 5.6.1 , but now the final state is an hexagonal 2D lattice of gold clusters. We will show that the choice of lattice does not influence the result of the calculation and is therefore arbitrary.

The initial and final state are schematically depicted in Figure B.4. The gold clusters are approximated by a spherical cap. The surface S_{cap} and volume V_{cap} of a spherical cap were given in Equation (5.7)

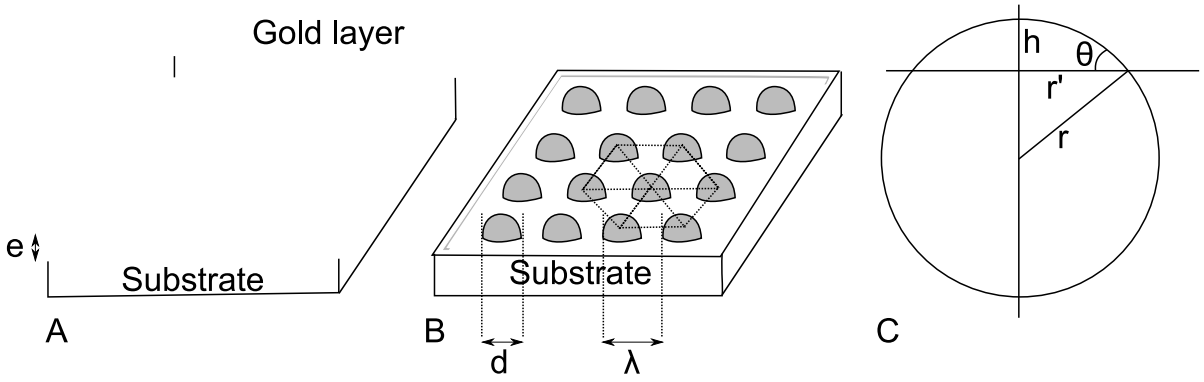

Figure B.4: (A) Initial state: a liquid layer of gold on a silicon substrate (B) Final state, dewetting from a liquid layer results in an hexagonal periodic network of clusters with a diameter d and hexagonal lattice parameter λ. (C) Schematic representation of a cluster that can be approximated by a truncated sphere with a radius r, a height of the cluster h and a contact angle θ.

In the case of an hexagonal 2D lattice the surface of the unit cell S_{unit} is given by

$$S_{unit} = 3\sqrt{\frac{3}{4}}\lambda^2 \tag{B.50}$$

There are now 3 gold clusters in each hexagonal unit cell (one cluster was present in the cubic unit cell). Therefore the change in free energy ΔF when going from the initial state to the final state can be expressed as

$$\begin{aligned}\Delta F =& \frac{S}{3\sqrt{\frac{3}{4}\lambda^2}}\left(3\pi r^2 \sin^2\theta\sigma_{cs}\right) + \frac{S}{3\sqrt{\frac{3}{4}\lambda^2}}\left(6\pi r^2(1-\cos\theta)\right)\sigma_c + \frac{S}{3\sqrt{\frac{3}{4}\lambda^2}}\left(3\sqrt{\frac{3}{4}\lambda^2 - 3\pi r^2\sin^2\theta}\right)\sigma_s \\ & - S\sigma_{cs} - S\sigma_c\end{aligned} \tag{B.51}$$

This can be rewritten to a dimensionless free energy change using the same approach as presented in Section 5.6.1:

$$\frac{\Delta F}{S\sigma_c} = \frac{\pi r^2}{\sqrt{\frac{3}{4}\lambda^2}}(2+\cos\theta)(1-\cos\theta)^2 - (1-\cos\theta) \tag{B.52}$$

The conservation of matter can be written for a hexagonal lattice as

$$3\sqrt{\frac{3}{4}}\lambda^2 e = 3\frac{1}{3}\pi r^3(1-\cos\theta)^2(2+\cos\theta) \tag{B.53}$$

To obtain Equation (5.16) by substitution of $\sqrt{\frac{3}{4}}\lambda^2$ (Equation (B.53)) into Equation (B.52).

B.4 Dewetting to a disordered array of clusters

Here the same analysis as presented in Section 5.6.1 is shown but no assumption is made about the periodicity of the lattice describing the gold clusters after dewetting from a liquid film. The initial and final state are illustrated in Figure B.5. The only assumption we make is that each cluster after dewetting occupies the same average area S and therefore the density ρ is described by

$$\rho = \frac{1}{S} \tag{B.54}$$

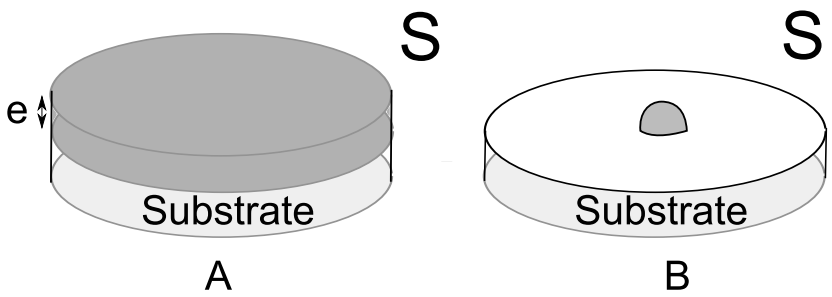

Figure B.5: (A) Initial state of a liquid film of thickness e and surface tension σ_f on an area S. (B) Final state, after dewetting one cluster is present on an are S.

The free energy change ΔF when going from the initial to the final state is given by

$$\Delta F = \sigma_f 2\pi r^2(1-\cos\theta) + \sigma_{fs}\pi r^2\sin^2\theta + \sigma_s(S-\pi r^2\sin^2\theta) - S(\sigma_{fs}-\sigma_f) \tag{B.55}$$

Substitute for $\sigma_{fs}-\sigma_s$ using the Youngs equation (Equation (5.11)), replace $\sin^2\theta = 1-\cos^2\theta$ and rewrite to obtain

$$\frac{\Delta F}{S\sigma_f} = \frac{\pi r^2}{S}(2+\cos\theta)(1-\cos\theta)^2 + (\cos\theta - 1) \tag{B.56}$$

The conservation of matter is given by

$$Se = \frac{1}{3}\pi r^3(2+\cos\theta)(1-\cos\theta)^2 \tag{B.57}$$

Substitution for S gives

$$\frac{\Delta F}{S\sigma_f} = \frac{3e}{r} + \cos\theta - 1 \qquad r_c = \frac{3e}{1-\cos\theta} \qquad \rho_c = \frac{1-\cos\theta}{9e^2\pi(2+\cos\theta)} \tag{B.58}$$

B.5 Dewetting from multiple layers including line tension

In this section we will review the simple model that was constructed in Section 5.6.2 but now include line tension. The possibility of line tension was first proposed by (Pethica, 1961) and (Widom, 1995) and implicates a change in contact angle for nanometer-sized droplets. In the case of a liquid gold (-silicon) layer dewetting on the sidewall of a nanowire, this analysis does not clarify the amount of line tension present in this system. However upper limits of the possible value of the line tension can be determined using the modified Youngs equation and the experimentally observed cluster diameter (see Section 5.6.2).

We start with Equation (5.9) and rewrite this to

$$\frac{\Delta F}{S} = \frac{\pi r^2}{\lambda^2}\sin^2\theta(\sigma_{cs} - \sigma_s) + \frac{2\pi r^2}{\lambda^2}(1-\cos\theta)\sigma_c + \sigma_s - \sigma_{cs} - \sigma_c \tag{B.59}$$

Now we can write the modified Youngs equation in a convenient way

$$\sigma_{cs} - \sigma_s = -\sigma_c\cos\theta - \frac{\tau}{r\sin\theta} \tag{B.60}$$

and substitute to obtain

$$\frac{\Delta F}{S} = -\frac{\pi r^2}{\lambda^2}\sin^2\theta(\sigma_c\cos\theta + \frac{\tau}{r\sin\theta}\frac{\sigma_c}{\sigma_c}) + \frac{2\pi r^2}{\lambda^2}(1-\cos\theta)\sigma_c + \sigma_c\cos\theta + \frac{\tau}{r\sin\theta}\frac{\sigma_c}{\sigma_c} - \sigma_c \tag{B.61}$$

We replace $\frac{\tau}{\sigma_c\sin\theta}$ by τ" for convenience and divide each term by σ_c to obtain

$$\frac{\Delta F}{S\sigma_c} = -\frac{\pi r^2}{\lambda^2}\sin^2\theta(\cos\theta + \frac{\tau"}{r}) + \frac{2\pi r^2}{\lambda^2}(1-\cos\theta) + \cos\theta - 1 + \frac{\tau"}{r} \tag{B.62}$$

We rewrite and substitute $-1+\cos^2\theta$ for $-\sin^2\theta$

$$\frac{\Delta F}{S\sigma_c} = \frac{\pi r^2}{\lambda^2}(2 - 3\cos\theta + \cos^3\theta) - \frac{\pi r^2}{\lambda^2}\frac{\tau"}{r}\sin^2\theta + \cos\theta - 1 + \frac{\tau"}{r} \tag{B.63}$$

We use the conservation of matter (Equation (5.15)) and substitute for λ^2

$$\frac{\Delta F}{S\sigma_c} = \frac{3e}{r} - \frac{(1-\cos\theta)3e\tau"}{r^2(1-\cos\theta)(2+\cos\theta)} + (\cos\theta - 1) + \frac{\tau"}{r} \leq 0 \tag{B.64}$$

to have dewetting. Each term is multiplied by r^2 and we obtain an ordinary quadratic equality that can be solved by the simple abc rule [3]. The possible critical radius and critical lattice parameter to have dewetting are now given by

$$r_c = \frac{3e+\tau"}{2(1-\cos\theta)} \pm \frac{\sqrt{(3e+\tau")^2 + 12e\tau"\frac{1+\cos\theta}{(2+\cos\theta)}}}{2(1-\cos\theta)} \tag{B.65}$$

[3] For this reason two solutions for r_c exist ($+\sqrt{}$ and $-\sqrt{}$). Solutions for r_c using $-\sqrt{}$ are negative and therefore of little physical meaning.

$$\lambda_c = (1 - \cos\theta)\sqrt{r_c^3}\sqrt{\frac{\pi(2 + \cos\theta)}{3e}} \tag{B.66}$$

A motor force for dewetting will be present only if $\lambda \geq \lambda_c$ and $d_{exp} \geq d_c$. We use the same surface energy values as in the previous section. We plot only the critical values (λ_c and d_c) as a function of contact angle since no analytical relation exists in this case to relate the contact angle with line tension and surface energy values. The shaded region shows were dewetting can occur, if $d_{exp} > d_c$ or $\rho_{exp} < \rho_c$. Line tension values of $1x10^{-9}$ and $1x10^{-10}$ Jm^{-1} were tried as positive and negative values. The results of these calculations are summarized in Table B.1. These results do not aid the estimation of the line tension τ, since different boundary values for θ are found if the experimental diameter or the experimental density is compared to the critical values, and θ is not known. Therefore we show the results of the calculations in the following but we do not draw further conclusions.

Table B.1: Summary of the calculations including line tension. The second and third columns indicate for which values of θ dewetting can occur, or the reason why the result of the calculation seems of little physical value (for example negative critical values).θ is in rad.

Line tension (J m^{-1})	d_c (θ)	ρ_c (θ)
-10^{-9}	negative d_c	$\theta > 0.8$
-10^{-10}	$0.4 < \theta < 0.5, \theta > 0.7$	$\theta > 0.4$
$+10^{-10}$	$\theta > 1.3$	$\theta > 0.8$
$+10^{-9}$	$\theta > 1.7$	$\theta \sim 2.3$

In Figure B.6 the critical lattice parameter (solid line) and the critical cluster diameter (dashed line) are plotted for negative and positive values of the line tension. Figure B.6A (a line tension of $-1x10^{-10}$ Jm^{-1}) indicates that for small contact angles the value of $d_c > \lambda_c$, this seems physically impossible since in this case the clusters touch and there will be no dewetting. However we should not forget that we are plotting critical values only, therefore a larger value of d or λ is possible if there is a driving force for dewetting (the free energy change is negative).

To see if this is the case we use equation B.64 to express the (dimensionless) change in free energy for the same line tension value ($-1x10^{-10}$ Jm^{-1}) for different cluster diameters in Figure B.7: for a cluster diameter of 4 (solid line), 8 (solid green line) and 12 nm (dashed line). Clearly dewetting can only occur for small cluster diameters (<4 nm) if $\theta \geq 1\,\mathrm{rad}$, which would indicate a positive line tension.

Decreasing the line tension to $-1x10^{-9}$ Jm^{-1} or more leads to negative critical values at all contact angles.

Also we can express again the critical cluster density using Equation (5.19). In Figure B.8 the critical cluster densities are plotted as a function of θ for negative and positive line tension values and also the experimental cluster density is plotted. The shaded areas indicate the values for θ where dewetting can occur, since a motor force for dewetting will be present only if $\rho_{exp} \leq \rho_c$.

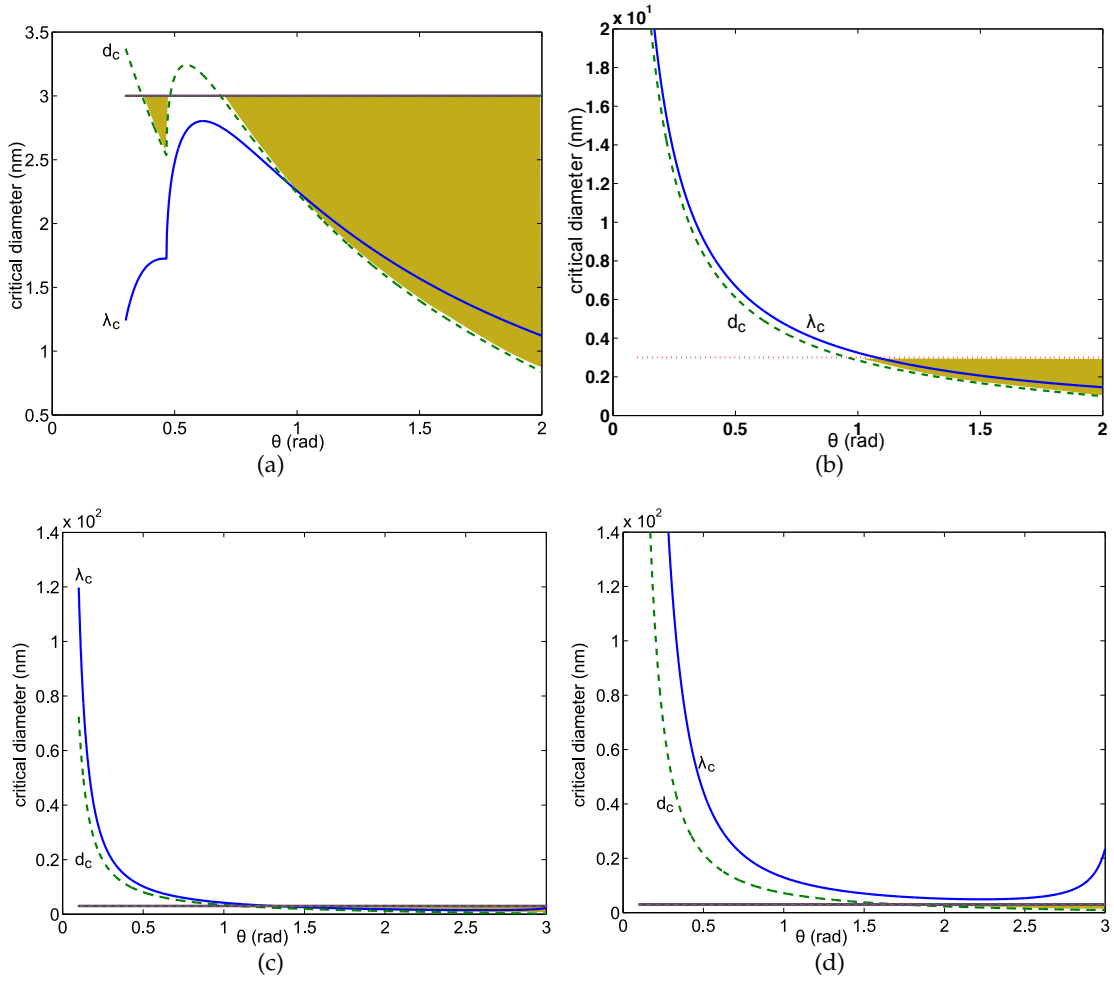

Figure B.6: (A) d_c (dashed line) and λ_c (solid line) as a function of θ for a negative line tension of -10^{-10} J m^{-1}. The experimental cluster diameter is indicated (dotted line). The shaded areas indicate the values for θ where dewetting can occur. Dewetting can occur if $d_c < d_{exp}$ for $0.4 < \theta < 0.5$ rad and $\theta > 0.7$ rad. (B) d_c and λ_c as a function of θ if no line tension is present. Dewetting can occur if $d_c < d_{exp}$ for $\theta > 1$ rad. (C) d_c and λ_c as a function of θ for a positive line tension of 10^{-10} J m^{-1}. Dewetting can occur if $d_c < d_{exp}$ for $\theta > 1.3$ rad. (D) d_c and λ_c as a function of θ for a positive line tension of 10^{-9} J m^{-1}. Dewetting can occur if $d_c < d_{exp}$ for $\theta > 1.7$ rad. The thickness of the liquid layer is taken to be 0.26 nm.

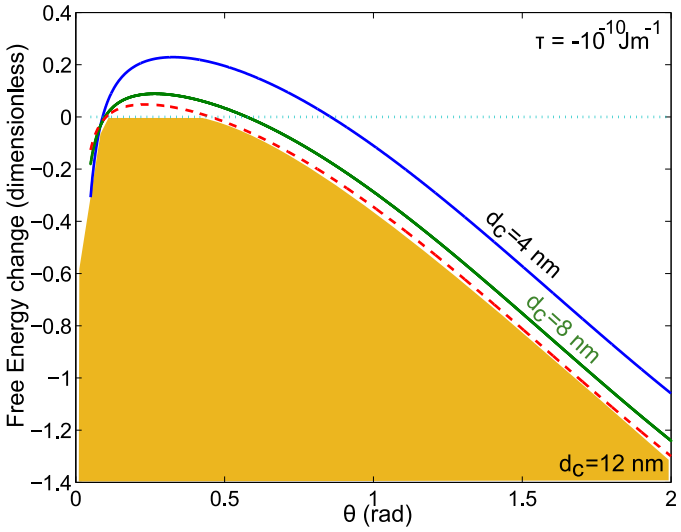

Figure B.7: (Color online) Dimensionless free energy change for varying contact angle for cluster diameters of 4 (solid blue line), 8 (solid green line) and 12 nm (dashed line).The line tension is $-10^{-10}\ Jm^{-1}$. The thickness of the liquid layer is taken to be 0.26 nm. The shaded area indicates the values for θ where dewetting can occur if $d_c = 12\,\mathrm{nm}$.

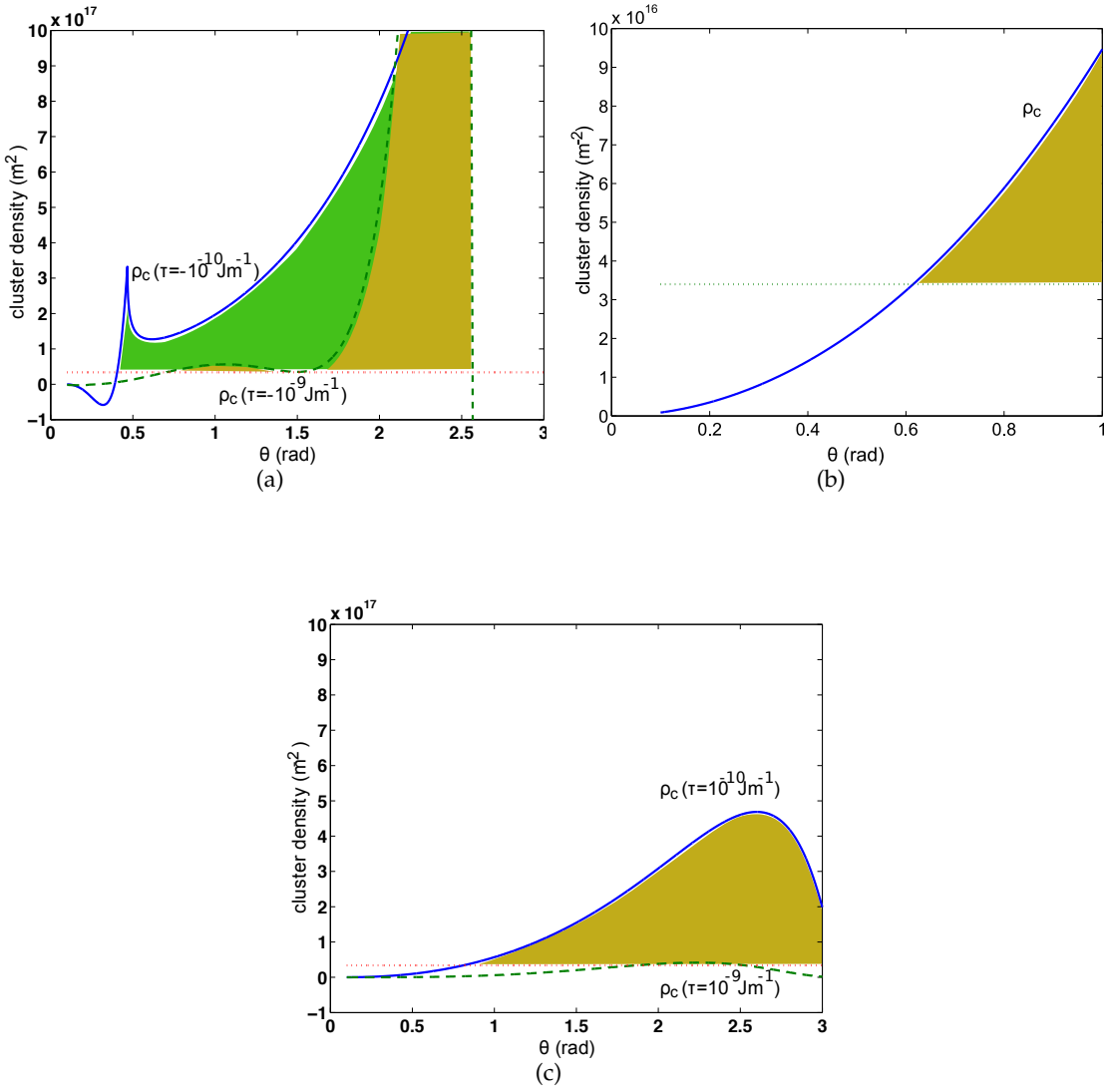

Figure B.8: (A) The critical cluster density depending on contact angle is plotted for negative line tension values: $-10^{-10}\ Jm^{-1}$ (solid line) and $-10^{-9}\ Jm^{-1}$ (dashed line). The experimental cluster density is plotted (dotted line). The shaded areas indicate the values for θ where dewetting can occur. Dewetting can occur if $\rho_c > \rho_{exp}$ for $\theta > 0.4\,\mathrm{rad}$ ($\tau = -10^{-10}\ Jm^{-1}$) or for $\theta > 0.8\,\mathrm{rad}$ ($\tau = -10^{-9}\ Jm^{-1}$). (B) The critical cluster density depending on contact angle is plotted for zero line tension. The experimental cluster density is plotted (dotted line). Dewetting can occur if $\rho_c > \rho_{exp}$ for $\theta > 0.61\,\mathrm{rad}$. (C) The critical cluster density depending on contact angle is plotted for positive line tension values: $10^{-10}\ Jm^{-1}$ (solid line) and $10^{-9}\ Jm^{-1}$ (dashed line). The experimental cluster density is plotted (dotted line). Dewetting can occur if $\rho_c > \rho_{exp}$ for $\theta > 0.8\,\mathrm{rad}$ ($\tau = 10^{-10}\ Jm^{-1}$) or for $\theta \approx 2.3\,\mathrm{rad}$ ($\tau = 10^{-9}\ Jm^{-1}$). .

C

COMPLEMENTARY INFORMATION & LIST OF NANOWIRE SAMPLES

This figure was published in (Aissou et al., 2008) and represents a successful example of a cross section TEM sample.

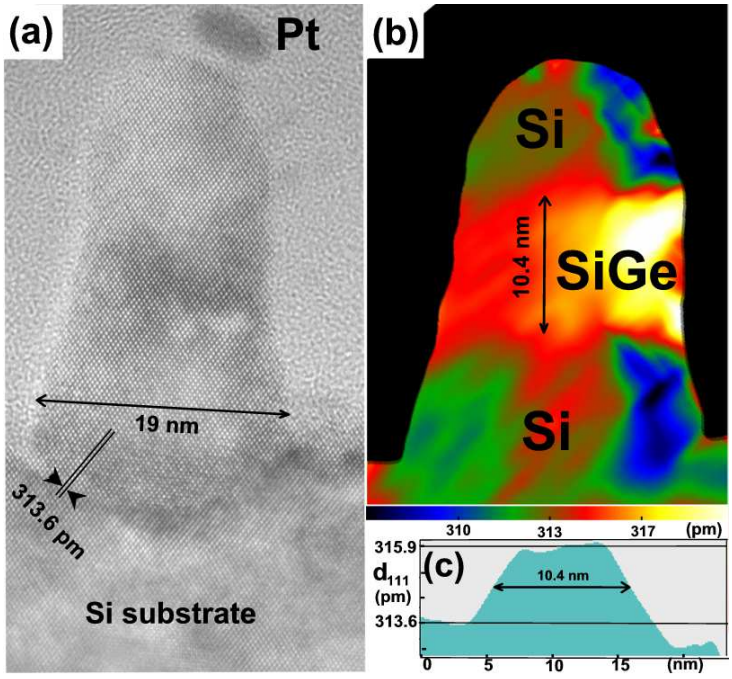

Figure C.1: : (a) HRTEM image of a silicon nanopillar containing a SiGe region. The nanopillar consist of 10 nm Si, 10 nm $Si_{0.8}Ge_{0.2}$ and 10 nm Si and is elongated along the vertical [001] direction. The image is taken along a lateral $\langle 110 \rangle$ direction. Note the remains of the Pt dot mask (dark particle). This Pt mask is not touching the nanopillar indicating that either it has been displaced or that part of the top of the nanopillar has been slightly edged during the TEM sample preparation. Two (111) planes separated by 313.6 pm are outlined near the Si substrate. A slight etching of the SiGe layer can be noticed. (b) (111) interplanar distance map in pm obtained from Figure 8a by using the Geometrical Phase Analysis (Hÿtch et al., 1998). The distances have been averaged over large areas ($5\times5 nm^2$). For this reason the areas at the edge of the wires are partly biased (averaged areas include vacuum). The regions where no (111) lattice fringes have been detected have been masked (dark areas) in order to suppress the noise in these regions. (c) (111) interplanar distance profile extracted along the central vertical stripe of fig. 8(b). The variation of the (111) lattice plane are clearly seen. In this profile, the width of the $Si_{1-x}Ge_x$ layer is measured equal to 1.04 nm and the distance of 315.9 nm corresponds to the (111) interplanar distance of a $Si_{84}Ge_{16}$ compound, biaxially stressed by a Si layer.

Sample number	Remarks catalyst/substrate	Catalyst deposition	anneal (℃)	T growth (℃)	Silane (mbar) partial pressure	growth time (mn) or other gasses
4110		colloïde 20nm	850	600	0.08	30
4112	substrate Si (100)	depot d'or 5 nm	850	600	0.08	30
4130				450	0.08	
4166		depot	850	550	0.08	15
4254	Au on Si (100)			550	0.08	
4255	Au on Si (111)			550	0.08	
4289			850	500	0.08	
4290		depot	850	600	0.08	15
4294		depot	850	650	0.13	8
4295		depot	850	600	0.13	8
4298	Pt on Si (100)					
4299	Au on Si (111)			550	0.13	
4300		depot	850	500	0.13	8
4301		depot	850	700	0.05	15
4308				500	0.05	
4312				450	0.05	
4322		depot d'or 2 nm	850	650	0.1	10
4324	Au on Si (111) looks strange: cooling d			550	0.05	
4342						
			850	575	0.08 ?	
4343			850	575	0.08	15
4344			850	625	0.08 ?	
4360				450	0.1	
4361				450	0.1	
4366		depot	850	575	0.08	15
4372		depot	850	650	0.08	15
4386		depot	850	575	0.13	8
4387		depot	850	575	0.05	15
4388		depot	850	625	0.05	15
4389			850	625	0.13	8
4395	Au on Si (111)			650	0.05	
4410			850	500	0.08	60
4432	Au on Si(111)	10 nm collo	850	430	0.19	25
4433	Au on Si(111)	10 nm collo	850	430	0.19	25
4434	Au on Si(111)	20 nm collo	850	430	0.19	25
4435	Au on Si(111)	20 nm collo	850	430	0.19	25
4436	Au on Si(111)	50 nm collo	850	430	0.19	25
4437	Au on Si(111)	50 nm collo	850	430	0.19	25
4438	PtSi on Si(111)	depot	800	800	0.08	30
4439	PtSi on Si(111)	depot	800	800	0.08	30
4454	PtSi on Si	depot	800	800	0.13	30
4462	PtSi on Si		800	600	0.13	30
4489	PtSi 1.2 nm on Si(100)		800	800	0.13 HCl 0.13	30
4501	PtSi on Si(111)	?				
4530	NiSi on Si(100)		800	800	0.13 HCl 0.2	10
4564	Au on Si(111)	50 nm collo	800	700	0.13	30
4565	Au on Si(110)	100 nm col	800	700	0.13	30

4566	Au on Si(111)	100 nm col	800	700	0.13		30
4576	Au on Si(111)	depot	850	550	0.26 --> 0.03	15 + 30	
4601	Au on Si(111)	10 nm colle	500	430	0.24	20+15	
4602	Au on Si(111)	20 nm colle	500	430	0.24	20+15	
4625	Au on Si(111)	depot 2 nm	850	600	0.19	20+10	
4626		200 nm col	700	600 - 430	0.13 --> 0.26	25 + 30	
4629	Au on Si(111)	depot 2 nm	850	600-430	0.19	10 + 45	
4630	Au on Si(111)	5 nm colloide		500	1.02		
4631	Au on Si(110)	10 nm colloide		500	1.02		
4632	Au on Si(111)	20 nm colloide		500	1.02		
4633	Au on Si(111)	50 nm colloide		500	1.02		
4634	Au on Si(111)	100 nm colloide		500	1.02		30
4638	Au on Si(111)	10 nm colle	500	430	0.19	20 + 10	
4639		5 nm colloide		500	0.52		
4640		10 nm colloide		500	0.52		
4641		20 nm colloide		500	0.52		
4642		50 nm colloide		500	0.52		
4643		100 nm colloide		500	0.52		
4657				600 - 360° (	0.13 - 1.02		
4665							
4666							
4686	Pt on Si nanocrystals deposited on 7 n			800			
4714		200 nm colloide		500	0.26	time chosen as to	
4715		100 nm colloide		500	0.26	keep quantity	
4716		50 nm colloide		500	0.26	silane 1 l	
4717		20 nm colloide		500	0.26		
4718		10 nm colloide		500	0.26		
4719		5 nm colloide		500	0.26		
4720		2 nm colloide		500	0.26		
4733		2 nm colloide		500	0.08	time chosen as to	
4734		5 nm colloide		500	0.08	keep quantity	
4735		10 nm colloide		500	0.08	silane 1 l	
4736		20 nm colloide		500	0.08		
4737		50 nm colloide		500	0.08		
4738		100 nm colloide		500	0.08		
4739		200 nm colloide		500	0.08		
4740		2 nm colloide		500	0.13	time chosen as to	
4741		5 nm colloide		500	0.13	keep quantity	
4742		10 nm colloide		500	0.13	silane 1 l	
4743		20 nm colloide		500	0.13		
4744		100 nm colloide		500	0.13		
4745		200 nm colloide		500	0.13		
4746		2 nm colloide		500	0.52	time chosen as to	
4747		5 nm colloide		500	0.52	keep quantity	
4748		10 nm colloide		500	0.52	silane 1 l	
4749		20 nm colloide		500	0.52		
4750		50 nm colloide		500	0.52		
4751		100 nm colloide		500	0.52		

4752		200 nm colloide			500	0.52		
4785		20 nm collo	500	430° - 500°		0.13	40 - 30 - 40	
4786		50 nm collo	500	430° - 500°		0.13	40 - 30 - 40	
4787		100 nm col	500	430° - 500°		0.13	40 - 30 - 40	
4792	Au on Si(111)			600 - ?° (-1		0.13 --> 1.02	? - 40	
4811	Au on Si(111)			600 - ?° (-1		0.13 --> 1.02		
4913	Au on Si(111)	depot 2 nm	900		650	0.1	doped sample. Silane 20 , Al 6/	
4967	Au on Si(111)	depot 2 nm			500	0.26		
5062	Au on Si(111)	depot 2 nm	850		575	0.13		30
5066	wires in nanoporous alu		550°		450	0.13		15
5121	électrodépo	100 nm col	500		500	1.02		30
5122	depot lysine	100 nm col	500		500	1.02		30
5240	Ni on Si							
5242	Au on Si(111)	100 nm col	500		500	1.02		
5255	Au on Si(111)	200 nm col	500		500	1.02		
5356	Cu on Si(100)		900		750		with HCl	
5357	Cu on Si(111)		900		750		with HCl	
5395	Pd							
5436	Au on Si(111)	100 nm col	500		500	1.02		30
5666		200 nm col	650		650	(1)0.26HCl0.13(2)0.26HCl0.03(3)0.26HCl0.13		
5738		200 nm col	650		650	(1) 0.26 HCl 0.50 (2) 0.13 HCl 0.09		
IBM A	gold colloids 60 nm				440	0.27		
IBM B	gold colloids 60 nm				460	0.13		

BIBLIOGRAPHY

Agarwal, A., Buddharaju, K., Lao, I., Singh, N., Balasubramanian, N., and Kwong, D. (2008). Silicon nanowire sensor array using topdown cmos technology. *Sensors and Actuators A*, 145146:207213.

Aissou, K., Baron, T., Kogelschatz, M., den Hertog, M., Rouvière, J., and Hartmann, J. (2008). Fabrication of well-organized and densely packed si nanopillars containing sige nanodots by using block copolymer templates. *Chemical Materials*, 20(19):61836188.

Ajayan, P., Schadler, L., Giannaris, C., and Rubio, A. (2000). Single-walled carbon nanotube-polymer composites: Strength and weakness. *Advanced Materials*, 12:750–753.

Alexandre, L. (2008). *Analyse des profils d'intensité diffractée en diffraction électronique en faisceau convergent pour la mesure des déformations locales.* PhD thesis, Universit Paul Cezanne, Aix-Marseille III.

Algra, E., Verheijen, M., Borgström, M., Feiner, L., Immink, G., van Enckevort, W., Vlieg, E., and Bakkers, E. (2008). Twinning superlattices in indium phosphide nanowires. *Nature*, 456:369–372.

Allaoui, A., Bai, S., Cheng, H., and Bai, J. (2002). Mechanical and electrical properties of a mwnt/epoxy composite. *Composites Science Technology*, 62:1993–1998.

Allen, J., Hemesath, E., Perea, D., Lensch-Falk, J., Li, Z., F.Yin, Gass, M., Wang, P., Bleloch, A., Palmer, R., and Lauhon, L. (2008). High-resolution detection of au catalyst atoms in si nanowires. *Nature Nanotechnology*.

Arbiol, J., i Morral, A. F., Estradé, S., Peiró, F., Kalache, B., i Cabarrocas, P. R., and Morante, J. (2008). Influence of the (111) twinning on the formation of diamond cubic/diamond hexagonal heterostructures in cu-catalyzed si nanowires. *Journal of Applied Physics*, 104:064312.

Arbiol, J., Kalache, B., i Cabarrocas, P. R., Morante, J. R., and i Morral, A. F. (2007). Inuence of cu as a catalyst on the properties of silicon nanowires synthesized by the vapour-solid-solid mechanism. *Nanotechnology*, 18:305606.

Atkins, P. (1999). *Atkins Physical Chemistry sixth edition*. Oxford University Press.

Ayache, J., Beaunier, L., Boumendil, J., Ehret, G., and Laub, D. (2007). *Sample preparation guide for Transmission Electron Microscopy*. PU Saint-Etienne.

Bailly, A., Renault, O., Barrett, N., Zagonel, L., Gentile, P., Pauc, N., Dhalluin, F., Baron, T., Chabli, A., Cezar, J., and Brookes, N. (2008). Direct quantification of gold along a single si nanowire. *Nano Letters*, 8(11):37093714.

Bals, S., Kabius, B., Haider, M., Radmilovic, V., and Kisielowski, C. (2004). Annular dark field imaging in a tem. *Solid State Communications*, 130:675680.

Bals, S., Kilaas, R., and Kisielowski, C. (2005). Nonlinear imaging using annular dark field tem. *Ultramicroscopy*, 104:281–289.

Bandet, J., Despax, B., and Caumont, M. (2002). Vibrational and electronic properties of stabilized wurtzite-like silicon. *Journal of Physics D: Applied Physics*, 35:234239.

Beleggia, M., Cardinali, G., Fazzini, P., Merli, P., and Pozzi, G. (2008). Influence of the speci,en surfaces on tem images of reverse-biased p-n junctions. *Institut of Physics Conference Series*, 169:427.

Benoit, J., Corraze, B., Lefrant, S., Bernier, P., and Chauvet, O. (2002). Electric transport properties and percolation in carbon nanotubes/pmma composites. *Material Research Society Symposium Proceedings*, 706:Z3.28.1–Z3.28.5.

Bermond, J., Métois, J., Egéa, X., and Floret, F. (1995). The equilibrium shape of silicon. *Surface Science*, 330:48–60.

Berthe, M., Stiufiuc, R., Grandidier, B., Deresmes, D., Delerue, C., and Stiévenard, D. (2008). Probing the carrier capture rate of a single quantum level. *Science*, 319:436.

Besson, J., Mokhtari, E., Gonzalez, J., and Weill, G. (1987). Two new forms of silicon. *Physical Review Letters*, 59:473.

Biberger, R., Benstetter, G., Schweinboeck, T., Breitschopf, P., and Goebel, H. (2008). Intermittent-contact scanning capacitance microscopy versus contact mode scm applied to 2d dopant profiling. *Microelectronics Reliability*, 48:13391342.

Björk, M., Knoch, J., Schmid, H., Riel, H., and Riess, W. (2008). Silicon nanowire tunneling field-effect transistors. *Applied Physics Letters*, 92:193504.

Björk, M., Schmid, H., Knoch, J., Riel, H., and Riess, W. (2009). Donor deactivation in silicon nanostructures. *submitted to Nature Nanotechnology*, 4:103.

Blavette, D., Cadel, E., Fraczkiewicz, A., and Menand, A. (1999). Three-dimensional atomic-scale imaging of impurity segregation to line defects. *Science*, 286(5448):2317 – 2319.

Brunet, M., Joud, J., Eustathopoulos, N., and Desré, P. (1976). Tension superficielle du germanium et d'alliages argent-germanium à l'état liquide. *Journal of Less-common Metals*, 51:69–77.

Buffat, P. and Borel, J. (1976). Size effect on the melting temperature of gold particles. *Physical Review A*, 13(6):2287.

Buffat, P., Flüeli, M., Spycher, R., Stadelmann, P., and Borel, J. (1992). Crystallographic structure of small gold particles studied by high-resolution electron microscopy. *Faraday Discussions*, 92:173–187.

Buttard, D., David, T., Gentile, P., Hertog, M. D., Baron, T., Ferret, P., and Rouvière, J. (2008). A new architecture for self-organized silicon nanowire growth integrated on a (100) silicon substrate. *Physica Status Solidi A*, page 1.

Cao, L., Laim, L., Ni, C., Nabet, B., and Spanier, J. (2005). Diamond-hexagonal semiconductor nanocones with controllable apex angle. *Journal of the American Chemical Society*, 127:13782–

13783.

Carim, A., Lew, K., and Redwing, J. (2001). Bicrystalline silicon nanowires. *Advanced Materials*, 13(13):1489.

Caroff, P., Dick, K., Johansson, J., Messing, M., Deppert, K., and Samuelson, L. (2008). Controlled polytypic and twin-plane superlattices in iiiv nanowires. *Nature Nanotechnology*, 4:50–55.

Cayron, C. (2007). Multiple twinning in cubic cystals: geometric/algebraic study and its application for the identification of the $\sigma 3^n$ grain boundary. *Acta Cryst.*, A63:11–29.

Cayron, C., den Hertog, M., Latu-Romain, L., Mouchet, C., Secouard, C., Rouvière, J., Rouviere, E., and Simonato, J. (2009). Odd electron diffraction patterns in silicon nanowires and silicon thin films explained by microtwins and nanotwins. *Applied Crystallography*, 42:242–252.

Chan, C., Peng, H., Liu, G., McIlwrath, K., Zhang, X., Huggins, R., and Cui, Y. (2008). High-performance lithium battery anodes using silicon nanowires. *Nature Nanotechnology*, 3:31.

Chapman, J. (1984). The investigation of magnetic domain structures in thin j. phys. d: Appl. phys.,foils by electron microscopy. *Jounal of Physics D: Applied Physics*, 17:623.

Chen, H., Gao, Y., Yu, H., Zhang, H., Liu, L., Shi, Y., Tian, H., Xie, S., and Li, J. (2004). Structural properties of silver nanorods with vefold symmetry. *Micron*, 35:469–474.

Chen, J., Gaydos, J., and Neumann, A. (1996). Contact line quadrilateral relation. generalization of the neumann triangle relation to include line tension. *Langmuir*, 12:5956.

Cherns, D. (1974). Direct resolution of surface atomic steps by transmission electron microscopy. *Philosophical Magazine*, 30:549.

Cho, K., Suk, S., Yeoh, Y., Li, M., Yeo, K., Kim, D., Park, D., Lee, W., Jung, Y., Hong, B., and Hwang, S. (2007). Temperature-dependent characteristics of cylindrical gate-all-around twin silicon nanowire mosfets (tsnwfets). *IEEE Electron Device Letters*, 28(12):0741.

Choi, S., Zhang, Z., Yu, W., Lockwood, F., and Grulke, E. (2001). Anomalous thermal conductivity enhancement in nanotube suspensions. *Applied Physics Letters*, 79:2252–2254.

Chung, J. and Rabenberg, L. (2006). Mapping of electrostatic potentials within core-shell nanowires by electron holography. *Applied Physics Letters*, 88:013106.

Cimalla, V., Stubenrauch, M., Weise, F., Fischer, M., Tonisch, K., Hoffmann, M., and Ambacher, O. (2007). Suspended nanowire web. *Applied Physics Letters*, 90:101504.

Cohen, G. and et al. (2007). Nanowire metal-oxide-semiconductor field effect transistor with doped epitaxial contacts for source and drain. *Applied Physics Letters*, 90:233110.

Cooper, D. (2006). *Off-axis electron holography of focused ion beam prepared semiconductor devices*. PhD thesis, Darwin College, University of Cambridge.

Cooper, D. (2009). x. *Ultramicroscopy*, x:x.

Cooper, D., Ailliot, C., Truche, R., Barnes, J., Hartmann, J., and Bertin, F. (2008). Experimental off-axis electron holography of focused ion beam-prepared si p-n junctions with different dopant concentrations. *Journal of Applied Physics*, 104:064513.

Cooper, D., Truche, R., Rivallin, P., Hartmann, J., Laugier, F., Bertin, F., and Chabli, A. (2007a). Medium resolution off-axis electron holography with millivolt sensitivity. *Applied Physics Letters*, 91:143501.

Cooper, D., Twitchett-Harrison, A., Midgley, P., and Dunin-Borkowski, R. (2007b). The influence of electron irradiation on electron holography of focused ion beam milled gaas p-n junctions. *Journal of Applied Physics*, 101:094508.

Cowley, J. (1992). Twenty forms of electron holography. *Ultramicroscopy*, 41:335.

Cowley, J. and Spence, J. (2000). *Handbook of Nanostructured Materials and Nanotechnology: Chaper 1 Nanodiffraction*. Academic Press.

Cui, Y., Lauhon, L., Gudiksen, M., Wang, J., and Lieber, C. (2001). Diameter-controlled synthesis of single-crystal silicon nanowires. *Applied Physics Letters*, 78:2214.

Dahmen, U., Hetherington, C., Pirouz, P., and Westmacott, K. (1989). The formation of hexagonal silicon at twin intersections. *Scripta Metallurgica*, 23(2):269.

David, T., Buttard, D., Schülli, T., Dallhuin, F., and Gentile, P. (2008). Structural investigation by gixrd and gisaxs of silicon nanowires : Evidence of a complex saw-tooth faceting. *Surface Science*, 602(15):2675–2680.

de Ruijter, W. and Weiss, J. (1993). Detection limits in quantitative off-axis holography. *Ultramicroscopy*, 50:269–283.

den Hertog, M., Rouviere, J., Dhalluin, F., Desré, P., Gentile, P., Ferret, P., Oehler, F., and Baron, T. (2008). Control of gold surface diffusion on silicon nanowires. *Nano Letters*, 8(5):1544.

den Hertog, M., Rouviere, J., Dhalluin, F., Gentile, P., Ferret, P., Ternon, C., and Baron, T. (2007). Gold catalyzed silicon nanowires: Defects in the wires and gold on the wires. *Proceedings MSM 2007 Camebridge*, 1:217.

Desré, P. (2006). *Chapitre II, Thermodynamique des solutions*. Unpublished.

Dhalluin, F. (2009). *Nanofils de silicium: Dépôt chimique en phase vapeur assisté par catalyseurs métalliques et prémices d'intégration*. PhD thesis, Universit Joseph Fourier - Grenoble I.

Dhalluin, F., Desré, P., den Hertog, M., Rouvière, J., Ferret, P., Gentil, P., and Baron, T. (2007). Critical condition for growth of silicon nanowires. *Journal of Applied Physics*, 102:094906.

Diarra, M., Niquet, Y.-M., Delerue, C., and Allan, G. (2007). Ionization energy of donor and acceptor impurities in semiconductor nanowires: Importance of dielectric connement. *Physical Review B*, 75:045301.

Dick, K., Deppert, K., Larsson, M., Mårtensson, T., Seifert, W., Wallenberg, L., and Samuelson, L. (2004). Synthesis of branched 'nanotrees' by controlled seeding of multiple branching events. *Nature Materials*, 3:380–384.

Dickson, E. and Pashley, D. W. (1962). Double positioning in silver and gold layers deposited on mica. *Philosophical Magazine*, 7:1315.

Dornel, E., Ernst, T., Barbé, J., Hartmann, J., Delaye, V., Aussenac, F., Vizioz, C., Borel, S., Maffini-Alvaro, V., Isheden, C., and Foucher, J. (2007). Synthesis of zno nanorod on bare si substrate using metal organic chemical vapor deposition. *Applied Physics Letters*, 91(23):233502.

Doyle, P. and Turner, P. (1968). Relativistic hartree-fock x-ray and electron scattering factors. *Acta Crystallographica Section A-Crystal Physics Diffraction Theoretical and General Crystallography A*, 24(3):390.

Dupré, C., Ernst, T., Maffini-Alvaro, V., Delaye, V., Hartmann, J., Borel, S., Vizioz, C., Faynot, O., Ghibaudo, G., and Deleonibus, S. (2008). 3d nanowire gate-all-around transistors: Specific integration and electrical features. *Solid-State Electronics*, 52:519–525.

Eastman, D. (1970). Photoelectric work functions of transition, rare-earth, and noble metals. *Physical Review B*, 2(1):1.

Eyben, P., Janssens, T., and Vandervorst, W. (2005). Scanning spreading resistance microscopy (ssrm) 2d carrier profiling for ultra-shallow junction characterization in deep-submicron technologies. *Materials Science and Engineering B*, 124125:4553.

Fazzini, P., Merli, P., Pozzi, G., and Ubaldi, F. (2005). Effects of beam-specimen interaction on the observation of reverse-biased p-n junctions by electron interferometry. *Physical Review B*, 72:085312.

FEI (2007). Application instructions titan 80-300 probe c_s corrector.

Fejes, P. (1977). Approximations for the calculation of high-resolution electron-microscope images of thin films. *Acta Crystallographica A*, 33:109.

Fissel, A., Bugiel, E., Wang, C., and Osten, H. (2006). Formation of si twinning-superlattice: First step towards si polytype growth. *Materials Science and Engineering B*, 134:138–141.

Fontcuberta i Morral, A., Arbiol, J., Prades, J., Cirera, A., and Morante, J. (2007). Synthesis of silicon nanowires withwurtzite crystalline structure by using standard chemical vapor deposition. *Advanced Materials*, 19:1347.

Formanek, P. (2004). *TEM-Holographie of Microelectronic Device Structures*. PhD thesis, Brandenburg University of Technology, Cottbus, Germany.

Fowles, G. (1989). *Introduction to modern optics*. Dover Publications, Inc., New York.

Frank, J. (1973). The envelope function of electron microscopic transfer function for partially coherent illumination. *Optik*, 38(5):519.

Fujita, T., Yamamoto, K., McCartney, M., and Smith, D. (2006). Reconstruction technique for off-axis electron holography using coarse fringes. *Ultramicroscopy*, 106:486491.

Gabor, D. (1948). A new microscopic principle. *Nature*, 161:777.

Geocities.com (2009). `http://www.geocities.com/bioelectrochemistry/nyquist.htm`.

Ghostagore, R. (1970). Experimental-condition dependence of phosphorus diffusivity in silicon. *Physical Review Letters*, 25(13):856.

Givargizov, E. (1975). Fundamental aspects of vls growth. *Journal of Crystal Growth*, 31:20.

Haider, M., Braunhausen, G., and Schwan, E. (1995). Correction of the spherical aberration of a 200 kv tem by means of a hexapole-corrector. *Optik*, 99:167.

Hannon, J., Kodambaka, S., Ross, F., and Tromp, R. (2006). The influence of the surface migra-

tion of gold on the growth of silicon nanowires. *Nature*, 440:69.

Hansen, M. and Anderko, K. (1958). *Composition of Binary Alloys*. McGraw-Hill, New York.

Hardy, D. (1967). *Dissertation*. PhD thesis, University of Cambridge.

Harscher, A. and Lichte, H. (1996). Experimental study of amplitude and phase detection limits in electron holography. *Ultramicroscopy*, 64:57–66.

Hassam, S., Gaune-Escard, M., Bros, J., and Bunsenges, B. (1983). Enthalpies of formation of ag-si, au-si and ag-au-si liquid alloys at 1423 k. *Physical Chemistry*, 87:785.

Hayes, T. (1980). *SEM*. SEM Inc., AMF O'Hare , Illinois.

He, R., Feng, X., Roukes, M., and Yang, P. (2008). Self-transducing silicon nanowire electromechanical systems at room temperature. *Nano Letters*, 8(6):1756–1761.

Hely, H. (1982). Testing of an improved corrected electron microscope. *Optik*, 60:353.

Hendriks, M., Radelaar, S., Beers, A., and Bloem, J. (1984). Additional x-ray and electron diffraction peaks of polycrystalline silicon films. *Thin Solid Films*, 113:59.

Hild, R., Seifert, C., Kammler, M., zu Heringdorf, F. M., Hoegen, M. H., Zhachuk, R., and Olshanetsky, B. (2002). Kinetics of au induced faceting of vicinal si(111). *Surface Science*, 512:117.

Hochbaum, A., Chen, R., Delgado, R., Liang, W., Garnett, E., Najarian, M., Majumdar, A., and Yang, P. (2008). Enhanced thermoelectric performance of rough silicon nanowires. *Nature*, 451:163.

Hofmann, S., Sharma, R., Wirth, C., Cervantes-Sodi, F., Ducati, C., Kasama, T., Dunin-Borkowski, R., Druckers, J., Bennett, P., and Roberston, J. (2008). Ledge-flow-controlled catalyst interface dynamics during si nanowire growth. *Nature Materials*.

Houben, L., Luysberg, M., and Brammer, T. (2004). Illumination effects in holographic imaging of the electrostatic potential of defects and pn junctions in transmission electron microscopy. *Physical Review B*, 70:165313.

Houdellier, F. (2006). *Contribution au développement du CBED et de l'holographie HREM pour l'analyse des déformations de couches épitaxiées*. PhD thesis, Institut National des Sciences Appliquées de Toulouse.

Hoummada, K., Mangelinck, D., Cadel, E., Perrin-Pellegrino, C., Blavette, D., and Deconihout, B. (2007). Formation of ni silicide at room temperature studied by laser atom probe tomography: Nucleation and lateral growth. *Microelectronic Engineering*, 84(11):2517–2522.

Hÿtch, M. J., Snoeck, E., and Kilaas, R. (1998). Quantitative measurement of displacement and strain fields from hrem micrographs. *Ultramicroscopy*, 74(9):131.

Ibers, J. (1958). Atomic scattering amplitudes for electrons. *Acta*, 178:11.

Iijima, S. (1991). Helical microtubules of graphitic carbon. *Nature*, 354:56.

Ikejiri, K., Noborisaka, J., Hara, S., Motohisa, J., and Fukui, T. (2007). Mechanism of catalyst-free growth of gaas nanowires by selective area movpe. *Journal of Crystal Growth*, 298:616.

Iqbal, Z. and Veprek, S. (1982). Raman scattering from hydrogenated microcrystalline and amorphous silicon. *Journal of Physics C: Solid State Physics*, 15:377–392.

Ishizuka, K. (1993). Optimized sampling schemes for off-axis holography. *Ultramicroscopy*, 52:1–5.

JEELS (2008). Journées eels `http://jeels2008.sp2mi.univ-poitiers.fr/`. webpage.

Jeon, M. and Kamisako, K. (2008). Synthesis of silicon nanowires after hydrogen radical treatment. *Materials Letters*, 62:3903.

Johansson, J., Karlsson, L., Patrik, C., Svensson, T., Mårtensson, T., Wacaser, B., Deppert, K., Samuelson, L., and Seifert, W. (2006). Structural properties of $\langle 111 \rangle$ b-oriented iiiv nanowires. *Nature Materials*, 5:574.

Kalkofen, B., Lisker, M., and Burte, E. (2005). Phosphorus diffusion into silicon after vapor phase surface adsorption of phosphine. *Materials Science and Engineering B.*, 124-125:288.

Kempa, T., Tian, B., Kim, D., Hu, J., Zheng, X., and Lieber, C. (2008). Single and tandem axial p-i-n nanowire photovoltaic devices. *Nano Letters*, 8(10):3456–3460.

Kilbride, B. and et al (2002). Experimental observation of scaling laws for alternating current and direct current conductivity in polymercarbon nanotube composite thin films. *Journal of Applied Physics*, 92:4024–4030.

Kim, K. and Kim, H. (2003). Synthesis of zno nanorod on bare si substrate using metal organic chemical vapor deposition. *Physica B*, 328:368371.

Kodambaka, S., Hannon, J., Tromp, R., and Ross, F. (2006a). Control of si nanowire growth by oxygen. *Nano Letters*, 6(6):1292.

Kodambaka, S., Tersoff, J., Reuter, M., and Ross, F. (2006b). Diameter-independent kinetics in the vapor-liquid-solid growth of si nanowires. *Physical Review Letters*, 96:096105.

Kodambaka, S., Tersoff, J., Reuter, M., and Ross, F. (2007). Germanium nanowire growth below the eutectic temperature. *Science*, 316:729.

Kohno, H., Ozaki, N., Yoshida, H., Tanaka, K., and Takeda, S. (2003). Misleading fringes in tem images and diffraction patterns of si nanocrystallites. *Crystal Research Technology*, 38(12):1082–1086.

Koops, H., Kuck, G., and Scherzer, O. (1977). Testing of an electron optical achromator. *Optik*, 48:225.

Korgel, B., Lee, D., Hanrath, T., Yacaman, M., Thesen, A., Matijevic, M., Kilaas, R., Kisielowski, C., and Diebold, A. (2006). Application of aberration-corrected tem and image simulation to nanoelectronics and nanotechnology. *IEEE TRANSACTIONS ON SEMICONDUCTOR MANUFACTURING*, 19(4):391.

Kreyszig, E. (1999). *Advanced Engineering Mathematics 8th edition*. John Wiley & Sons, Inc.

Krivanek, O. (1991). Tahoe workshop on eels.

Kruse, P., Schowalter, M., Lamoen, D., Rosenauer, A., and Gerthsen, D. (2006). Determination of the mean inner potential in iiiv semiconductors, si and ge by density functional theory and electron holography. *Ultramicroscopy*, 106:105–113.

Lancon, F., Penisson, J., and Damen, U. (2000). Quasicrystalline gold interface with a hypo-friction property. *Europhysics Letters*, 49:603.

Latu-Romain, L., Mouchet, C., Cayron, C., Rouviere, E., and Simonato, J. (2008). Growth parameters and shape specific synthesis of silicon nanowires by the vls method. *Journal of Nanopartle Research*, 1388-0764 (Print) 1572-896X (Online):0.1007/s11051–007–9350–3.

Lee, S., Kim, T., Lee, S., Choi, K., and Yang, P. (2007). High-brightness gallium nitride nanowire uv-blue light emitting diodes. *Philosophical magazine*, 87(14):2105–2115.

Lee, S., Minegishi, T., Park, J., Park, S., Ha, J., Lee, H., Lee, H., Ahn, S., Kim, J., Jeon, H., and Yao, T. (2008). Ordered arrays of zno nanorods grown on periodically polarity-inverted surfaces. *Nano Letters*, 8(8):2419–2422.

Lehmann, M. (2004). Influence of the elliptical illumination on acquisition and correction of coherent aberrations in high-resolution electron holography. *Ultramicroscopy*, 100:9–23.

Lehmann, M., Völkl, E., and Lenz, F. (1994). Reconstruction of electron off-axis holograms: a new and fast alternative method. *Ultramicroscopy*, 54:335 344.

Lenz, F. (1988). Statistics of phase and contrast determination in electron holograms. *Optik*, 79(1):13–14.

Li, C., Gu, C., Liu, Z., Mi, J., and Yang, Y. (2005). Iron-catalytic growth of prism-shaped single-crystal silicon nanowires by chemical vapor deposition of silane. *Chemical Physics Letters*, 411:198.

Lichte, H. (1991). Optimum focus for taking electron holograms. *Ultramicroscopy*, 38:12–22.

Lichte, H. (2008a). Esteem holography workshop. Dresden.

Lichte, H. (2008b). Performance limits of electron holography. *Ultramicroscopy*, 108(3):256.

Ligowski, M., Moraru, D., Anwar, M., Mizuno, T., Jablonski, R., and Tabe, M. (2008). Observation of individual dopants in a thin silicon layer by low temperature kelvin probe force microscope. *Applied Physics Letters*, 93:142101.

M. Fernández-Serra, C. A. and Blase, X. (2006). Surface segregation and backscattering in doped silicon nanowires. *Physical Review Letters*, 96:166805.

Mankos, M., Scheinfein, M., and Cowley, J. (1996). Electron holography and lorentz microscopy of magnetic materials. *Advanced Imaging Electron Physics*, 98:323–426.

Massalski, T. (1990). *Binary Alloy Phase Diagram*. American Society for Metal, Metals Park, OH, 2nd edition.

Masseboeuf, A. (2008). *De l'observation du magnétimse à l'échelle du nanomètre*. PhD thesis, Universit Joseph Fourier - Grenoble I.

Matijevic, M., Stegmann, H., Essers, E., and Benner, G. (2007). Recent results of an in-column energy filter tem with monochromator. *Microscopy and Microanalysis*, 13(2):1160.

Matteucci, G., Missiroli, G., Nichelatti, E., Migliori, A., Vanzi, M., and Pozzi, G. (1991). Electron holography of long-range electric and magnetic fields. *Journal of Applied Physics*, 69(4):1835–1842.

Mayers, B. and Xia, Y. (2002). One-dimensional nanostructures of trigonal tellurium with various morphologies can be synthesized using a solution-phase approach. *Journal of Materials Chemistry*, 12(6):1875.

McQuarrie, D. and Simon, J. (1997). *Physical Chemistry, a molecular approach*. University Science Books.

Midgley, P. (2001). An introduction to off-axis electron holography. *Micron*, 32:167–184.

Minoda, H., Yagi, K., zu Heringdorf, F. M., Meier, A., Kähler, D., and von Hoegen, M. H. (1999). Gold-induced faceting on a si(001) vicinal surface: Spot-profile-analyzing leed and reflection-electron-microscopy study. *Physical Review B*, 59(3):2363.

Missiroli, G., Pozzi, G., and Valdre, U. (1981). Electron interferometry and interference electron microscopy. *Journal of Physics E*, 14:649–671.

Miyamoto, Y. and Hirata, M. (1978). x. *Journal of the Physical Society of Japan*, 44:181.

Molina, S., Sánchez, A., Beltrán, A., Sales, D., Ben, T., Chisholm, M., Varela, M., Pennycook, S., Galindo, P., Papworth, A., Goodhew, P., and Ripalda, J. (2007). Incorporation of sb in inas/gaas quantum dots. *Applied Physics Letters*, 91:263105.

Moore, A., Saha, S., Prasher, R., and Shi, L. (2008). Phonon backscattering and thermal conductivity suppression in sawtooth nanowires. *Applied Physics Letters*, 93:083112.

Mouchet, C. (2008). *Croissance de nanofils de silicium et de Si/SiGe*. PhD thesis, Institut Polytechnique de Grenoble.

Müller, P. and Métois, J. (2008). Anisotropy of the surface thermodynamic properties of silicon. *Thin Solid Films*, 517(1):65–68.

Nam, C. and Fischer, J. (2008). Self-branching in gan nanowires induced by a novel vapor-liquid-solid mechanism. In *MRS Proceedings*, volume session JJ4.3, page 832.

Nicollian, E. and Brews, J. (1982). *MOS (Metal Oxide Semiconductor Physics and Technology*. John Wiley & Sons.

Niquet, Y., Lherbier, A., Quang, N., Fernndez-Serra, M., Blase, X., and Delerue, C. (2006). Electronic structure of semiconductor nanowires. *Physical Review B*, 73:165319.

Oehler, F., Gentile, P., Baron, T., den Hertog, M., Rouvière, J., and Ferret, P. (2009a). Morphology of silicon nanowires grown in presence of trimethylaluminium. *submitted to Nanotechnology*, x(x):x.

Oehler, F., Gentile, P., Baron, T., Ferret, P., and Magnea, N. (2009b). Controlling the growth of si nanowires with reactive chlorine: beyond the classical vapour-liquid-solid model. *to be submitted*, x(x):x.

Olsen, R., Bădescu, S., Ying, S., and Baerends, E. (2004). Adsorption and diffusion on a stepped surface: Atomic hydrogen on pt(211). *Journal of Chemistry and Physics*, 120:11852.

Ourmazd, A., Rentschler, J., and Taylor, D. (1986). Direct resolution and identification of the sublattices in compound semiconductors by high-resolution transmission electron microscopy. *Physical Review Letters*, 57:3073.

Pan, L., Lew, K., Redwing, J., and Dickey, E. (2005). Effect of diborane on the microstructure of

boron-doped silicon nanowires. *Journal of Crystal Growth*, 277:428.

Pan, Z., Dai, Z., and Wang, Z. (2001). Nanobelts of semiconducting oxides. *Science*, 219:1947.

Park, W., Kim, D., Jung, S., and Yia, G. (2002). Metalorganic vapor-phase epitaxial growth of vertically well-aligned zno nanorods. *Applied Physics Letters*, 80:4232.

Park, Y., Lee, S., Oh, J., Park, C., and Kang, T. (2005). Self-assembled gannano-rods grown directly on (1 1 1) si substrates: Dependence on growth conditions. *Journal of Crystal Growth*, 282:313–319.

Parsons, J. and Hoelke, C. (1984). Hexagonal germanium and high-resolution electron microscopy. *Philosophical Magazine A*, 50:329.

Pashley, D. and Stowell, M. (1963). Electron microscopy and diffraction of twinned structures in evaporated films of gold. *Philosophical Magazine*, 8(94):1605.

Peng, H., Xie, C., Schoen, D., and Cui, Y. (2008). Large anisotropy of electrical properties in layer-structured in_2se_3 nanowires. *Nano Letters*, 8(5):1511–1516.

Pennycook, S. (2002). Structure determination through z-contrast microscopy. *Advances in Imaging and Electron Physics*, 123:173.

Pennycook, S. and Nellist, P. (1999). Z-contrast scanning transmission electron microscopy. *Impact of Electron and Scanning Probe Microscopy on Materials Research*, pages 161–207.

Penzaa, M., Rossi, R., Alvisi, M., Cassanoa, G., Signorea, M., Serrab, E., and Giorgi, R. (2008). Pt- and pd-nanoclusters functionalized carbon nanotubes networked films for sub-ppm gas sensors. *Sensors and Actuators B*, 135:289297.

Perea, D., Lensch, J., May, S., Wessels, B., and Lauhon, L. (2006). bla. *Journal of Applied Physics*, 85:271.

Pethica, B. (1961). bla. *Repports Programme Applied Chemistry*, 46:14.

Poland, C., Duffin, R., Kinloch, I., Maynard, A., Wallace, W., Seaton, A., Stone, V., Brown, S., MacNee, W., and Donaldson, K. (2008). Carbon nanotubes introduced into the abdominal cavity of mice show asbestos-like pathogenicity in a pilot study. *Nature Nanotechnology*, 3:423–428.

Popescu, R., Muller, E., Wanner, M., Gerthsen, D., Schowalter, M., Rosenauer, A., Bottcher, A., Loffler, D., and Weis, P. (2007). Increase of the mean inner coulomb potential in au clusters induced by surface tension and its implication for electron scattering. *Physical Review B*, 76(23):235411.

Potapov, P., Verbeeck, J., Schattschneider, P., Lichte, H., and van Dyck, D. (2007). Inelastic electron holography as a variant of the feynman thought experiment. *Ultramicroscopy*, 107:559–567.

Prades, J., Arbiol, J., Cirera, A., Morante, J., and i Morral, A. F. (2007). Concerning the $506\,cm^{-1}$ band in the raman spectrum of silicon nanowires. *Applied Physics Letters*, 91(12):123107.

Putnam, C., Filler, M., Kayes, B., Kelzenberg, M., and Atwater, H. (2007). Nanoscale chemical characterization of vapor-liquid-solid grown silicon wires by secondary ion mass spetrometry. In *MRS Fall Proceedings*, page 835.

Radi, G. (1970). Complex lattice potentials in electron diffraction calculated for a number of crystals. *Acta Crystallographica Section A-Crystal Physics Diffraction Theoretical and General Crystallography A*, 26(1):41.

Rau, W., Schwander, P., Baumann, F., Höppner, W., , and Ourmazd, A. (1999). Two-dimensional mapping of the electrostatic potential in transistors by electron holography. *Physical Review Letters*, 82(12):2614.

Reddick, W. and Amaratunga, A. (1995). Silicon surface tunnel transistor. *Applied Physics Letters*, 67:495.

Ressel, B., Prince, K., and Heun, S. (2003). Wetting of si surfaces by ausi liquid alloys. *Journal of Applied Physics*, 93:3886.

Rodenburg, J. (2008). `http://www.rodenburg.org/guide/t700.html`. webpage.

Rose, H. and Kisielowski, C. (2005). On the reciprocity of tem and stem. *Microscopy and Microanalysis*, 11(2):2114.

Ross, F., Tersoff, J., and Reuter, M. (2005). Sawtooth faceting in silicon nanowires. *Physical Review Letters*, 95:146104.

Schattschneider, P., Nelhiebel, M., Souchay, H., and Jouffrey, B. (2000). The physical significance of the mixed dynamic form factor. *Micron*, 31:333345.

Schmid, H., Björk, M., Knoch, J., Karg, S., Riel, H., and Riess, W. (2009). Doping limits of grown in situ doped silicon nanowires using phosphine. *Nano Letters*, 9(1):173–177.

Schmid, H., Björk, M., Knoch, J., Riel, H., Riess, W., Rice, P., and Topuria, T. (2007). Patterned epitaxial vapor-liquid-solid growth of silicon nanowires on si(111) using silane. *Journal of Applied Physics*, 103:024304.

Schmidt, V. and Gösele, U. (2008). Confidential meeting for node project.

Schmidt, V., Senz, S., and Gösele, U. (2004). The shape of epitaxially grown silicon nanowires and the influence of line tension. *Applied Physics A*, 80(4):445.

Schmidt, V., Senz, S., and Gösele., U. (2005). Diameter-dependent growth direction of epitaxial silicon nanowires. *Nano Letters*, 5:931.

Schmidt, V., Senz, S., and Gösele, U. (2007a). Diameter dependence of the growth velocity of silicon nanowires synthesized via the vapor-liquid-solid mechanism. *Physical Review B*, 75:045335.

Schmidt, V., Senz, S., and Gösele, U. (2007b). Inuence of the si/sio_2 interface on the charge carrier density of si nanowires. *Applied Physics A*, 86:187 191.

Schofield, M., Beleggia, M., Zhu, Y., and Pozzi, G. (2008). Characterization of jeol 2100f lorentz-tem for low-magnification electron holography and magnetic imaging. *Ultramicroscopy*, 108:625–634.

Seehofer, L., Huths, S., Falkenberg, G., and Johnson, R. (1995). Gold-induced facetting of si(111). *Surface Science*, 329:157.

Shpyrko, O., Streitel, R., Balagurusamy, V., Grigoriev, A., Deutsch, M., Ocko, B., Meron, M., Lin, B., and Pershan, P. (2006). Surface crystallization in a liquid ausi alloy. *Science*, 313:7.

Silvaco International (2007). Atlas user manual. Santa Clara, CA.

Singh, N. and et al. (2006). High-performance fully depleted silicon nanowire (diameter =5nm) gate-all-around cmos devices. *IEEE Electron Device Letters*, 27:383.

Slezák, J., Ondřejček, M., Chvoj, Z., and Cháb, V. (2000). Surface diffusion of au on si (111): A microscopic study. *Physical Review B*, 61(23):16121.

Spence, J. and Zuo, J. (1992). *Electron Microdiffraction*. Plenum Press, New York.

Spoon, H. (2003). *Mid-infrared Spectroscopy of Dusty Galactic Nuclei*. PhD thesis, University of Groningen.

Stadelmann, P. (2008). `http://cimewww.epfl.ch/people/stadelmann/jemsWebSite/jems.html`. webpage.

Stoddard, N., Duscher, G., Windl, W., and Rozgonyi, G. (2005). A new understanding of near-threshold damage for 200 kev irradiation in silicon. *Journal of Materials Science*, 40:3639–3650.

Stokes, H. (2008). `http://stokes.byu.edu/diamond.htm`.

Sun, Y., Graff, R., Strano, M., and Rogers, J. (2005). Top-down fabrication of semiconductor nanowires with alternating structures along their longitudinal and transverse axes. *Small*, 1(11):1052–1057.

Sze, S. (1985). *Semiconductor devices Physics and Technology*. John Wiley & Sons.

Tavendale, A. and Pearton, S. (1983). Deep level, quenched-in defects in silicon doped with gold, silver, iron, copper or nickel. *Journal of Physics C: Solid state Physics*, 16:1665.

TEAM (2008). Team project.

Thelander, C., Fröberg, L., Rehnstedt, C., Samuelson, L., and Wernersson, L. (2008). Vertical enhancement-mode inas nanowire field-effect transistor with 50-nm wrap gate. *IEEE Electron Device Letters*, 29:206.

Thibault, J., Rouvière, J., and Bourret, A. (1996). *Materials Science and Technology, Volume 4, Electronic Structure and Properties of Semiconductors, chapter 7, Grain Boundaries in Semiconductors*. Wiley-VCH.

Tipler, P. (1999). *Physics*. W.H. Freeman and Copmany/ Worth Publishers.

T.Kawashima, Mizutani, T., Nakagawa, T., Torii, H., Saitoh, T., Komori, K., and Fujii, M. (2008). Control of surface migration of gold particles on si nanowires. *Nano Letters*, xx:xx.

Tsakalakos, L. (2008). Nanostructures for photovoltaics. *Materials Science and Engineering: R*.

Tuan, H., Ghezelbash, A., and Korgel, B. (2008). Silicon nanowires and silica nanotubes seeded by copper nanoparticles in an organic solvent. *Chemistry of Materials*, 20(6):2306.

Turner, M., Golovko, V., Vaughan, O., Abdulkin, P., Berenguer-Murcia, A., Tikhov, M., Johnson, B., and Lambert, R. (2008). Selective oxidation with dioxygen by gold nanoparticle catalysts derived from 55-atom clusters. *Nature*, 454:981–983.

Twitchett, A., Dunin-Borkowski, R., Broom, R., and Midgley, P. (2004). Quantitative electron

holography of biased semiconductor devices. *Journal of Physics: Condensed Matter*, 16:S181.

Twitchett, A., Dunin-Borkowski, R., and Midgley, P. (2002). Quantitative electron holography of biased semiconductor devices. *Physical Review Letters*, 88(23):238302.

Twitchett-Harrison, A., Yates, T., Newcomb, S., Dunin-Borkowski, R., and Midgley, P. (2007). High-resolution three-dimensional mapping of semiconductor dopant potentials. *Nano Letters*, 7(7):2020–2023.

van der Walt, G. (2009). `http://4.bp.blogspot.com/_1okg6FxI_og/SSvqIG82MrI/AAAAAAAACyA/TiaRNYXEcY0/s1600/Blog+-+Double.jpg`.

Verbeeck, J., van Dyck, D., Lichte, H., Potapov, P., and Schattschneider, P. (2005). Plasmon holographic experiments: theoretical framework. *Ultramicroscopy*, 102:239255.

Verd, J., Abadal, G., Teva, J., Gaudó, M. V., Uranga, A., Borrisé, X., Campabadal, F., Esteve, J., Costa, E. F., Pérez-Murano, F., Davis, Z., Forsén, E., Boisen, A., and Barniol, N. (2005). Design, fabrication, and characterization of a submicroelectromechanical resonator with monolithically integrated cmos readout circuit. *Journal of Microelectromechanical Systems*, 14(3):508.

Völkl, E., Allard, L., and (Editors), D. J. (1999). *Introduction to Electron Holography*. Academic / Plenum Publishers, New York, ISBN 0-306-44920-X.

Voyles, P., Muller, D., Grazul, J., Citrin, P., and Gossmann, H. (2002). Atomic-scale imaging of individual dopant atoms and clusters in highly n-type bulk si. *Nature*, 416:826.

Wagner, R. (1966). Branching, kinking and defect formation during vls growth. *Proceedings of an international conference on crystal growth*, page 347.

Wagner, R. and Doherty, C. (1968). Mechanism of branching and kinking during vls crystal growth. *Journal of the Electrochemical Society: Solid State Science*, 115:93.

Wagner, R. and Ellis, W. (1965). wires. *Trans. Met. Soc. AIME*, 233:1053.

Walck, S. and McCaffrey, J. (1997). The small angle cleavage techique applied to coatings and thin films. *Thin Solid Films*, 399:308.

Wang, J., Rahman, A., Klimeck, G., and Lundstrom, M. (2005). Bandstructure and orientation effects in ballistic si and ge nanowire fets. *IEEE*, 4.

Wang, Y., Schmidt, V., Senz, S., and Gösele, U. (2008). Epitaxial growth of silicon nanowires using an aluminium catalyst. *Nature Nanotechnology*.

Watanabe, T. (1985). Structural effects on grain boundary segragation, hardening and fracture. *Journal de Physique*, C4(13):555–566.

Wentorf, R. and Kasper, J. (1963). Two new forms of silicon. *Science*, 139:338.

Werner, P., Zakharov, N., Gerth, G., Schubert, L., and Gösele, U. (2006). On the formation of si nanowires by molecular beam epitaxy. *International Journal of Materials Research*, 97:1008.

Widom, B. (1995). bla. *Journal of Physical Chemistry*, 99:2803.

Wiethoff, C., Ross, F., Copel, M., von Hoegen, M. H., and zu Heringdorf, F. M. (2008). Au stabilization and coverage of sawtooth facets on si nanowires grown by vapor-liquid-solid

epitaxy. *Nano Letters*, 8(9):3065–3068.

Wikipedia (2009). `http://en.wikipedia.org/wiki/Moire`.

Wilcoxon, J., Martin, J., Parsapour, F., Wiedenman, B., and Kelley, D. (1998). Photoluminescence from nanosize gold clusters. *Journal of Chemical Physics*, 108(21):9137.

Williams, D. and Carter, C. (1996). *Transmission Electron Microscopy*. Springer.

Wong, Y., Yahaya, M., Salleh, M. M., and Majlis, B. Y. (2005). Controlled growth of silicon nanowires synthesized via solid-liquid-solid mechanism. *Science and Technology of Advanced Materials*, 6:330.

Wu, Y., Cui, Y., Huynh, L., Barrelet, C., Bell, D., and Lieber, C. (2004). Controlled growth and structures of molecular-scale silicon nanowires. *Nano Letters*, 4:433.

Xia, Y., Yang, P., Sun, Y., Wu, Y., Mayers, B., Gates, B., Yin, Y., Kim, F., and Yan, Y. (2003). One-dimensional nanostructures: Synthesis, characterization, and applications. *Advanced Materials*, 15(5):353.

Xiang, J. and et al. (2006). Ge/si nanowire heterostructures as high-performance field-effect transistors. *Nature*, 441:489.

Yamamotoa, K., Tanji, T., and Hibino, M. (2000). Hologram simulation for off-axis electron holography. *Ultramicroscopy*, 85:35–49.

Yamasaki, J., okunishi, E., Sawada, H., and Tanaka, N. (2007). Direct observation of site hopping of individual dopant atoms in si crystal by cs-corrected stem. *Microscopy and Microanalysis*, 13(2):1186.

Yang, C., Zhong, Z., and Lieber, C. (2005). Encoding electronic properties by synthesis of axial modulation-doped silicon nanowires. *Science*, 310:1304.

Yao, J., Liu, Z., Liu, Y., Wang, Y., Sun, C., Bartal, G., Stacy, A., and Zhang, X. (2008). Optical negative refraction in bulk metamaterials of nanowires. *Science*, 321(5891):930.

Zelsacher, R., Wood, A., Bacher, E., Prax, E., Sorschag, K., Krumrey, J., and Baumgart, J. (2007). A novel sims based approach to the characterization of the channel doping profile of a trench mosfet. *Microelectronics Reliability*, 47(9-11):1585–1589.

Zhang, X. (2001). *Electrochemistry of silicon and its oxide*. Springer New York.

Zhang, Y., Iqbal, Z., Vijayalakshmi, S., and Grebel, H. (1999a). Stable hexagonal-wurtzite silicon phase by laser ablation. *Applied Physics Letters*, 75:2758.

Zhang, Y., Iqbal, Z., Vijayalakshmi, S., and Grebelb, H. (1999b). Stable hexagonal-wurtzite silicon phase by laser ablation. *Applied Physics Letters*, 75(18):2758.

Zhang, Y., Iqbal, Z., Vijayalakshmi, S., Qadri, S., and Grebel, H. (2000). Formation of hexagonal-wurtzite germanium by pulsed laser ablation. *Solid Sate Communications*, 115:657.

Zhou, G. and Zhang, Z. (1998). Transmission electron microscopy study of si nanowires. *Applied Physics Letters*, 73:677.

Zhou, G., Zhang, Z., and Yu, D. (1999). Growth morphology and micro-structural aspects of si nanowires synthesized by laser ablation. *Journal of Crystal Growth*, 197:129.

Zuo, J. (2004). Measurements of electron densities in solids: a real-space view of electronic structure and bonding in inorganic crystals. *Rep. Prog. Phys.*, 67:2053.

5 Cours Berriat, 38000 Grenoble, France
Tel. +33 6 88 54 42 10
Email: martien.den-hertog@grenoble.cnrs.fr
Dutch nationality, born December 29, 1980

Curriculum Vitae – Martien den Hertog

Academic Background

2009 • Doctorate Physics (mention très bien), CEA-Grenoble INAC-SP2M-LEMMA, Univerité Joseph Fourier, France. Advisor: Dr. J.L. Rouvière. Thesis: *Caractérisation de nanofils de silicium par microscopie électronique en transmission*. Funded by the European Community under the Sixth Framework Programme for the Marie Curie Host Fellowships for Early Stage Research Training (EST) "CHEMTRONICS" Contract Number MEST-CT-2005-020513.

2005 • Master of Science programme "Chemistry and Physics" (with honours), Department of Chemistry and Debeye Institute, University of Utrecht, the Netherlands. Advisor: Prof. Dr. A. Polman. Thesis: *Pulsed CO_2 laser printing and smoothing of Si quantum dot solids* . Advisor: Prof. Dr. P. van der Straten. Thesis: *Measuring the temperature of a Rb MOT using an oscillating magnetic field* .

2003 • Bachelor of Science Chemistry (with honours), Department of Chemistry, University of Utrecht, the Netherlands. Advisors: Prof. Dr. A. Meijerink and Dr. P. Vergeer. Thesis: *Cooperative quantumsplitting In the $(YbxY_{0.99-x})_2O_3$:Tb1% system.*

Employment

Since 2009 • Postdoc, CNRS Institut Néel, Grenoble, France.

2006-2009 • Doctorate, CEA-Grenoble INAC-SP2M-LEMMA, France.

2003-2004 • Employee of Utrecht Chemistry shop: an organisation to advise consumers and non-profit organisations on chemistry related topics

Professional Activities

Participation in Research Projects

2008-2009 • Informal collaboration with IBM Zurich focused on dopant characterization in silicon nanowires, a personal initiative.

2006-2009 • *Chemtronics*, transversal programme coupling fundamental and applied sciences around nano-objects and give the participating international PhD students a broad training involving industry and valorization of scientific findings. Funded by the European Community under the Sixth Framework Programme for the Marie Curie Host Fellowships for Early Stage Research Training (EST) "CHEMTRONICS" Contract Number MEST-CT-2005-020513.

2006-2009 • *Chimtronique*, broad transversal programme coupling fundamental and applied sciences around nano-objects, funded by the Funded by the European Community Marie Curie, French national research agency (ANR) and CARNOT projects.

2006-2009 • *Développement de métrologies 2D et 3D pour la cartographie des dopants dans les nanostructures de semiconducteur (CARTODOP)*, funded by French national research agency (ANR).

2006-2009 • *Propriétés Electroniques d'Assemblages Autoorganisés à base de Nanofils (PREEANs)*, funded by the French national research agency (ANR).

Teaching

2009 • Practical training course on TEM sample preparation (9 hours), Prominas Marie Curie Conferences and training courses, Grenoble, France.

References

- Dr. Jean-Luc Rouvière, researcher working on Transmission Electron Microscopy at CEA-Grenoble, INAC, LEMMA. Email: jean-luc.rouviere@cea.fr
- Prof. Dr. Albert Polman, scientific group leader and director of the FOM-Institute for Atomic and Molecular Physics (AMOLF), Amsterdam, The Netherlands. He is associated with the University of Utrecht as a professor of nanophotonics and is part-time visiting associate in the Faculty of Applied Physics at the California Institute of Technology (CALTECH), Pasadena. Email: A.Polman@amolf.nl

Professional Activities (continued)

- Prof. Dr. Peter van der Straten, researcher in the Atom Optics group, Debye Institute, University of Utrecht, the Netherlands. Email: p.vanderstraten@phys.uu.nl

Miscellaneous

Language Skills

- Dutch (native)
- French (proficient)
- English (proficient)
- Spanish (moderate)
- German (basic).

Software Skills

- Origin
- Femlab
- Gnuplot
- Matlab
- Digital Micrograph
- Deckbuild, Tonyplot (Silvaco simulation software)
- MS Office, Latex

Invited Seminars

2008 • Laboratoire Nanophysique et Semiconducteurs (NPSC), Grenoble, France, *Structural and electronic properties of silicon nanowires*, 19 september.

Conferences

2009 • Microscopy of Semiconduction Materials, Oxford, U.K., *Dopant mapping in silicon nanowires using Off-axis Electron Holography*, oral presentation.

2008 • European Microscopy Conference, Aachen, Germany, *Control of gold surface diffusion on silicon nanowires*, poster presentation.

2008 • Holography workshop 2008, Dresden, Germany, *Electron Holography of silicon nanowires*, oral presentation.

2007 • Société Franąise des Microscopies Colloque 2007, Grenoble, France, *Structural properties of Gold Catalyzed Silicon Nanowires: Defects in the wires and Gold on the Wires*, oral presentation.

2007 • GDR nanofils, Lyon, France, *Defects in the wires and Gold on the Wires*, oral presentation.

2007 • Microscopy of Semiconduction Materials, Camebridge, U.K., *Gold Catalyzed Silicon Nanowires: Defects in the wires and Gold on the Wires*

2006 • Trends iN Nanotechnology 2006, Grenoble, France, *Evidence of gold on lateral surfaces of gold catalyzed silicon nanowires*, poster presentation that received an award.

2006 • JMC, Toulouse, France. GDR nanofils, Lille, France. Poster presentations.

Extra curricular activities

2001-2006 • Climbing instructor for the Utrecht Student Alpine Association.

2004-2005 • Member of the Chemistry faculty board, University of Utrecht.

2003-2005 • Head of the committee of (climbing) education of the Utrecht Student Alpine Association. Design and implementation of a new education system allowing education of more people with the same amount of resources (instructors and time).

2002-2003 • Member of the board of the Utrecht Student Alpine Association. Achievements: sorting out the finances of the Club and generating an effective and steady growth of members of 40 %.

2001 • Climbing instructor education.

1999 • Intensive Spanish language courses in Salamanca.

Publications

As a first author

2009 • M. den Hertog, H. Schmid, D. Cooper, J.L. Rouviere, M.T. Björk, H. Riel, P. Rivallin, S. Karg and Walter Riess.
Mapping active dopants in single silicon nanowires using off-axis electron holography, accepted for publication in Nanoletters.

2009 • M. den Hertog, J.L. Rouviere, H. Schmid, D. Cooper, M. T. Bjrk, H. Riel, F. Dhalluin, P. Gentile, P. Ferret, F. Oehler, T. Baron, P. Rivallin, S. Karg and W. Riess.
Off axis holography of doped and intrinsic silicon nanowires: Interpretation and influence of fields in the vacuum, Proceeding MSM (2009) Oxford.

2008 • M.I. den Hertog, J.L. Rouviere, F. Dhalluin, P.J. Desré, P. Gentile, P. Ferret, F. Oehler and T. Baron.
Control of Gold Surface Diffusion on Si Nanowires, Nanoletters **8**, p. 1544 (2008).

2007 • M.I. den Hertog, J.L. Rouviere, F. Dhalluin, P. Gentile, P. Ferret, C. Ternon and T. Baron.
Gold Catalyzed Silicon Nanowires: Defects in the wires and Gold on the Wires,
Proceeding MSM (2007) Camebridge p. 217.

As a contributing author

2009 • C. Cayron, M. Den Hertog, L. Latu-Romain, C. Mouchet, C. Secouard, J.L. Rouviere, E. Rouviere and J.P. Simonato.
Odd electron diffraction patterns in silicon nanowires and silicon thin films explained by microtwins and nanotwins, Journal of Applied Crystallography **42**, p. 242-252 (2009).

2009 • F. Oehler, P. Gentile, T. Baron, M. Den Hertog, J.L. Rouviere, P. Ferret.
The morphology of silicon nanowires grown in the presence of trimethylaluminium, Nanotechnology **20**, p. 245602 (2009).

2009 • Salem B, Dhalluin F, Baron T, Jamgotchian H, Bedu F, Dallaporta H, Gentile R, Pauc N, den Hertog MI, Rouviere JL, Ferret P.
Chemical-vapour-deposition growth and electrical characterization of intrinsic silicon nanowires, Materials Science and Engineering B **159-60**, p. 83 (2009).

2008 • P. Gentile, T. David, F. Dhalluin, D. Buttard, N. Pauc, M. Den Hertog, P. Ferret and T. Baron.
The growth of small diameter silicon nanowires to nanotrees, Nanotechnology **19**, p. 125608 (2008).

2008 • D. Buttard, T. David, P. Gentile, M. Den Hertog, T. Baron, P. Ferret and J.L. Rouviere.
A new architecture for self-organized silicon nanowire growth integrated on a (100) silicon substrate, Physica Status Solidi A **205**, p. 1606, (2008).

2007 • F. Dhalluin, P.J. Desré, M.I. den Hertog, J.L. Rouviere, P. Ferret, P. Gentil and T. Baron.
Critical condition for growth of silicon nanowires, Journal of Applied Physics **102**, p. 094906 (2007).

2005 • P. Vergeer, T. J. H. Vlugt, M. H. F. Kox, M. I. den Hertog, J. P. J. M. van der Eerden and A. Meijerink.
Quantum cutting by cooperative energy transfer in $Yb_xY_{1-x}PO_4$*:*Tb^{3+}, Physical review B **71**, p. 014119 (2007).

In Preparation

2009 • M. den Hertog, C. Cayron, J.L. Rouviere, F. Oehler, P. Gentile, F. Dhalluin and T. Baron.
Characterization of misleading twin defects in silicon nanowires, manuscript in preparation, to be submitted to Nanoletters.

Patents

2008 • F. Oehler, M. den Hertog, J.L. Rouviere and F. Dhalluin
BD10175
PROCÉDÉ DE PRÉPARATION DE NANOSTRUCTURES PAR DÉPÔT CHIMIQUE EN PHASE VAPEUR.

Résumé

Le but de cette thèse a été à la fois de mieux comprendre les mécanismes de croissance de nanofils de silicium fait par le procédé Vapeur Liquide Solide, et aussi de contrôler la structure cristalline, la composition chimique et les propriétés électroniques grâce à la microscopie électronique en transmission (MET).

Un premier sujet de recherche a été le comportement du catalyseur d'or pendant la croissance. Nous avons démontré que pendant la croissance, l'or peut diffuser sur les flancs des nanofils. Ensuite nous avons trouvé les paramètres de croissance pour contrôler cette diffusion : la pression partielle du silane et la température. Selon les paramètres de croissance les propriétés des flancs des nanofils sont modifiées lorsque le silane est absorbé sur les flancs, ce qui empêche ensuite l'or de diffuser. Il y a également un effet de taille sur le phénomène de diffusion.

Dans un deuxième temps, une étude des propriétés cristallographiques des nanofils a été menée. Nous avons étudié la direction de croissance et l'apparition de facettes sur les flancs. En général, peu de défauts sont présents dans les fils catalysés par or avec le silane comme précurseur. Lorsque d'autres métaux catalyseurs ou gaz précurseurs sont introduits, la densité des défauts, surtout celle des macles verticales, peut augmenter considérablement. Pour cette raison des grains différents présents dans le cristal peuvent se superposer dans l'image MET ou cliché de diffraction, ce qui est interprété dans la littérature comme étant une phase hexagonale. Grâce à une tranche de fil préparée par FIB nous démontrons clairement qu'il ny a pas de phase hexagonale. Néanmoins une haute densité de macles peut immiter une phase hexagonale sur quelques plans atomiques.

Enfin, une étude des dopants actifs par holographie électronique a été réalisée. Nous montrons pour la première fois un contraste de dopants dans les nanofils fins avec une modulation du dopage axial. Le but de ces mesures est de déterminer la concentration en dopants. La mesure des dopants d'une concentration de 10^{18} at. cm^{-3} par rapport au silicium intrinsèque est possible dans des fils de 60 nm de diamètre. La comparaison entre expériences et simulations du potentiel montre que l'état de surface, et plus précisément la quantité de charge sur ou proche de la surface, sont extrêmement importants pour la distribution du potentiel dans une telle structure. La quantité de charge sur l'interface fils-oxyde est de l'ordre de -1x10^{12} e.c. (charge électronique) cm^{-2}, ce qui s'accorde parfaitement avec la quantité de charge trouvée par mesures du transport.

Mots-clés : nanofils, silicium, TEM, holographie, défaut, dopage, phosphine, diffusion d'or, démouillage.

Abstract

The goal of this thesis was to better understand and control nanowire growth by the Vapour Liquid Solid method, by means of structural, chemical and electronic characterization of nanowires using transmission electron microscopy.

A first subject of study was the behavior of the gold catalyst particle. We have shown that control can be obtained over gold diffusion from the catalyst particle over the nanowire sidewall, by changing the growth parameters, which in turn influence the nanowire sidewall properties. The quantity of absorbed silane at the nanowire sidewall seems to be the important parameter, that depends both on silane partial pressure and temperature and also an effect of nanowire size was observed.

A second topic was the crystallographic properties of the wires. The growth direction and sidewall faceting were studied. In general the crystalline quality of wires grown with a gold catalyst using silane was high. If other catalyst materials or precursor gasses were used more defects were observed. Especially in nanowires grown with a Ni catalyst and with a gold catalyst in combination with TMA, many vertical twin defects are present, as observed in an FIB prepared wire section sample. Therefore the different grains can superpose in the TEM image/DP, which can be falsely interpreted as a wurtzite hexagonal crystal structure. Clear evidence shows that in the observed nanowires no hexagonal phase (with long range order) was present, but a high twin defect density can mimic a hexagonal structure on the length of a few atomic planes.

A third theme was active dopant detection using off-axis electron holography. We show for the first time doping contrast in thin (60 nm) nanowires with axially modulated doping. Using off axis electron holography the electrical properties of nanowires with axially modulated doping were studied, with the goal to determine the active dopant concentration. We show that active dopant detection is possible in nanostructures such as nanowires. Doping concentrations as low as 10^{18} at. cm^{-3} can be detected with respect to intrinsic silicon in nanowires as thin as 60 nm. Potential simulations have been performed to better understand the experimental results. Comparison of experiments and simulations shows that the surface properties of these nanostructures, and more specifically the amount of charge present at or near the surface, are extremely important for the potential distribution in the structure. The estimated amount of charge present at the wire-oxide interface is -1x10^{12} e.c. (electron charges) cm^{-2}, which is in excellent agreement with the amount of charge estimated from transport measurements.

Keywords : nanowires, silicon, TEM, holography, defects, doping, phosphine, gold diffusion, dewetting.